Investigations of the Nature, Properties and Distribution of Defects in Diamond

by

Sinéad Mottishaw

Submitted to the University of Warwick

for the degree of

Doctor of Philosophy

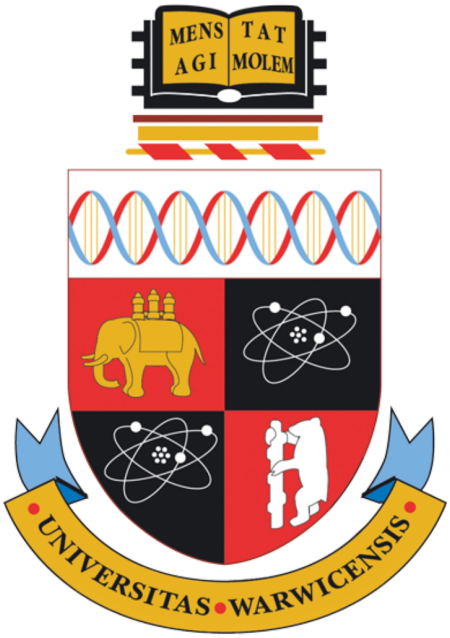

Department of Physics

September 2017

Contents

List of Figures

List of Tables

Acknowledgements

I would like to thank Professor Mark Newton for his patience and supervision and I would also like to thank Dr Gavin Morley for his advice and guidance.

Thank you also to Dr Mark Munday and Dr Jacqueline Hall at E6 global innovations for the provision of samples and helpful discussions.

Dr Brad Cann, Dr David Fisher, Dr Philip Martineau and Christina Martins at De Beers, Maidenhead have also been extremely helpful, and I wish to thank them for their time and guidance with samples, equipment and deciphering results.

In the second year of my PhD, I enjoyed a fortnight in Japan at the Atomic Energy Agency in Takasaki. I would like to thank Professor Junuchi Isoya and Dr Shinobu Onoda along with the rest of the group for their hospitality.

I am grateful to Dr John Craven from the University of Edinburgh for his valuable technical assistance.

I am indebted to the rest of the diamond group here at Warwick without whom I would not have got this far. I would like to express a heartfelt thank you to Matthew, Ben One and Ben Two for their expertise and patience over the years, and to Colin, Phil, Angelo, Enrik, Claudio, Mika and Anton for motivation, enthusiasm and cake.

I would like to thank my parents and my sister, Fionnuala, for their support and confidence in me. And finally, I would like to thank my husband, Matthew, for his unwavering love and encouragement.

Declaration and Published Work

I declare that the work presented in this thesis is my own except where stated otherwise, and was carried out entirely at the University of Warwick, during the period of October 2013 to September 2017, under the supervision of Dr M. E. Newton. The research reported here has not been submitted, either wholly or in part, in this or any other academic institution for admission to a higher degree. Some parts of the work reported and other work not reported in this thesis have been published or have been submitted for publication, as listed below.

Published Papers

B. L. Green, S. Mottishaw, B. G. Breeze, A. M Edmonds, U. F. S. D'Haenens-Johansson, M. W. Doherty, S. D. Williams, D. J. Twitchen and M. E. Newton. *The neutral silicon-vacancy centre in diamond: spin polarization and lifetimes.* Physical Review Letters, 119(9), 96402 (2017)

Conference Presentations

S. Mottishaw, B. L. Green. and M. E. Newton, *Polarisation and relaxation of the neutral silicon vacancy*, 68th De Beers Diamond Conference, University of Warwick, Coventry, United Kingdom, poster presentation (2017)

S. Mottishaw, B. L. Green, C. Wedge and M. E. Newton, *Investigating the energy level structure of silicon vacancy centre in diamond*, 67th De Beers Diamond Conference, University of Warwick, Coventry, United Kingdom, poster presentation (2016)

S. Mottishaw, B. L. Green, C. Wedge and M. E. Newton, *Wavelength dependence*

of the polarisation of silicon vacancy centres, iMR-CDT Conference, Marwell Zoo Conference Centre, Winchester, United Kingdom, oral presentation (2016)

S. Mottishaw, *Colour centres in diamond*, Café Academique, University of Warwick, Coventry, United Kingdom, oral presentation (2015)

S. Mottishaw, *Quantum computing using diamond*, Postgraduate Physics Seminar, University of Warwick, Coventry, United Kingdom, oral presentation (2015)

S. Mottishaw, C. Wedge and M. E. Newton, *Towards optically detected magnetic resonance from the neutral silicon vacancy centre in diamond*, 66th De Beers Diamond Conference, University of Warwick, Coventry, United Kingdom, poster presentation (2015)

S. Mottishaw, C. Wedge and M. E. Newton, *Properties of silicon in diamond measured using electron paramagnetic resonance*, iMR-CDT Conference, University of Warwick, Coventry, United Kingdom, poster presentation (2015)

S. Mottishaw and M. E. Newton, *The silicon vacancy centre in diamond*, St Andrews - Dundee EPR Group Meeting, University of Dundee, Dundee, United Kingdom, oral presentation (2014)

Sinéad Mottishaw

September 2017

Abstract

This thesis presents investigations into the nature, properties and distribution of defects in diamond grown by the methods of chemical vapour deposition (CVD) and high pressure, high temperature (HPHT) synthesis. The experimental techniques used include electron paramagnetic resonance, optical absorption, cathodoluminescence, photoluminescence and secondary ion mass spectroscopy (SIMS).

The optical spin polarisation of the neutral silicon vacancy defect (SiV^0) was shown to be strongly enhanced by resonant excitation at the zero-phonon energy, although there was significant sample to sample variation in the magnitude. The spin polarisation mechanism is different to that observed for the negatively charged nitrogen vacancy defect in diamond and more than one mechanism may be generating spin polarisation. The spin-lattice relaxation time (T_1) of the SiV^0 ground state was found to change by six orders of magnitude between room temperature and 11 K, where T_1 exceeded 25 seconds. At room temperature the achievable optical ground state spin polarisation is limited by the rapid spin-lattice relaxation.

Irradiation and annealing studies of silicon doped CVD diamond samples showed that the silicon vacancy concentration can be increased by irradiation and annealing. However, the same processing conditions can also reduce the concentration of grown-in silicon vacancy defects. This work suggests that the relative incorporation efficiency of silicon in different forms in homoepitaxial CVD diamond may depend on the orientation of the substrate, and that the details of post growth silicon vacancy defect production, especially in boron doped diamond, are not yet well understood.

HPHT samples in which the ^{13}C isotopic abundance had been increased up to approximately 10% were studied. The variation of the abundance of ^{13}C with distance from the seed was studied using Raman spectroscopy and SIMS, and the nitrogen incorporation by infrared microscopy. Possible explanations of the variations in both are discussed.

The incorporation of point and extended defects into diamond grown by heteroepitaxial CVD was studied in a nitrogen doped sample and another grown with efforts to exclude nitrogen. The samples were highly birefringent when observed through cross-polarisers and exhibited strong dislocation related photoluminescence, suggesting significant concentrations of dislocations and dislocation bundles. The nitrogen doped heteroepitaxial CVD sample contained point defects in relative concentrations typically observed in nitrogen doped homoepitaxial CVD diamond; the total nitrogen impurity concentration exceeded 2,000 ppb, whereas in the intrinsic heteroepitaxial CVD sample it was less than a few ppb. Both samples contained a significant concentration of silicon vacancy defects and the photoluminescence spectra indicated that the point defects were subject to significant strain arising from both extended and point defects.

Abbreviations

[X]	Concentration of X
B_0	Static magnetic field
B_1	Microwave magnetic field
B_{mod}	Modulation magnetic field
CVD	Chemical Vapour Deposition
cw	Continuous wave
DFT	Density Functional Theory
E	Energy
EPR	Electron Paramagnetic Resonance
FTIR	Fourier transform infrared
FWHM	Full width at half maximum
g_e	g value for free electron
HPHT	High Pressure High Temperature
IR	Infrared
k_b	Boltzmann constant
M	Magnetisation
m_s	Electron spin state
PL	Photoluminescence
ppb	Parts per billion atomic density
ppm	Parts per million atomic density
Q	Quality factor

S	Spin of an electron
SIMS	Secondary Ion Mass Spectroscopy
T_1	Spin-lattice relaxation time
T_2	Spin-spin relaxation time
UV/vis	Ultraviolet/visible
ZPL	Zero-phonon line
λ	Wavelength of light
μ_B	Bohr magneton
μ_N	Nuclear magneton
$\langle hkl \rangle$	a general hkl direction
$[hkl]$	a specific hkl direction
$\{h\,k\,l\}$	a general hkl plane
(hkl)	a specific hkl plane

Come up and be a kite,

And fly a diamond night.

Kate Bush

Chapter 1

Introduction

First discovered alluvially in India, diamond is a material which has attracted interest since early human history due to its unique properties [1]. These include the brilliance or 'fire' which is created by the materials high refractive index and dispersion. Diamonds have also found uses due to their extreme hardness, in fact the name comes from the Greek word 'adamas' which means unbreakable [2]. They were traditionally used as a cutting tool of glass and other materials [3]. As a result of their size and value they have attracted much violence throughout history [2].

Modern applications for diamonds are manifold. These include drill bits for oil drilling, use as an abrasive, dielectric windows, heat sinks and lasing media [4, 5, 6]. Various applications utilising specific defect centres in diamond have also been investigated such as single photon sources [7], quantum bits and nano-magnetometry [8, 9].

1.1 Structure and Properties

Carbon is a tetravalent atom which can bond to form many different structures. The ground state orbital electron configuration is $1s^2 2s^2 2p^2$, but this undergoes hybridisation to bond in different ways. Carbon can form diamond and graphite. Single layers of graphite are called graphene and can form fullerenes and carbon nanotubes. Carbon allotropes have many different unique and useful properties.

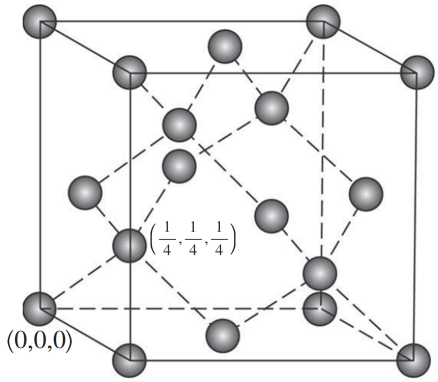

Figure 1.1: *Diamond unit cell showing two intersecting face-centred cubic lattices. One starting at* $(0,0,0)$ *and one at* $\left(\frac{1}{4},\frac{1}{4},\frac{1}{4}\right)$.

Graphite is the phase which is most stable at room temperature and pressure. However diamond is a long lived metastable state due to the large energy barrier between it and graphite.

Graphite is made up of layers in which each carbon atom is covalently bonded to three other atoms in sp^2-hybridised orbitals. This leaves one delocalised electron, from each carbon atom, which can move in the space between the layers. Graphite is an electrical conductor in this plane. The layers are held together by weak van der Waals forces.

The carbon atoms in diamond are covalently bonded to four others by sp^3-hybridised orbitals [10]. All the outer shell electrons are occupied by bonding so impurity-free diamond does not conduct electricity. This bonding forms a tetrahedral structure. The lattice is made up of two face-centred cubic structures with an atom at $(0,0,0)$ and $\left(\frac{1}{4},\frac{1}{4},\frac{1}{4}\right)$ for each intersecting unit cell, as shown in figure 1.1. The bonding is rigid and the bond length is short, 1.5 Å [11], resulting in a dense structure. For graphite, density is 2.3 g/cm^3 compared to 3.5 g/cm^3 for diamond.

This chemical structure results in a material with an exceptional array of properties. Diamond has the highest hardness of any natural material and is extremely hard wearing [12]. It is very chemically stable so can be used in harsh environments or in biological environments [10]. It is optically transparent to a large range of wavelengths.

Diamond has a large band gap and when doped can create an n-type or p-type semiconductor and can be used for making semiconductor devices [13]. However, due to the dense lattice, solubility of impurities can be very low, depending on

the atomic size mismatch. Doping has successfully been performed with phosphorus for n-type and boron for p-type. The donor/acceptor levels are deeper than for other semiconductor systems which means that, at room temperature, few are ionised [14]. Diamond also has a number of superior electronic properties compared to other materials; some of which are shown in table 1.1.

	Silicon	**SiC**	**GaN**	**Diamond**
Bandgap (eV)	1.1	3.2	3.4	5.5
Breakdown Field ($MVcm^{-1}$)	0.3	3	5	20
Electron Mobility ($cm^2V^{-1}s^{-1}$)	1450	900	440	4500
Hole Mobility ($cm^2V^{-1}s^{-1}$)	480	120	200	3800
Thermal Conductivity ($Wcm^{-1}K^{-1}$)	1.5	5	1.3	24

Table 1.1: *Properties of different semiconductors compared to diamond. Table from reference [15].*

Diamond has a much higher breakdown field than other semiconductor materials so can withstand higher electric fields and insulate across very thin layers, reducing device size and price. Diamond has higher electron and hole mobility than alternatives so is useful for high frequency devices. The high thermal conductivity means that diamond devices can dissipate heat more efficiently than other semiconductors and are more easily cooled, so can improve thermal performance [16, 17]. New methods for fabricating diamonds mean cheaper devices can be made and with chemical vapour deposition (CVD) thinner devices can also be produced [17].

1.2 Diamond Types

A perfect diamond lattice is made up of solely carbon atoms tetrahedrally bonded. Defects can interrupt this lattice and may be classified as point defects or as extended defects. Extended defects include dislocations, vacancy clusters and inclusion clusters. Point defects are impurities, self-interstitials or vacancies. The colour of the diamond depends on the defects present which create energy levels in the band gap and absorb wavelengths of light in the visible spectrum. A

famous example of this is the Hope Diamond which is blue because of the high concentration of boron atoms.

Type I more than 1 ppm nitrogen	**Type Ia** Type IaA Type IaB **Type Ib**	98% of natural diamonds nitrogen atoms in pairs, colourless nitrogen aggregates, yellow single nitrogen, yellow
Type II less than 1 ppm nitrogen or boron > nitrogen conc.	**Type IIa** **Type IIb**	few impurities, colourless boron, p-type semiconductors, blue

Table 1.2: *The classification of diamond into different types depending on quantity and concentration impurities present.*

Diamonds are classified into types by the presence and form of the impurities nitrogen and boron. This is shown in table 1.2. Diamond are formally classified using infra-red absorption to measure the impurities present [18]. Type I diamonds contain more than 1 ppm nitrogen [19]. This type can be split into Ia and Ib and further split into IaA and IaB. Type Ia diamonds are those which contain nitrogen which has aggregated [20]. Most natural diamonds fall into this Ia category as nitrogen tends to aggregate over geological time scales [21]. Some exhibit regions of IaA and IaB. In type IaA nitrogen atoms are in pairs, this does not cause absorption in the visible spectrum. Type IaB diamonds have larger aggregates of nitrogen and these can absorb visible light, creating either a yellow or brown diamond, depending upon the aggregation state. Type Ib contain single substitutional nitrogen [19]. Diamonds made by the high temperature high pressure (HPHT) method usually fall into this category. Progress is being made reducing the nitrogen contamination in HPHT so this method can be used to make type II also. Type II diamonds contain less than 1 ppm of nitrogen. Type IIa contain few impurities and undoped CVD diamonds are usually of this type. They may be colourless or may have some plastic deformation which creates a colour but this can be removed by HPHT processing. Type IIb diamonds contain a larger boron concentration than nitrogen concentration and can often be blue [22]. As mentioned previously boron doping can create a p-type semiconductor and testing this was an early method of defining the type.

1.3 Motivation for Study

Defect centres in diamond are utilised in a number of important applications such as single photon emission, magnetic field and temperature sensing and quantum bits. Currently the nitrogen vacancy centre is the most highly researched defect centre, but in this work the silicon vacancy centre is investigated as it has properties which contrast to the nitrogen vacancy and may be useful for some applications. The motivation behind the first and last experimental chapters (Chapter 5 and Chapter 8) of this thesis is to investigate the creation and properties of this centre; both in the negative and neutral charge state. Creating specific concentrations of the chosen defect is key to viability for these applications in the future. A variation of the protocol used for creating nitrogen vacancy centres was implemented for silicon vacancy and the result of this in two different diamonds was tested. The method of quantification was Electron Paramagnetic Resonance. This technique was also used to further investigate the centres created. The silicon vacancy centre exhibits electron spin polarisation of the ground state, a property required for magnetic field and temperature sensing. This property was investigated to understand the energy level polarisation mechanism. In order to interpret the defect behaviour the energy levels must be understood. The relaxation behaviour at different temperatures was measured to discern the electronic structure.

The second experimental chapter (Chapter 6) discusses four samples made by HPHT. The motivation for investigating this is both to understand the HPHT process but also to investigate the potential for using this method for fabrication of isotopically enriched diamonds. Diamonds which are isotopically pure ^{12}C or ^{13}C have useful applications such as heat spreaders and stress anvils [23].

A new method of making single crystal CVD diamonds is to use a lattice matched silicon wafer as the substrate. Two single crystal diamonds made using this method are the subject of the penultimate experimental chapter (Chapter 7). This method has potential for diamond based devices and heat spreaders as thin layers with large surface areas can be fabricated, potentially at a reduced cost. In this chapter the differences between these two samples and samples made by homoepitaxial CVD are investigated to understand any potential drawbacks and differences of the new method.

1.4 Thesis Outline

The outline of the thesis is presented below.

Chapter 2 presents the background literature which underpins the rest of the thesis. It includes a discussion on the formation of diamond. Defects in diamond are also described as are the applications which utilise their different properties.

Chapter 3 discusses the theory behind the technique of both pulsed and continuous wave Electron Paramagnetic Resonance. This is followed by the theory of the other techniques employed including optical absorption, photoluminescence and cathodoluminescence and finally Secondary Ion Mass Spectroscopy.

Chapter 4 describes the experimental techniques used including the equipment and methods. This again includes both pulsed and continuous wave Electron Paramagnetic Resonance, absorption, photoluminescence and cathodoluminescence and finally Secondary Ion Mass Spectroscopy.

Chapter 5 explores the relaxation rates and electron spin polarisation behaviour of two different samples containing silicon vacancies and one sample containing nitrogen vacancies. This was performed using Electron Paramagnetic Resonance. The samples are investigated using photoluminescence to understand their differing behaviour.

Chapter 6 examines results from a suite of high pressure high temperature diamonds with varying ratios of ^{12}C and ^{13}C isotopes. The uniformity of the isotope ratio across each sample was investigated using a variety of techniques to understand the high pressure high temperature doping process.

Chapter 7 presents results from two diamonds which were grown by heteroepitaxial chemical vapour deposition on a silicon wafer. A number of different techniques were used to study these samples to understand the differences between them and homoepitaxial chemical vapour deposition diamonds.

Chapter 8 presents results from an investigation into irradiation and annealing of silicon doped diamond. Two different samples were studied and their different behaviour is discussed.

1.5 Samples

The samples which are used throughout the thesis are presented in table 1.3.

Sample Reference	Synthesis Method
NL636-01	HPHT
NL636-02	HPHT
NL636-03	HPHT
NL636-04	HPHT
Sample 5	CVD
Sample 6	CVD
Sample 7	CVD
Sample 8	CVD
Sample 9	CVD
Sample 10	HPHT
Sample 11	CVD
Sample 12	CVD
Sample 12	CVD
Sample 13	CVD
Sample 14	CVD
Reference sample	HPHT
Intrinsic	Heteroepitaxial CVD
Nitrogen doped	Heteroepitaxial CVD

Table 1.3: *Reference table for sample growth methods.*

Chapter 2

Diamond Literature Review

2.1 Introduction

In this chapter the relevant background literature will be presented. This includes a review of different methods for obtaining diamonds, a discussion of the defects which may be present and finally novel uses for these defects.

2.2 Synthesis Methods

Diamond is an allotrope of carbon made up of tetrahedrally bonded carbon atoms. It has a rigid structure due to covalent bonding between the atoms. The phase diagram for carbon can be seen in figure 2.1. As can be seen from the diagram, it is graphite, not diamond, that is thermodynamically stable at room pressure and temperature. However, as the energy barrier for conversion between diamond and graphite is large, diamond is a long lived metastable state.

Diamonds form naturally under the Earth's surface under certain pressures and temperatures. Industrial methods of creating diamonds include high pressure high temperature (HPHT) synthesis and chemical vapour deposition (CVD) both of which reliably produce high quality diamonds and can be selectively doped. Nitrogen is likely to be present in most manufactured diamonds due to incorporation of atmospheric nitrogen in HPHT and impurities in starting gases and chamber leaks in CVD, additionally nitrogen can be added intentionally to speed up growth. Silicon is often present in CVD diamonds due to unintentional contamination from

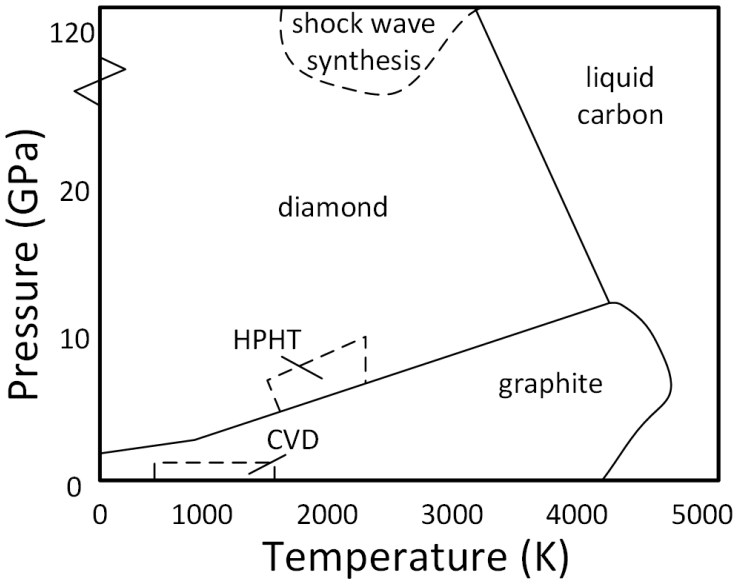

Figure 2.1: *Carbon phase diagram, showing the regions in which HPHT, shock wave synthesis and CVD growth occur. Note: CVD area is not to scale. Image recreated from [24].*

the silica reaction chamber.

2.2.1 Natural Diamonds

Natural diamonds grow 140 to 170 km below the Earth's crust in the mantle. The established theory is that they may take billions of years to form and may have been forming for up to 75% of the Earth's lifetime [25]. They form at pressures of between 4.5 and 6 GPa and temperatures between 900°C and 1300°C [26, 25] and are brought to the surface by volcanic eruptions. These diamonds can then be found either alluvially (in river beds) or may be mined.

2.2.2 Meteoric Diamonds

Meteorites are also a source of diamond, which may be produced on impact but may also be present in interstellar dust [27]. It is not certain how this diamond dust is formed as the pressures which a planet would supply would be necessary but following this the diamond would have to escape the high gravity of the planet [27]. Additionally, a process similar to CVD could occur in pre-supernovas. This is further suggested by the presence of the noble gases neon and xenon in these

diamonds. These diamonds have been investigated because it is suggested that a single, massive supernova may have exploded near the forming Solar System, and therefore the content of these diamonds may act as a record for astrophysicists of the forming of the solar system [27]. Some of the nano-diamonds discussed later are thought to have been made by meteorites on impact [27]. The region of the phase diagram where this occurs is labelled 'shock wave synthesis' in figure 2.1.

2.2.3 High Pressure High Temperature Synthesis

The HPHT method simulates the natural formation of diamonds in the Earth's mantle with the addition of a solvent metal. A diamond seed is surrounded by a carbon source, usually in the form of graphite, with a metal which when molten acts as a solvent. This method is commonly used industrially for creating diamond grit but for the creation of single crystal diamond a seed is required. One of the first to investigate this was the Nobel laureate Henri Moissan in the early twentieth century, who claimed to have made diamond by heating sugar contained in molten iron, although his results were later disputed [1].

Later experiments, in the 1950s, by General Electric using a belt press successfully produced diamonds [28]. This method was developed by Tracy Hall and others. Hall used a belt press to produce pressures in excess of 10 GPa and temperatures above 2000°C. A solvent metal was used to reduce the pressure and temperature required for synthesis. A group in Sweden also produced verifiable diamonds around the same time, however this work was not published until later [29].

The carbon phase diagram in figure 2.1 shows the region in which HPHT synthesis occurs. It can occur without a solvent metal but using one reduces the pressure and temperature required to create diamond. Now HPHT methods are widely used for making diamonds [28]. The temperatures used are usually above 1300°C ($\sim$ 1600 K) and the pressures are between 5 and 6 GPa. Higher temperatures and pressures can be used but this creates more difficulties experimentally. The growth rate is $\sim$ 10 mg/hour and diamonds are often grown for up to 100 hours, which can create diamonds greater than 5 carats (1 gram). HPHT synthetics are commonly used in industry and are sold on the high street in jewellery.

One common HPHT method for growing single crystals involves using a temperature gradient. In this set-up the carbon source is molten at the top and the diamond seed is 20 to 50°C colder at the bottom [26]. The carbon source dis-

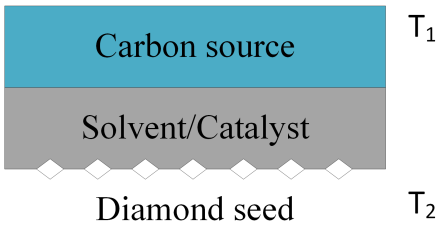

Figure 2.2: *HPHT growth capsule showing temperature gradient where* $T_1 > T_2$.

solves in the molten metal solvent and, as it moves down the temperature gradient (because of convection currents and concentration gradients) it becomes supersaturated and precipitates out at the seed, growing the diamond. This is shown in figure 2.2. The speed of the growing diamonds is determined by the temperature difference, with a common temperature difference of 20°C. The morphology and impurity uptake are determined by the seed temperature [30]. There are more details about the specifics of this method in Chapter 6.

HPHT diamonds can be isotopically doped by changing the composition of the carbon source in the growth capsule. Boron doping can be performed by adding boron carbide to the growth capsule along with a graphite source, but may also be an unintentional inclusion [31]. Nitrogen is often an unintentional addition as it is present as a contaminant in the ceramic capsule components, atmosphere and carbon source. Nitrogen can also be added intentionally to replicate the concentrations found in natural diamonds by the addition of sodium azide [32]. Silicon can be intentionally added to the graphite in the growth cell. In HPHT diamonds silicon vacancies are more abundant in {1 1 1} growth sectors [33].

2.2.4 Chemical Vapour Deposition

Chemical Vapour Deposition (CVD) is more commonly used to grow diamonds for research as it is a more flexible method, in terms of doping. It is a technique which can be used for growing polycrystalline and single crystal films. The diamonds form in significantly lower pressure and lower temperature conditions when compared to HPHT, see figure 2.1. Homoepitaxial CVD diamonds are grown using a diamond substrate from an ionised mixture of molecules which forms a plasma. The substrate used may be a natural diamond or an HPHT diamond. Non-diamond substrates, such as silicon, may be used for heteroepitaxial CVD. This technique can be used to grow polycrystalline diamond but it is very challenging to make single crystal diamond this way. This is discussed further in the

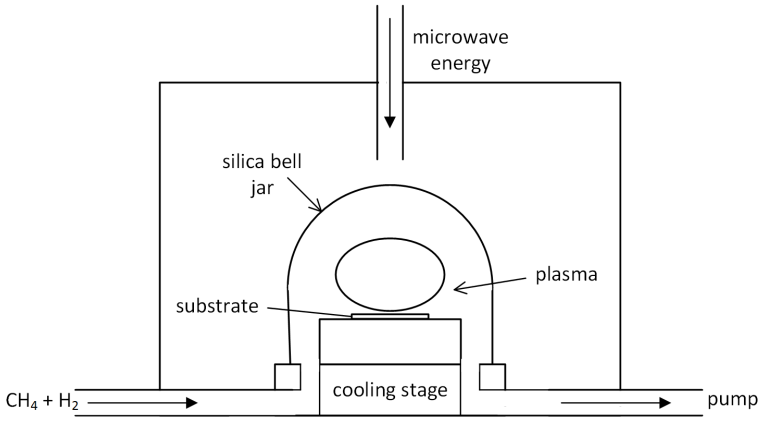

Figure 2.3: *CVD reactor showing substrates on cooling plate in plasma, bell jar and microwave energy input. Image recreated from [34].*

next section. The growth is a reaction driven by kinetics rather than thermodynamics and occurs under metastable conditions [23]. It is generally used for covering larger areas such as a 150 mm by 2 mm films. HPHT processing may be done after CVD to improve the optical properties of the diamond.

CVD processes include microwave plasma, current discharge and hot filament. Microwave plasma CVD is the most commonly used CVD process, especially when single crystals are being formed, because there is much less contamination than with other processes (as no filaments or electrodes are required) and it can be run for a longer period of time resulting in a larger diamond. Optical and electronic grade single crystals can be made with this method. Figure 2.3 shows a microwave plasma CVD reactor.

The microwaves are typically produced by a magnetron, as shown in figure 2.3, and the plasma is ignited and the diamond is grown at pressures of 13 to 33 kPa. Higher pressures can be used but this would also require a higher power microwave source to split the increased number of gas molecules. This results in a faster growth rate [23]. The diameter of the plasma ball can be ∼6 cm and may reach temperatures of 2800 K but this will depend on microwave frequency and pressure.

The environment usually consists of, among other gases, high purity CH_4 and H_2. Either plasma activation or heat (∼2500 K) is used to turn these gases into radicals which then react with the surface of the growing diamond. All the CVD diamonds used in this thesis have been made by plasma activation. In the standard growth model the microwave energy causes two main chemical reactions which are shown

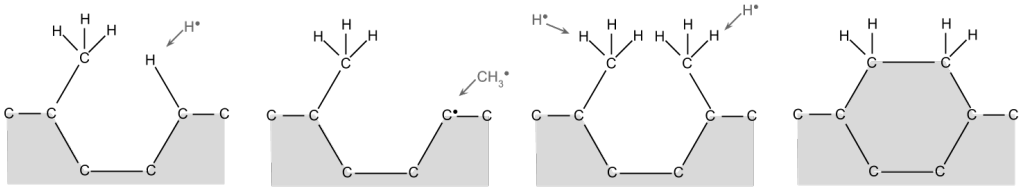

Figure 2.4: *The steps of hydrogen abstraction and carbon addition onto a* {1 1 0} *surface in the standard model. Recreated from [35].*

in equation 2.1 and 2.2 [35, 36, 37].

$$H_2 \rightarrow 2H^{\bullet} \tag{2.1}$$

$$CH_4 + H^{\bullet} \rightarrow CH_3^{\bullet} + H_2 \tag{2.2}$$

Hydrogen is critical to the reaction as it stabilises the diamond surface by H-termination and it also etches graphite which is deposited during growth. The reaction which occurs at the surface involves a hydrogen radical removing a hydrogen atom from the surface leaving an unbonded carbon orbital. A $CH_3^{\bullet}$ radical will then add to the surface. The process is shown in figure 2.4. Diffusion and convection occur on the surface.

The diamond substrate is removed either by laser sawing, a lift-off process involving graphitisation and etching of a layer between the diamond and substrate or polishing [23].

Other molecules can also be added to the reaction mixture including O_2 to change the surface chemistry. This will also affect the growth rate and surface quality and may be incorporated into the diamond [6]. For a deeper discussion see reference [38]. During CVD growth dopants can also be added intentionally or unintentionally. Nitrogen (N_2) is often present in the reaction chamber as an impurity of the starting gases [39]. It can also be added to speed up the growth [40]. It causes surface roughening in the form of polycrystalline regions and twins. This is thought to be due to impurities interrupting the step growth of the diamond. These effects can be somewhat improved by adding silicon into the reaction chamber [6]. Nitrogen also affects the mechanical properties of diamond; it reduces the hardness and increases toughness in high concentrations, and deteriorates the electronic properties [6].

A p-type or an n-type diamond semiconductor can be made using boron or phosphorous respectively [41]. Due to diamond's excellent material properties, includ-

ing the highest thermal conductivity of any material, it is likely that diamond devices will become more widespread in the future. Example devices include temperature and pressure sensors and Schottky devices [41].

Silane (SiH_4) can be added to produce a silicon containing diamond [40]. However most diamonds made by CVD are likely to contain silicon as this is a common impurity from the walls of the reactor and from the quartz bell jar [40]. Silicon may also be added to reduce surface roughness and brown colour caused by nitrogen inclusion [40]. Silicon vacancy defects do not normally occur in natural diamonds, when they do occur other silicon related CVD peaks are missing, so they are used to differentiate naturals from CVD [42]. Studying the negative silicon vacancies is a common way of distinguishing natural from industrial grown diamonds [42].

Heteroepitaxial Chemical Vapour Deposition

Some of the diamonds studied in this thesis are made by heteroepitaxial CVD by Augsburg Diamond Technology. Heteroepitaxial CVD is similar to homoepitaxial CVD but the diamond substrate is replaced by a substrate of a different material. Homoepitaxial diamond requires a diamond substrate and as such is limited by the size of diamonds available. The advantage of the heteroepitaxial method is that the substrate used can be larger so can be used to fabricate larger diamonds. The main issue with the method is lattice mismatch which usually results in polycrystalline diamonds. This method will be discussed in more detail in Chapter 7.

2.2.5 Nanodiamond Production

Nanodiamonds have many promising applications as they can act as an isolated colour centre and thus a nanoscale magnetic sensor. They are also less toxic than alternative semiconductor systems and other forms of carbon, so can potentially be used in biological environments [43]. Nanodiamonds can be produced by many different methods, including HPHT, CVD and shock wave synthesis. The first were made in the 1960s in the USSR using detonation [44]. Nanodiamonds can be produced using plasma-assisted CVD on iridium [45]. This allows the colour centres to be isolated and manipulated and individually enhanced using a nanocavity.

2.3 The ^{13}C Isotope in Diamond

Diamonds are made of carbon atoms, most of which are the ^{12}C isotope. ^{13}C is a stable isotope of carbon with a natural abundance of 1.109%. In CVD diamonds the ratio of the isotopes will vary depending on the presence in starting gases. In HPHT diamonds the carbon source can also have varying ratios of the isotopes, resulting in different ratios to natural diamonds. ^{13}C interrupts the periodic lattice of diamond, as it is a heavier isotope then ^{12}C, and can reduce the phonon mean-free path, changing the thermal conductivity. More discussion and detail about these effects can be found in Chapter 6.

2.4 Point Defects in Diamond

Defects in diamond are disruptions to the tetrahedral arrangement of the carbon atoms which may either be point defects or extended defects. Extended defects include dislocations, vacancy clusters and inclusions. Point defects include missing atoms, substitutional atoms and interstitial atoms and these will be the subject of this section. The presence of some of these defects can be seen by the naked eye as, in large quantities, they change the colour of the diamond, due to energy levels in the band gap which can absorb photons in the visible spectrum.

Defects can either be intrinsic or extrinsic. Intrinsic defects are either interstitial carbon atoms or missing carbon atoms or larger complexes of these. Extrinsic defects incorporate interstitial or substitutional atoms which are not carbon. Diamond has a rigid lattice of strong, covalent sp^3 bonds with a high bond density due to closely spaced carbon atoms. These factors result in limited space between atoms, so there are usually relatively few impurities except from small atoms such as nitrogen, boron and hydrogen.

The charge state of defects depends on the defect environment and will be different depending on the concentration and nature of other defects. Defects can act as donors or acceptors of electrons depending upon their relative energy levels within the band gap. Charge states can also be changed by the application of energy in the form of illumination or heat as this supplies electrons with enough energy to change state.

Defects can be identified by their characteristic electron paramagnetic resonance

(EPR) spectrum or by optical absorption or emission. An EPR spectrum is characteristic of the electron environment. The spectrum can give information about local nuclei and symmetry. For more information about these spectra, please see section 3.2. Defects can absorb or emit radiation at a frequency which is characteristic of the defect itself and hence acts as a 'fingerprint' for each defect type; the zero-phonon line (ZPL). For more details of how this can be used to identify defects please refer to section 3.7. The information presented here about each defect is that which is most relevant to the remainder of the thesis and as such is not exhaustive list of properties. The electronic structure presented for each defect includes the energy levels most relevant to this discussion. Defect identification, annealing behaviour and symmetry are discussed. For a fuller discussion please refer to reference [33] or for a full review specifically about nitrogen vacancy in diamond, reference [46].

2.4.1 Intrinsic Defects

The Split-Interstitial

The split-interstitial defect (denoted R2) is produced by electron irradiation and may also be referred to as $I_{\langle 001\rangle}$. R2 consists of one interstitial carbon atom along a $\langle 001\rangle$ direction [47]. It is created when an atom moves from its normal position to an interstitial site, leaving a vacancy. Hence it is created at a similar rate to the vacancy during irradiation [47]. The EPR spectrum arises from a thermally excited $^3A_2$ spin triplet state with $S = 1$ which is 50 meV above the $^1A_2$ ground state. The symmetry is D_{2d} which has been discovered using uni-axial stress [48].

Higher Order Self-Interstitial Complexes

The di-split self interstitial in the $\langle 001\rangle$ direction is denoted R1. Two non-bonding 2p orbitals contain two electrons giving rise to an effective spin of $S = 1$ which can be seen in EPR. The defect has C_{1h} symmetry. It is stable up to temperatures of 600 K. It was identified by studying the ^{13}C hyperfine interactions by Twitchen et al. [49].

The two carbon split-interstitials separated by a carbon atom is donated H3 and has a photoluminescence peak at 503.4 nm [50, 51]. 5RL is thought to be the same

defect with a different charge state [50]. The symmetry of both is C_{3v} [50].

The three self-interstitials is donated O3 and has C_2 symmetry [52]. It can be created by low temperature irradiation and is also created at temperatures at which R1 and R2 are annealed out. The centre has an effective spin $S = 1$.

Additionally there are other higher order complexes involving self-interstitials.

The Vacancy

Vacancies are unoccupied lattice sites. They are often present in diamonds and in large concentrations they create a green colour in the diamond.

Crystal Structure Vacancies have tetrahedral symmetry and their point group is T_d; though symmetry is reduced in some diamonds due to local strain [53].

Electronic Structure The neutral vacancy consists of four dangling carbon bonds each with one unpaired electron. The ground state electron configuration for the neutral vacancy is $a^2t_2^2$ which gives rise to the doubly degenerate many electron state ^1E (amongst others neglected here, see reference [54] for full details). The triply degenerate excited state is $a^1t_2^3$ which gives rise to $^1T_2$ (amongst others). The ZPL, at 741 nm, is created by the ground state to excited state transition and is named 'GR1'. There is an additional, weaker, transition at 744 nm. This is created by a transition between a ^1A state and the excited state, $^1T_2$. The ^1E ground state was identified using uni-axial stress. Additionally the neutral vacancy gives rise to the 'GR2-8' absorption band which is formed of 12 sharp lines. These are related to interactions with bound hole excitons [53].

Negative vacancies have an extra electron. The ground state has $a^2t_2^3$ electron configuration which gives rise to the many electron ground state $^4A_2$ (amongst others). The excited state has an $a^1t_2^4$ electron configuration which gives rise to the many electron state $^4T_1$ (amongst others). A transition between these two levels is the origin of the ZPL [55] which can be identified optically by absorption at 393.6 nm, called 'ND1'. The ND1 band is not seen in emission as the incoming photons required for photoluminescence change the negative vacancies into neutral ones. This means the negative vacancy does not emit at the ZPL in photoluminescence.

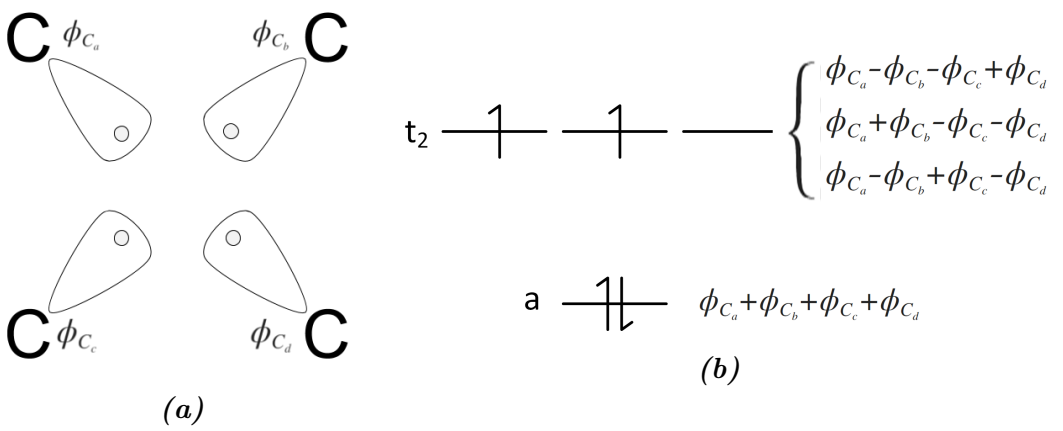

Figure 2.5: *Orbitals of the neutral vacancy centre. Showing an electron configuration. The a state is the bonding configuration and the t_2 is the combination of three orthogonal anti-bonding orbitals.*

The negative vacancy has been identified in EPR by Isoya et al. [55]. The effective spin is $S = \frac{3}{2}$. Optical illumination can be used to ionise V^- to V^0 in the excited state, $^5A_2$, and this state can also be seen in EPR [56].

Charge Transfer Vacancies can be negatively or neutrally charged and it is assumed they can also be positive though this has not been conclusively found. Positive and negatively charged vacancies are expected to exist in conjunction [57]. Changes between the charge states can be induced by UV illumination or heating [53]. Heating causes negative vacancies to become neutral and illumination reverses this effect, depending upon the other defects within the material.

The charge state of the vacancies in a sample is related to what other species are present. High nitrogen samples will donate an electron as shown in equation 2.3. High boron concentrations will cause the reverse reaction by donating a hole [53].

$$V^0 + X^0 \leftrightarrow V^- + X^+ \tag{2.3}$$

Production and Annealing Behaviour Vacancies can be intentionally introduced by electron irradiation or other high energy irradiation [33]. They are more easily produced near dislocations or strained regions of diamond [33].

Vacancies are static at room temperature but become mobile with an activation energy of approximately 2.3 eV. This can be reached though annealing at temper-

atures of 600°C and greater [50]. At this temperature the vacancies have enough energy to move in the diamond and they may be annihilated by dislocations, edges, interstitial carbon atoms and (in polycrystalline diamonds) grain boundaries. Other low energy sites to which they may migrate include defect centres. Nitrogen is an effective trap for vacancies and nitrogen vacancies will form. However most natural diamonds are type Ia (nitrogen in pairs or aggregates). In these diamonds there are similar amounts of neutral and negative vacancies [55]. Nitrogen aggregates are also an effective trap for vacancies and H3 (two nitrogen atoms and a vacancy) and H4 (four nitrogen atoms and two vacancies) will be created. In diamonds doped with silicon, silicon atoms are also an effective trap for vacancies, forming silicon vacancies and di-vacancies [53]. Vacancies can also pair with other vacancies creating di or tri-vacancies [58].

The Di-Vacancy The di-vacancy may be created when a diamond with a high vacancy concentration and few other traps is annealed. It is identified by the 'TH5' absorption band with the ZPL at 487.5 nm. It has an effective spin of $S = 1$ and can be identified by an EPR signal [59].

It is formed after irradiation and annealing at 400°C of type IIa and Ia diamonds. The di-vacancy concentration is inversely related to that of the neutral vacancy. It is annealed out at 1000°C, which is thought to be caused by the di-vacancies annihilating at grain boundaries and dislocations [58].

2.4.2 Extrinsic Defects

Nitrogen Related Defects

Nitrogen is usually present in some form in most natural, HPHT synthesised and in some CVD diamonds. In large concentrations it creates a yellow coloured diamond, depending on the aggregation state, or if large quantities of nitrogen vacancies are present the diamond will be pink. Other aggregation states will give other colours.

Single Substitutional Nitrogen Single substitutional nitrogen is present in HPHT diamonds and in CVD diamonds. Type Ib diamonds, in which single substitutional nitrogen is the most common defect, are rare for natural diamonds

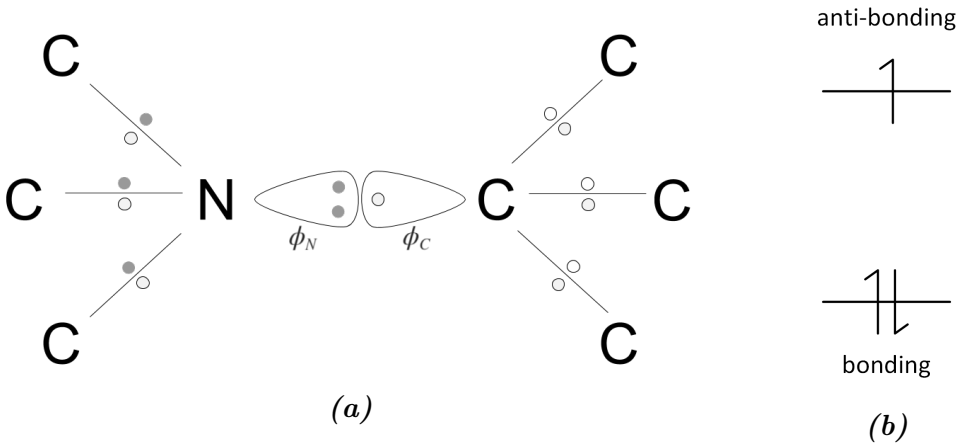

Figure 2.6: *(a) shows orbitals of the neutral nitrogen single substitutional centre. Empty circles indicate a carbon electron and filled circles indicate a nitrogen electron. (b) shows an electron configuration.*

as over geological time scales nitrogen forms pairs or higher order aggregates.

Crystal Structure The nitrogen atom forms covalent bonds with three adjacent carbon atoms. Additionally two electrons form a full orbital. This is shown in figure 2.6a. The N-C bonds are longer than the normal C-C bonds by 28% and the nearest neighbour C-C bonds are shorter by 5% as the other carbon atoms relax away from the nitrogen atom [60].

Electronic Structure Neutrally charged single substitutional nitrogen can be identified in EPR [61]. The symmetry of the defect is C_{3v} and the ground state has $S = \frac{1}{2}$. The nitrogen atom has $I = 1$. The hyperfine interaction creates three sets of lines in the EPR spectrum. This is discussed further in section 3.2.5.

The orbital structure of a single substitutional nitrogen is shown in figure 2.6a. Nitrogen has five electrons available for bonding, as its electron configuration is $1s^2 2s^2 2p^3$, and these bond to three carbon orbitals leaving one lone pair. The other carbon atom is left with one unbonded electron. The electron wave functions combine to produce the bonding ($\frac{\alpha\phi_C+\beta\phi_N}{\sqrt{\alpha^2+\beta^2}}$) and anti-bonding ($\frac{\alpha\phi_C-\beta\phi_N}{\sqrt{\alpha^2+\beta^2}}$) states shown in figure 2.6b. The bonding arrangement has lower energy than the anti-bonding one. These are filled with the three available electrons.

Charge Transfer Substitutional nitrogen is usually neutrally charged but it may donate an electron to an acceptor defect (such as boron or a vacancy) and

form a positive nitrogen atom as demonstrated by equation 2.4.

$$N_s^0 + X^0 \leftrightarrow N_s^+ + X^- \tag{2.4}$$

Production Single substitutional nitrogen is present in HPHT diamond and in CVD diamonds. In CVD grown diamonds single substitutional nitrogen has highest concentrations in the {1 1 1} sectors and is usually absent from the {1 0 0} and {1 1 3} sectors [23].

Di-nitrogen There are two different forms of di-nitrogen; A-centres and H1a.

The A-centre is formed of two adjacent substitutional nitrogen atoms [62]. As both of the nitrogen atoms are bonded to three carbon atoms and have a full dangling bond the species is chemically inert. It is present in type IaA diamond. The creation of the centre is thought to be vacancy assisted [62].

Two nitrogen atoms may also be adjacent in interstitial sights, this is called H1a and has D_{2d} symmetry. This complex has been identified optically by doing experiments under stress by Liggins [63]. It has a local mode at 1420 cm^{-1}. The centre may be created by a aggregation of A-centres and carbon interstitials [63].

Nitrogen Aggregates Larger complexes of nitrogen can exist, especially in natural diamonds or those which have been annealed for more than $\sim$ 100 hours. These complexes include B-centres which consist of four nitrogen atoms adjacent to a vacancy. They form in diamonds which contained A-centres and were then annealed, though it is not clear if this is related to A-centres joining together or migration of nitrogen atoms. B-centres or most often present in type IaB diamonds. Other complexes include H3 and H4, which were discussed in the vacancy section as they consist of an A-centre with an additional vacancy and a B-centre with an additional vacancy respectively [64]. N3 was one of the first defects seen optically and has also been predicted by Goss et al. [65, 66]. It consists of one vacancy surrounded by three nitrogen atoms.

The Nitrogen Vacancy Nitrogen vacancies consist of two missing carbon atoms replaced with one nitrogen atom, as shown in figure 2.7. The nitrogen atom bonds to three of the nearest neighbour carbon atoms, leaving three dangling carbon

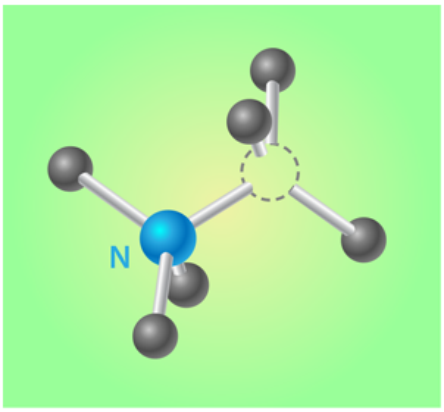

Figure 2.7: *The nitrogen vacancy centre [67].*

bonds. The N-V axis of the defect is orientated along a {1 1 1} direction. The centre does not have inversion symmetry and the point group is C_{3v}. This creates an electronic dipole and means that nitrogen vacancies interact strongly with incoming photons; the phonon side band is large compared to the ZPL as shown in figure 2.8 [46].

Electronic Structure The negative nitrogen vacancy has a ground state $S = 1$ and can be identified by a ZPL at 638 nm. It was first identified in EPR using optical illumination as this electron spin polarises the defect and causes an increase in the signal [68].

The symmetry of the defect is C_{3v} and ZPL transition is created by a transition from spin triplet ground state $^3A_2$ to the ^3E excited state.

The orbital structure of a negative nitrogen vacancy is shown in figure 2.9a. Nitrogen has five electrons available for bonding and these bond to three carbon orbitals leaving one lone pair as was discussed previously for single substitutional nitrogen. The adjacent vacancy has one electron and there are three carbon orbitals which remain unbonded. The electron wave functions combine to produce the states shown in figure 2.9b. The lone pair of the nitrogen, has the lowest energy, the bonding orbital of the carbon atoms is higher and the anti-bonding orbital of the carbon atoms is highest. These are filled with six electrons as shown in the figure but alternative arrangements are possible. This configuration is the lowest energy according to Hund's rule when obeying the Pauli exclusion principle. The three possible configurations of $a_N^2 a_C^2 e^2$ give rise to the many electron states $^1A_1$, $^3A_2$ and ^1E. The respective energy of these levels must be worked out experimentally. An electron can be promoted from the a_C to the e_C level resulting in the configu-

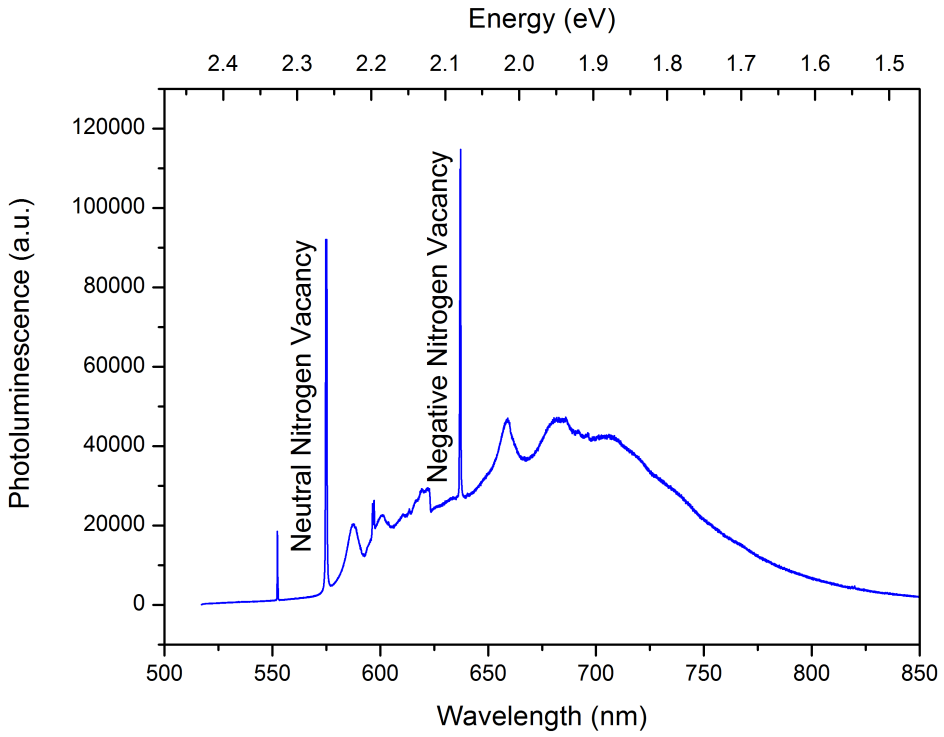

Figure 2.8: *A photoluminescence spectrum of the charge states of the nitrogen vacancy, taken at 77 K.*

ration $a_N^2 a_C^1 e^3$. This gives rise to two more many electron states; ^1E and ^3E. The final energy configuration is shown in figure 2.10a. The $S = 1$ states are split into different m_s levels, which will be discussed in section 2.5.2.

The neutral nitrogen vacancy has a $S = 3/2$ ground state and is identified by a ZPL at 575.5 nm [69]. The ZPL is created by a transition from the ^2E ground state to the $^2A_1$ excited state. This was identified optically by uni-axial stress splitting [69]. It is not detected in EPR possibly due to dynamic Jahn-Teller distortion of the ground state, although the excited state has been identified by Edmonds et al. [70].

The electron configuration is similar to the negative state but with one less electron. This creates the ground state configuration $a_N^2 a_C^2 e^1$ which gives rise to the many electron state ^2E. When one electron is promoted the configuration becomes $a_N^2 a_C^1 e^2$ giving rise to the many electron states ^2A,$^4A_2$ and ^2E. These energy levels are shown in figure 2.10b.

Charge Transfer The negative nitrogen vacancy can be suppressed by boron doping as the boron acts as an acceptor and the centre becomes neutral or positive.

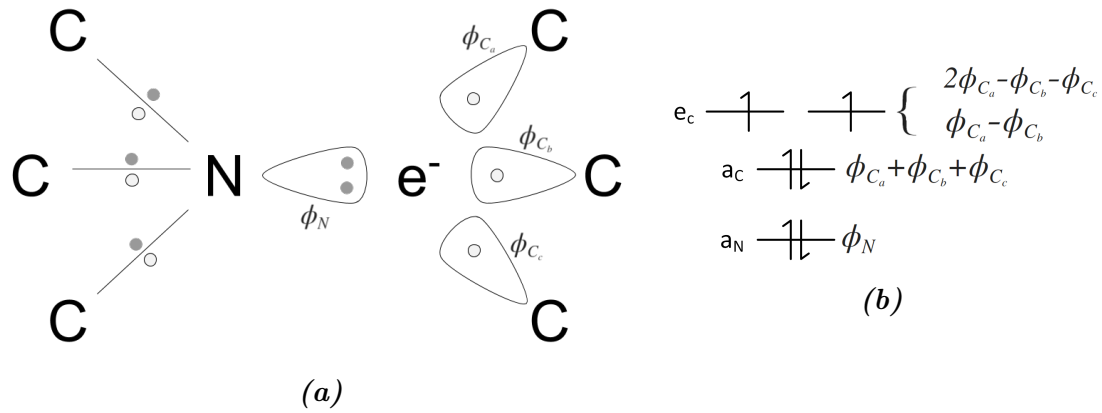

Figure 2.9: *(a) shows orbitals of the negative nitrogen vacancy centre. Empty circles indicate a carbon electron and filled circles indicate a nitrogen electron. (b) shows an electron configuration.*

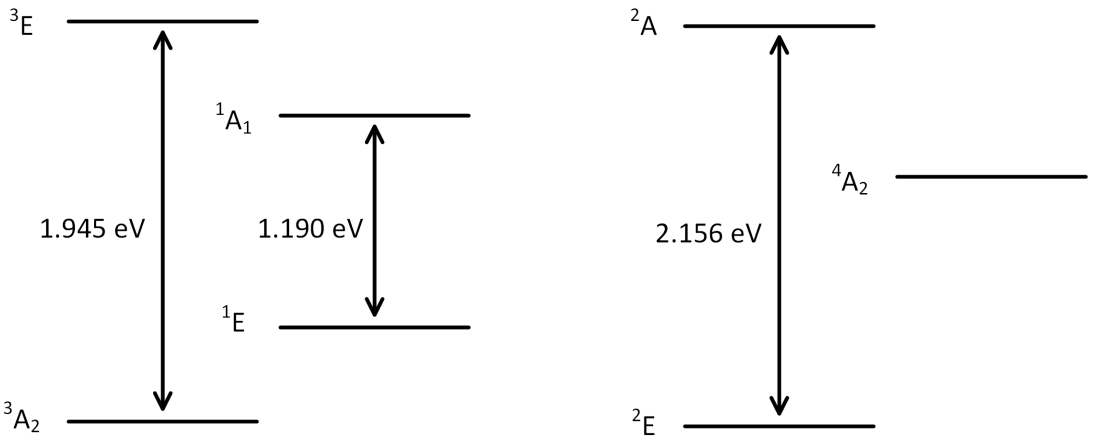

(a) *Energy levels of the negative nitrogen vacancy.*

(b) *Energy levels of the neutral nitrogen vacancy.*

Figure 2.10: *Energy levels of the neutral and negative nitrogen vacancy. Figure adapted from [46].*

Production Implantation of nitrogen ions or electron irradiation will cause damage to the crystal structure creating vacancies and interstitials. After this an annealing procedure can be used which allows migration of vacancies to create nitrogen vacancy centres. The standard annealing procedure uses three anneals at different temperatures; 400°C, 800°C and 1200°C [71]. The first anneal supplies enough energy for the migration of interstitials to vacancies, dislocations and edges. The second anneal supplies enough energy for the migration of the vacancies. These too can migrate to dislocations and edges. It is also energetically favourable to form nitrogen vacancy centres as it reduces the local strain around the nitrogen atom [72]. Single substitutional nitrogen is an effective trap for vacancies [73]. The third anneal causes dissociation of di-vacancies [58].

The negative nitrogen vacancy centre is present in type Ib diamonds which have been electron irradiated and annealed at 550°C and in type II diamonds which have undergone N^+ ion implantation and have been annealed at 700°C [33]. The centre can be annealed out at temperatures of 1500°C.

The neutral nitrogen vacancy centre is present in type Ib diamonds which have been electron irradiated and annealed at 500°C and type IIa diamonds which have undergone N^+ ion implantation and have been annealed at 500°C [33]. The centre can be annealed out at temperatures of 1400°C.

Both charge states can be suppressed by electron irradiation as this creates interstitials which can recombine with the vacancies, creating single substitutional nitrogen.

Silicon Related Defects

The Silicon Vacancy Interest in the silicon vacancy has increased in recent years due to parallels with the nitrogen vacancy. The silicon vacancy has advantages over the nitrogen vacancy including a greater emission in the ZPL compared to the phonon side band. The negative silicon vacancy has excellent spectral stability due to the dipole symmetry [74] and has also been demonstrated for use as a single photon emitter [75] at room temperature and as solid state quantum-bits (qubits) [76].

Crystal Structure The silicon vacancy structure was first modelled by Goss et al. using density functional theory [66]. It forms a split vacancy structure, aligned

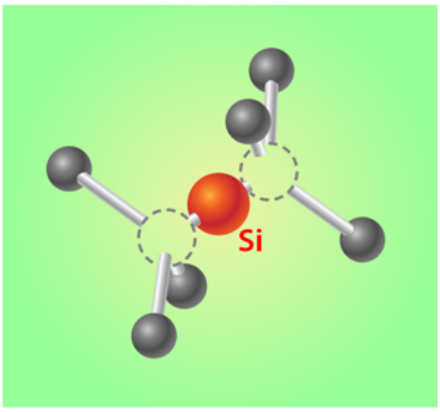

Figure 2.11: *The silicon vacancy centre [67].*

along the ⟨111⟩ direction, see figure 2.11. The silicon atom is much larger than the carbon atom it replaced. It does not fit easily in the vacancy left by the carbon atom and so sits between the two vacancies where there is more space. Silicon atoms are an effective trap for vacancies so when diamonds with vacancies and silicon atoms present are annealed, the silicon split vacancy structure is formed. Silicon vacancies are also effective traps for vacancies so if there are many silicon vacancies present silicon di-vacancies can also form [77]. A silicon atom in the split vacancy structure is surrounded by six broken carbon bonds. It can lie along four possible orientations, the four equivalent [111] axes [78]. It has a trigonal axis and inversion symmetry. The centre has D_{3d} symmetry, which has been confirmed by stress experiments by Sternschulte et al. [79]. For more detail about this identification see reference [80].

Electronic Structure The energy level diagram of the two charge states of the defect are shown in figure 2.12 and the ZPL emissions these create are shown in figure 2.13.

The neutral silicon vacancy has an electron arrangement $1s^2 2s^2 2p^6 3s^2 3p^2$ and an effective spin of $S = 1$ [82]. This spin configuration means the centre has an EPR signal. The EPR name is 'KUL1'. The ZPL is at 946 nm and was identified to be the neutral silicon vacancy by D'Haenens-Johansson et al by studying diamonds with different ratios of the 28 and 29 silicon isotopes [77].

Silicon has four electrons available for bonding. There are six carbon orbitals which remain unbonded. The electron wave functions combine to produce the states shown in figure 2.14b. These are filled with the ten electrons as shown in the figure but alternative arrangements are possible.

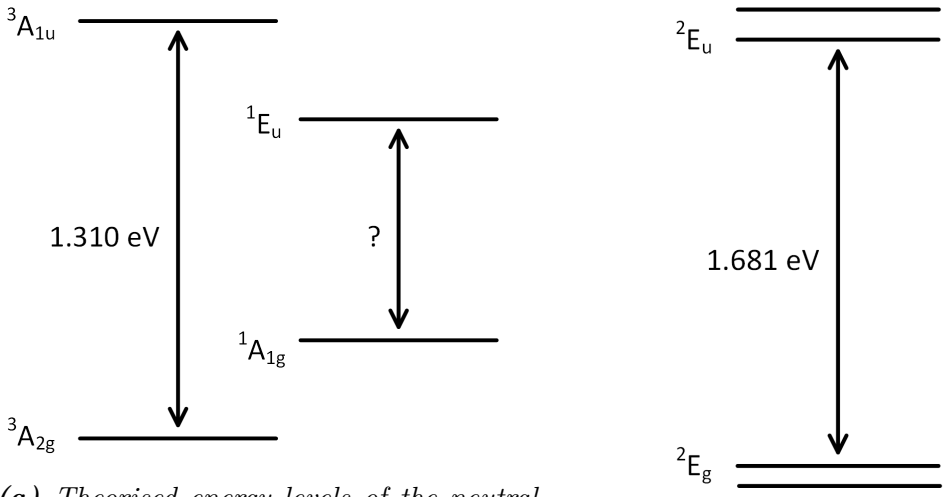

(a) *Theorised energy levels of the neutral silicon vacancy as an analogue to the nitrogen vacancy centre [81].*

(b) *Energy levels of the negative silicon vacancy.*

Figure 2.12: *Energy levels of the negative and neutral charge state of the silicon vacancy. Both the excited and ground state of the negative silicon vacancy are split [33].*

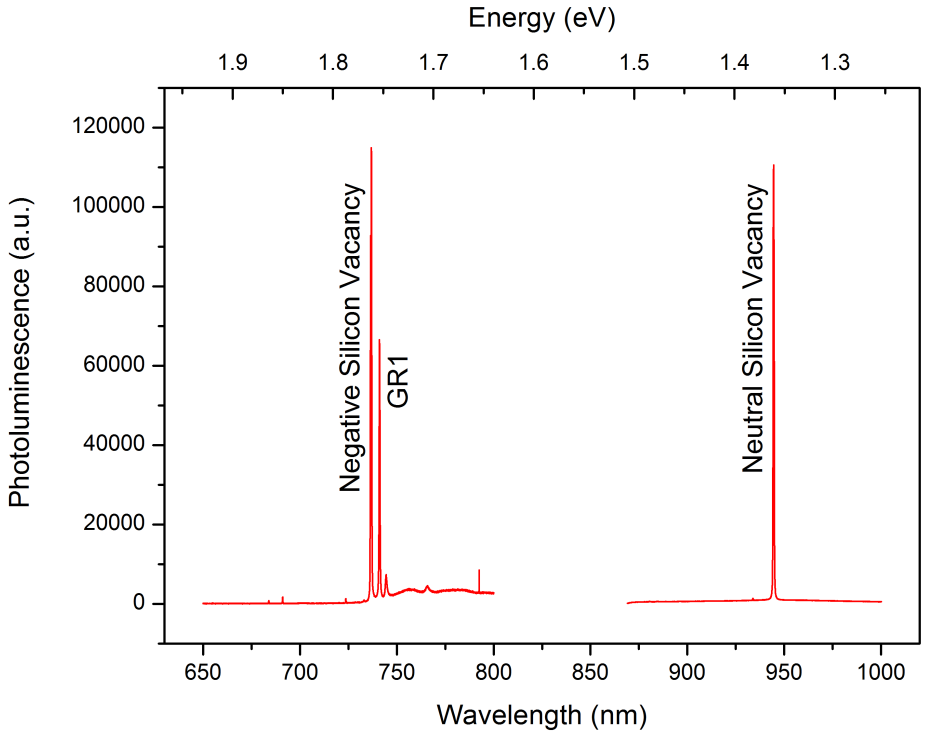

Figure 2.13: *A photoluminescence spectrum of silicon vacancy defects.*

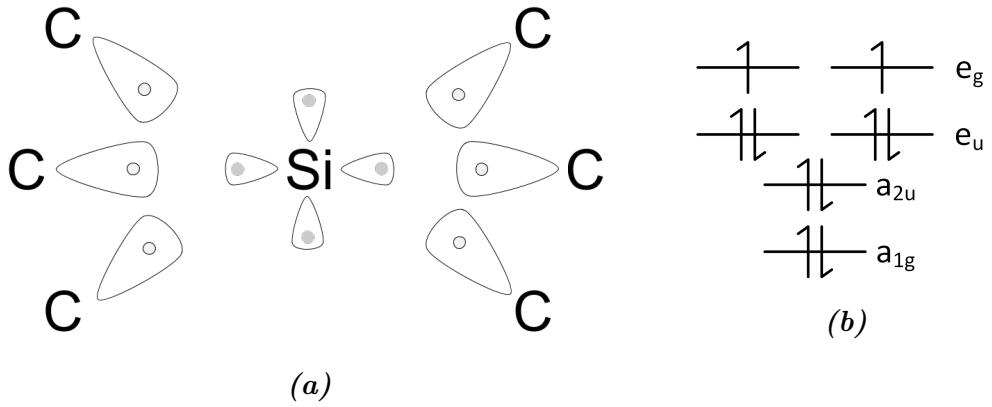

Figure 2.14: *(a) shows orbitals of the neutral silicon vacancy centre. (b) shows the lowest electron configuration.*

The ground state is $a_{1g}^2 a_{2u}^2 e_u^4 e_g^2$. An electron can be promoted from the lower e_u to the upper e_g level. The excited state is $a_{1g}^2 a_{2u}^2 e_u^3 e_g^3$. This gives rise to the many electron states shown below.

$$\begin{aligned} a_{1g}^2 a_{2u}^2 e_u^4 e_g^2 &\rightarrow {}^3A_{2g} + {}^1E_g + {}^1A_{1g} \\ a_{1g}^2 a_{2u}^2 e_u^3 e_g^3 &\rightarrow {}^3A_{1u} + {}^1A_{1u} + {}^3A_{2u} + {}^1A_{2u} + {}^3E_u + {}^1E_u \end{aligned}$$

The energy of these levels must be worked out experimentally. The final energy configuration was shown in figure 2.12a.

The negative silicon vacancy has eleven electrons. The ground state has an effective spin $S = 1/2$ [82]. The EPR signal of the ground state has not been seen due to dynamic Jahn-Teller splitting of the state: a spontaneous lowering of symmetry which removes degeneracy. Using stress may change the ground state energy levels and make an EPR signal visible.

The energy levels of the negative nitrogen vacancy centre are shown in figure 2.12b. Both the ground state and excited state are E states. The negative silicon vacancy has the highest emission in the ZPL compared to the phonon side band of any colour centre in diamond at room temperature and at low temperatures [83]. It also has a high count rate. The ZPL has a width of 0.7 nm at room temperature [84] and more than 80% of the luminescence from the centre is at the ZPL, compared to ∼3% for the nitrogen vacancy [85]. The negative silicon vacancy is the brightest single photon emitter in diamond [84]. This is discussed in more detail in section 2.5.1.

The negative silicon vacancy ZPL (1.68 eV) is split into twelve lines at low temperature, in three groups which scale with the abundance of the three silicon isotopes (28, 29, 30). The four lines caused by each isotope are created by the splitting of the ground and excited states. These states each split into two as shown in figure 2.12b. These states are already split, so a magnetic field is not required to split them, as the nitrogen vacancy requires. This makes the silicon vacancy useful for some applications.

The splitting of the excited and ground state means that the centre can be optically coherently controlled. This means control is faster than for the nitrogen vacancy which requires a magnetic field [86]. All-optical control is possible for the silicon vacancy [86] and individual centres can be studied [83]. Optically detected magnetic resonance (ODMR) was measured and reported by Pingault et al. in 2017 [87].

Charge Transfer Optical illumination in the UV range can be used to change neutral silicon vacancies into negative ones, but this effect decays after several hours. Heating to 577°C causes the opposite [77].

Boron doping can change negative silicon vacancies into neutral ones by accepting an electron, so diamonds with high boron doping often have more neutral than negative silicon vacancies [88]. The negative silicon vacancy has higher concentrations in diamonds with high nitrogen concentrations, due to these centres donating an electron.

Production An effective way of creating diamonds containing silicon vacancies is introducing silicon using Si^+ ion implantation and annealing. Silicon vacancies can be introduced into silicon doped diamonds by electron irradiating them, which introduces vacancies, followed by annealing. However, for a diamond which already has silicon vacancies this may reduce their concentration by creating interstitials and vacancies which, when annealed, may recombine with the silicon vacancies already present changing them to silicon substitution atoms or silicon di-vacancies.

Silicon vacancies can also be created when the diamond is forming or grown by CVD [70]. These defects may be preferentially orientated, and their direction is perpendicular to the growing diamond surface [81]. This may be because when a diamond is growing in layers, once a layer contains a silicon atom, larger than the carbon atom which was replaced, a vacancy is likely to occur on top of this. This

can be used to understand the direction a diamond grew in.

Other Silicon Related Defects

Silicon Vacancy Hydrogen The neutral silicon vacancy decorated with a hydrogen atom was identified by Edmonds et al. [80] and the theoretic basis for this defect structure was calculated by Goss et al. [89]. In EPR it is called 'KUL3'. The centre was identified by studying the ^{1}H and the ^{29}Si hyperfine resonances in EPR. The centre is annealed out at 1400°C [90].

Silicon Di-vacancy This defect has been predicted by Goss et al. and should be present in diamonds which have a large silicon and vacancy concentration and have been annealed [89]. Silicon vacancies are efficient traps for vacancies so silicon di-vacancies will form in annealed silicon vacancy containing diamonds. It should be active in EPR as S=1/2, but it has not yet been seen.

Silicon Di-vacancy Hydrogen Goss et al. predicted the existence of silicon di-vacancy hydrogen [89] and they have been studied in CVD diamonds. These centres are often present due to the high content of hydrogen in the reactants used for CVD. The defect has been seen in EPR and has the name 'WAR3' [91]. It was found to preferentially orientate in CVD diamonds grown on a {1 1 0}-orientated surface but can also be created post growth. The defect has an effective spin $S = 1/2$ and C_{1h} symmetry.

2.5 Applications

Traditional applications for diamond have utilised its material properties, including its high hardness. These applications include drill bits for oil drilling and for Vickers hardness testers where a diamond is used to test the hardness of other materials.

New applications utilise the different properties of HPHT and CVD diamond. HPHT diamonds have been used for stress anvils [23]. Type Ib diamonds are used in X-ray diffraction stress and type IIa (colourless) are used in stressed Raman

and FTIR experiments, using pressures up to 300 GPa. CVD diamonds (type IIa) have the advantage of having fewer impurities. These have been used for applications including radiation detectors, a medium for Raman lasers and biological applications. Both types of diamond have also been used in jewellery and heat spreaders [23].

Diamonds are also interesting for use in quantum applications due to the properties of the defects within them. The properties can be utilised for single photon emission [92], measuring magnetic fields [9, 93] and temperature sensing [94]. These applications are the subject of this section.

2.5.1 Single Photon Emission

One of the most promising technological applications for colour centres in diamond is single photon sources. These are needed for quantum information processing which looks set to be an important technology in the future [95].

Many different types of single photon sources are currently being investigated. These include quantum dots and a variety of defect centres in diamond. A critical advantage of diamond is that it can be used at room temperature whereas quantum dots require cryogenic cooling.

One of the most promising competitors are quantum dots in InGaAs but only one dot in 1000 works [96]. The multitude of diamond systems being investigated include chromium [97], xenon [98], nickel [99] and oxygen related [100] defect centres. The negative nitrogen vacancy centre has also been used [95], however, it also requires cryogenic cooling for emission of indistinguishable photons due to the high fraction of photons which are emitted in the phonon side band. The brightest centre seen to date was the negative silicon vacancy [7].

Diamond is a favourable material to utilise because of the ease of creating defects and the defect structural stability. Diamond has a low magnetic noise environment which means the defect spins are accessible. Diamond is also a very stable material which means that small particles can be made from it. As mentioned above it can be used at room temperature which is a huge advantage. The defects within the material are photostable [84].

The main rival to the superiority of the negative silicon vacancy centre is the nitrogen vacancy, the most studied defect in diamond. The two defects are stoi-

chiometrically the same but there are many differences between the two centres; the silicon vacancy centre has advantages for single photon applications. The main advantage of the silicon vacancy centre is the high emission in the ZPL, as discussed in section 2.4.2, in comparison the nitrogen vacancy has very low quantum efficiency in its ZPL.

The contrasting emission in the ZPL is due to their difference in phonon coupling [74]. Both the neutral and negative silicon vacancy have a small phonon side band due to their inversion symmetry [101]. The inversion symmetry of the defect means there is a smaller electron dipole and therefore photons do not interact with the centres as strongly as for the nitrogen vacancy. The silicon vacancy has a small Huang-Rhys factor, the number which describes vibronic coupling, of $S = 0.08$ [84, 102].

The nitrogen vacancy has a major disadvantage, due to its wide ZPL, which is the reason so many different systems are being investigated. The maximum output so far seen from nitrogen vacancy is two million counts per second compared to negative silicon vacancy which has been demonstrated to have six million [95].

Some methods have been investigated for improving the emission at the ZPL. These include using nano-cavities which are small structures which enhance emission at a particular frequency [92] and using nano-pillars of diamond which would help getting light in and out.

Another advantage to negative silicon vacancy is that the ZPL is emitted in a region where there is little background fluorescence from intrinsic diamond. This is also true of the neutral silicon vacancy [84]. This does not reduce the importance of having very high purity diamond to reduce noise. The ZPL of the negative silicon vacancy can be doubled using non-linear optics. It would then be at 1480 nm which has been demonstrated already [103]. This is within the region of current optical communication, 1310 nm to 1550 nm, which means this could be used in current systems. The ZPL from the neutral silicon vacancy, at 946 nm is even better for communications as without doubling it can be used with some of the optical fibres now used, without too much attenuation.

The lifetime of the excited state of the negative silicon vacancy is 1 to 5 ns, compared to 10 to 20 ns for the nitrogen vacancy [74, 95]. The silicon vacancy is thus more useful as photons will be emitted quicker. The shorter lifetime results in a higher emission rate.

It seems pretty certain that these systems are going to be important in the future but there are many obstacles to overcome. There has been proof of principle but more work needs to be done [84, 95, 104]. Nanodiamonds have much potential. They are better both due to the lack of internal reflection and lack of background fluorescence. Silicon vacancy containing nanodiamonds have been made on iridium using CVD by Neu et al. [84]. These nanodiamonds showed no background fluorescence, were stable, had linewidths which were smaller than normal, had 88% emission in the ZPL and in 2016 were the brightest emitter found so far in diamond [105]. Nanodiamonds also have longer relaxation times [106]. Work has also been done on decreasing the size of these nanoparticles by Vlasov et al. [104]. This is important for biological applications such as probing cells. Theoretically these silicon vacancy containing nanodiamonds are stable down to 1.6 nm though this is a size which which is currently impossible to make in the lab. However Vlasov et al. managed to test very small nanodiamonds which had come to Earth in a crater of presolar origin. These contained silicon vacancy and were stable although they did not perform as well as previous silicon vacancy nanodiamond samples. They showed blinking which reduced their efficiency.

There are a number of developments which are still being made. The most important include: suppressing multiphonon events, improving efficiency and stability and ensuring the centres are maintenance free. The silicon vacancy centre appears to be a good option for these quantum applications but more work needs to be done.

2.5.2 Magnetometry with NV^-

Magnetometry has been performed with single negative nitrogen vacancy centres by Balasubramanian et al. [9]. Magnetometry is done using optically detected magnetic resonance by utilising the differing fluorescence from the different spin states. When electrons are excited up from the ground state using light energy, $m_s = 0$ electrons are excited up and relax back as expected, however $m_s = \pm 1$ electrons are not. There is a reasonable probability (the crossing transition ratio is 40% [46]) that these electrons will take an alternative relaxation pathway, inter-system crossing, via the $^1A_1$ and ^1E states (see figure 2.15). If this occurs relaxing electrons will preferentially populate the $m_s = 0$ level. After a few excitation-relaxation cycles, the majority of the electrons will be in the $m_s = 0$ level. This is the origin of the electron spin polarisation. The $m_s = 0$ state is called the 'light'

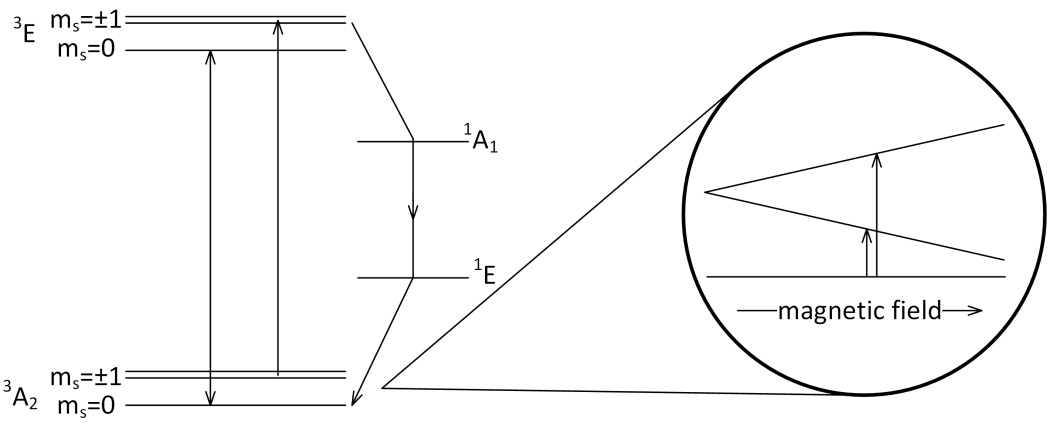

Figure 2.15: *Energy levels of NV^- under illumination and behaviour of ground state electron spin configurations as magnetic field increases. Figure reproduced from [107].*

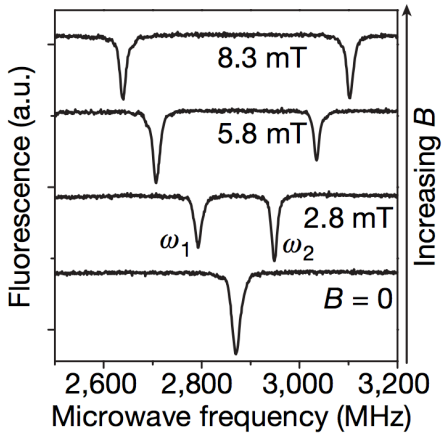

Figure 2.16: *Absorption of microwaves under different magnetic fields. Graph from [9].*

state and the $m_s = \pm 1$ is called the 'dark' state. The $m_s = 0$ state fluoresces under optical illumination and the $m_s = \pm 1$ does not as it undergoes intersystem crossing. If the fluorescence is monitored, this fluorescence will dip if electrons move from the $m_s = 0$ state to the $m_s = \pm 1$ state. This can be done using finely tuned microwaves. When a magnetic field is applied, the $m_s = +1$ and the $m_s = -1$ states change relative to each other in energy. This can be seen in figure 2.15. Fluorescence will now show two dips, one for the $m_s = 0$ transition to $m_s = +1$ and one from $m_s = 0$ to $m_s = -1$. These two dips can be measured and calibrated so their difference can be used to measure the local magnetic field. These results for the Balasubramanian group can be seen in figure 2.16.

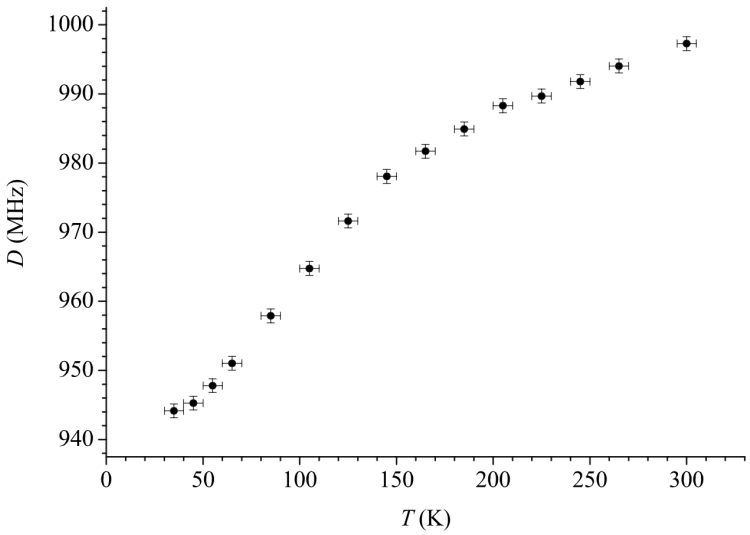

Figure 2.17: *The relationship between zero-field splitting and temperature in the neutral silicon vacancy. Image from [80].*

2.5.3 Temperature Sensing

Temperature sensing has been demonstrated using nitrogen vacancy centres with length scales of a few tens of nanometres [94]. This uses the centres change in zero-field splitting (D) with temperature. The neutral silicon vacancy has a steeper relation between ground state splitting and temperature (due, in part, to the sharp change of T_1 with temperature discussed in Chapter 5) and therefore would be more sensitive for temperature sensing applications [80]. This relationship is shown in figure 2.17. The nitrogen vacancy has a change of $\frac{dD}{dT} = -74 \quad \text{kHzK}^{-1}$ [108]. The gradient in the silicon vacancy is $\frac{dD}{dT} = -337 \quad \text{kHzK}^{-1}$ and linear in the temperature range 50 to 150 K. The average gradient between 50 and 300 K is $\frac{dD}{dT} = -202 \quad \text{kHzK}^{-1}$.

2.5.4 Quantum Bits

A quantum bit is an analogue to a classical bit in that it stores information as 1 or 0. A quantum bit can also be in a superposition of 1 and 0, so it can store additional information.

There are many systems currently being tested for use as quantum bits including colour centres in diamond. The nitrogen vacancy has many ideal properties including the ability to control and read-out specific centres [109, 110].

The negative silicon vacancy can also be used as a quantum bit. It has one main advantage; the splitting of the ground and excited states, see figure 2.12b. This removes the requirement of a magnetic field to split the levels [111]. All-optical coherent control of silicon vacancies has been demonstrated by Becker et al. [106].

Chapter 3

Theory

3.1 Introduction

In this chapter the theory behind the techniques used and the phenomena observed throughout this thesis will be discussed. This includes a discussion of continuous wave electron paramagnetic resonance which was used to investigate the structure, local nuclei and symmetry of defects and pulsed electron paramagnetic resonance which was used to investigate the spin-spin and spin-lattice relaxation rates and mechanisms. Optical absorption is discussed. Infrared absorption was used to investigate characteristic vibrations and ultraviolet and visible absorption was used to investigate these vibrations along with electronic transitions of different defects. Raman spectroscopy was used to investigate lattice scattering. Photoluminescence and cathodoluminescence spectroscopy were used to investigate photon emission from defects. Secondary ion mass spectrometry was used to measure elemental concentrations.

3.2 Electron Paramagnetic Resonance

Electron paramagnetic resonance (EPR) is a technique which allows systems with unpaired electron spin to be investigated [112]. It is a quantitative technique and is used to measure concentrations of paramagnetic defects in diamond [113].

The EPR spectrum can be used to identify the species present as the spectra is shaped by the interactions. Including the Zeeman interaction which gives rise

to the characteristic g-value and the hyperfine interaction which can be used for identification of chemical constituents and the localisation of unpaired electron probability density.

3.2.1 The Magnetic Moment of a Free Electron

The magnetic moment of an electron is an intrinsic property related to its angular momentum [112]. The energy (U) of a magnetic moment in a field, $\boldsymbol{B}$, is given by equation 3.1, where $\boldsymbol{\mu}$ is the magnetic moment.

$$U = -\boldsymbol{\mu} \cdot \boldsymbol{B} \tag{3.1}$$

The magnetic moment is proportional to $\boldsymbol{J}$, the angular momentum. $\boldsymbol{J}$ is a sum of the orbital angular momentum, $\boldsymbol{L}$, and the spin angular momentum, $\boldsymbol{S}$. If it is assumed that orbital angular momentum is quenched, this allows the magnetic moment of a free electron to be related to the electron's spin as given by equation 3.2, where g_e is the free electron g-factor and μ_B is the Bohr magneton.

$$\boldsymbol{\mu} = -g_e \mu_B \boldsymbol{S} \tag{3.2}$$

If $\boldsymbol{B}$ is assumed to be in the z-direction the energy of the electron is given by equation 3.3, where m_s is the quantum number for the spin state.

$$U = g_e \mu_B B m_s \tag{3.3}$$

The Landé factor, g_e, is a correction factor required by the classical model as it is being used to model a fundamentally quantum system and is 2.0023 for free electrons. For an electron in a crystal g_e will be a matrix which may be anisotropic. If there is a non-zero orbital angular momentum ($\boldsymbol{L}$) the magnetic moment is given by equation 3.4.

$$\boldsymbol{\mu} = -\mu_B \left(g_e \boldsymbol{S} + \boldsymbol{L}\right) \tag{3.4}$$

The mixing of the states with non-zero angular momentum can be contained within $\boldsymbol{g}$, as a matrix. This can then be used to give an expression for the energy of the state, as shown in 3.5.

$$U = \mu_B \left(\boldsymbol{B^T} \cdot \boldsymbol{g} \cdot \boldsymbol{S}\right) \tag{3.5}$$

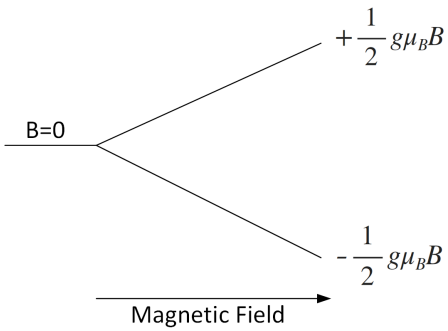

Figure 3.1: *Zeeman splitting between two levels, α, the upper level, and β, the lower level.*

3.2.2 The Electron Zeeman Interaction in a Solid

The electron Zeeman interaction describes the energy of an electron in a magnetic field [114]. An electron when placed in a magnetic field may either align or anti-align with the field. This gives rise to two spin states, one low energy and one high energy, described by m_s the quantum number for the spin state. To change an electron from one state to the other energy must be absorbed or emitted by the electron. The energy required to change an electron from one spin state to the other is given by equation 3.6, where β is the starting state and α is the final state. The selection rules require $|\Delta m_s| = 1$ and m_s is quantised.

$$\Delta U = U_\alpha - U_\beta = g\mu_B B|\Delta m_s| \tag{3.6}$$

This energy gap forms the basis of EPR experiments. This energy can be probed by applying electromagnetic energy and measuring its absorption as the electron spins flip.

Resonance

The basis of an EPR experiment is the absorption of electromagnetic radiation. It creates an oscillating magnetic field perpendicular to the applied field. The resonance condition is when the Zeeman energy and the electromagnetic energy are equal and hence the electrons can absorb the energy and undergo a magnetic dipole transition. This is when the electromagnetic energy is equal to ΔU; $\Delta U = h\nu$. Figure 3.1 shows the energy of the two spin states changing with increasing magnetic field. At each field there is a electromagnetic energy which fulfils the

resonance condition and can change the spin state.

For an ensemble of electrons the probability of the population in each of the two energy levels in figure 3.1 at thermal equilibrium can be determined by Maxwell-Boltzmann statistics and is given by the Boltzmann distribution law in equation 3.7 [115, 116]. In this equation N_α is the number of electrons in energy state α and N_β is the number of electrons in energy state β, where β is the lower energy state. As can be seen from the equation at zero-field the levels become equal.

$$\frac{N_\alpha}{N_\beta} = exp\left(-\frac{g\mu_B B}{k_B T}\right) \tag{3.7}$$

At room temperature $k_B T$ is greater than the Zeeman energy so the exponential can be expanded in to a series as given in equation 3.8.

$$\frac{N_\alpha}{N_\beta} = 1 - \frac{g\mu_B B}{k_B T} \tag{3.8}$$

There will be similar numbers of up and down spin electrons, with slightly more in the lower energy configuration with the ratio $\alpha : \beta$ of 1000:1001. Hence, the net absorption of microwave energy will be small.

In X-band experiments a field of around 3000 G is used. The energy difference between up and down spin electrons is electromagnetic radiation in the microwave region. In order to calculate the Zeeman energy the microwave energy is fixed and the magnetic field is swept and the absorption of the microwaves is measured. This was chosen, as opposed to sweeping the microwave source at a fixed field, as a resonator is used to store the microwave energy and this has a fixed size. The wavelength of microwaves is a few centimetres which means a resonator designed to contain them is a very convenient size for diamond samples.

3.2.3 The Effective Spin Hamiltonian

The Hamiltonian is the operator in quantum mechanics that represents energy. When the electron wave function is an eigenfunction of the Hamiltonian it has a precise energy given by the eigenvalue of the Hamiltonian. It consists of a spin part and a spatial part. It can be simplified by integrating over all spatial variables leaving the spin part; this equation is termed the 'spin Hamiltonian'. This form

is very useful in the understanding of EPR spectra as it describes the interactions of an electron and it's environment [117]. It can be expressed for an unpaired electron in a lattice, as given by equation 3.9. Each of the terms of this equation describe different interactions of the electron spins in the system [118].

$$\hat{H} = \underbrace{\mu_B \boldsymbol{B^T} \cdot \boldsymbol{g} \cdot \hat{\boldsymbol{S}}}_{\text{electron Zeeman}} + \underbrace{\hat{\boldsymbol{S}}^T \cdot \boldsymbol{D} \cdot \hat{\boldsymbol{S}}}_{\text{spin-spin}} + \sum_{i=1}^{N} (\underbrace{\hat{\boldsymbol{S}}^T \cdot \boldsymbol{A}_i \cdot \hat{\boldsymbol{I}}_i}_{\substack{\text{electron-nuclear} \\ \text{hyperfine}}} - \underbrace{\mu_N g_N \boldsymbol{B^T} \cdot \hat{\boldsymbol{I}}_i}_{\text{nuclear Zeeman}} + \underbrace{\hat{\boldsymbol{I}}_i^T \cdot \boldsymbol{P}_i \cdot \hat{\boldsymbol{I}}_i}_{\substack{\text{nuclear} \\ \text{quadrupole}}} + \dots) \tag{3.9}$$

In equation 3.9 the first term is the electron Zeeman interaction and the second is the spin-spin interaction. The remainder of the terms are summed over the nuclei in the system and these consist of the electron-nuclear hyperfine interaction, the nuclear Zeeman interaction and the is the nuclear quadrupole. These interactions will be discussed in the following sections and the terms within the equation will be defined.

3.2.4 The Nuclear Zeeman

The nuclear Zeeman interaction arises from the interaction of the nuclei with the magnetic field, similarly to the electron Zeeman interaction [114]. However, depending upon the nuclei the interaction is at least 600 times weaker than the electron Zeeman interaction. It is isotropic and usually has little effect on the EPR spectrum. It is dependent on the spin quantum number, I_z, and g_n both of which are intrinsic properties of the nucleus. I_z is quantised. The Hamiltonian for this is shown in equation 3.10, assuming B is in the z-direction.

$$\hat{H} = -\sum_{i=1}^{N} \mu_N g_n B \hat{I}_z \tag{3.10}$$

Analogously to the EPR resonance Nuclear Magnetic Resonance (NMR) can occur with a nucleus absorbs energy and changes state. This energy is shown in equation 3.11.

$$\Delta U = U_{\alpha(n)} - U_{\beta(n)} = g_n \mu_n B |\Delta M_I| \tag{3.11}$$

The nuclear Zeeman may be seen in an EPR spectrum in the form of weak satellites

which arises from double spin-flip transitions. These transitions involve flipping of the electron and nuclear spin simultaneously and are forbidden.

3.2.5 The Hyperfine Interaction

The hyperfine interaction describes the effect on an electron of the local magnetic nuclei. The effective field at an electron is the sum of the field applied and the local field which arises from nearby nuclei [119]. The two fields can be added vectorially.

$$\boldsymbol{B_{eff}} = \boldsymbol{B} + \boldsymbol{B_{local}} \tag{3.12}$$

The interaction between the electron and local nuclei is called the hyperfine interaction. The Hamiltonian which relates this is given in equation 3.13, with the magnetic field in an arbitrary direction.

$$\hat{H} = \hat{\boldsymbol{S}}^{\boldsymbol{T}} \cdot \boldsymbol{A} \cdot \hat{\boldsymbol{I}} \tag{3.13}$$

The hyperfine matrix, $\boldsymbol{A}$, has both an isotropic and anisotropic part as given by equation 3.14, where A_0 is the isotropic part and $\boldsymbol{T}$ the anisotropic part.

$$\boldsymbol{A} = A_0\mathbf{1} + \boldsymbol{T} \tag{3.14}$$

The isotropic part is given by the coupling constant A_0, given in equation 3.15, and arises from the Fermi contact interaction, where the unpaired electron probability density is localised at the nucleus.

$$A_0 = \frac{2\mu_0}{3} g\mu_B\mu_N |\Psi(0)|^2 \tag{3.15}$$

The anisotropic part is caused by the dipolar interaction between the electron and local nuclei and is given by the expression in equation 3.16.

$$\boldsymbol{T} = \begin{pmatrix} -b & 0 & 0 \\ 0 & -b & 0 \\ 0 & 0 & 2b \end{pmatrix} \quad where \quad b = \frac{\mu_0}{4\pi} \frac{g_e g_N \mu_B \mu_N}{\langle r^3 \rangle} \tag{3.16}$$

This interaction is dependent on the distance between the electron and nuclei (r) and is still present at zero-field. It causes the absorption lines to change field

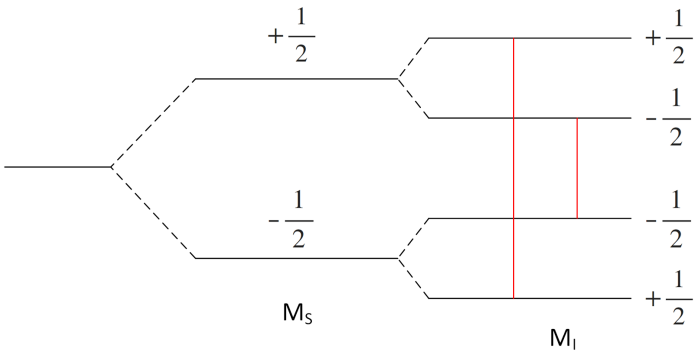

(a) *Spin state splitting caused by the electron Zeeman interaction and the electron-nuclear hyperfine in hydrogen. Red line indicates the allowed transition. Image recreated from [112].*

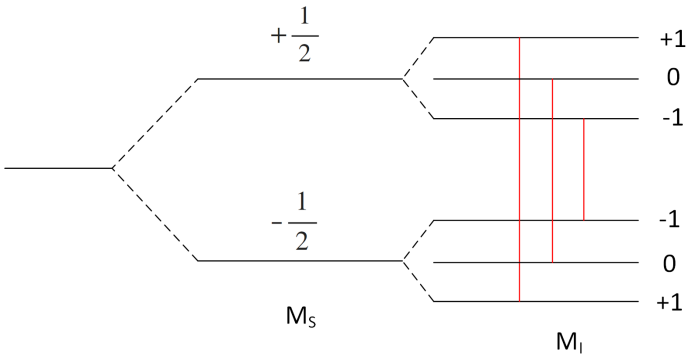

(b) *Spin state splitting caused by the electron Zeeman interaction and the electron-nuclear hyperfine in single substitutional nitrogen. Red line indicates the allowed transition.*

Figure 3.2: *Spin state splitting caused by the electron Zeeman interaction and the electron-nuclear hyperfine in single substitutional nitrogen.*

position as the crystal is rotated as the angle between the magnetic field and the vector between the nuclei and electron change.

The quantisation of the nuclear spin results in a discrete set of magnetic environments. For example a hydrogen atom has $S = \frac{1}{2}$ and $I = \frac{1}{2}$. This results in four different combinations of states shown in figure 3.2a. According to the selection rules, $\Delta m_S = \pm 1$ and $\Delta m_I = 0$, thus there are two allowed transitions.

The single substitutional nitrogen defect has $S = \frac{1}{2}$ and $I = 1$. This results in three nuclear spin states $m_I = -1, 0, +1$ so there are three different local environments that an electron can experience. This means there are three different frequencies of electromagnetic energy absorbed when the magnetic field is scanned. A simulated EPR spectrum of an ensemble of electrons adjacent to a nitrogen atoms is shown in figure 3.3a.

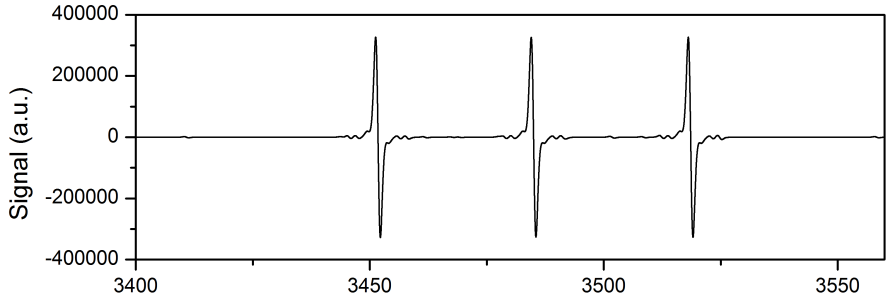

(a) *An EPR spectrum of an ensemble of electrons split into three by the hyperfine interaction by a nearby nitrogen nucleus. The field is applied along a* ⟨001⟩ *direction.*

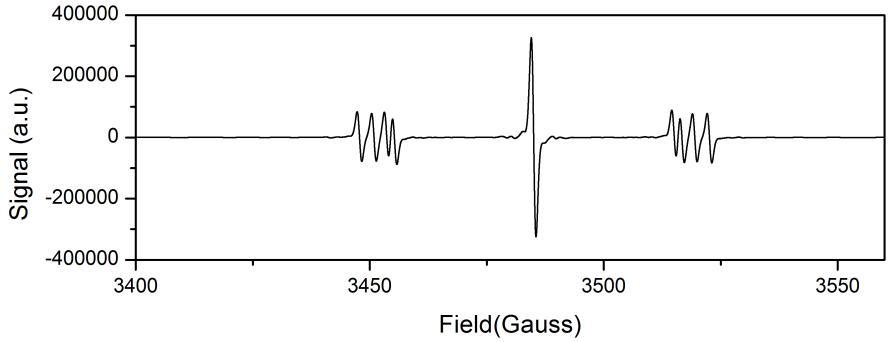

(b) *The effect of the external field being applied at no particular crystallographic direction.*

Figure 3.3: *Simulated EPR spectrum of a bulk sample of electrons at nitrogen defect centres in diamond.*

In diamond there is high symmetry, due to the regular structure of the atoms. The single substitutional nitrogen defect has C_{3v} symmetry. This means there are four different orientations which the defect can take. Each of these orientations has a different angle between the symmetry axis and the magnetic field. The anisotropic hyperfine interaction splits the absorption lines into four the position of which depends on the position of the diamond in the magnetic field. This splitting can be seen in the two outer lines of figure 3.3b. The middle line does not split because the nitrogen nuclei for the $m_s = 0$ state are neither aligned nor anti-aligned with the field, thus a change in the field direction does not affect these nuclei. These absorptions, along with their position, allow identification of the unpaired electron's environment.

3.2.6 Electron-Electron Dipole Interaction

The electron-electron dipole interaction is an anisotropic dipole interaction between nearby electrons, described by $\boldsymbol{D}$. It only applies when $S > \frac{1}{2}$. The local electron field changes the energy of the m_s states. The effect is applied field independent. At zero-field it removes the ground state degeneracy, hence it may be called Zero Field Splitting (ZFS). It is shown in equation 3.17.

$$\hat{H} = \hat{\boldsymbol{S}}^T \cdot \boldsymbol{D} \cdot \hat{\boldsymbol{S}} \tag{3.17}$$

$\boldsymbol{D}$ depends on the angle between the symmetry axis and the applied magnetic field. For the neutrally charged silicon vacancy the effective spin is $S = 1$, this creates two absorption lines in EPR. However, the defect has a symmetry axis along $\langle 111 \rangle$ so has four different possible orientations; $[1\,1\,1]$, $[\bar{1}\,1\,\bar{1}]$, $[1\,\bar{1}\,\bar{1}]$ and $[\bar{1}\,\bar{1}\,1]$. As each of these has a different angle between the symmetry axis and the magnetic field $\boldsymbol{D}$ is different for each, hence the lines do not overlap, unless the field direction is $\langle 001 \rangle$ and thus makes the same angle ($54.74°$) to all four directions.

3.2.7 Nuclear Quadrupole

The nuclear quadrupole is the interaction of the nuclear charge distribution and the surrounding electric field created by the electrons [120]. It is only included in the effective spin Hamiltonian when $\boldsymbol{I} > \frac{1}{2}$, where $\boldsymbol{I}$ is the nuclear spin. The effect is contained with in $\boldsymbol{P}$, the nuclear quadrupole coupling matrix, in the spin Hamiltonian as shown in equation 3.18.

$$\hat{H} = \sum_{i=1}^{N} \hat{\boldsymbol{I}}_{\boldsymbol{i}}^T \cdot \boldsymbol{P_i} \cdot \hat{\boldsymbol{I}}_{\boldsymbol{i}} \tag{3.18}$$

As s-orbitals are symmetric they do not have an effect but s-orbitals of other nuclei and p-orbitals do change the local field gradient.

The effect on the EPR spectra is a small shift in the lines. Additionally, it causes state mixing between the m_s and m_I states and hence causes forbidden transitions to become allowed. This effect can to studied to understand the electric charge distribution surrounding a nucleus.

3.3 Bloch Equations

The Bloch equations were first outlined by Felix Bloch in the 1940s to describe the behaviour of magnetic moments of nuclei [121]. They are also applicable to the behaviour of electron moments. The Bloch equations describe the changes in bulk magnetisation of a sample over time. They include the relaxation of the magnetisation, T_1 and T_2, which will be discussed in section 3.4. Described here will be the basic equations but for a more complete picture please see reference [112].

An ensemble of spins can be described by the bulk magnetisation. In a constant magnetic field, assuming no relaxation effects, the bulk magnetisation will change with time as given by equation 3.19.

$$\frac{d\boldsymbol{M}}{dt} = \gamma_e \boldsymbol{M} \times \boldsymbol{B} \quad where \quad \gamma_e = \frac{g\mu_B}{\hbar} \tag{3.19}$$

If $\boldsymbol{B}$ is aligned in the z-direction, $\boldsymbol{B} = (0, 0, B_0)$, this gives equations 3.20, 3.21 and 3.22.

$$\frac{dM_x}{dt} = \gamma_e B_0 M_y \tag{3.20}$$

$$\frac{dM_y}{dt} = -\gamma_e B_0 M_x \tag{3.21}$$

$$\frac{dM_z}{dt} = 0 \tag{3.22}$$

These equations can be solved to give equations 3.23, 3.24 and 3.25, where M_z^0 is the magnetisation at $t = 0$ in the z-direction and $M_\perp^0$ is the magnetisation at $t = 0$ in the xy plane. ω_B is the Larmor frequency.

$$M_x = M_\perp^0 cos(\omega_B t) \tag{3.23}$$

$$M_y = M_\perp^0 \sin(\omega_B t) \tag{3.24}$$

$$M_z = M_z^0 \tag{3.25}$$

These demonstrate that the magnetisation oscillates around the z-direction, with a frequency given by ω_B. If the applied field changes the magnetisation, M_x, M_y and M_z, will align to the new field at a certain rate. This is given by the spin-lattice relaxation rate (T_1) for M_z and by the spin-spin relaxation rate (T_2) for M_x and M_y. This can be included in equations 3.20, 3.21 and 3.22 as an extra term.

This is given by equations 3.26, 3.27 and 3.28.

$$\frac{dM_x}{dt} = \gamma_e B M_y - \frac{M_x}{T_2} \tag{3.26}$$

$$\frac{dM_y}{dt} = -\gamma_e B M_x - \frac{M_y}{T_2} \tag{3.27}$$

$$\frac{dM_z}{dt} = \frac{M_z^0 - M_z}{T_1} \tag{3.28}$$

During an EPR experiment a microwave field is also applied to the sample. The magnetic field component (B_1) will interact with the spins and therefore must be included in the Bloch equations. It is an oscillating magnetic field with components $B_{1x} = B_1 \cos(\omega t)$, $B_{1y} = B_1 \sin(\omega t)$ and $B_{1z} = 0$. Including these gives equations 3.29, 3.30 and 3.31 which fully describe the magnetisation during an EPR experiment.

$$\frac{dM_x}{dt} = \gamma_e(BM_y - B_1 \sin(\omega t) M_z) - \frac{M_x}{T_2} \tag{3.29}$$

$$\frac{dM_y}{dt} = \gamma_e(B_1 \cos(\omega t) M_z - BM_x) - \frac{M_y}{T_2} \tag{3.30}$$

$$\frac{dM_z}{dt} = \gamma_e(B_1 \sin(\omega t) M_x - B_1 \cos(\omega t) M_y) - \frac{M_z - M_z^0}{T_1} \tag{3.31}$$

3.3.1 Line Shape

The Bloch equations described in section 3.3 can be used to predict the line shape of an EPR line. The first step is to translate the Bloch equations into the rotating frame. This frame is defined as rotating around z in the same direction as the B_1 field, with frequency ω. This gives equations 3.32, 3.33 and 3.34.

$$\frac{dM_{x\phi}}{dt} = -(\omega_B - \omega) M_{y\phi} - \frac{M_{x\phi}}{T_2} \tag{3.32}$$

$$\frac{dM_{y\phi}}{dt} = (\omega_B - \omega) M_{x\phi} + \gamma_e B_1 M_z - \frac{M_{y\phi}}{T_2} \tag{3.33}$$

$$\frac{dM_z}{dt} = -\gamma_e B_1 M_{y\phi} - \frac{M_z - M_z^0}{T_1} \tag{3.34}$$

These equations can be solved to give equations 3.35, 3.36 and 3.37.

$$M_{x\phi} = -M_z^0 \frac{\gamma_e B_1 (\omega_B - \omega) T_2^2}{1 + (\omega_B - \omega)^2 T_2^2 + \gamma_e^2 B_1^2 T_1 T_2} \tag{3.35}$$

$$M_{y\phi} = +M_z^0 \frac{\gamma_e B_1 T_2}{1 + (\omega_B - \omega)^2 T_2^2 + \gamma_e^2 B_1^2 T_1 T_2} \tag{3.36}$$

$$M_z = +M_z^0 \frac{1 + (\omega_B - \omega)^2 T_2^2}{1 + (\omega_B - \omega)^2 T_2^2 + \gamma_e^2 B_1^2 T_1 T_2} \tag{3.37}$$

The $\gamma_e^2 B_1^2 T_1 T_2$ term can usually be ignored as B_1 is small, in the absence of microwave power saturation. Magnetic field susceptibility is given by $\chi = M/H$. It is made up of two components, the real and the imaginary part, $\chi = \chi' + i\chi''$, where χ' is dispersion and χ'' is absorption. These are the Bloch susceptibilities and are defined by equations 3.38 and 3.39.

$$\chi' = +\kappa \mu_0 M_{x\phi} / B_1 \tag{3.38}$$

$$\chi'' = -\kappa \mu_0 M_{y\phi} / B_1 \tag{3.39}$$

Where κ is a dimensionless parameter describing the medium and μ_0 is the permeability of a vacuum. The absorbed power can be determined from the susceptibility as shown by equation 3.40.

$$P(\omega) = \frac{\chi'' \omega B_1^2}{\mu_0 V} \tag{3.40}$$

Where V is the volume of the sample. This means $P \propto \chi'' \propto M_{y\phi}$. As shown in equation 3.36, $M_{y\phi}$ has the form of a Lorentzian equation. An example Lorentzian is shown in equation 3.41.

$$L(x) \propto \frac{\Gamma}{(x - x_0)^2 + \Gamma^2} \tag{3.41}$$

Under the assumptions used in the Bloch equations EPR lines are Lorentzian in shape but line broadening may occur homogeneously or inhomogeneous depending

on the source.

Linewidth Broadening Mechanisms

A short T_2 can cause broadening of the EPR linewidth. At low temperatures when T_2 is long the lower limit of the linewidth is the result of distant unresolved hyperfine interactions. However, as T_2 becomes short the linewidth is broadened. In equation 3.40 the absorbed power for continuous wave EPR was presented. From this, an expression can be derived for the linewidth [112].

$$\Gamma = \frac{1}{|\gamma_e| T_2}\left(1 + \gamma_e^2 B_1^2 T_1 T_2\right)^{\frac{1}{2}} \tag{3.42}$$

If saturation effects are ignored the following assumption can be made.

$$if \quad \gamma_e^2 B_1^2 T_1 T_2 \ll 1 \quad then \quad \Gamma \propto \frac{1}{T_2} \tag{3.43}$$

The linewidth can therefore be broadened by a short T_2.

Other sources of homogeneous broadening may also be present and these may be affected by T_2 [112]. Homogeneous broadening occurs when the instantaneous local field is changing over time. Mechanisms which contribute to this effect include spin-spin interactions, which arise when magnetic fields caused by individual spins interact with each other, and electron-spin-nuclear interactions, which arise when magnetic field caused by nuclei interact with those caused by electrons.

Inhomogeneous broadening arises due to inhomogeneity of the magnetic field and anisotropic spin interactions [112]. These cause different spins packets to experience different local field and hence an EPR line may be made up of multiple slightly different lines from these spin packets.

3.3.2 Saturation

During microwave saturation, there is more microwave energy than can be absorbed by the EPR transition. According to Boltzmann statistics, at thermodynamic equilibrium and finite temperatures, there will be more electrons at the lower energy level than the higher one. Net absorption will occur as electrons from the lower level absorb microwave photons and move to the higher energy

level. However, this net absorption will only continue whilst there are more electrons in the lower energy. This requires relaxation. Over time electrons will relax back down to their equilibrium state, as was discussed in section 3.3. If microwave photons are coming in faster than the electrons can relax back down, they will no longer be absorbed. In this situation the microwave power absorbed is not proportional to the number of unpaired electrons present so the measurement will no longer be quantitative. This can be described by the saturation term $\gamma_e^2 B_1^2 T_1 T_2$ in equation 3.37.

According to the saturation term in the Bloch equations saturation is dependent on the two relaxation times T_1 and T_2. As these are dependent on the temperature so too are saturation effects.

3.4 Pulsed EPR

A pulsed EPR experiment allows relaxation times to be measured [118]. As with continuous wave EPR the spins align to an external magnetic field. However, instead of a continuously applied microwave energy, pulses are used. The magnetic field and microwave energy are chosen to be on resonance. This allows the microwave energy to rotate the magnetisation of the electron spins. Pulses used are in a much shorter time scale than the relaxation times of the sample. Measuring the spin packets as they relax back to their ground state configuration allows the relaxation times to be measured. Electron spin is a quantum mechanical property, but the magnetisation of a bulk sample of many spins can be treated as a classical property.

The magnetisation of the electrons in a magnetic field is aligned parallel to the field, in the z-direction. Whilst individual electrons precess around the field at the Larmor frequency, they do not precess in phase so there is no overall magnetisation in the x-y plane only parallel to the field [118].

Initially the electron spin orientations are determined by Boltzmann statistics, more electrons align with the field as this is the lowest energy configuration. Microwaves can supply energy to these electrons changing their spin state into one which does not align with the external field. Microwave energy can rotate the magnetisation away from the magnetic field direction by different amounts depending on the duration and power of the pulse. Electrons in higher energy states

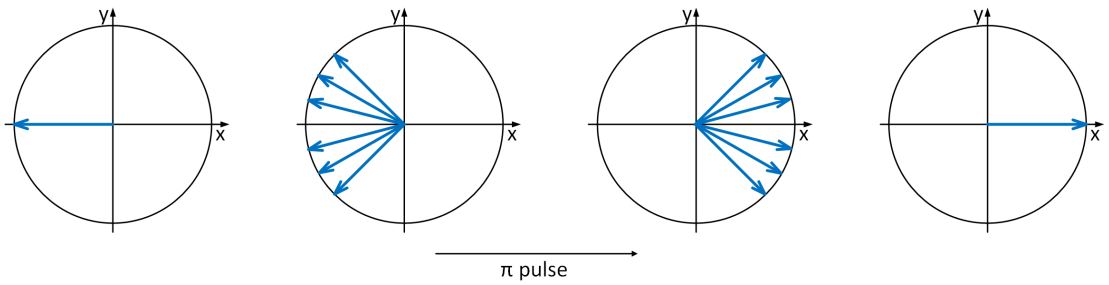

Figure 3.4: *Diagram of electron packet spin evolution in the x-y plane. The magnetic field is aligned to the z-direction. After the spin packets are rotated in the the x-y plane they begin to relax. After the π pulse they the spin packets flip. Their relaxation, which remains the same in terms of magnitude and direction, causes them to form a coherent echo in the positive x-direction.*

will return to their original configuration by dissipating their energy to their surroundings. The two main mechanisms for this are dissipating energy to other spins or to the surrounding lattice.

A signal is produced by the electron spins precessing in phase in the xy detection plane [118].

3.4.1 Measuring an Echo

Measuring an echo is performed by rotating the magnetisation into the detection plane (the x-y plane) using two microwave pulses called a read-out sequence [118, 122]. A microwave pulse, with tip angle $\pi/2$, is used which rotates the electron spins from the z-direction into the negative x-direction. Figure 3.4 shows the detection plane, with the first image showing the spin packets all pointing in the negative x-direction. Once rotated the spin packets will begin to relax away from their initial position, via spin-spin relaxation, i.e. loosing their energy to other spins. After time τ this is followed by a π pulse, as shown in the diagram, which rotates the spins to the positive x-direction. As the spin packets are still relaxing in the same direction with the same speeds, an echo signal will occur when the spins align in the positive x-direction. This alignment will take time τ. This sequence is called a Hahn Echo. These spins may also undergo spin-lattice relaxation during the pulse sequence. In this type of relaxation spins return to the z-direction by dissipating their energy to the lattice. This will reduce the echo. The size of the echo gives information about the degree and direction of the initial spin magnetisation and the relaxation which may have occurred.

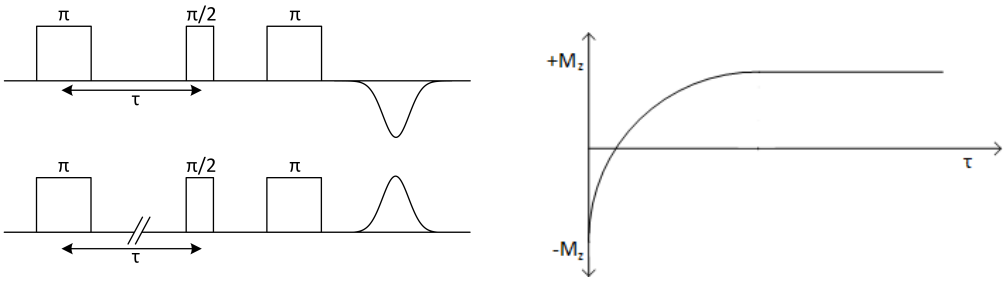

(a) *Pulse sequence for inversion recovery.*

(b) *Recovery after inversion.*

Figure 3.5: *Pulse sequence used to measure inversion recovery.*

3.4.2 Spin Lattice Relaxation Time

Over time, the magnetisation which has been rotated away from the magnetic field direction by a pulse will relax back to the magnetic field direction [118, 122]. This occurs because the system is no longer in thermal equilibrium. This happens by two relaxation processes; the spin lattice relaxation time and the transverse relaxation time. The spin lattice relaxation time (T_1) is determined by the time required to return to the z-direction. The electromagnetic energy which the microwaves supplied is lost over time to the lattice as the magnetisation returns to the z-direction.

Measuring T_1

The T_1 time can be measured by using an inversion recovery pulse sequence. This pulse sequence is shown in figure 3.5a. An inversion recovery pulse sequence involves inverting the spins with a π pulse and then performing the read-out sequence as discussed in section 3.4.1 consisting of a $\pi/2$ and π pulse to get a measurable echo in the detection plane. The time between the initial pulse and the read-out sequence, τ, is incrementally increased each time the experiment is repeated. This gives a measure of the inversion recovering, as can be seen in figure 3.5b.

The Bloch equation 3.31 can be solved to model this relaxation, giving equation 3.44.

$$M_z(t) = M_z(0)(1 - 2e^{-\tau/T_1}) \tag{3.44}$$

This equation can be used to fit the inversion recovery shown in figure 3.5b and T_1 can be calculated.

3.4.3 T_1 Relaxation Mechanisms

In this section the mechanisms by which T_1 relaxation occurs will be discussed. According to the Boltzmann statistics discussed previously (section 3.2.2) at finite temperatures there will be more electrons present at the lower energy level than the higher one. An incoming photon of microwave energy can induce an electron to move from the lower to the higher energy level or visa versa. Over time the two energy levels would become equally populated. However, this does not occur because relaxation causes re-population of the lower level. T_1 relaxation involves electrons spontaneously moving to the lower energy state by dissipating energy to the lattice [115, 123]. Solving the rate equation for the change in electron states gives equation 3.44, an exponential decay in magnetisation.

Despite the fact that photon-spin interactions are stronger than phonon-spin interactions at room temperature there are many more phonons present so the phonon relaxation mechanisms can compete with the photon excitation mechanisms, at low temperatures these phonons are less prevalent so the phonon-spin interaction reduces. This causes the relaxation mechanism to take longer [124].

The interaction between the lattice vibrations and the electrons can take different forms depending on the phonon energies and density. As T_1 relaxation is determined by the time taken for the electron spin energy to dissipate into the lattice, experimental data can help understanding these interactions. Which relaxation mechanism dominates is dependent on temperature as this determines the number and energy of the phonons present. By understanding these different mechanisms experimental changes in T_1 over temperature can be modelled to understand the actual behaviours. Equation 3.45 describes the changes in T_1 with temperature [115].

$$\frac{1}{T_1} = aT + bT^n + \frac{c}{exp(\Delta/kT) - 1} \tag{3.45}$$

In this equation the first term models the direct process, the second, the Raman process and the third, the Orbach process. T is the temperature. Δ is the energy gap between the spin state at the level into which the electron is excited by the phonon during the Orbach process. a, b and c are coefficients which can be varied

to fit experimental data.

Direct Process

The direct process is the process by which an electron loses or gains energy by emitting or absorbing a phonon. The phonon will have energy equivalent to the difference between the two energy states the electron has moved between. The direct process can only occur with phonons which have exactly this energy, hence it's likelihood depends on the number of phonons at the correct energy. The effect is linear with temperature because a higher temperature environment has more phonons.

The direct process tends to dominate at low temperatures and at higher fields [123]. In equation 3.45 it is the first term.

Raman Process

The Raman process is a phonon process which occurs below the Debye temperature [123]. In diamond the Debye temperature is 2200 K [125]. A phonon is absorbed and subsequently emitted. The electron is excited to a virtual level and then relaxes back down. The change in energy of the phonon before and after the interaction is transferred to or from the electron and allows it to change energy state. Any phonon which has enough energy can be absorbed and hence the process is strongly temperature dependent. In equation 3.45 the term which relates to the Raman process is bT^n. Where n depends on which type of spin state the electron is changing between.

Despite being a two phonon process, one phonon is absorbed and another of a different energy is emitted, the Raman process is much more likely to occur when compared to the direct process. This is because the direct process requires a phonon which has exactly the right energy, whereas the Raman process can absorb any phonon which has high enough energy.

Orbach

The Orbach process is independent of field [123]. It is a process which involves the electron absorbing a phonon with energy Δ. This causes the electron to be excited

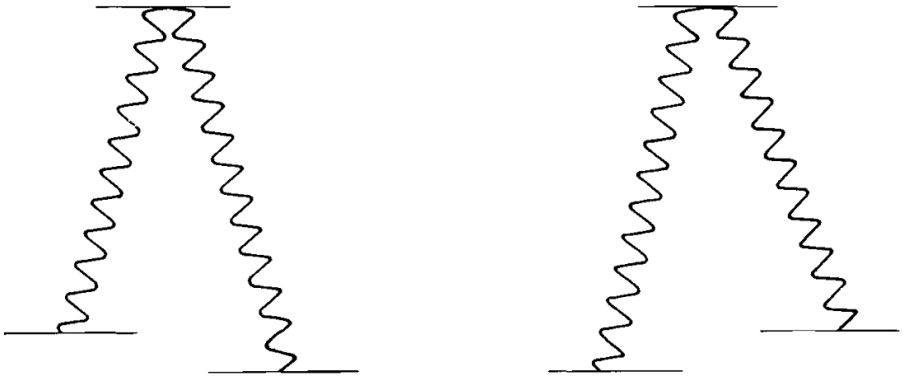

(a) *Electron moves to a lower energy level via the Orbach process.*

(b) *Electron moves to a higher energy level via the Orbach process.*

Figure 3.6: *The Orbach process showing a phonon, with energy Δ, promoting an electron to a higher energy level and subsequently a phonon being emitted as the electron relaxes back down to a different energy level. Figure from [115].*

up to a higher energy level. Another phonon, of a different energy, is emitted and the electron relaxes back down and thus has changed energy level. This process is shown in figure 3.6. This differs from the Raman process because the electron gets excited up to a real level.

The process depends on the number of phonons available which have energy Δ and hence is temperature dependent. In equation 3.45 it is the final term.

Two additional process may also be relevant to the relaxation; local mode and thermally activated.

Local Mode

It may be difficult to distinguish between local mode interactions and thermally activated interactions when studying T_1 behaviour [123]. The local mode mechanism involves a spin dissipating it's energy into the heat bath. It occurs when a specific vibrational local mode pairs to an unpaired electron. As diamond has a symmetric, charge balanced, lattice, this effect only occurs where a defect is present. A defect, for example a single substitutional nitrogen atom, can vibrate with a characteristic frequency and the unpaired electron at the nitrogen atom will move. This causes a change in the environments of the surrounding electrons as a charge is moving and hence creating a field. This causes a change to the other electrons' orbital angular momentum and hence via spin-orbit coupling dissipates

energy to the thermal bath [123]. In diamond, the energy of these defect vibrations (1244 cm^{-1}) is much higher than the energy of the microwaves (1 cm^{-1}). This means this energy dispersion mechanism does not usually occur.

Thermally Activated

Thermally activated relaxation is a process where spin energy is dissipated to the lattice. It is created when a molecule undergoes motion. This may be in the form of rotation or vibration, either of which could change the symmetry of the crystal. If this motion occurs on the time scale of T_1 it will affect EPR spectra measurements. Energy is transferred to the lattice via molecular motion, for example methyl group rotation [126].

3.4.4 Transverse Relaxation Times

The transverse relaxation time (T_2) is determined by the time it takes for the electrons spins to disperse in the x-y plane and hence the average magnetisation in this plane to reduce to zero [118, 122]. This occurs by electrons dispersing their energy to other spins.

Measuring T_2

T_2 can be measured using a pulsed experiment. A $\pi/2$ pulse is used to rotate the magnetisation into the x-y plane. The spins are left for a time, τ, to decay back to equilibrium and are then measured by a π pulse (see figure 3.7). This allows the decay of magnetisation in the x-y plane to be measured.

Equation 3.46 shows the Bloch equations solved for M_{xy}. By fitting this equation to the recovery shown in figure 3.7b T_2 can be calculated.

$$M_{xy}(t) = M_{xy}(0)e^{-\tau/T_2} \tag{3.46}$$

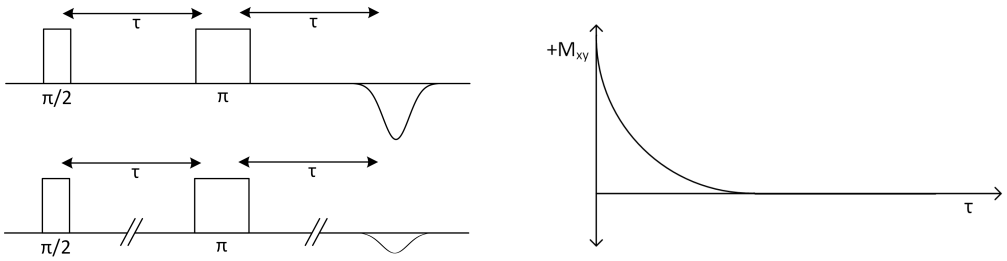

(a) *Pulse sequence for echo decay.*

(b) *Decay of echo.*

Figure 3.7: *Pulse sequence used to measure echo decay.*

3.4.5 T_2 Relaxation Mechanisms

T_2 relaxation occurs via spin-spin interactions [115, 123]. It is very difficult to directly measure a true T_2 as any mechanism which changes the phase of the electrons will reduce magnetisation in the x-y plane. Hence T_m, the phase memory time, is usually what is measured and this will be shorter than the true T_2.

T_m arises from any mechanism which changes the frequency of a spin packet, and hence stops that spin packet from aligning with the rest to form the echo [122]. Local non-resonant electron spins and nuclei will change the local field and cause spectral diffusion. A shift in frequency may be caused by librational motion of a defect centre or nuclear spin flip-flops.

3.5 Optical Absorption

Optical spectroscopy uses the absorption or emission of photons for defect characterisation [127]. Absorption is characterised by the change in intensity of a particular energy of light before and after the sample. Transmission through the sample causes a decrease in intensity: $I_0 \rightarrow I$. If the sample thickness is given by dx the change in intensity is given by equation 3.47.

$$dI(x) = -I(x) \cdot \alpha \cdot dx \tag{3.47}$$

This equation can be integrated to give $\ln(I) = -\alpha x + C$. The integration constant can be calculated using the boundary condition that at $x = 0$, $I = I_0$. This gives $C = \ln(I_0)$. The equation now reads $\ln(I) = -\alpha x + \ln(I_0)$. This can be rearranged

to give equation 3.48. In this equation T is defined as transmission.

$$\text{transmission(T)} = \frac{I}{I_0} = e^{-\alpha x} \tag{3.48}$$

Absorbance can then be calculated from the transmission, as shown in equation 3.49.

$$\text{absorbance(A)} = \log_{10} \frac{I_0}{I} = -\log_{10} T \tag{3.49}$$

Equation 3.49 is known as the Beer-Lambert law [128]. Both of the previous equations do not take into account reflected light. For diamond this may be a significant factor due to the high refractive index. Equation 3.50 shows a calculation for T which includes the reflected light, R. However this still ignores multiple reflections.

$$T = (1 - R)^2 \quad e^{-\alpha x} \tag{3.50}$$

A plot which shows absorbance over a range of wavelengths of light helps characterisation as absorption is related defects and other intrinsic processes of the sample.

3.5.1 Absorbance of Diamond

Diamond is a material with very high transmission for most wavelengths except in the two phonon region (see figure 3.8) between 2.6 and 6.2 μm. Transmission occurs up to the band gap energy which is at 5.47 eV (0.23 μm) [127].

3.5.2 Fourier Transformed Infrared

IR absorption is defined as absorption of light at wavelengths longer than 700 nm. Photons are absorbed by the material, depending on their wavelength, and create phonon vibrations within the material. It it is a method of investigating the bond vibrations within a crystal. These are at lower energies than the electronic transitions discussed in section 3.5.3. In a perfect diamond crystal the characteristic bond vibration energy is 1332 cm^{-1}. Energy less than this is not absorbed because it does not create an electronic dipole due the symmetry of the crystal and because it is made up of purely carbon atoms. One carbon atom moving creates a

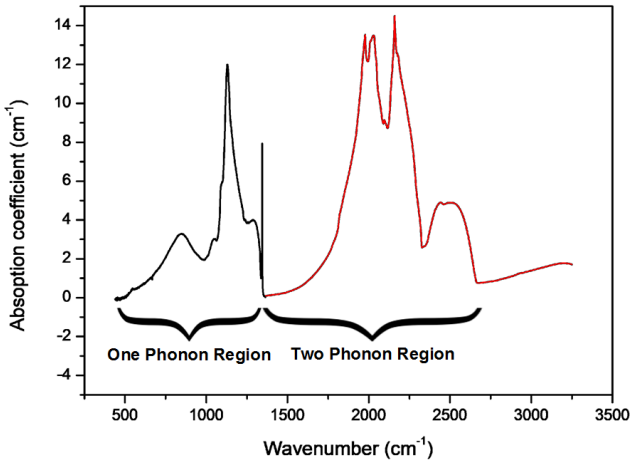

Figure 3.8: *Example infrared absorption spectrum of a reference sample with a concentration of 220 ppm of single substitutional nitrogen.*

net charge but does not create a dipole as it's movement is equal and opposite to that of it's neighbours. However if this net charge is vibrated by a second phonon, then this will cause absorption because a dipole is created. This is why an intrinsic diamond lattice only absorbs in the multiphonon region.

Vibrations with in the crystal can either be intrinsic or extrinsic. Intrinsic vibrations are characteristic phonons of the material as discussed above. Whereas extrinsic vibrations are vibrations of defects within the lattice. Defects reduce the symmetry of the lattice and hence create net charges. They can absorb a phonon in the one phonon region as these create dipoles.

IR spectroscopy is used to study the one, two and three phonon region of the diamond spectra. It is particularly useful for looking at different forms of nitrogen and single substitutional boron.

3.5.3 Ultraviolet/Visible

The UV/vis region is defined as absorption of light less than 700 nm in wavelength though it is possible to study slightly higher wavelengths [127]. UV/vis spectra are used to look at the vibronic absorption of defects within diamond samples.

The band gap of diamond, at 225 nm, is in the UV/vis region. The diamond band gap is indirect so an electron absorbing a photon also requires a phonon to move

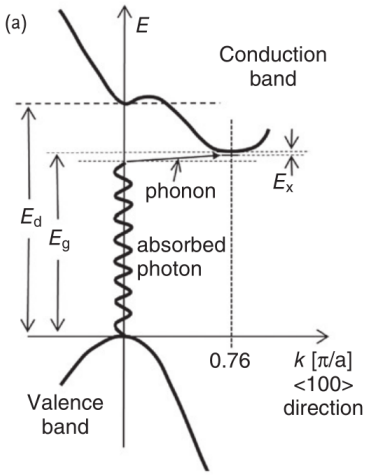

Figure 3.9: *The indirect band gap of diamond. Image from [127].*

in momentum as well as potential energy to get to the bottom of the excited state. This is shown in figure 3.9. If a phonon is not present the absorption occurs at a higher energy than the band gap, as it has to get to a higher energy than the bottom of the excited level, than would occur if it were a direct band gap material.

Vibronic absorption occurs when an electron, within a defect, absorbs a photon of light and changes from the ground state to the excited state. This mechanism is shown in figure 3.10 and is discussed in more detail in section 3.7.

3.6 Luminescence

Experiments which cause a sample to interact with light and luminesce fall into two main categories, depending on the mechanism present. Light may either be scattered, elastically or inelastically, or it may be absorbed. If the light is scattered elastically this is called Rayleigh scattering. Raman scattering is inelastic scattering. The photon loses energy to the lattice in the form of a lattice vibration. Raman scattering gives information about the lattice. The photoluminescence effect is stimulated emission after absorption of a photon. The absorption and emission during photoluminescence (PL) is caused by impurities, and hence can be used to give information about the type and relative concentrations [127]. These will be discussed below.

3.6.1 Raman Microscopy

The Raman line is created when the incoming photons are inelastically scattered, having undergone the Stokes effect. The photon loses energy to the lattice in the form of a phonon. A phonon is an intrinsic vibration characteristic to the material, in diamond it has an energy of 1332 cm^{-1} so a line is seen in the spectrum which is equivalent to the laser energy minus the phonon energy [127].

Raman linewidths are determined by the sample purity. Optical phonon travel through the material is affected by static scattering points which disrupt the periodicity. Impurity atoms, such as nitrogen, increase the linewidth [129]. This will be discussed further in Chapter 6.

3.6.2 Photoluminescence

Photoluminescence (PL) is the absorption and subsequent emission of photons. The energy of the incoming photons causes defects in the material to luminesce. Photons are supplied by the laser at a chosen wavelength. The material absorbs these photons by promoting electrons to higher energy levels, after a short time the electrons relax back and emit another photon. The emitted photon may have a characteristic energy of the defect from which it was absorbed and subsequently emitted. Depending on the temperature of the measurement a zero-phonon line emission may be seen when an electron relaxes from the bottom of the excited state to the bottom of the ground state. At higher temperatures it is also likely that a vibronic side band will be seen. This is created when electrons relax back down from the excited state to the middle of the ground state rather than the bottom. so is at lower energy. This is shown in figure 3.10. Electrons may sit in the middle of the excited state if there are many lattice phonons around, which occurs more at higher temperatures. This is discussed further in section 3.7.

3.7 Vibronic Absorption and Emission

The mechanism by which defects absorb and emit are shown in figure 3.10. This shows an example electronic structure with the vibronic levels. At low temperatures there are few phonons around so electrons are most likely to be present at the bottom of the ground state band. Absorption and emission can occur with a

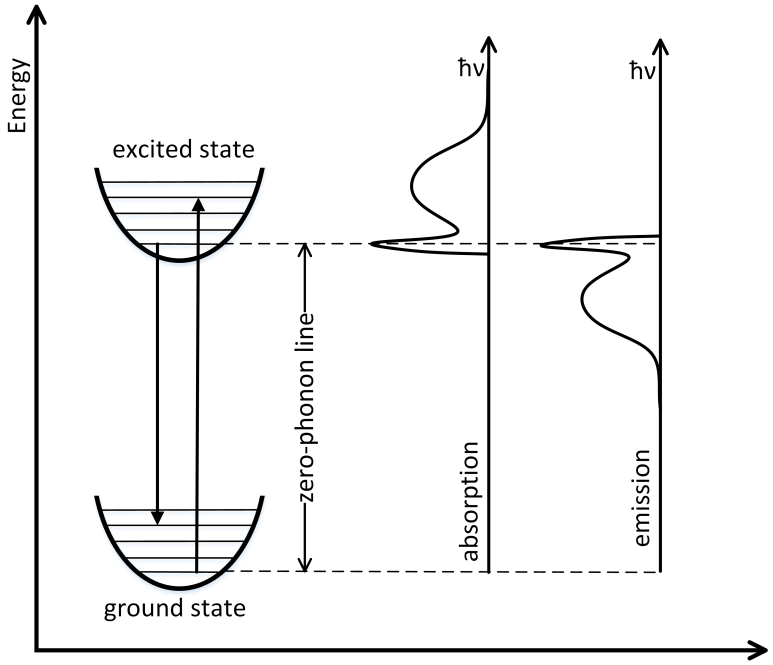

Figure 3.10: *Vibronic structure of a defect. Zero-phonon line in emission and absorption showing creation of phonon side band [130].*

photon which has the equivalent energy to the zero-phonon line (ZPL). Absorption can also occur at energies above this energy as this will excite the electron into a higher vibronic band of the excited state. Hence the vibronic side band for absorption is at a higher energy.

Emission occurs at the ZPL and at lower energies as the electron can relax into higher vibronic levels of the ground state. These electrons will relax back down to the bottom of the energy level emitting a phonon at a later point. The relative sizes of the ZPL and the vibronic side band is determined by a number of factors including the temperature; the ZPL becomes sharper as the sample becomes colder [33].

3.8 Cathodoluminescence

Cathodoluminescence (CL) was employed to image the growth structure of the diamonds [131]. During CL an electron gun is used to bombard the surface of the sample with high energy electrons. This causes stimulated emission of photons, analogously to PL. In PL laser energies of up to 4 eV are used, however, during CL the excitation energy used is of the order of keV. This amount of energy allows electrons to be excited up from the valence band to the conduction band (the

band gap of diamonds is 5.47 eV). The electron hole pair can recombine which can create recombination emission. Alternatively the electrons relax back down to the valance band via the defect levels within the band gap. Photons are emitted as the electron loses energy during each one of these transitions. This is discussed further in Chapter 6. In figure 6.4 the green colour relates to a nitrogen defect (neutral di-nitrogen vacancy), cathodoluminescence can be used as a qualitative measure to study the changes in defect incorporation of the sample.

3.9 Secondary Ion Mass Spectroscopy

SIMS was employed to find out carbon isotope and impurity concentrations. It is a destructive technique which sputters away the sample surface and analyses the resulting ions using a mass spectrometer [132, 133, 134]. The sputtering is done by a focused ion beam and which ions are used depends on the material being sputtered. For diamond caesium ions are used to investigate the ^{13}C ions and negative oxygen ions are used for nitrogen. Caesium is used for smaller ions as it has a better yield and sputters more effectively because it is heavier. The caesium ions are created by heating a caesium containing compound until it becomes gas and then letting the vapour hit a heated tungsten plate until thermally ionised. The negative oxygen ions used are in the form of a plasma (a plasma is a state of matter like a liquid or a gas but it is made up of ions which means it can be manipulated by a magnetic field). The plasma is created by flowing a gas between an anode and cathode. The cathode emits electrons which cause the gas to ionise and from a plasma. An extraction electrode forms the plasma into a beam and a mass filter is used to remove unwanted ions. The main advantage of the negative oxygen ions is they prevent a charge build up on the surface.

Once the ions have been formed into a beam they are directed towards the surface to be investigated. This is done in high vacuum. A very small amount of material is etched so the analysis is very local. The surface is usually etched in 1 to 2 nm depth round pits. The secondary ions ejected from these pits are then collected and steered towards a mass analyser. This sputtering process is poorly understood so normally a standard sample is used for comparison as it is very challenging to model the process. Usually a ratio between two different species is examined as this leads to more accurate measurements.

The secondary ions are removed from the surface using an immersion lens or an

extraction lens (for this work a immersion lens was used). The sample is held at a high positive or negative voltage, depending on the ions so they accelerate away from the surface and towards the mass analyser. In the case of nitrogen the ion being measured is N^{3-} so the sample surface is negatively charged. For insulators, such as diamond, the surface is first coated with a thin layer gold so the surface charge is even. A transfer lens is used to transfer the ions to the mass spectrometer.

A contrast aperture is used before the spectrometer. The aperture size is chosen depending upon what information is required. A small aperture will result in better spatial resolution and a larger aperture will result in a larger ion intensity.

The ions are then accelerated around a corner in a magnetic field. This magnetic field is measured by either a Hall probe or by measuring the relaxation of spin flipped hydrogen atoms by NMR. Which technique is used depends on which ions are being measured. The curvature of each ion depends on the mass to charge radio. A moveable slit at the end allows the investigated ion to be selected.

Once the correct ions have been selected their concentration can be measured by secondary ion detectors. These are also in a very high vacuum. Many different types of detector are used but the main types are a Faraday cup or an electron multiplier. A Faraday cup is made up of a hollow conducting electrode. The colliding ions create electrons which go to ground and create a potential drop which is measured to measure the count rate. An electron multiplier consists of multiple dynodes which produce 1, 2 or 3 electrons when an ion hits them. These electrons are accelerated possibly to another dynode where more electrons are produced. A metal anode collects and measures these electrons.

In Chapter 6 this technique was used to study the carbon isotope ratios.

Chapter 4

Experimental Techniques

4.1 Introduction

This chapter presents the experimental techniques used in this thesis. First continuous wave electron paramagnetic resonance (EPR) is discussed, followed by pulsed EPR. The methods used for illumination of samples during these experiments is detailed. Next the optical techniques are given; including infrared and ultraviolet/visible absorption, photoluminescence (PL) and cathodoluminescence (CL). Finally the experimental method for secondary ion mass spectroscopy (SIMS) is presented.

4.2 Electron Paramagnetic Resonance

4.2.1 Continuous Wave Electron Paramagnetic Resonance

Experimental Details

Continuous wave EPR experiments were performed using a Bruker EPR Spectrometer. The magnet used was an ER 073 with an ER 083 power supply. The microwave bridge used was an ER 041x at X-Band with a lowest microwave power of 60 dB (200 nW) or an ER 041gx with a lowest microwave power of 90 dB (200 pW). The resonator used was a Bruker TE_{011} cylindrical cavity. The sample was held on a rexolite rod or two axis goniometer.

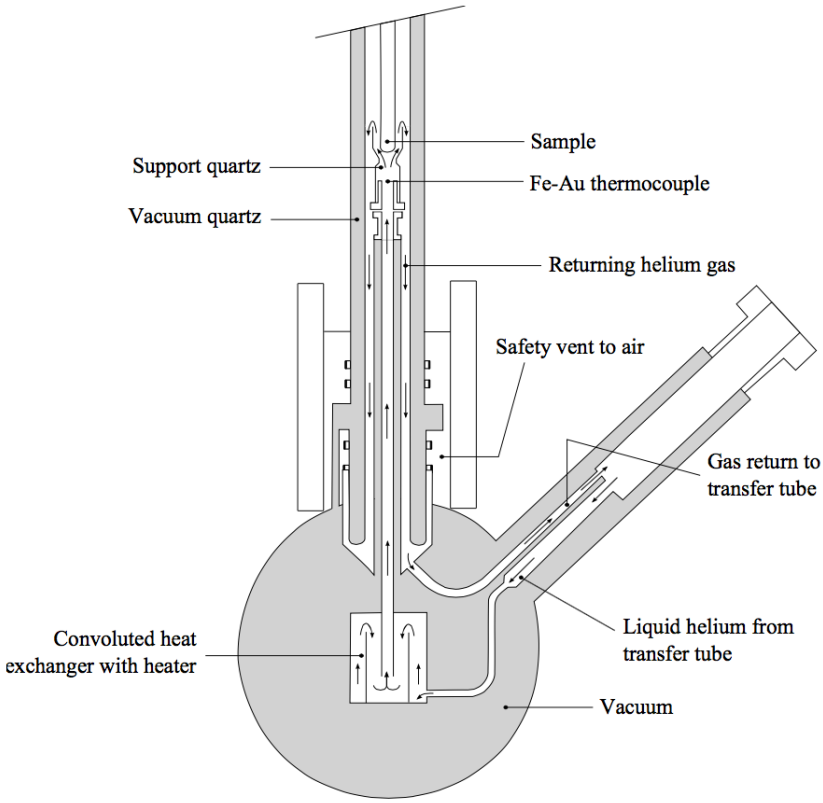

Figure 4.1: *Schematic of ESR 900. Image from [81].*

The EPR spectra obtained were fitted with the 'EPRsimulator' program for Matlab, detailed in Dale's thesis [135].

Cooling

Measurements were carried out at a variety of different temperatures ranging from 8 K to 300 K using an Oxford Instruments ESR900 continuous flow cryostat. Figure 4.1 shows a schematic. Both liquid helium and liquid nitrogen were used. The cryostat continuously flowed gaseous helium/nitrogen over the sample. The temperature was controlled by an Oxford Instruments ITC5035 which was connected to the temperature sensor and the heater in the gas flow of the ESR900.

The basic requirements of EPR are to place the sample in a homogeneous magnetic field, apply microwave energy and measure how much of the energy is absorbed. The components required for these experiments are discussed below.

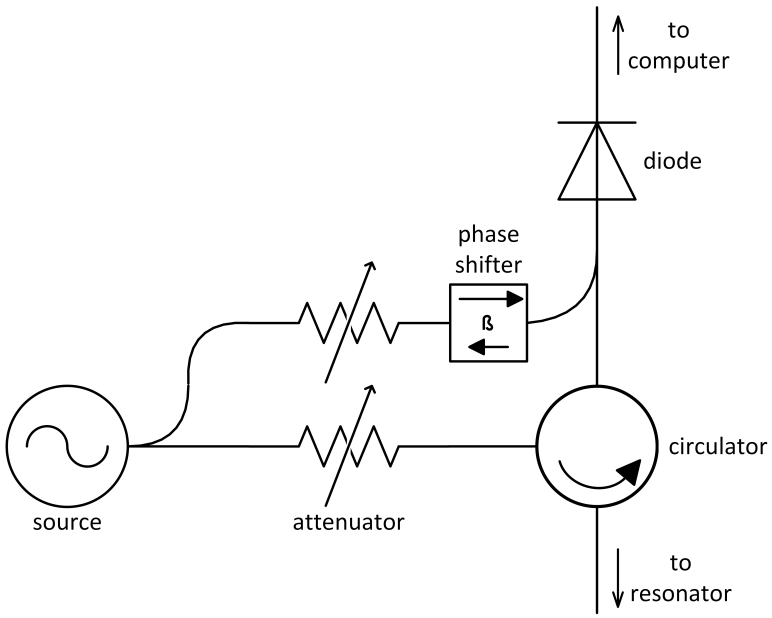

Figure 4.2: *Diagram of the key components of the microwave bridge. Figure adapted from [136].*

The Microwave Bridge

The microwave bridge controls the microwave source and subsequent microwave detection, a schematic of which is shown in figure 4.2. A higher microwave frequency source will result in a larger difference in field position between signals from different g-factors and, in the absence of microwave power saturation, better sensitivity when differentiating closely spaced signals. However this will also require a smaller cavity resonator to contain the radiation and hence a smaller sample [112]. When a higher frequency source is used a higher magnetic field is also required, which makes maintaining the uniformity of the field increasingly challenging. A **microwave source** frequency is chosen as a balance of these two factors. The region chosen is called X-band and is characterised by a frequency of 9.75 GHz and a resonant field of 3480 Gauss, for $g \approx 2$ absorption [136].

The microwave source used in this work was a Gunn diode and for the pulsed work this was used in conjunction with a travelling wave tube (TWT) to amplify the power. A resonator is designed to hold a particular frequency of radiation and as such fixes the frequency used. For this reason a fixed microwave frequency is chosen while the field is swept [136].

An **attenuator** is used to attenuate the output power of the source. A high power may be useful for some samples but many samples exhibit significant mi-

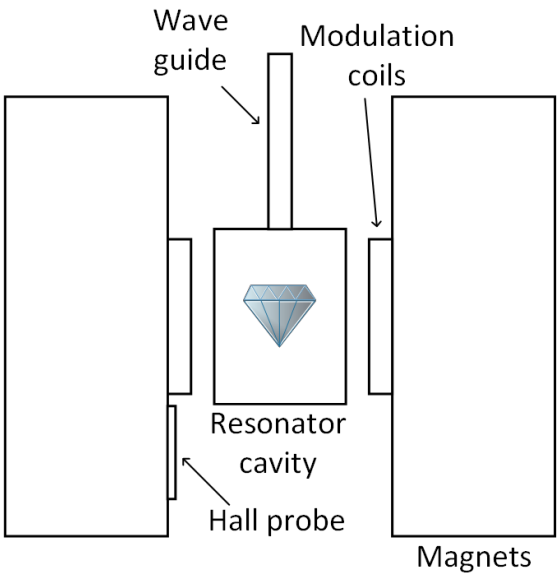

Figure 4.3: *Diagram of EPR magnets.*

crowave power saturation and hence a lower power is required for quantitative measurements [112].

A **circulator** is then required to supply the cavity with microwaves and then send any reflected microwaves to the detector. When critically coupled all the microwave energy will be contained within the cavity and none will be reflected. However once the sample absorbs some microwave energy the resonance conditions will no longer be met and some microwaves will be reflected. The circulator allows both the microwaves from the source to reach the resonator and only reflected microwaves from the resonator to reach the detector [112].

When microwaves are reflected they reach the **detector diode**. The diode converts the microwave energy into a current. In the linear region of the detector diode the current is proportional to the square root of the microwave energy. This should occur in the region of 200 μA. A **reference arm** supplies extra microwave energy from the source to the diode via an attenuator and a phase shifter (to match the phase after a different path length) to keep the diode in the linear region.

The Resonator

The resonator is central to the EPR spectrometer and is shown in figure 4.3. A resonator is a cavity or dielectric resonator used to store microwave energy.

When on resonance there are standing waves created by constructive interference within the resonator, which allow the energy to be stored [112]. A resonator is chosen such that the resonant mode has the maximum magnetic field and minimum electric field in the centre of the resonator where the sample sits. An example of a cylindrical cavity resonator in transverse electric (TE_{011}) mode is shown in figure 4.4. The electric and magnetic fields can be modelled by Maxwell's equations, as depicted in the diagram.

Two key factors when evaluating the sensitivity of a resonator are the quality factor (Q) and the filling factor (η). η ranges between one and zero. The signal is directly proportional to the product of both of these factors so both must be maximised. However, they have competing requirements; Q is largest when the sample is small compared to resonator size (if the sample is lossy) and the filling factor is largest when the sample and the resonator are comparable in size. The Q of a resonator is expressed by equation 4.1.

$$Q = \frac{2\pi(\text{energy stored per cycle})}{\text{energy disipated per cycle}} \tag{4.1}$$

This indicates that for high Q the ohmic losses must be minimised. Ohmic losses occur when the sample non-resonantly absorbs energy via the electric field, hence the sample must be placed at the electric field minimum. Additionally, rexolite sample holders (either a rod or a goniometer depending on sample orientation requirements) are used to hold the sample in place, as they are non-conducting and do not have an EPR signal. The inside of the cylindrical cavity resonator used is coated in silver and gold to aid conduction of the electric current in the cavity walls and avoid energy losses [136].

Equation 4.2 gives the η of a cavity. In practice this is very difficult to calculate as B_1 needs to be known in detail so when comparing a sample to a reference it is best to use samples of similar size at the same position in the resonator.

$$\eta = \frac{\int^{sample} B_1^2 dV}{\int^{cavity} B_1^2 dV} \tag{4.2}$$

In equation 4.2 B_1 is the magnetic field created by the microwaves. The numerator is an integration of the magnetic field over the sample volume and the denominator is an integration of the magnetic field over the cavity volume. For cylindrical cavities the Q is high but the η is low as the sample is small compared to the resonator. For dielectric resonators (such as the one used for pulsed experiments)

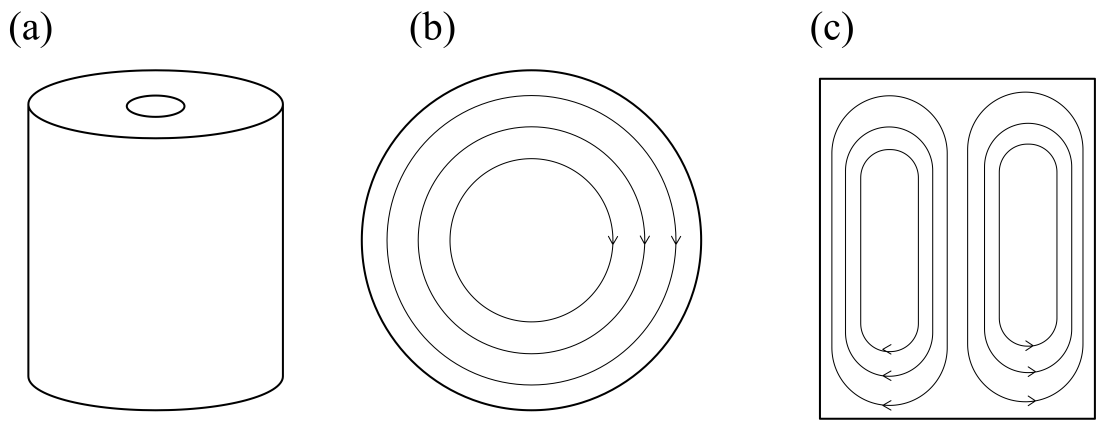

Figure 4.4: *Cylindrical cavity operating in the TE_{011} mode. (a) Cavity. (b) Electric-field contours. (c) Magnetic field contours. Figure adapted from [112].*

Q is low and η is high. This is an advantage as it reduces the ringing time of the resonator. Ringing time will be discussed further in section 4.2.3.

A **waveguide** is used to transport the microwaves from the bridge to the resonator. The size is selected depending on the frequency of the microwaves. A variable **iris** is used to impedance match the waveguide to the resonator [112]. The change in impedance matching changes the amount of microwave energy transmitted and reflected. This allows the resonator and the waveguide to be critically coupled; no microwave energy is reflected back.

Electromagnets are used to create a homogeneous magnetic field [136]. The field is not linearly dependent on the current supplied and exhibits hysteresis. A **Hall probe** is placed in the magnet to feedback the actual field measured into the magnetic field controller and allow for adjustments to be made. The Hall probe is kept at a constant temperature, slightly above room temperature, to ensure changes in voltage measured are not temperature related [112].

4.2.2 Modulation

Phase sensitive detection is employed to increase the signal-to-noise ratio. This is done using the **Helmholtz coils** which are placed inside the magnet as shown in figure 4.3. The magnetic field (B_0) is modulated sinusoidally and microwave reflection is detected at the same modulation frequency. The only signals detected are at the modulation frequency using a lock-in detector. This allows the prevalent low frequency noise to be excluded [136]. A modulation frequency of 100 kHz is normally used. The amplitude and frequency must be chosen carefully to avoid

distorting the line shape.

A modulation amplitude must be chosen to be smaller than 0.2 times the peak-to-peak distance of the EPR lines, if a true line shape is required [112]. If true line shape is not required a larger modulation amplitude can be used to increase sensitivity. This can still be used to give a quantitative measure as the line is integrated to get the signal, and modulation broadening does not change this area. However, narrowly split lines may appear as one. The modulation frequency must also be chosen so as not to increase with the linewidth. Modulation side bands can occur if the modulation frequency is similar to the linewidth in Gauss. 100 kHz is 0.15 Gauss (for $g = 2$ electrons) and thus is usually hidden by the line. The EPR spectrum in figure 3.3a shows a derivative line shape of a slow passage experiment. During a slow passage experiment equilibrium is maintained and the stable solutions to the Bloch equations apply. The derivative line shape is due to the modulation.

Quantitative Electron Paramagnetic Resonance

The integrated intensity of an EPR signal of a particular magnetic dipole transition is proportional to the number of unpaired electron spins undergoing the transition [112, 137]. This can be used to calculate the concentration of the defect at which the spins exist by comparison to a sample of known concentration [138]. The factors which need to be compared are shown in equation 4.3. The equation only applies when there is no microwave saturation as it assumes there are Boltzmann populations.

$$[x] = [ref]\frac{I_x}{I_{ref}}\sqrt{\frac{(P_{\mu w})_{ref}}{(P_{\mu w})_x}}\frac{M_{ref}}{M_x}\frac{(B_m)_{ref}}{(B_m)_x}\frac{g_{ref}^2}{g_X^2}\frac{S(S+1)_{ref}}{S(S+1)_x}\frac{(t_{aq})_{ref}}{(t_{aq})_x}\frac{G_{ref}}{G_x}\frac{N_{ref}}{N_x} \quad (4.3)$$

In this work the experimental parameters of the sample to be measured and the reference were kept the same as far as possible. This included maintaining the same microwave power (P), modulation amplitude (B_m), conversion time (t_{aq}), gain (G) and number of scans (N). The sample position within the resonator was also kept the same as far as possible so they both experience the same magnetic and electric field. In equation 4.3 I_x (I_{ref}) is the EPR signal intensity of the unknown sample (reference sample), M_x (M_{ref}) is the unknown sample (reference sample) mass, g_x (g_{ref}) is the unknown sample (reference sample) g-factor and S_x (S_{ref}) is the species (reference sample) spin. These factors were taken into

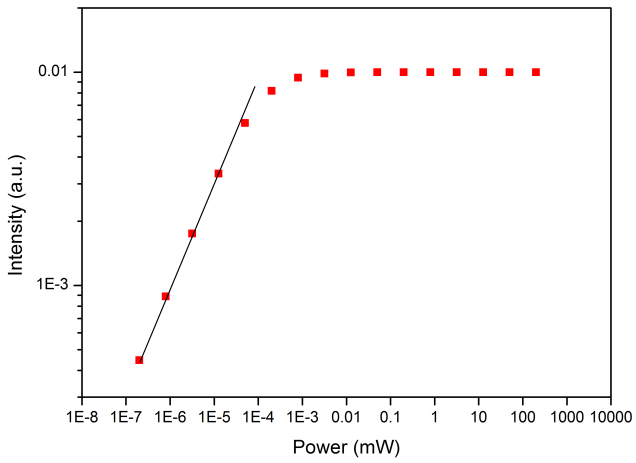

Figure 4.5: *Increasing microwave power causing homogeneous microwave power saturation.*

account when concentrations were measured. The reference sample used for all quantitative EPR measurements was a type Ib single-sector HPHT synthesised sample containing 270±30 ppm of N_s^0. The concentration of N_s^0 was measured by S. Liggins by FTIR [63].

Another important issue when taking quantitative measurements was to avoid microwave saturation. Microwave saturation occurs when the energy in the resonator is larger than that which the sample can absorb by magnetic dipole transitions, per unit time without perturbing the Boltzmann population distribution. This leads to a non-Boltzmann population distribution as the spin-lattice relaxation rate is not fast enough to return the populations to a Boltzmann distribution. This causes the integrated intensity of the EPR signals to no longer be proportional to the unpaired electron concentration within the sample. Figure 4.5 shows intensity proportional to the square root of power at low powers, as was presented in equation 4.3. At high powers intensity is not proportional to the square root of power, and hence the equation no longer applies. The theory of this process is discussed in more depth in section 3.3.2. Many of the samples discussed in this thesis were studied at low temperature. At lower temperatures relaxation rates become slower and hence saturation is more likely. For this reason very low microwave powers were required. A 90 dB microwave bridge was used for the low temperature measurements.

4.2.3 Pulsed Electron Paramagnetic Resonance

Experimental Details

Pulsed EPR was performed with a Bruker Elexsys E580 spectrometer with a Bruker Super XFT-EPR bridge which went down to 60 dB or 200 nW. The dielectric resonator used was an ER 4118 X-MD5 X-band dielectric ring resonator. The inner diameter was 5 mm, and hence was of a similar size to the samples used, so had a high η.

Sample Cooling

Cooling was performed with an Oxford Instruments continuous flow liquid helium cryostat controlled by an Oxford Instruments ITC5035.

The Pulsed Electron Magnetic Resonance Spectrometer

A pulsed EPR spectrometer is similar to a continuous wave spectrometer but has a few key differences: a travelling wave tube (TWT) is added to amplify the microwave power to create high power pulses; and a pulse programmer is also required to manage the pulses, the TWT and the detection. The pulses are normally are 16 to 34 ns long and during this time the detection circuitry must be protected. The resonator will hold the microwave energy, leading to 'ringing', the circuitry must also be protected from this. The microwave pulses are of much higher power than the signals to be detected and hence the circuitry is very sensitive. Defence pulses are used to protect the detector and this is also controlled by the pulse programmer. This means there is a deadtime after each pulse before a signal can be detected [122].

Unlike in a continuous wave experiment a high quality factor (Q) is not advantageous to a pulsed experiment. A high Q will result in a longer ringing time. This increases the deadtime and hence makes Free Induction Decay (FID) and echoes (discussed in section 3.4) more difficult to measure as they may be hidden by ringing. A low Q is created by over-coupling the resonator. The Q was only 150 when over-coupled, compared to 5000 for the cylindrical cavity resonators used for continuous wave EPR. Less energy is stored in the resonator when there is a

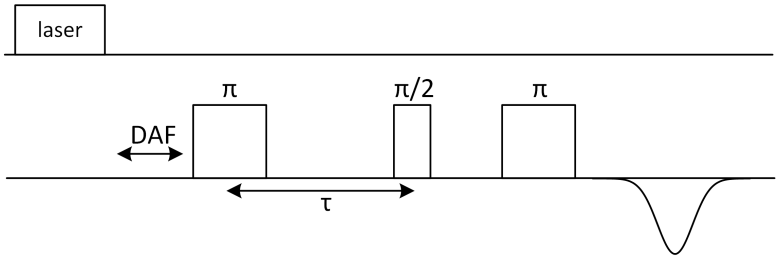

Figure 4.6: *Pulse sequence including laser pulse.*

lower Q [118]. To increase the signal the resonator often has a very high η as the resonator and sample are of similar sizes.

Quadrature detection is used during pulsed experiments in order to measure both the amplitude and phase of an echo. This means information is detected in two directions in the detection plane. Small inaccuracies in the relative phase and gain of these two detectors can create quadrature artefacts. To remove these, phase cycling is used. The same pulse sequence is applied positively and negatively to each channel, removing the zero frequency artefacts. The pulse sequence is also sent through the two different channels, allowing errors in the individual channels to be removed [122]. Phase cycling also has the advantage of removing unwanted FID and echo signals.

Pulse Sequence

In section 3.4 the pulse sequences used for this work were presented. In this section the experimental requirements for these sequences will be discussed. The main pulse sequence employed was 'inversion recovery', as shown in figure 3.5. This pulse sequence was used to measure the spin lattice relaxation time (T_1). A spectrum is shown in figure 5.15 which can be seen to be similar to the theoretic exponential return to equilibrium shown in figure 3.5b. The data was fitted in OriginPro using equation 3.44 to give a value for T_1.

In order to get sufficient signal from SiV^0 and NV^- optical spin polarisation was used to enhance the electron population of the $m_s = 0$ spin state. This increased the echo measured by enhancing the population difference between the $m_s = 0$ and the $m_s = \pm 1$ levels and hence enhancing the absorption and emission respectively. A pulse sequence which includes this illumination is shown in figure 4.6. U1 is the laser trigger which switches the laser on and off and DAF is the delay after flash which will be discussed in section 4.2.4. The laser pulse length used was 1.5 ms.

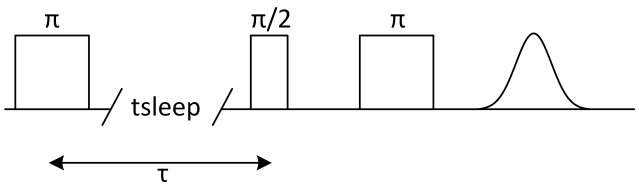

Figure 4.7: *Pulse sequence including tsleep.*

At low temperatures, $< 30K$, the relaxation time T_1 becomes very long, > 10 seconds. This meant the relaxation parameter, τ, had to be very long too (in the order of seconds). The spectrometer had a limit of one second on the total length of the TWT pulse train, which made measurements at these temperatures impossible. For this reason *tsleep* was used. This allowed the pulse programmer to switch off for a short time ($\sim 10\ ms$), as shown in figure 4.7. Including *tsleep* allowed a much longer time to elapse before the detection pulse sequence occurred, and hence the recovery of the echo could be measured. The slowest relaxation time measured was 25 seconds. The τ between the inversion pulse and the detection sequence was stepped out by 6 seconds ($600 \times$ *tsleep*) after each pulse.

4.2.4 Optical Illumination

In this section the experimental techniques used for optical illumination will be presented. Optical illumination was used during continuous wave EPR to measure the effect on electron spin polarisation. Pulses of illumination were applied before pulse sequences to enhance the signal to noise ratio.

Continuous Illumination

Illumination for the continuous wave EPR was supplied by an optical fibre 1 mm in diameter, which was polished to a mirror finish on both ends. The diamond was glued onto the end of the optical fibre, with the minimum amount of glue between the end of the fibre and the diamond to minimise absorption. The other end of the optical fibre was inside a laser safe box. A laser diode was focused, using a lens, on the end of the fibre. The laser used was mounted in a TCLDM9 Thorlabs Laser Diode Mount. The laser diodes used are listed in table 4.1. All of the lasers in the table are laser diodes with the exception of 1064 nm which is a Diode Pumped Solid State laser, a LCM-S-112 made by Laser 2000.

Wavelength (nm)	Power (mW)	Manufacturer
1064	210	Laser 2000
980	1000	Roithner LaserTechnik
915	1000	Roithner LaserTechnik
830	1000	Thorlabs
785	1000	Roithner LaserTechnik
532	1000	Roithner LaserTechnik
450	1600	Roithner LaserTechnik

Table 4.1: *Details of the lasers used.*

The power was measured at the sample by measuring the power at a break in the optical fibre which, again, had been polished flat. Before doing the experiment the relationship between the power at the break and the power at the diamond was measured. When the power at the break was 300 mW the power at the sample was 82 mW. The break was polished and connerctorised to make it easier to match the two ends of the fibre back together after the power measurement had been taken.

Acousto-Optic Modulation

During pulsed experiments an Acousto-Optic Modulator (AOM) was used to control the switching of the laser. This allowed the pulse programmer of the spectrometer to send the U1 trigger to the AOM and thus control when the laser was on. The AOM used was an Isomet AOM model 1250C with a wavelength range from 442 nm to 1.5 μm. An AOM uses the interaction between light and sound in a crystalline material. A crystal is selected which changes refractive index as an acoustic wave travels through it. The acoustic wave is created by a radio frequency going though a piezoelectric material [139]. This creates compression and rarefaction (the opposite of compression) in the crystal causing periodic changes in the refractive index. The velocity of these periods is determined by the choice of material. The AOM in question used lead molybdate. If the laser light enters the piezoelectric crystal at the Bragg angle it interacts with the periodic changes in refractive index and this causes diffraction of the beam into multiple modes, as shown in figure 4.8. The zeroth mode is the laser light going straight though and the first mode will switch on and off as the radio frequency is switched on and off. The first mode was focused on the end of the fibre. Careful alignment of the laser

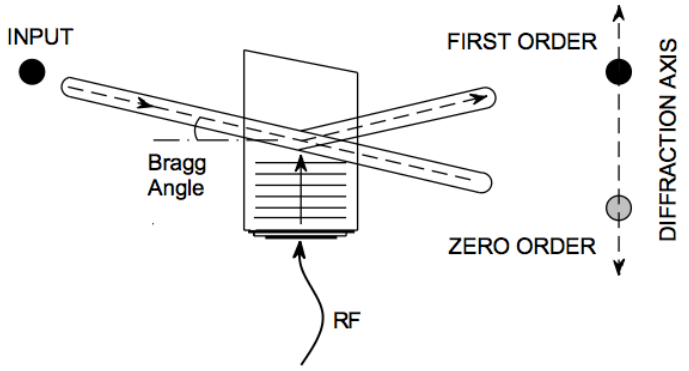

Figure 4.8: *Diagram of incoming beam at Bragg angle and zeroth and first order diffraction. Image from [139].*

at exactly the Bragg angle and selection of the radio frequency power ensures the maximum diffraction into the first mode.

The diffraction efficiency of an AOM is determined by equation 4.4 and the total efficiency is determined by equation 4.5. The maximum total efficiency reached using the 532 nm laser diode was 28%.

$$\text{diffraction efficiency} = \frac{I_{1st}}{I_{0th}} \tag{4.4}$$

$$\text{total efficiency} = \frac{I_{1st}}{I_{LASER}} \tag{4.5}$$

At first a 915 nm laser was used but the efficiencies obtained were extremely low. The 532 nm laser was then chosen, as aligning an AOM gives significantly higher efficiency with a visible laser as it can be seen whilst aligning. The efficiency of the 532 nm laser was reduced by multiple issues, however, which arise from using a laser diode instead of a laser.

The main issue with using laser diodes is the beam shape. An AOM has a beam waist at a certain location in the crystal through which the beam must travel in order to be diffracted. The incoming beam also has to be at the Bragg angle. However, when using a diode the beam diameter is often too wide to fit into the AOM and it has to be focused using a lens. This focusing means the light is not uniformly parallel and that some of the light entering the AOM is not at the Bragg angle and is therefore not diffracted. From this arises a compromise between how much light enters the AOM and the proximity of the light to the Bragg angle. In figure 4.9 the effect of this can be seen. Only the central portion of the light is

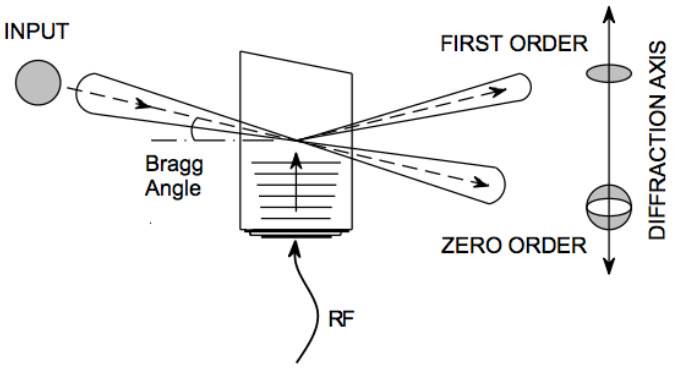

Figure 4.9: *Focusing into AOM and resulting Bragg angle errors. Image from [139].*

diffracted into the first order.

Another issue with using an AOM is the switching time. Figure 4.10a shows the trigger from the spectrometer (blue) and the response from the AOM (yellow). On closer inspection of the response time, a delay is evident, see figure 4.10b. The time from the U1 trigger start until the AOM was fully on was ∼882 ns. This delay is caused by the switching time of the AOM and is determined by how fast the radio waves take to reach the point where the laser light is going through the crystal. The switching time may also be reduced by the non-ideal beam shape. Due to this delay a 900 ns was added to the 'delay after flash' in any programs including AOM switching, as seen in figure 4.6.

4.3 Optical Absorption and Emission

4.3.1 Infrared Spectrometer

FTIR spectroscopy is used to study the one, two and three phonon region of the diamond spectra. Intrinsic diamond does not absorb in the one phonon region (below 1332 cm^{-1}) but defects do. It is particularly useful for looking at different forms of nitrogen and single substitutional boron.

IR spectra were obtained with a PerkinElmer FTIR System Spectra GX spectrometer and were taken at room temperature. The spectrometer consists of an interferometer, a schematic of which is shown in figure 4.11. An interferometer is

(a) *Oscilloscope image of U1 spectrometer output triggering AOM. The U1 pulse, shown in blue, is 1.5 ms long.*

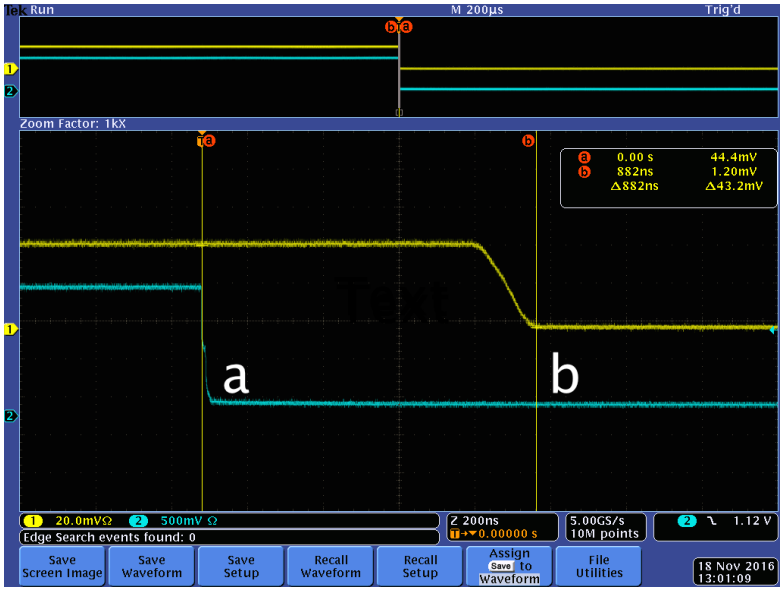

(b) *Oscilloscope image of end of trigger to laser fully on. 'a' indicates the U1 pulse switching on and 'b' indicates the laser being on. The time between the start of the U1 pulse and laser fully on is ∼882 ns.*

Figure 4.10: *Oscilloscope measurement of AOM switching efficiency. Blue is the trigger from the pulse spectrometer which triggers the AOM and yellow is the laser response.*

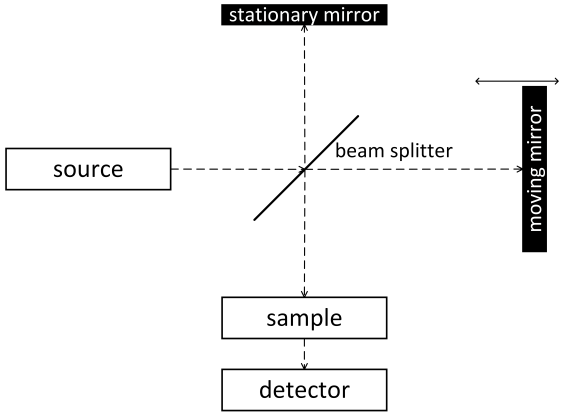

Figure 4.11: *Schematic of an interferometer. Moving mirror scans with a frequency of ∼10 kHz.*

composed of a broadband light source. This light is split into two beams using a beam splitter; a half-silvered mirror which is coated in aluminium and allows half the light to be transmitted and half to be reflected. These two beams of light are then reflected by a stationary mirror and a moving mirror respectively. The two beams are then recombined. The result is then shone onto the detector. This gives an interferogram which can be Fourier transformed to produce the source spectrum. The same is done with a sample in place. The two Fourier transformed spectra can be compared and the absorption of the sample will be given by the difference.

The two sources used were a tungsten halogen lamp in conjunction with a quartz beam splitter for the near-IR range and a temperature stabilised wire coil at 1350 K in conjunction with a potassium bromide (KBr) beam splitter for the mid-IR region.

The IR spectra obtained were fitted with the 'SpectrumManipulator' program for Matlab, detailed in Dale's thesis [135]. This program compares the absorption spectrum with spectra of samples with known concentration in order to calculate concentrations of the species within.

4.3.2 UV/visible Spectrometer

The UV/visible absorption spectrometer used was a PerkinElmer Lambda 1050 UV/vis/NIR spectrometer which has a range of 175 nm to 3300 nm. When taking measurements below room temperature this was used in conjunction with an Oxford Instruments optical cryostat and an Oxford Instruments ITC5035 temper-

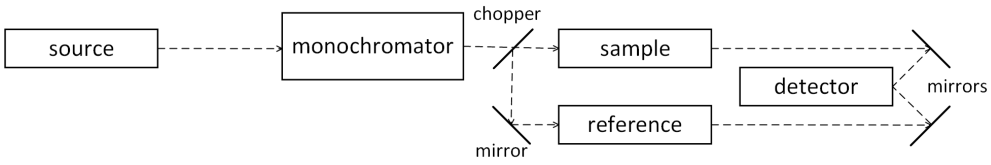

Figure 4.12: *Schematic of light path within UV/visible spectrometer.*

ature controller. The two sources used were a deuterium halogen lamp for the UV region and a tungsten halogen lamp for the visible and NIR region.

Unlike the FTIR spectrometer discussed previously, a UV/visible spectrometer measures the absorption of each wavelength in turn. A schematic of the spectrometer is shown in figure 4.12. It consists of a broadband light source which is spread into a rainbow using a diffraction grating. A single wavelength can then be selected by using slits. The size of the slits used and the number of lines on the grating determine the resolution of the scan. Once the wavelength is selected, the beam of light is split in two by a chopper. One of the resulting beams goes through the sample and the other passes though the reference. The spectrum is created by measuring the absorption by the sample at each wavelength and comparing this to the reference beam.

The absorption was measured. The intensity of light is measured differently depending on the range. A photomultiplier tube (PMT) is used in the range from 170 to 800 nm. An indium gallium arsenide (InGaAs) detector is used in the range from 800 to 1500 nm. A zinc selenide (ZnSe) detector is used in the range from 1500 to 3500 nm.

4.3.3 Raman/Photoluminescence Spectrometer

Both Raman and photoluminescence (PL) measurements were performed with a Renishaw inVia Raman Microscope. Cooling to liquid nitrogen temperatures was performed with a Linkam THMS600 optical cryostat. A selection of different excitation wavelengths were used as detailed in table 4.2.

A Raman/photoluminescence spectrometer works by shining a laser on to a sample and interpreting the scattered light. A schematic of this is shown in figure 4.13. The laser is focused down to a sharp point using a lens and a pinhole. It is then reflected up to a dichroic mirror which reflects the laser but not the light at different frequencies. The dichroic reflects the laser light onto a second mirror

Wavelength (nm)	Laser Type
325/442	Helium-cadmium
532	Solid state diode
633	Helium-neon
785	Solid state diode

Table 4.2: *Lasers used with Raman/photoluminescence spectrometer.*

where it then is focused by an objective lens onto the sample. The inelastically and elastically scattered light is then collected by the objective and is reflected to the dichroic. At this point much of the light intensity is lost because it is not scattered towards the lens. The dichroic only transmits light which is not at the wavelength of the laser, and the laser light that was inelastically scattered can pass through. An edge filter is also used at this point to remove any remaining laser light. The luminescence spectra of the material is separated out into its different wavelength components using a diffraction grating. A lens allows one wavelength to be measured at a time by a charge-coupled device (CCD). The wavelength versus the photon count can be plotted. In the case of a Raman experiment this can give information about the strain and isotopic content of the sample and in the case of a PL experiment this can give information about the defects present.

The Raman line is a signal produced by Stokes scattering. It is equivalent to the laser wavelength minus the characteristic phonon of energy of the material being studied. It can be used to normalise spectra. The signal is produced by the inelastically scattered light, however, this forms a minority of the light collected from the sample, approximately one photon in 100000. The photoluminescence (PL) signal also consists of significantly less light that the reflected laser light. It is imperative to remove as much of the laser light as possible in order to detect the smaller Raman or PL signal.

4.3.4 Fluorescence and Phosphorescence Imaging

Fluorescence and phosphorescence imaging was performed by a DiamondView^{TM}. The instrument images the fluorescence and phosphorescence of diamond samples after ultraviolet illumination by a xenon flashlamp [140].

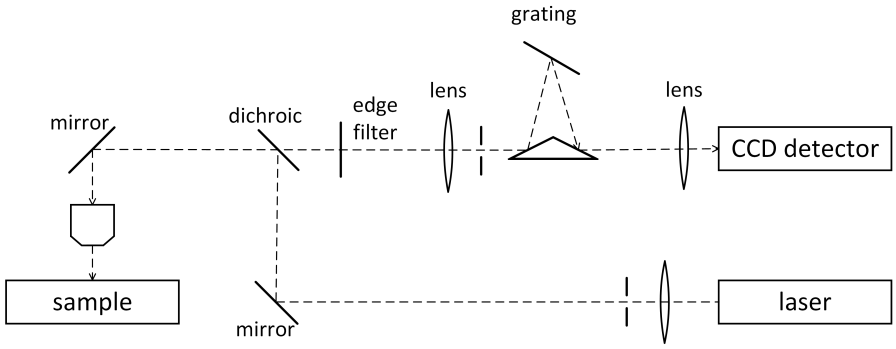

Figure 4.13: *Schematic of light path within Raman spectrometer.*

4.4 Cathodoluminescence

A cathodoluminescence experiment involves studying visible light emitted from a sample which has been bombarded with electrons. For more details about the theory of this refer to section 3.8.

The sample surface is bombarded with electrons using a high voltage cathode gun (at 4 to 30 keV) and the resulting emitted photons are studied with an visible light microscope. The sample is kept in a vacuum.

A cathodoluminescence microscope was used to qualitatively study the samples discussed in Chapter 6. The CL images were taken with a cold cathode, CITL 8200 Mk 3A mounted on a Nikon Optiphot petrological microscope at the Grant Institute at the University of Edinburgh.

4.5 Sample Preparation

Samples required preparation for both EPR and optical measurements. EPR required samples which were small enough to fit in the resonator and, for optical illumination, required one side to be polished flat to allow the light to enter. For some EPR measurements the crystallographic direction of the sample was also important so that the field could be aligned along certain directions. Optical absorption measurements required two parallel polished faces.

4.5.1 Laser Cutting and Polishing

Laser cutting and polishing of sample set NL636 was done at De Beers, Maidenhead by Hugh Leach. For this sample set, 1.6 mm slices were taken and polished to be parallel on both sides. Laser cutting and polishing of other samples was done at Warwick using an Oxford Lasers class 4 diode-pumped solid-state Nd:YAG laser operating at 355 nm.

4.5.2 Acid Cleaning

Acid cleaning was done before measurements to ensure the diamond surface was clean of glue, grease and other impurities. The acid used was sulphuric acid supersaturated with potassium nitrate. A second clean was done with just sulphuric acid to ensure no potassium nitrate salt was left on the surface. Both of these cleans were done at 250°C for 30 minutes. Once the diamond was cooled it was rinsed with water and dried.

4.6 Electron Irradiation

Electron irradiation was performed at the Takasaki Advanced Radiation Research Institute in Japan. The facility in Takasaki was equipped with a 2 MeV electron accelerator. It consists of a high-voltage generation device and an electron-acceleration device. A high voltage is generated by a Cockcroft-Walton circuit. This was in a sulphur hexafluoride gas which ensures the voltage does not discharge. Electrons are produced by a heated filament and are accelerated downwards towards the sample on a water cooled table. The samples were wrapped in aluminium foil and taped to the surface to ensure they did not move during the irradiation.

For the two silicon vacancy containing samples discussed in Chapter 8, the current used was 12 mA and the irradiation took 6 hours. The electron gun head was 10 cm by 60 cm. According to work by Hunt 1.51 vacancies are created per incident electron when using a voltage of 2 MeV [141]. This assumes that electrons are produced uniformly throughout the sample, however, damage is more likely to be created in the volume closest to the electron gun. This resulted in a theoretical vacancy concentration of 11.5 ppm.

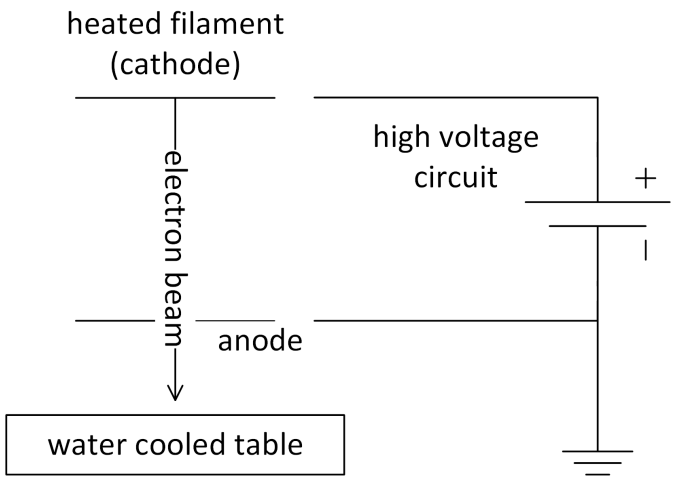

Figure 4.14: *Schematic of electron irradiation. A grid and magnetic lenses are also used to focus the electron beam.*

4.7 Annealing

Annealing was used to create silicon vacancies in silicon containing diamonds after they had been electron irradiated. Before the procedure the samples were acid cleaned as detailed in section 4.5.2. This was done using a horizontal tube furnace made by Elite Thermal Systems LTD, which was held at atmospheric pressure. There was a heating element and the temperature was measured using a thermocouple. Once the furnace was at temperature the diamond was placed in the centre of the quartz tube and nitrogen gas flowed over the sample to avoid oxidation of the diamond surface. This was especially important for the higher temperature treatments, which were done at 800°C.

4.8 SIMS

SIMS was used to make quantitative measurements of the concentration of ^{13}C and nitrogen impurities. The SIMS system used was the NERC ion microprobe facility at the Grant Institute at the University of Edinburgh. The spectrometer was a Cameca IMS-1270. The samples were first plated in gold to ensure that the surface did not become electrically charged during the measurement. The thickness was $< 0.2\ \mu m$. Before taking each measurement the gold coating was etched to reveal the diamond surface below. Each etched hole was 20 μm in diameter.

The ^{13}C isotope changes were measured by comparison to the count rate for ^{12}C.

The count rate of nitrogen would normally be compared to ^{13}C; however in the samples studied in this work both ^{13}C and nitrogen were changing. For the work presented here the nitrogen SIMS signal was measured by count rate alone.

Chapter 5

The Neutral Silicon Vacancy Defect

5.1 Introduction and Objectives

In this chapter the electron spin properties of the neutral silicon vacancy (SiV^0) are presented having been investigated using the tools of optical spectroscopy and electron paramagnetic resonance. As discussed in section 2.4.2, the neutral silicon vacancy may have a promising future in quantum devices and as such is worth further investigation. The most well researched defect in diamond remains the negative nitrogen vacancy (NV^-) but increasingly researchers are looking for alternatives. The Debye-Waller factor is low in NV^-, at ~ 0.04 [142], caused by low emission probability in the zero-phonon line (ZPL) and higher emission probability in the phonon side band (the Debye-Waller factor is defined as the ratio of the ZPL to the phonon side band). SiV^- has also been investigated as its Debye-Waller factor is higher, ~ 0.8 [84]. However SiV^- has one main disadvantage; short spin-lattice relaxation times. This arises due to the large spin-orbit coupling which allows phonon assisted spin-state decoherence. At 5 K the spin-lattice relaxation time (T_1) remains short at 40 ns [106].

As will be discussed in more detail in Chapter 8 silicon vacancy containing diamonds can be produced by various different methods including grown in by Chemical Vapour Deposition (CVD) or High Pressure High Temperature (HPHT) synthesis or produced by post processing methods including electron irradiation, ion implantation and annealing.

The SiV^0 defect has previously been investigated with EPR. The defect symmetry is D_{3d} and this has been confirmed by theoretical work by Goss et al. [89]. The defect ground state is an $S = 1$ $^3A_{2g}$ state [70] which has been confirmed by Gali et al. [88]. The defects ground state can be optically spin polarised at low temperatures [81]. SiV^0 has a ZPL at 946 nm (1.31 eV) and a Debye-Waller factor of ~ 0.9 [143, 142]. It undergoes charge transfer, becoming negative under optical illumination in the UV range and returning to neutral after heating [81]. This is thought to be an interaction with neutral and positively charged single substitutional nitrogen, as shown in equation 5.1. SiV^0 gives rise to photo-conduction below ∼830 nm [144].

$$N_s^0 + SiV^0 \underset{heat}{\overset{hf}{\rightleftharpoons}} N_s^+ + SiV^- \tag{5.1}$$

The aim of studying SiV^0 was to discover if it has more useful properties than current alternatives. Other groups have also turned their attention to this defect and individual silicon vacancy centres have been studied [143] and it has been found to be selectively orientated under certain CVD synthesis conditions [77].

In this work the properties of the SiV^0 centre were investigated by measuring the efficiency of electron spin polarisation with different energies of illumination. Two different samples were studied to discover if the spin polarisation effects seen were sample dependent and to understand possible interactions of SiV^0 with other defects. The spin-spin and spin-lattice relaxation times were also measured at different temperatures.

5.1.1 Electron Spin Polarisation

Electron spin polarisation, a phenomenon seen in both NV^- and SiV^0, occurs when the population of the different m_s levels in the ground state are no longer in thermal equilibrium; as given by Boltzmann statistics. In EPR the effect exhibits itself by changing the absorption and emission of the EPR resonances. There exist parallels between the proposed energy levels of the two centres, as can be seen in figure 5.1. It was initially expected that the electron spin polarisation mechanism would also be similar.

The mechanism for the spin polarisation of the ground state NV^- centre involves optical illumination exciting electrons from the ground state ($^3A_2$) to the excited

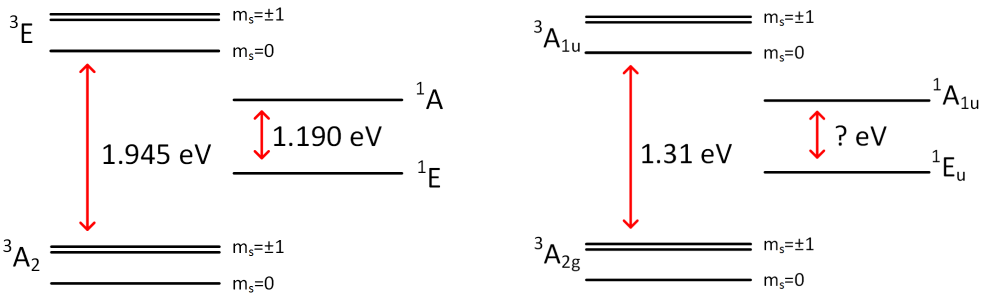

(a) *Energy levels of the NV^-.* ***(b)*** *Energy levels of the SiV^0.*

Figure 5.1: *Energy levels of NV^- and SiV^0. As proposed by [46] and [145], respectively.*

state (^3E) [46]. The relaxation behaviour of the electron at this point will depend on the spin state. If the electron is $m_s = 0$ it has a high probability of relaxing back down to the ground state emitting a photon. However if an electron is $m_s = \pm 1$ there is a significant likelihood (probability is ∼40% [46]) that it will undergo intersystem crossing and will relax to the ground state via the two intermediate, singlet states (^1A and ^1E). These states preferentially relax into the $m_s = 0$ ground state. This was discussed further in relation to magnetometry in section 2.5.2. After the illumination has been exciting electrons for a few cycles the majority of electron population will have relaxed into the $m_s = 0$ state leading to a much higher population in the $m_s = 0$ state state than Boltzmann statistics predict. This can be detected by EPR, as absorption from the $m_s = 0$ state to the $m_s = +1$ is enhanced while emission from the $m_s = 0$ state to the $m_s = -1$ state is enhanced. Electron spin polarisation is one of the properties which makes the nitrogen vacancy centre so useful. The spin state can be optically initialised and the resulting spin state can be read-out via photoluminescence [46].

In the first part of this chapter the electron spin polarisation for the SiV^0 centre is measured using different illumination energies and at different temperatures to investigate the possible electron spin polarisation mechanisms.

5.2 Sample Details

Three samples were studied, sample 5, sample 7 and sample 8. Sample 5 is a CVD diamond grown on a {1 0 0}-orientated HPHT diamond. It was co-doped with boron and silicon (see figure 8.1a). One silicon layer was grown between two boron layers. The sample was then electron irradiated and annealed to create

silicon vacancies as discussed in Chapter 8 with a final concentration of 4.0±0.4 ppb of SiV^0.

Sample 7 is a CVD diamond grown on a {1 1 3}-orientated HPHT diamond substrate. It was irradiated with 1.5 MeV of electrons and then annealed at 900°C for four hours. This resulted in 75±8 ppb of SiV^0. Sample 8 is a CVD diamond grown on a {1 1 0}-orientated HPHT diamond substrate which was also irradiated and annealed at 2400°C. The final SiV^0 concentration was 40±4 ppb.

	SiV^0 Concentration (ppb)	N_s^0 Concentration (ppb)
Sample 5	4±0.4	undetectable
Sample 7	75±8	-
Sample 8	40±4	62±6
Sample 9	20±2	250±25

Table 5.1: *Concentrations of SiV^0 and N_s^0 in sample 5, 7, 8 and 9. The N_s^0 concentration of sample 7 was not measured.*

5.3 Experimental Techniques

Photoluminescence (PL) was used to characterise the defects in the different samples. More details about the system used can be found in section 4.3.3.

Electron paramagnetic resonance (EPR) was used to measure the electron spin polarisation of the ground state of the neutral silicon vacancy. Continuous wave EPR experiments were undertaken to measure the degree of electron spin polarisation under optical excitation with different wavelengths of lights. In addition to experiments performed with lasers diodes at distinct energies a tuneable laser (model CTL 950) was borrowed from TOPTICA Photonics. This laser could be swept over the wavelengths from 915 to 985 nm.

Pulsed EPR experiments were used to find the relaxation times at different temperatures. For the pulsed EPR experiments the spectrometer controlled the laser switching and supplied a short pulse of light to the sample before the pulsed EPR measurement was taken in order to increase the signal by electron spin polarisation. The pulse sequence is shown in figure 5.2. This allowed the echo signal-to-noise ratio to be significantly increased without causing optical pumping during the

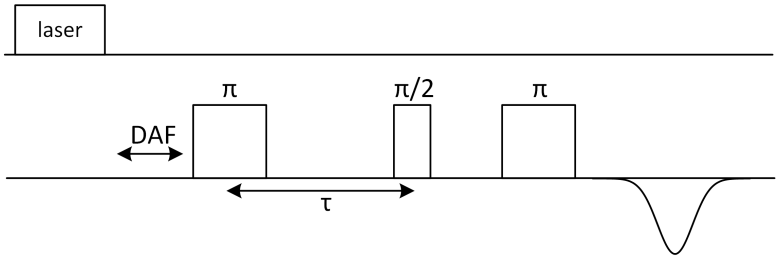

Figure 5.2: *Pulse sequence including laser pulse.*

measurement. Measurements of both the spin-lattice and the spin-spin relaxation times were performed using this technique. The details of both spectrometers are in section 4.2 along with information about how the different wavelengths of light were supplied.

5.3.1 Measuring Electron Polarisation

The SiV^0 has D_{3d} symmetry [146], $S = 1$ and a positive zero-field splitting (D) of 942 MHz at 300 K [80, 70]. This results in ground state splitting into $m_s = -1, 0, +1$ states. An ensemble of randomly orientated SiV^0 centres results in an EPR spectra with four pairs of lines, each arising from an ensemble of centres at one of the four equivalent $\langle 111 \rangle$ orientations. The field position of the lines depends on the angle between the symmetry axis $\langle 111 \rangle$ and the magnetic field direction. When the field direction is along one of the $\langle 111 \rangle$ type directions one pair of lines is created by the centres parallel to the field. The three other pairs of lines now appear on top of each other as they make the same angle to the field direction, 109°. In the absence of preferential orientation and microwave power saturation this gives EPR signals with ratios 1:3:3:1 for a dark spectrum. In the light, electron spin polarisation will cause an increase in absorption and emission from the defects which are parallel to the magnetic field. An example of such a spectra is shown in figure 5.3.

As can be seen from figure 5.3 the two outermost lines are much larger than the others; one in emission and one in absorption. This sample was illuminated during this scan and this has the effect of enhancing the population of the $m_s = 0$ level. The difference between an illuminated and an unilluminated scan can be seen in figure 5.4. The inset in this figure shows a higher population in the $m_s = 0$ level when the centre is polarised which causes absorption and emission into the $m_s = +1$ level and $m_s = -1$ level respectively, and hence an increase in these

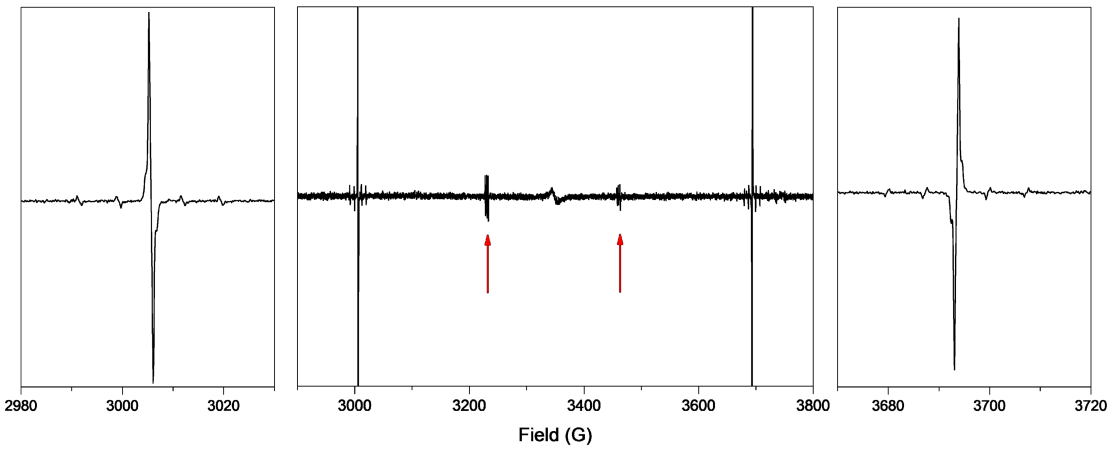

Figure 5.3: *Spectra of an ensemble of polarised silicon vacancy centres. Data taken at 100 K with illumination from a 532 nm laser diode. The field direction is parallel to* ⟨111⟩*. The red arrows mark the two pairs of three equivalent sites which are 109° to the field direction. The two outermost lines arise from the one site whose symmetry axis is parallel to the field, shown in more detail in the graphs at either side.*

lines. It is also clear from these spectra that spin polarisation efficiency is highly dependent on orientation within the magnetic field as it is only the outermost lines (those with symmetry axis parallel to the magnetic field) which show a large change under electron spin polarisation.

For the results presented in this chapter the degree of electron spin polarisation had to be quantified in order to discover which wavelengths of light were most efficient at generating spin polarisation.

Calculating the Electron Spin Polarisation

The electron spin polarisation was measured by comparing the pair of EPR lines which belong to the same orientation; the one with its symmetry axis parallel to the magnetic field direction. The lines were fitted and their intensity was calculated. This was compared to the EPR line's intensity without illumination in order to quantify the degree of enhancement. At most temperatures below room temperature the unilluminated cw EPR lines were microwave power saturated. This meant with the spectrometers available it was not possible to use a low enough microwave power that the transitions could relax at a sufficient rate to keep the spin populations at equilibrium values. This was especially true at liquid

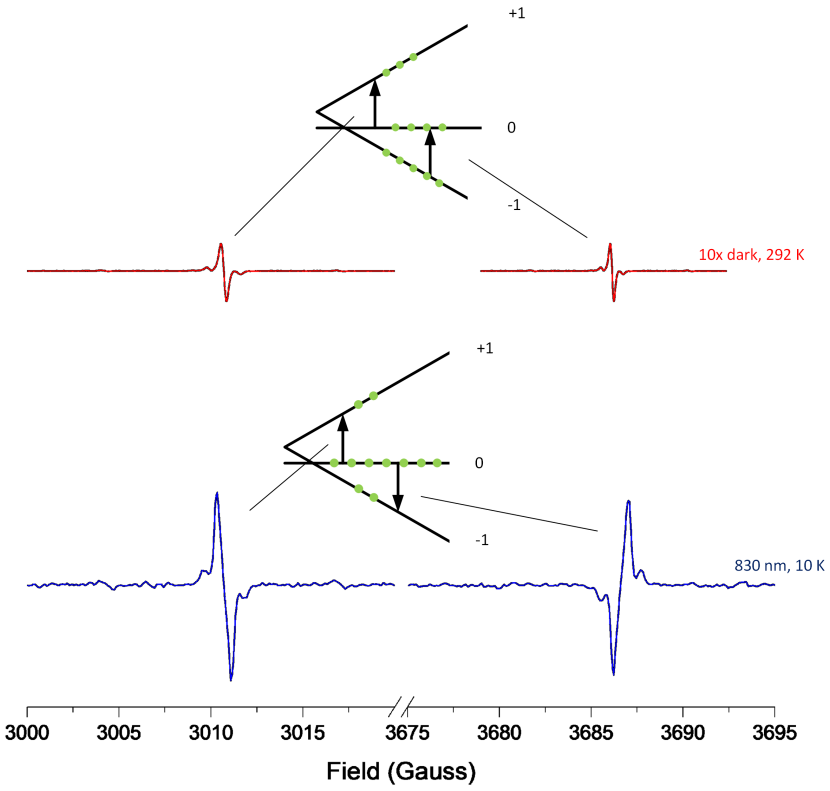

Figure 5.4: *EPR signal without illumination at 292 K (red) and with illumination at 10 K (blue). The inset shows spin levels of the SiV^0 ground state in both the unpolarised (where the $m_s = 0 \rightarrow +1$ transition creates the low field line and the $m_s = -1 \rightarrow 0$ transition creates the high field line) and polarised state (where the $m_s = 0 \rightarrow +1$ transition creates the low field line and the $m_s = -1 \leftarrow 0$ transition creates the high field line). Not a true representation of line width due to over modulation. Image after [145].*

helium temperatures as the spin lattice relaxation time (T_1) becomes very long.

In order to work out the ground state electron spin polarisation it was necessary to work out the unsaturated value for the intensity of the EPR lines at low temperature in the dark. This was done by measuring the EPR signal at room temperature, where it is unsaturated. The theoretical spin state occupation probabilities were then calculated at any temperature relative to the room temperature values to get a theoretical dark EPR transition intensity. This allowed the spin state occupation probabilities under illumination to be calculated. Once these numbers had been determined the electron spin polarisation percentage can then be calculated by comparing the light and dark occupation probabilities of the polarised level, the $m_s = 0$ level. The assumption is made, for the purpose of this calculation, that the $m_s = \pm 1$ states have equal populations. At the fields at which these measurements were taken ($\sim$3000 G) the $m_s = +1$ is the highest spin level, $m_s = 0$ is the middle and $m_s = -1$ is the lowest. This can be surmised from the sign of the zero-field splitting [80]. For a spectrum like figure 5.4 the low field line arises from absorption in the $m_s = 0 \rightarrow +1$ transition and the high field line arises from emission in the $m_s = -1 \leftarrow 0$ transition.

The spin occupation probabilities of the levels in the dark can be calculated using Boltzmann statistics and are labelled p^d_{-1}, p^d_0 and p^d_{+1} respectively. It is assumed that, as demonstrated in equation 5.2, the total population of the ground state is not changing; the defect concentration is remaining the same and not transferring into a long lived excited state.

$$p^d_{-1} + p^d_0 + p^d_{+1} = 1 \tag{5.2}$$

The energies of the different levels are given by E_{+1}, E_0 and E_{-1}. The energy separations between the different spin levels can thus be calculated; $\epsilon_{0,+1} = E_{+1} - E_0$ and $\epsilon_{-1,0} = E_0 - E_{-1}$. The dark occupation probabilities are given by equations 5.3, 5.4 and 5.5.

$$p^d_{-1} = \frac{1}{Z} \tag{5.3}$$

$$p^d_0 = \frac{exp(-\epsilon_{-1,0}/k_B T)}{Z} \tag{5.4}$$

$$p^d_{+1} = \frac{exp(-(\varepsilon_{0,+1} + \varepsilon_{-1,0})/k_B T)}{Z} \tag{5.5}$$

Z is the partition function and is given by equation 5.6.

$$Z = 1 + exp\left(\frac{-\epsilon_{-1,0}}{k_B T}\right) + exp\left(\frac{-(\epsilon_{-1,0} + \epsilon_{0,+1})}{k_B T}\right) \tag{5.6}$$

The difference in occupation probabilities is given by η. The EPR intensities are proportional to η as this gives a likelihood of transition. In equation 5.7 and 5.8 the subscript $+1, 0$ indicates the transition of the low field line and $0, -1$ of the high field line.

$$\eta_{+1,0} = p_0 - p_{+1} \tag{5.7}$$

$$\eta_{0,-1} = p_{-1} - p_0 \tag{5.8}$$

In order to calculate the occupation probabilities in the light, η^l must be calculated. Thus the ratio of the occupation probability differences is equal to that of the EPR intensities in the light and dark, as given by equation 5.9.

$$\frac{\eta^l}{\eta^d} = \frac{I^l}{I^d} \tag{5.9}$$

However, I^d is unknown because at low temperatures microwave power saturation causes the signal to become unquantifiable as discussed previously. It is known at room temperature where microwave power saturation does not occur. The theoretical dark intensity can be calculated, as shown in equation 5.10, by using the intensity at room temperature and the occupation probability differences, as calculated previously using Boltzmann statistics.

$$\frac{I^d_T}{I^d_{RT}} = \frac{\eta^d_T}{\eta^d_{RT}} \tag{5.10}$$

The theoretical occupation probability difference can then be calculated from the intensity of the EPR line in the light using equation 5.11.

$$\eta^l_T = \eta^d_T \frac{I^l_T}{I^d_T} = \eta^d_{RT} \frac{I^l_T}{I^d_{RT}} \tag{5.11}$$

Using equations 5.2, 5.7, 5.8 and 5.11 the theoretic occupation probabilities in the light can now be calculated using the light and dark intensities. This is shown in equations 5.12, 5.13 and 5.14.

$$p^l_{+1} = \frac{1}{3}\left[1 - 2\left(\eta^d_{RT}\frac{I^l_T}{I^d_{RT}}\right)_{+1,0} - \left(\eta^d_{RT}\frac{I^l_T}{I^d_{RT}}\right)_{0,-1}\right] \tag{5.12}$$

$$p_0^l = \frac{1}{3}\left[1 + \left(\eta_{RT}^d \frac{I_T^l}{I_{RT}^d}\right)_{+1,0} - \left(\eta_{RT}^d \frac{I_T^l}{I_{RT}^d}\right)_{0,-1}\right] \tag{5.13}$$

$$p_{-1}^l = \frac{1}{3}\left[1 + \left(\eta_{RT}^d \frac{I_T^l}{I_{RT}^d}\right)_{+1,0} + 2\left(\eta_{RT}^d \frac{I_T^l}{I_{RT}^d}\right)_{0,-1}\right] \tag{5.14}$$

The degree of optical spin polarisation, ξ, can then be calculated as given in equation 5.15.

$$\xi = \frac{p_0^l - p_0^d}{p_{+1}^d + p_{-1}^d} \times 100\% \tag{5.15}$$

Once the percentage electron spin polarisation can be calculated, for different of wavelengths, temperatures and samples, it can be compared.

5.4 Experimental Results

5.4.1 EPR Results

Laser Power Saturation of Polarisation

The relationship between the laser power used and the resulting integrated area of the low field EPR signal can be seen in figure 5.5. Increasing laser power shows a proportional increase in EPR signal and optical power saturation was not seen. The electron spin polarisation is optically power limited. The highest point indicated on the graph relates to ξ =2% electron spin polarisation, at 78 K. The EPR electron spin polarisation results presented in this chapter are not the maximum possible polarisation percentage with each wavelength as with more optical power a larger polarisation would be seen.

Symmetry of ^{13}C Hyperfine Satellites

In figure 5.6 a close up of the low field SiV^0 line can be seen. The ^{13}C satellites can be seen around the central line. The six nearest neighbour ^{13}C satellites overlap confirming the symmetry to be D_{3d}. This scan was taken at 10 K, at higher temperatures the satellites are in the same positions, indicating the symmetry

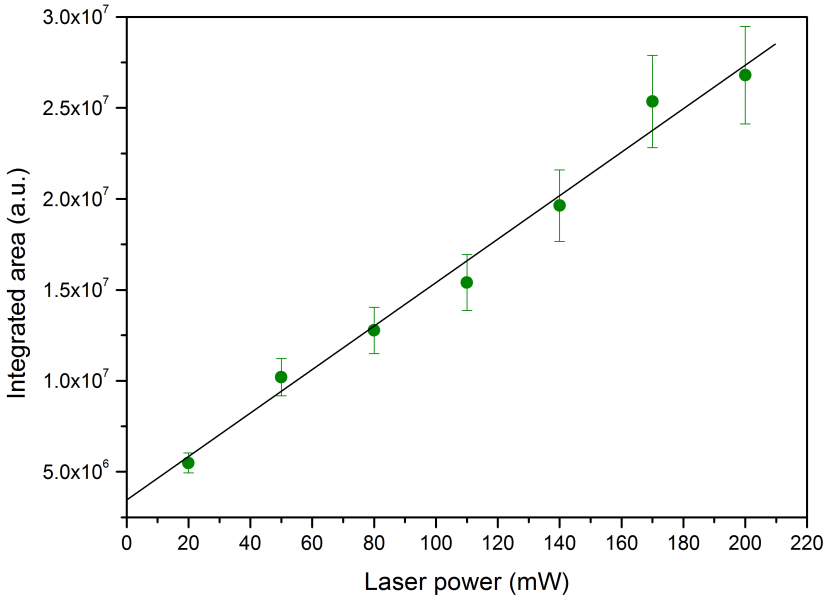

Figure 5.5: *EPR signal as a function of laser power, with the 940 nm laser diode. Data taken at 78 K. The linear relationship indicates the EPR signal is not optically saturating.*

does not change with temperature.

5.4.2 Wavelength and Temperature Response of Electron Spin Polarisation

The wavelength dependence of the electron spin polarisation in sample 5 can be seen in figure 5.7a. These data was taken using laser diodes at discrete wavelengths and the electron spin polarisation was calculated from the resulting EPR lines using the method outlined in section 5.3.1. In these data optical excitation energies below the ZPL can be seen to cause small but significant electron spin polarisation.

Previous investigations of the wavelength dependence of electron spin polarisation have been carried out by D'Haenens-Johansson [81]. For that work a broadband source in the form of an arc lamp was used. Wavelength dependence was studied using a series of long-pass filters (280 to 780 nm), these were used to vary the cut off wavelength of the light. The resulting dependence at 100K is shown in figure 5.7b. This shows an estimated cut-off of 1.3 eV, below which electron spin polarisation should not occur. This is approximately the ZPL of the neutral silicon vacancy (1.31 eV), and is what would be expected if the electron spin polarisation

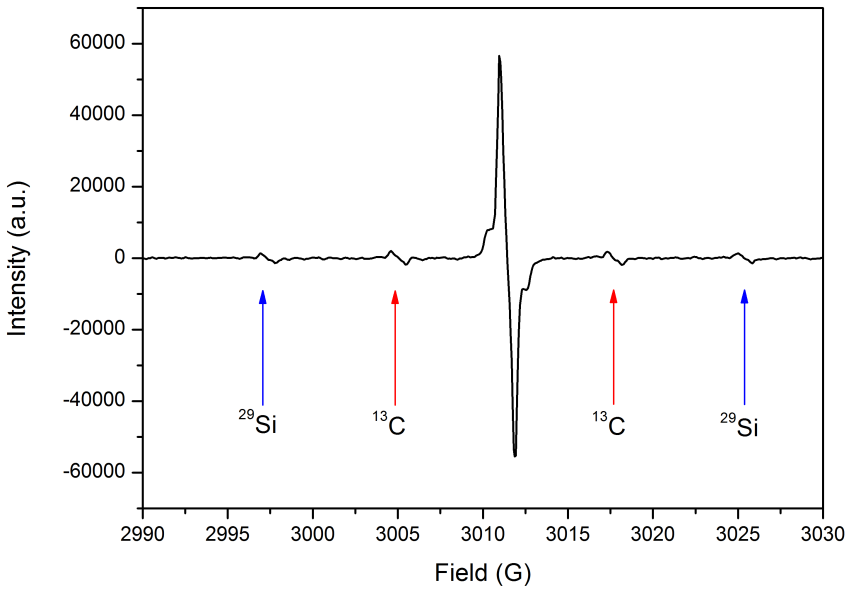

Figure 5.6: *Symmetry of the SiV^0 defect at 10K. This is the low field line of the site with symmetry axis parallel to the magnetic field. The ^{13}C and ^{29}Si hyperfine lines can be seen either side in red and blue respectively, with the same comparative intensity as would be seen at room temperature. There are 6 nearest neighbour ^{13}C atoms at 1.1% abundance and there is one ^{29}Si at 4.9% abundance.*

mechanism was analogous to that of NV^-. However, the use of long pass filters means the data is not optically power corrected. These data contrasts to the data obtained using individual illumination energies. The difference in experimental set-up may explain the difference in behaviour seen.

Electron polarisation measurements were also taken at 10 K and at 30 K, see figure 5.8. At both these temperatures there was a very different pattern to that at 100 K. The electron spin polarisation seen with excitation energy closest to the ZPL was significantly higher than at any other energy.

The data presented here from the work of D'Haenens-Johansson was taken with a microwave attenuation of 60 dB (200 nW) whereas the data collected for this thesis used 84 dB (0.8 nW). This is two and a half orders of magnitude lower microwave power and hence will induce less microwave power saturation. This may contribute to the differences in electron spin polarisation percentage presented.

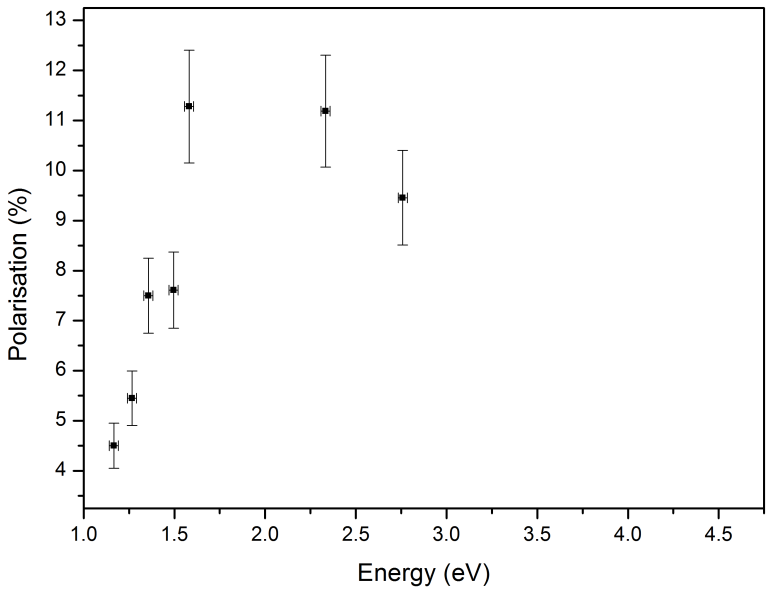

(a) *Data taken at 100 K on sample 5. These data were taken using a series of laser diodes with discrete energies, each of which was 80 mW at the sample.*

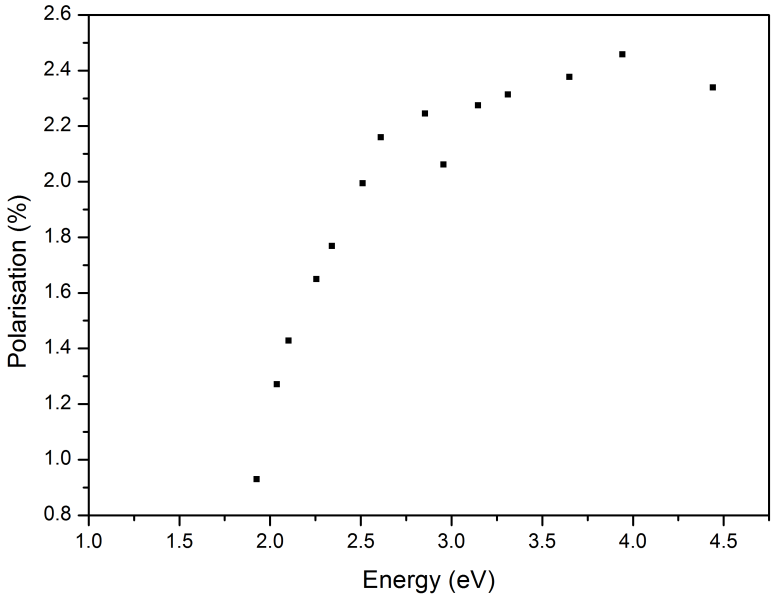

(b) *Previous data taken by Dr D'Haenens-Johansson [81] at 100 K on sample 9. These data were taken using the arc lamp and a series of long pass filters.*

Figure 5.7: *Comparison of data taken at 100 K with diodes at individual wavelengths and with an arc lamp. The ZPL of SiV^0 is at 1.31 eV.*

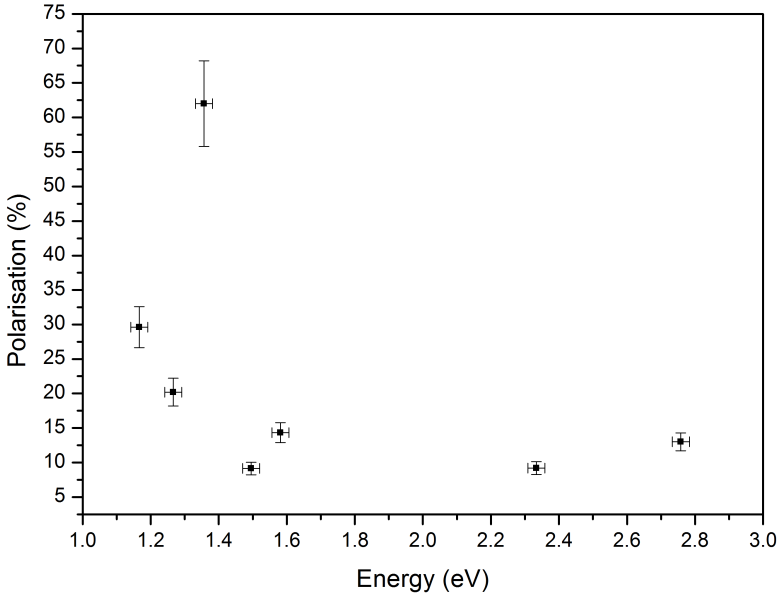

(a) *Polarisation with different illumination energies taken at 10 K.*

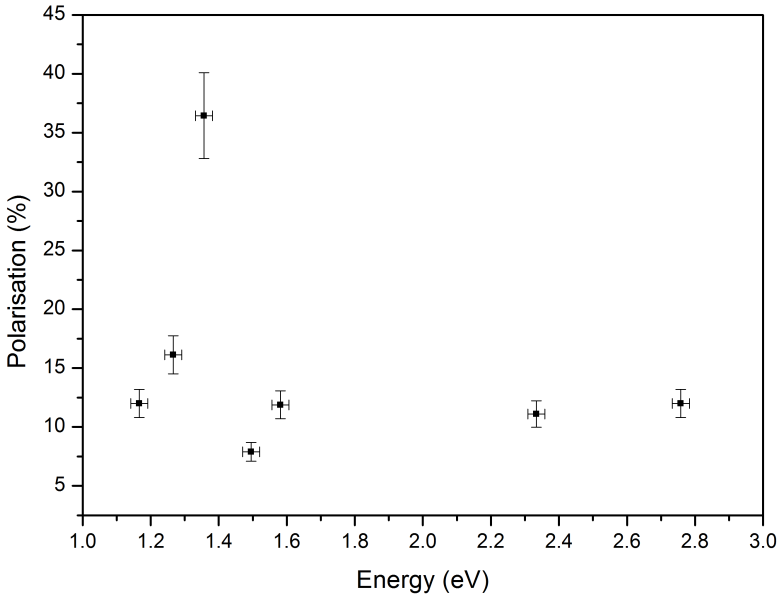

(b) *Polarisation with different illumination energies taken at 30 K.*

Figure 5.8: *Polarisation dependence on illumination energy in sample 5. For each measurement there was 80 mW of laser power at the sample. The highest data point on each diagram is associated with the diode used which has energy closest to the ZPL.*

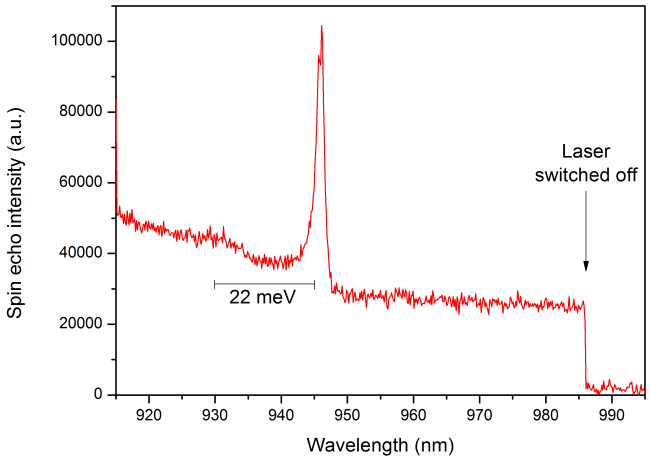

Figure 5.9: *Intensity of echo from low field line of defect with symmetry axis parallel to magnetic field of sample 5 measured at 10 K while sweeping the incident laser wavelength. These data was taken by Dr Green [145].*

Tunable Laser Study

As discussed in the experimental details section a tunable laser was acquired to study the effect of resonant excitation. This allowed measurements to be taken of the electron spin polarisation response as the illuminating wavelength was slowly swept. A two pulse Hahn echo was measured as the wavelength was swept to discover the effect on electron spin polarisation. The resulting changes, measured at 10 K, can be seen in figure 5.9. This shows a large increase in the low field line echo intensity at 946 nm, the ZPL. This result mirrors that taken with the laser diodes of sample 5 at 10 K as shown in figure 5.8a.

Wavelength Dependence in Sample 8

In order to explore the electron spin polarisation effects further another sample was investigated. The data is shown in figure 5.10. Sample 8 showed significant electron spin polarisation using illumination close to the ZPL. Unlike sample 5 at 30 K this electron spin polarisation was not higher than other wavelengths.

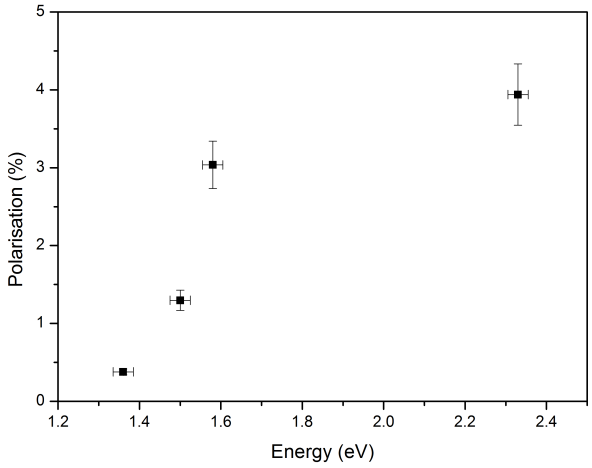

(a) *Electron spin polarisation with different illumination energies taken at 30 K.*

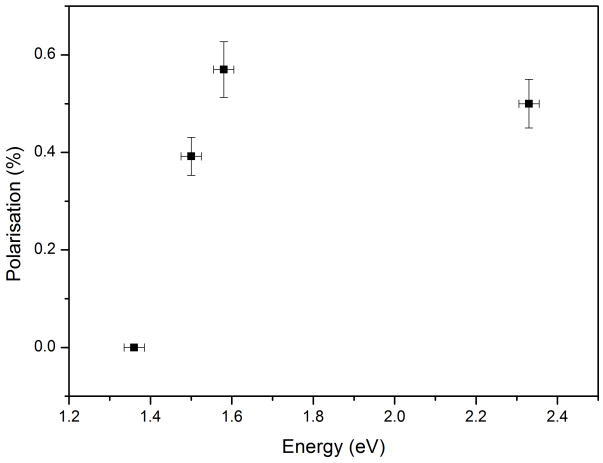

(b) *Electron spin polarisation with different illumination energies taken at 100 K.*

Figure 5.10: *Sample 8 electron spin polarisation dependence on illumination energy. Polarisation calculated from the intensities of the low field and high field line from the defect with symmetry axis parallel to the magnetic field.*

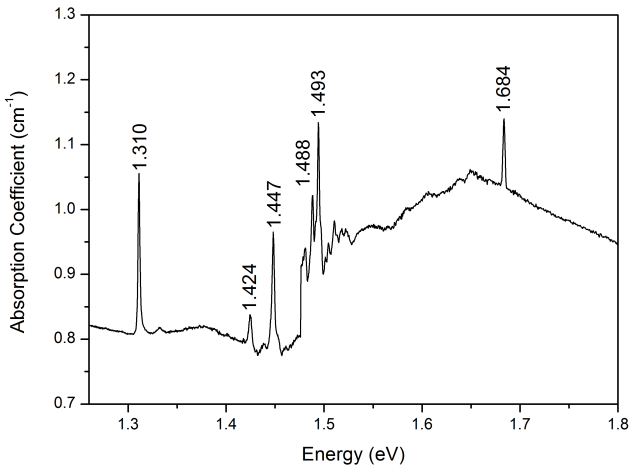

Figure 5.11: *Absorption of the neutral and negative silicon vacancy at 4 K in sample 11. The peaks at 1.447 eV and 1.493 eV are related to the photoconductivity threshold at 1.5 eV [144]. The ZPL of SiV^0 can be seen at 1.310 eV and of SiV^- at 1.684 eV. Data taken by Dr D'Haenens-Johansson.*

5.4.3 Optical Spectroscopy

A UV/vis absorption spectrum of sample 11 is shown in figure 5.11. This shows absorption at the neutral and negative silicon vacancy.

Photoluminescence (PL) measurements were taken of the samples studied for this work. The PL comparison is shown in figure 5.12. The concentrations of negative and neutral silicon vacancy and neutral vacancy appear higher in sample 5. The neutral silicon vacancy concentration as calculated by EPR are shown in table 5.1. The disparity between the EPR results and the PL comparison in sample 5 may arise due to the layering, as discussed in section 5.2, the sample had one layer of silicon doping between two of boron doping. The PL measurements were taken on the top of the sample, which was one of the boron doped layers. EPR measures the average concentration, whereas PL is specific to one region.

5.4.4 T_1 and T_2 Relaxation Behaviour in NV^- and SiV^0

Relaxation Behaviour of NV^-

Before taking spin-lattice relaxation measurements for the neutral silicon vacancy the method used was implemented and tested by taking measurements on the

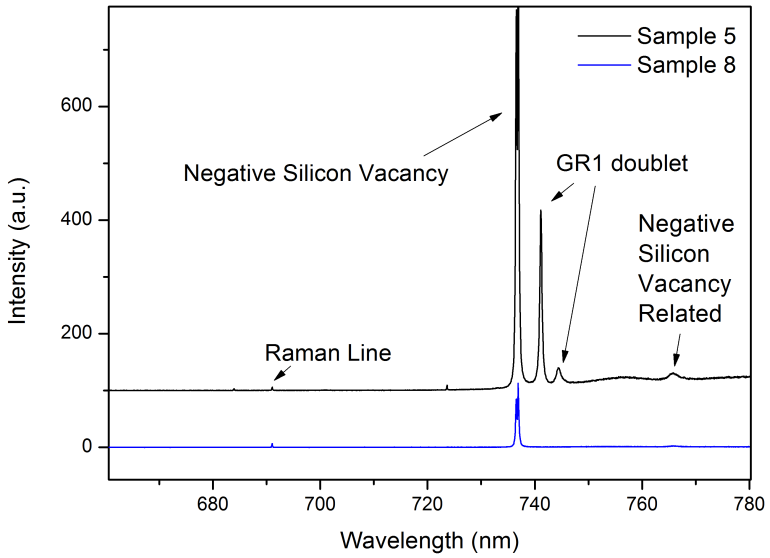

(a) 633nm excitation. The sample 5 line is offset for clarity.

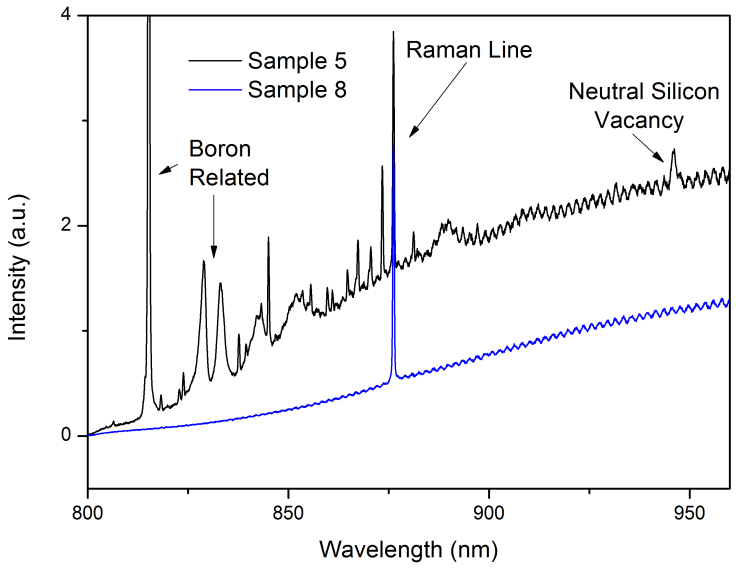

(b) 785nm excitation.

Figure 5.12: *Raman line normalised PL of the two samples compared at 77 K.*

nitrogen vacancy and comparing these to previous results using other methods. The method of illuminating the sample with a laser to cause electron polarisation increased in EPR signal, however, as discussed in section 5.3.1, illuminating a sample causes an increase in relaxation rate due to optical pumping. In order to measure the true T_1, the sample must be in darkness for the spin relaxation measurement. This was achieved using an Acousto-Optic Modulator (AOM) which was controlled by the spectrometer to switch the illumination off before the echo detection sequence took place using the method detailed in Chapter 4.

The functioning of the AOM was checked using a oscilloscope but it remained worthwhile to check the results obtained using the method were in agreement with previous NV^- T_1 values.

These results are shown in figure 5.13. As sample 10 had a concentration in between the two Jarmola diamonds plotted, the T_1 results are as expected [147].

Previous Methods for Measuring Spin Relaxation Times

Previously measuring the spin-lattice relaxation (T_1) time in the dark has proved challenging due to the low neutral silicon vacancy concentrations in available samples. Previous experiments have required continuous illumination, in order to enhance the signal enough to make it measurable. This has meant the relaxation time being measured is not the actual relaxation time but an effective relaxation time, limited by the optical pumping rate. Below a certain temperature the optical pumping rate exceeds that of the relaxation rate T_1 as shown in figure 5.14a and hence makes T_1 impossible to measure. The relaxation rates measured previously are shown in figure 5.14b.

In this work this issue was not encountered due to the AOM method as mentioned above. This could also be confirmed by measuring the relaxation rates in the dark and comparing them to those measured with the AOM. This was checked at three temperatures (as dark measurements took much longer to get a reasonable signal to noise due to the very small echo which was being measured) and gave the same result, within error. These results are shown in table 5.2.

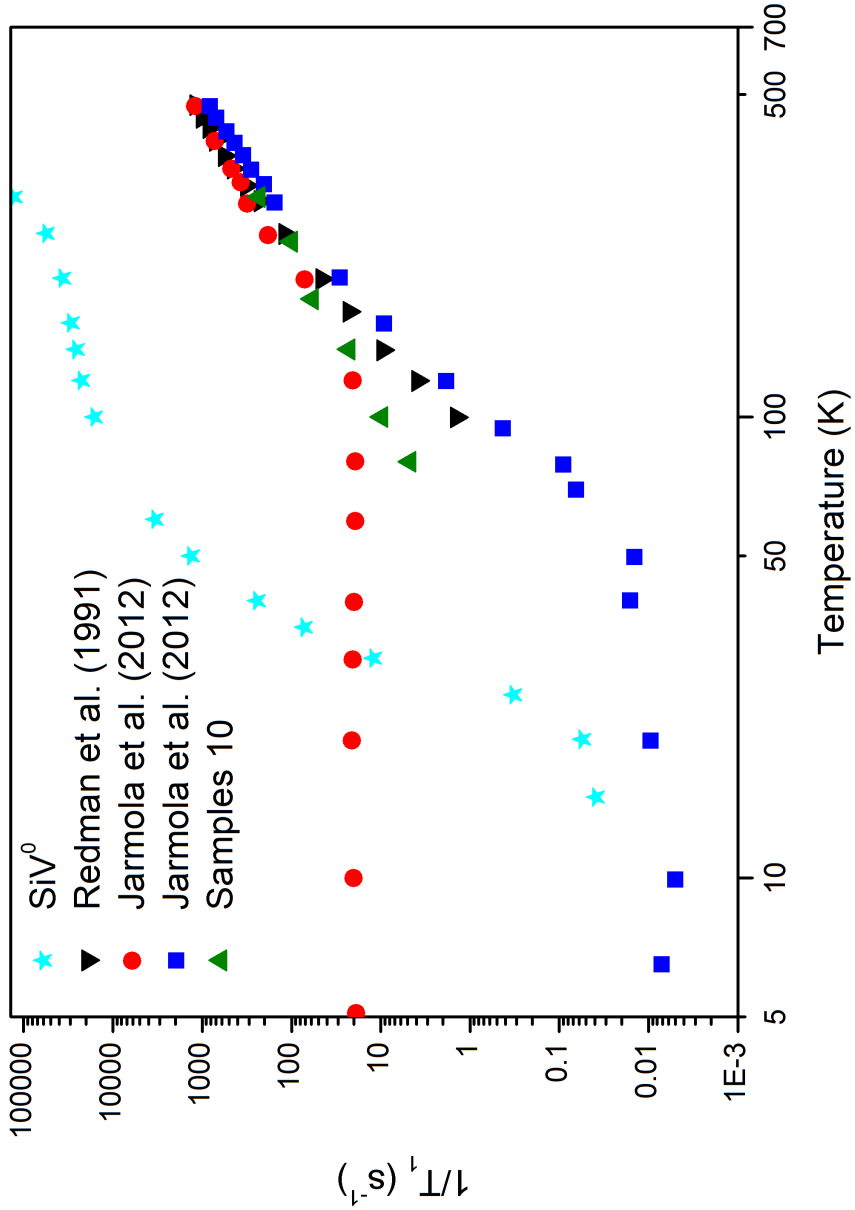

Figure 5.13: *Comparison of NV^- spin-lattice relaxation data taken with the AOM method to previous NV^- relaxation data [147, 148]. The red (circles) Jarmola data was for a high nitrogen concentration diamond (40-60 ppm) and the blue (square) data was for a lower nitrogen concentration diamond (10-30 ppm). The concentration of nitrogen in sample 10, tested with the AOM, was 40 ppm. The data for SiV^0 is also included.*

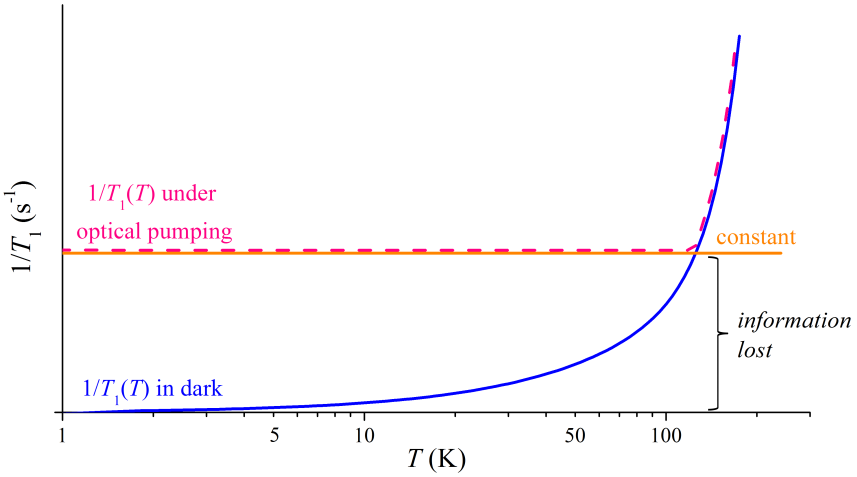

(a) *Optical pumping makes collecting true T_1 when illuminated at low temperatures impossible as it limits longer relaxation rates.*

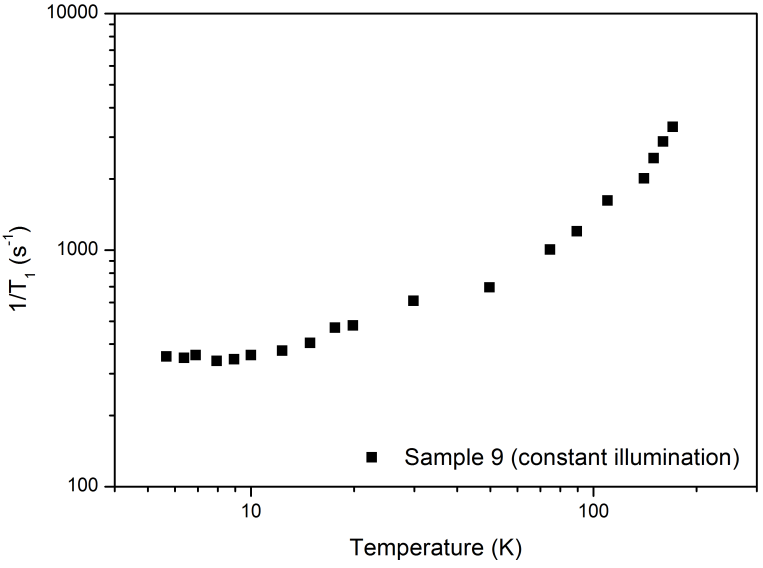

(b) *T_1 measured under constant illumination with arc lamp of sample 9. Measurement taken by Dr D'Haenens-Johansson [81].*

Figure 5.14: *Issue arising from data taken with constant optical illumination.*

Temperature (K)	T_1 Relaxation Time (Dark)	T_1 Relaxation Time (AOM)
30	-	82000±8200 μs
60	290±29 μs	300±30 μs
100	61±6.1 μs	62±6.0 μs
290	7.8±0.8 μs	8.3±0.8 μs

Table 5.2: *T_1 relaxation times of SiV^0 in sample 7 low field line measured with and without the AOM. B is parallel to $\langle 111 \rangle$. Measurement error approximately 10%.*

5.4.5 Temperature Dependence of Spin-Lattice Relaxation Time

An example inversion recovery spectra is shown in figure 5.15. The data can be fitted in the form of equation 5.16.

$$M_z(t) = M_z(0)(1 - 2e^{-\tau/T_1}) \tag{5.16}$$

The spin-lattice relaxation time dependence on temperature is shown in figure 5.13. The variation of T_1 is large, six orders of magnitude between room temperature and 11 K. At room temperature T_1 becomes very short (approximately 2000 ns).

5.4.6 Temperature Dependence of Spin-Spin Relaxation Time

The spin-spin relaxation (T_2) times were also measured, at fewer temperatures. They were measured by performing a two pulse echo sequence, and measuring the echo as the time between the two pulses was increased. These results are presented in table 5.3.

Temperature (K)	T_2 Relaxation Time
30	110±11 μs
100	62±6.2 μs
290	2.0±0.2 μs

Table 5.3: *T_2 relaxation times of SiV^0 in sample 7 measured by Hahn echo.*

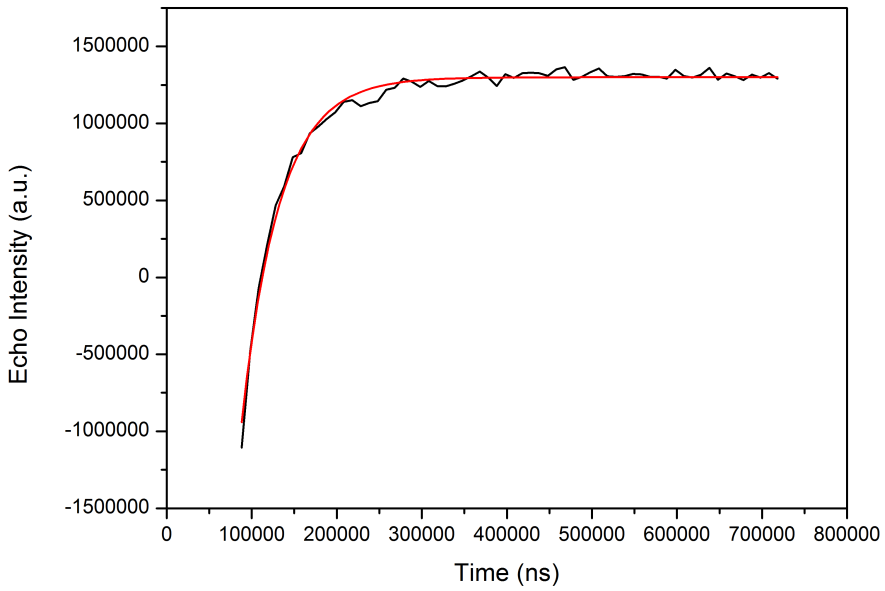

Figure 5.15: *Fitting a three pulse inversion recovery sequence of SiV^0 at 120 K. An AOM was used to enhance the signal.*

5.4.7 EPR Linewidth Changes

Very short relaxation times, compared to the time spent measuring a transition in continuous wave EPR, are known to broaden the linewidth of the spectra. As discussed in section 5.4.5 the spin-lattice relaxation times of SiV^0 become very short at 300 K and above. This allows the work presented here to be connected to previous work on linewidths at temperatures above 300 K [80].

T_2 is normally unchanged by changing temperature (unless the total number of spins interacting is changing due to a concentration change). When T_1 becomes very short this limits T_2 as relaxation rotates spins back to the z-direction before relaxation in the xy-plane occurs. T_2 is thus T_1 limited and measuring T_2 can be an indirect way of measuring T_1.

T_2 can be obtained by measuring the change in EPR linewidth. At low temperatures when T_2 is long the lower limit of the linewidth is the result of distant unresolved hyperfine interactions. However, as T_2 becomes short the linewidth is broadened. In section 3.3.1 the absorbed power for continuous wave EPR was

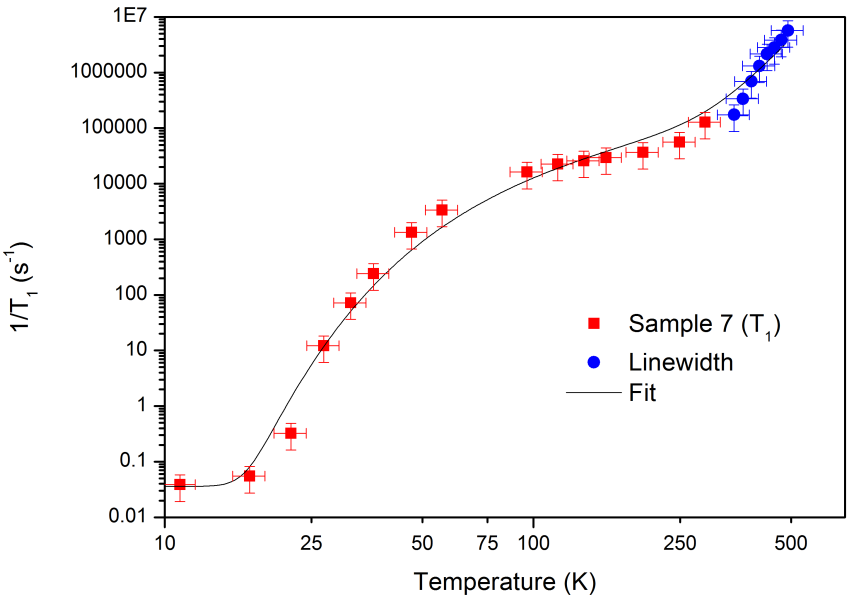

Figure 5.16: *Relationship between spin-lattice relaxation time of SiV^0 and temperature in the dark. The fit discussed in section 5.5.2 is also included. The spin-lattice relaxation from linewidth is also included. Linewidth data is from [80].*

presented. From this, an expression can be derived for the linewidth [112].

$$\Gamma = \frac{1}{|\gamma_e|\, T_2}\left(1 + \gamma_e^2 B_1^2 T_1 T_2\right)^{\frac{1}{2}} \tag{5.17}$$

If saturation effects are ignored the following assumption can be made.

$$if \quad \gamma_e^2 B_1^2 T_1 T_2 \ll 1 \quad then \quad \Gamma \propto \frac{1}{T_2} \tag{5.18}$$

This means that T_2 can be estimated from the inverse linewidth using $\gamma_e = 28.025$ MHZ mT^{-1}. T_1 can then be calculated.

At temperatures above 30 K $2T_1 \approx T_2$, see table 5.2 and 5.3. T_2 is T_1 limited. A constant was also added to the T_1 calculated at each temperature to take into account the unresolved ^{13}C couplings: the constant was taken as the difference between the linewidth and the measured T_1 at 300 K.

The T_1 data including that obtained from the linewidth is shown in figure 5.16.

5.5 Discussion

5.5.1 Polarisation Wavelength Dependence

Figure 5.5 indicates a linear relation between the laser power incident on a sample and the enhancement of the EPR signal which results. This indicates that higher electron spin polarisation levels than seen in this work could be obtained if higher power lasers are used. For the NV^- defect it is possible to achieve 97% electron spin polarisation in the ground state using a laser spot size of $\sim 1\ \mu m^2$ and 1 mW of power [149]. The fluence achievable in the current ensemble measurement (using 100 mW) is four orders of magnitude lower due to the requirement to illuminate the entire sample ($\sim$1 mm^2). As the relationship of spin polarisation with available power was linear, this indicates that if a higher fluence could be used, higher spin polarisation would be reached. The linear proportionality also suggests that only one photon is involved in the electron spin polarisation process when pumping at 940 nm.

The two samples investigated showed different SiV^0 electron spin polarisation behaviour as a function of excitation wavelength. Sample 5 showed a strong dependence on proximity of the illumination energy to the ZPL particularly at low temperatures. The electron spin polarisation efficiency at 10 K changed from an average of 10% away from the ZPL to 63% at it. This effect was not seen for sample 8. Sample 8 showed a small degree of electron spin polarisation at the ZPL, 0.4%, but this was significantly less efficient than higher energies, 4% at 30 K. This sample showed a decrease in electron spin polarisation with decreasing illumination energy. The relative spin polarisation can be compared, however, the absolute percentages quoted here may be larger than the true values because of the method used to calculate them. Difference may arise due to the calculation of the theoretical dark intensity or because of charge transfer. The efficiency at higher illumination energies could indicate a charge transfer effect. Charge transfer is known to occur with above band gap excitation: a photocurrent can be created within a diamond which contains SiV^0 with energy as low as 1.49 eV (830 nm) [144] so it is likely that charge transfer can occur at at least some of the energies employed during the experiment (1.17 to 2.76 eV). The measured electron spin polarisation increases may therefore be at least partially due to charge transfer between SiV^- and SiV^0 leading to a greater population of SiV^0. Nevertheless, electron spin polarisation was verified by measuring enhanced absorption (emission)

to (from) the $m_s = 0$ state. It is not clear from the data whether the ionisation of SiV^- directly results in polarised SiV^0, or if ionisation is followed by subsequent electron spin polarisation by the same optical excitation.

Sample 5 was investigated further using a tuneable laser. Again this result showed a marked increase in the EPR signal at the energy of the ZPL (see figure 5.9). This experiment directly links the SiV^0 EPR spectrum with the 946 nm ZPL. This experiment also shows that there exists at least one internal electron spin polarisation mechanism and that other defects are not necessarily required as a intermediate step in the electron spin polarisation of the SiV^0. Other mechanisms may also result in electron spin polarisation but further work is required. On closer inspection the ZPL electron spin polarisation was split, see inset in figure 5.9. This is possibly related to two different strain environments within the diamond creating two ZPLs which overlap.

These experiments demonstrate that an internal electron spin polarisation mechanism exists, but additional mechanisms may operate but are sample dependent.

Differences with Previous Results

In figure 5.7 the data taken for this project and previous data can be seen to differ significantly. These contrasting data may be due to the broadband source. The arc lamp has a relatively uniform light output distribution over the wavelengths studied, see figure 5.17. This means that when long-pass filters are used less total power will be incident on the sample at longer wavelengths (lower photon energies). This reduction in light intensity may explain the reduction in electron spin polarisation at lower energies, as seen in figure 5.7b. The cut off for these data is 1.3 eV. It is expected that if these data was normalised to the power of the arc lamp at each point a lower energy cut-off would be seen. This makes it challenging to compare the data presented here to previous data.

In figure 5.7a the cut off appears to be closer to 1.0 eV. Each of the discrete energies used for these data was normalised to the same power (80 mW) at the sample and therefore does not suffer from the same power complications as the arc lamp (as discussed in the previous paragraph): this may explain why lower energies still show a significant degree of electron spin polarisation.

The measurements taken at 10 K and at 30 K, see figure 5.8 showed a very different pattern to that at 100 K. The electron spin polarisation seen with excitation energy

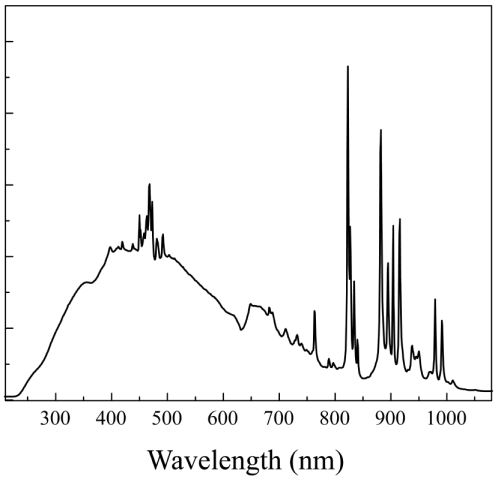

Figure 5.17: *Spectrum of a Xenon arc lamp from [150].*

closest to the ZPL was significantly higher than at any other energy.

Polarisation Temperature Dependence

The absorption spectrum of silicon vacancy containing diamond is shown in figure 5.11: the strongest absorption occurs at both silicon vacancy ZPLs (SiV^0 at 946 nm and SiV^- at 737 nm) when compared to the remainder of the spectrum. The strong absorption in the ZPLs compared to the phonon side band, especially compared to $NV^{-/0}$ spectra, are due to the inversion symmetry of the defect (see figure 2.8) which causes a smaller dipole moment than for nitrogen vacancies and thus means a weaker vibronic coupling [77]. The increased absorption at the ZPL could account for why, at low temperatures, a higher electron spin polarisation occurs at the ZPL. However, this effect changes with temperature as, at higher temperatures, electron spin polarisation is not stronger at the ZPL but the absorption still is. The different wavelength variation seen at 100 K and colder temperatures is not currently understood and requires further work.

The increased electron spin polarisation at low temperature is related to the very long T_1 relaxation time (see section 5.5.2). This result was presented in figure 5.13. Illumination will populate the $m_s = 0$ level. This will compete with T_1 which will return the populations to the Boltzmann distribution. Slower relaxation times will allow the electron spin polarisation of $m_s = 0$ to build up further as the illumination is applied.

Discussion of Intermediate Level

There exists an intermediate trapping state which has previously been described by D'Haenens-Johansson [81]. The trapping state was introduced because of the decrease in photoluminescence of SiV^0 at low temperature. As figure 5.18b shows PL in the ZPL reduces as temperature reduces, which is not what would be expected from the absorption behaviour (shown by the red dashed line). This implies electrons are getting trapped at low temperatures in an intermediate level.

In figure 5.18a the ground state and the excited state can be seen with the intermediate level 5 meV below the excited state. The trapping level has an effective spin of $S = 0$ whereas the ground state is $S = 1$ so the transition is forbidden and hence non-radiative. However, it may occur if spin-orbit coupling allows state mixing.

At low temperatures electrons will not have enough thermal energy to escape the level; at 20 K $k_bT = 1.7$ meV. However, these electrons must be relaxing back to the ground state as luminescence does not cease completely. If this occurs these electrons may relax to the ground state in a non-radiative transition. This effect reduces at higher temperatures as electrons can now be thermally excited back to the excited level and relax back down to the ground state, radiatively.

At low temperatures these electrons can relax back non-radiatively, via intersystem crossing, and polarise the ground state. This intermediate state is shown in relation to the other energy levels in figure 5.19.

Polarisation with Excitation Energy Below the ZPL

For sample 5 and sample 8 electron spin polarisation was seen when illumination energy below the ZPL was used. There are a number of possible mechanisms which could be occurring. Either electron spin polarisation is not caused by an internal mechanism and another species is being polarised and transferring its polarisation onto the silicon vacancy. This seems unlikely due to the degree of electron spin polarisation's strong dependence on proximity to the ZPL of silicon vacancy.

Another possible mechanism involves electrons being directly excited to one of the intermediate states, shown in figure 5.19, which is at a lower energy than the excited level. If it is the case that relaxation via these states causes ground state

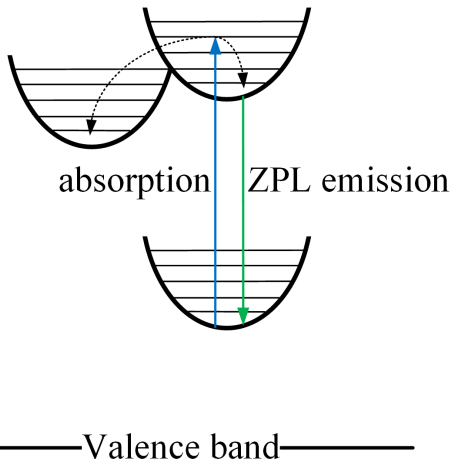

(a) Intermediate level structure. Picture recreated from [81].

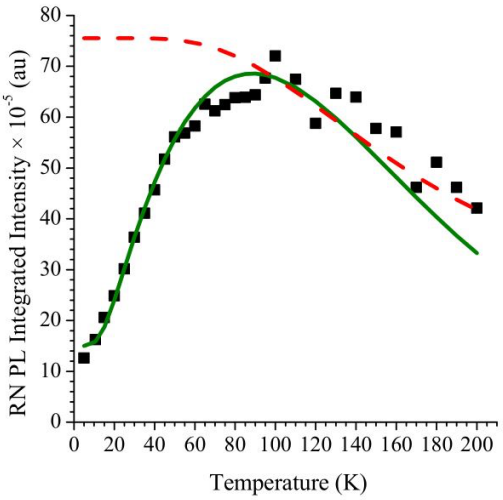

(b) PL emission of the 1.13 eV zero-phonon line as a function of temperature with 785 nm illumination. The red dashed line shows the absorption of the defect. Graph from [81].

Figure 5.18: *Effect of the intermediate level of photoluminescence at low temperature.*

electron spin polarisation then polarisation could be occurring without the need for the electron to be excited to the $(^3A_{1u})$ excited state.

Sample Differences

The samples studied showed different behaviour: in sample 5 a significant increase in the electron spin polarisation was seen with the laser diode closest to the ZPL but for sample 8 this effect was not seen instead higher photon energies created a higher electron spin polarisation. It could be the case that some samples do not exhibit the link between electron spin polarisation and ZPL or that the other polarisation mechanisms present are stronger so the link can not be detected.

Sample 5 had an undetectable level of nitrogen and was co-doped with boron with a concentration of 0.54 ppm. The sample was inhomogeneously doped, as discussed in section 8.2.1, so different regions will have different silicon vacancy concentrations. Sample 8 was not boron doped and the concentration of single substitutional nitrogen was 62 ppb. Single substitutional boron impurities in diamond may donate a hole to silicon vacancy, increasing the concentration of the neutral rather than the negative state. In addition to this effect boron may also interact with the silicon vacancy via an unknown mechanism to increase the

strength of the electron spin polarisation at the ZPL. Further work is required to understand the link to boron and which other species present may also be having an effect.

5.5.2 Pulsed Results Discussion

Differences with Previous T_1 Measurements of SiV^0

Comparing previous T_1 measurements of SiV^0 with those presented here, a difference becomes apparent (see figure 5.14b). The sample used previously was not used for the work here as it was no longer available, sample differences may cause small T_1 differences. Additionally this difference has arisen due to previous T_1 data being collected during sample illumination whereas the data presented here is taken without illumination. The relaxation data presented here shows a much slower rate at low temperature than had been previously measured by D'Haenens-Johansson [81]: this is because previous measurements had not measured intrinsic relaxation rates but the optical pumping induced relaxation rate. This is especially prominent at low temperatures as the optical pumping used for previous studies becomes an important factor, see figure 5.14. The optical pumping induced relaxation and the T_1 in the dark were very similar above 100 K but at 100K and below the light relaxation rate was faster than the dark relaxation rate.

An additional factor arises due to the broadband spectrum of the arc lamp. As discussed previously different wavelengths of light may be causing electron spin polarisation mechanisms and charge transfer. These effects may also have an effect on the relaxation time.

Processes Involved

The main processes involved in T_1 relaxation were discussed in section 3.4.3 and these include direct, Raman, Orbach and other thermally activated processes. The equation presented in section 3.4.3 was used to perform a phenomenological fit on the data presented here. The thermally activated part was not included as this did not improve the fit and would be over parametrising. Equation 5.19 shows the

final relation, including a constant offset.

$$\frac{1}{T_1} = a + bT^n + \frac{c}{exp(\Delta/kT) - 1} \tag{5.19}$$

Fitting to the shape shown in figure 5.16, $a = 0.036 \pm 0.004$ s $^{-1}$, $b = 5.0 \pm 0.5 \times 10^{-13}$ s $^{-1}$K^{-7}, $c = 1.5 \pm 0.2 \times 10^5$ s $^{-1}$, $\Delta = 22 \pm 2$ meV and $n = 7$ [145]. The value for Δ closely matches that of the local vibrational mode seen in figure 5.9. The form of this equation is very similar to that of NV$^-$ [147]. For NV$^-$ $n = 5$.

Thermally activated processes involve dissipating energy from the spins to the lattice by undergoing motion such as vibration or rotation which will reduce the symmetry of the defect. This effect will occur more at higher temperatures and below a certain temperature, the lack of thermal energy will cause this motion to stop. At higher temperatures the symmetry will be a sum of the different lattice configurations that motion changes between. At lower temperatures one of the symmetry configurations will be frozen in. The position of the ^{13}C isotope lines can give information about the symmetry of the defects environment as they arises from the nearest neighbour ^{13}C atoms. Figure 5.6 shows the spectrum, including the ^{13}C hyperfine lines, at 10 K. These lines overlap at 10 K and at 292 K, indicating a change in symmetry has not occurred. For this reason thermally activated processes were assumed not to be occurring.

The direct process was also not included as the lowest data point taken was at 11 K. The mean energy of the phonon density of states increases with increasing temperature. The temperatures at which these data were taken the mean phonon energy is much larger than spin state difference. At 0.5 K the mean energy is 10 GHz so above this temperature there will be no phonons with low enough energy to change the m_s level. The experiment was performed at temperatures above 11 K so the direct process was not included.

The Raman process involves absorption and subsequent emission of a phonon, to and from a virtual state. This takes the form bT^n and is modelled in the equation with $n = 7$ because the energy levels are a non-Kramers doublet [145].

The Orbach effect involves an electron being excited to a higher energy level state Δ above the starting energy state and then relaxing back down to a different m_s state [118, 115]. It is also included in the model.

T_1 of SiV^0 and NV^- Compared

The relaxation times of the neutral silicon vacancy are comparable to those of the negative nitrogen vacancy at low temperatures, but at room temperature they are almost three orders of magnitude apart and very different behaviour is seen, see figure 5.13. Compared to the nitrogen vacancy the changes of T_1 of the SiV^0 with temperature are much larger. T_1 ranges between 8.3 μs at room temperature to 25 s at 15 K. This explains the difficulty of measuring significant electron spin polarisation at room temperature; T_1 is very short causing the electron spin polarisation to decay quickly.

5.5.3 Possible Mechanisms

At low temperatures electron spin polarisation is highly dependent on the energy of illumination applied, with the most efficient polarisation occurring with illumination closest to the ZPL. This indicates that there exists an internal spin polarisation mechanism (other mechanisms may also exist). Two different mechanisms for this have been suggested [145] and these are shown in figure 5.19. The first mechanism (shown in figure 5.19(a)) is like that of NV^- in that it involves intersystem crossing from the ZPL excited state. It involves relaxation via the ^1E_u state, which causes preferential population of the $m_s = 0$ state. The second mechanism (shown in figure 5.19(b)) shows excitation and relaxation to and from an intermediate level, unlike the mechanism for the NV^-. This level is a triplet state, $^3A_{2u}$, in between the ground and excited states. Relaxation occurs via relaxation to this state and via the ^1E_u singlet state, and again this causes preferential population of the $m_s = 0$ state. These mechanisms may be occurring in conjunction with other mechanisms.

At energies which are below the ZPL, it is possible that spin-orbit coupling weakly allows a transition from the ground state into the ^1E_u state. Electrons could be excited to this state by the illumination and then relax preferentially populating the $m_s = 0$ level. It is possible that for electron spin polarisation the electrons do not have to relax from the excited state ($^3A_{2u}$), but instead can just relax from the ^1E_u state.

It is surprising given the high Debye-Waller factor that electron spin polarisation occurs at a wide range of energies; it appears that polarisation occurs where

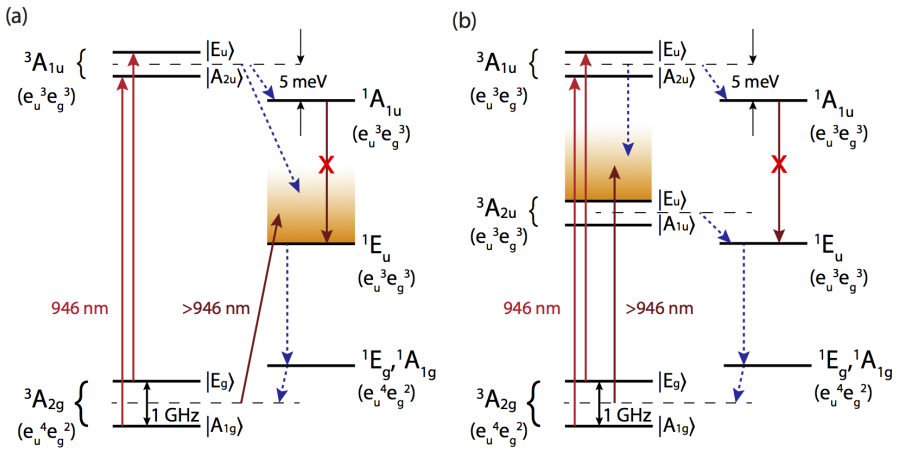

Figure 5.19: *Two suggested energy level mechanisms [145]. The dashed lines indicate non-radiative transitions, the red lines indicate radiative transitions and the red crosses indicate forbidden transitions. (a) is an NV⁻ like mechanism. (b) is a electron spin polarisation mechanism where electron excitation to the intermediate level causes polarisation.*

absorption does not. Particularly, at energies below the ZPL, where less absorption occurs, polarisation still occurs. This is not the case for the NV^-. This may arise due to different spin polarisation mechanisms at different energies.

5.6 Conclusions

The temperature and illumination effects on the electron spin polarisation have been studied. This work has given insight into the energy level structure and spin characteristics of the neutral silicon vacancy defect in diamond.

The temperature and wavelength dependence of the spin polarisation mechanism has been investigated in multiple samples and this has conclusively linked the neutral silicon vacancy to the 946 nm ZPL. A maximum optical-power limited spin polarisation of 60% has been achieved for near-ZPL excitation. The main findings are presented below:

- Spin polarisation occurs with excitation energy below the ZPL.
- At least one of the spin polarisation mechanisms present is internal and occurs most efficiently with illumination at the ZPL.
- It is possible that the internal electron spin polarisation mechanism is occurring concurrently with other spin polarisation mechanisms.

- Charge transfer occurs at energies above the ZPL indicating SiV^- may be changing directly into SiV^0 in the spin polarised state or non-polarised SiV^0 which is subsequently polarised by the incoming light.
- The electron spin polarisation mechanisms are sample dependent; the mechanisms may depend upon other species within the sample such as boron or nitrogen.
- It is evident that there may be multiple spin polarisation mechanisms and the behaviour is more complex than that of NV^-.

T_1 changes by six orders of magnitude from 11 K to room temperature resulting in T_1 comparable to NV^- at low temperature but three orders of magnitude shorter at room temperature. Phenomenological modelling of the temperature dependence of T_1 has revealed this is primarily due to ground-state coupling to a low-energy phonon ($\hbar\Omega = 22$ meV).

Further work includes understanding why different samples behave in different ways, exploring what effect other defects within the material have on the electron spin polarisation and thus understanding the different electron spin polarisation mechanisms present. Uni-axial stressed experiments will be performed. Applying stress while measuring the photoluminescence allows the degeneracy of the energy levels of the silicon vacancy to be explored further. This could be used to confirm the assignment of the ${}^3A_{1u}$ level to the excited state of the transition which makes up the ZPL.

Chapter 6

HPHT Synthesis of Isotopically Enriched Diamond

6.1 Introduction and Objectives

In this chapter a suite of high pressure high temperature (HPHT) synthesised diamonds were investigated. The effects of isotopic enhancement of the carbon source and of the carbon within the metal solvent on the final isotopic distribution in the diamonds produced were studied in order to understand the uptake of ^{13}C during HPHT synthesis. The carbon isotope ratio is of interest because it affects the exploitable material properties of diamond.

Creating diamonds which consist of a single carbon isotope is less challenging than for other elements which have heavier atomic masses [23]. Carbon is one of the lighter elements and hence there is a larger percentage mass difference between the 12 and 13 isotopes, making them easier to differentiate. This also means that changing the isotopic ratio has a large effect on the material properties [23].

One of the properties of isotopically enriched diamonds is increased thermal conductivity [151]. Diamond already has a high thermal conductivity, three times that of copper [152, 153]. Maximum thermal conductivity is reached when the diamond is either 100% ^{12}C or ^{13}C and the lowest thermal conductivity is when there is a 50:50 mix [151]. Reducing the ^{13}C concentration from natural abundance by one percent (to 0.01%) increases the peak thermal conductivity by more than 25% at room temperature [151]. Changing the ^{13}C concentration from natu-

ral abundance to 100% changes the room temperature thermal conductivity from 22.0 to 33.2 W/(cm.K), a 50% increase [151]. At higher temperatures the thermal conductivity changes more dramatically with isotopic concentration [151].

In metals thermal conduction occurs by the movement of electrons in the conduction band, whereas in diamond it occurs by the movement of phonons, therefore, in diamond thermal conductivity is determined by phonon velocity and phonon mean-free path. Phonon velocity remains relatively unchanged when changing the isotope; it changes by four percent when comparing an isotopically pure ^{12}C to ^{13}C diamond. The isotopic ratio has a much larger effect on phonon mean-free path. The phonon mean-free path can also be affected by grain boundaries, dislocations, vacancies and impurities (nitrogen for example), because at sufficient concentration these defects cause phonon scattering. This scattering can be due to phonons interacting directly with an impurity or can occur due to the local strain. An isotopically pure ^{12}C or ^{13}C intrinsic diamond has no alien atoms to cause phonon scattering and hence has a high periodicity so phonon mean-free path is longer and thermal conductivity is higher. Due to the high Debye temperature of diamond intrinsic phonon-phonon scattering is also low. Small crystal size polycrystalline diamonds exhibit much lower thermal conductivity due to the scattering caused by grain boundaries [10]. The conductivity may also be directional if the grain size or shape is directional [10].

The high thermal conductivity of diamonds with low fractions of isotopic impurities makes them very useful for heat spreaders. Heat spreaders are often used to connect areas of heat to heat sinks. Heat generated when computing is proportional to computing power so heat sinks are becoming increasingly important as computers become more powerful [6]. Diamond is better than metal for high end applications, such as in laser diodes, because their thermal conductivity is higher and their thermal expansion more closely matches that of silicon. Additionally they are electric insulators, if undoped, so will not short a circuit. CVD thin film diamonds are making this more affordable [154].

The Raman line of isotopically pure ^{13}C diamond (at 1281.2 cm^{-1}) has a high dependence on stress, making it a useful stress indicator, especially in high stress applications such as diamond stress cells [155, 156]. A very thin layer of pure ^{13}C on a diamond anvil can be monitored as the stress changes. This small volume, close to the sample, gives an approximation to a hydrostatic stress measurement. The ^{13}C Raman peak changes quasilinearly with pressure up to 100 GPa, although at 13 GPa it overlaps with the 1332.5 cm^{-1} peak from the diamond anvils [155].

Figure 6.1: *Morphologies of NL636-02, NL636-03 and NL636-04 before cutting. (a) from the top and (b) from the side. It can be seen that the morphologies are different, with sample NL636-04 becoming cubic. Samples are* ~ 4 mm $\times 6$ mm $\times$ 6 mm.

The objective of studying the diamonds presented in this chapter was to understand the enrichment process and isotope uniformity during HPHT synthesis as this will have a large effect on the properties of the diamond.

6.2 The Samples and the Growth Methods

A suite of HPHT diamonds supplied by Element Six containing different ^{13}C concentrations were investigated. Four diamonds were studied with nominal ^{13}C concentrations ranging from 1.01% (natural abundance) to 10.0%. The uniformity of the ^{13}C isotope uptake was investigated.

Additionally, four samples fabricated by General Electric (GE) were also studied for comparison purposes as they had ^{13}C enrichment of known concentration.

The isotopically enriched doped diamonds are shown in figure 6.1, showing their cubo-octahedral growth morphology. In figure 6.2 a close up can be seen, showing the seed on the bottom surface. A slice was taken from each diamond, cutting from the seed to the growth surface. Each of the four, polished diamond slices can be seen in figure 6.3 and in figure 6.4. The idealised growth morphology can be seen in figure 6.5. The optical microscope images show the seed on the right hand side and the different growth planes can be seen growing out from the seed. The seed and planes are labelled in the figure. From the variation in nitrogen content, as determined by the yellow colour, it can be seen that the sectors have varied in relative growth speed as the sample has grown. In sector $(1\,\bar{1}\,0)$ and $(\bar{1}\,1\,0)$ in figure 6.3b, for example, the paler yellow regions do not follow the straight lines but seem to have been larger at some point during the growth process.

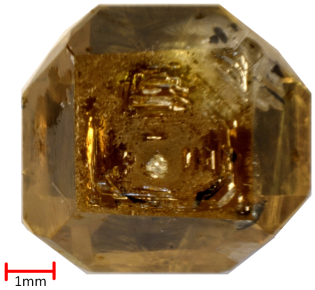

Figure 6.2: *The NL636-03 sample before laser cutting. This is the bottom surface. The seed crystal can be seen as the small white dot in the centre.*

One of the challenging aspects of studying these diamonds was ensuring the different types of measurement were taken in the same location, so they could be compared. This was done by studying the different sectors in the diamond using optical and cathodoluminescence (CL) microscopy, establishing where the seed was and taking the measurement along the line from the seed to the growth surface, which intersected the growth surface at the 90° angle. This gave the same position for each technique. When the 'location' of each measurement is plotted this refers to the position along this line. However for each of the different techniques, the pixel size and number of measurements along this line was different. In figure 6.3 the two dashed lines between which all the data were taken are shown.

6.2.1 HPHT Growth Methods

The diamonds were made by the HPHT process using the temperature gradient method in a belt press (see figure 6.6). When using this method a solvent is usually chosen which has the lowest eutectic with carbon in solution to reduce the pressure and temperature required [158]. In this case a cobalt-iron (CoFe) alloy was used. Temperatures between 1300°C and 1500°C are typically used in conjunction with 5 to 6 GPa of pressure. These diamonds typically take between fifty and one hundred hours to form [23].

Temperature Gradient Method

HPHT diamonds are routinely grown using the temperature gradient method. This is a method which grows on seed crystals in the presence of a solvent, which contains carbon, and a carbon source, see figure 6.7. The seed crystals, embedded

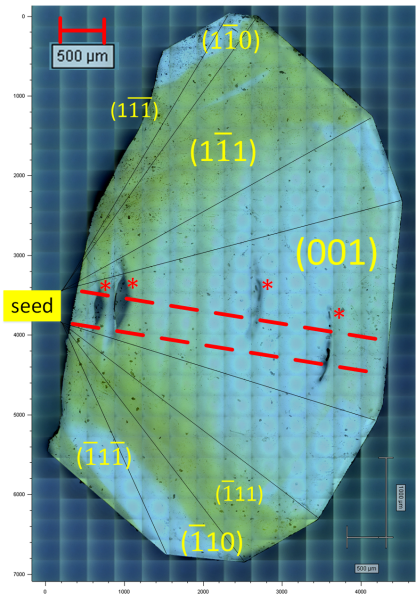

(a) *NL636-01 (111) slice. The stars indicated metal inclusions, most likely from the solvent, CoFe.*

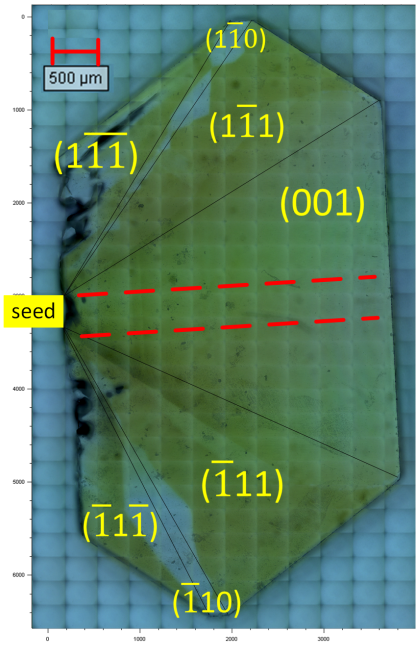

(b) *NL636-02 (111) slice.*

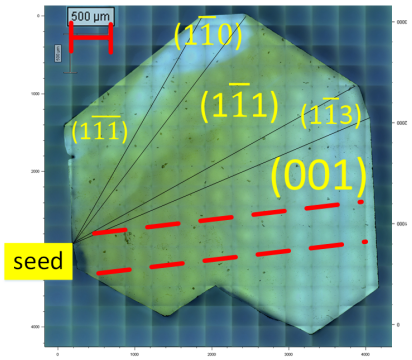

(c) *NL636-03 (111) slice.*

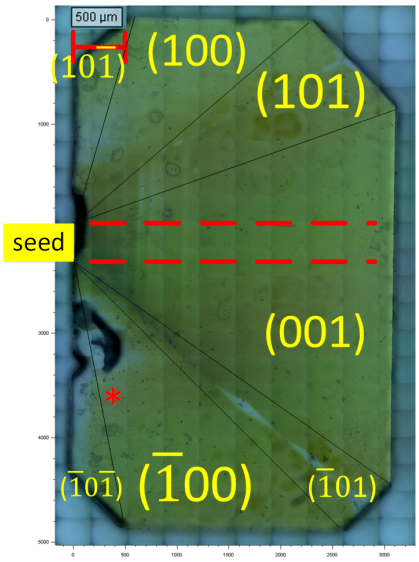

(d) *NL636-04 (001) slice.*

Figure 6.3: *Optical microscope images of each diamond slice showing the seed and the different growth regions. The red dashed lines indicate the area in which the Raman, FTIR and SIMS measurements were taken; from the seed on the left to the growth surface on the right. The stars indicate inclusions, which are likely CoFe from the solvent. The small dots in the image may be inclusions in the form of metal carbonites, also resulting from the solvent. These images where taken with an Renishaw inVia Reflex Raman Microscope with an 50x objective and an automatic stage.*

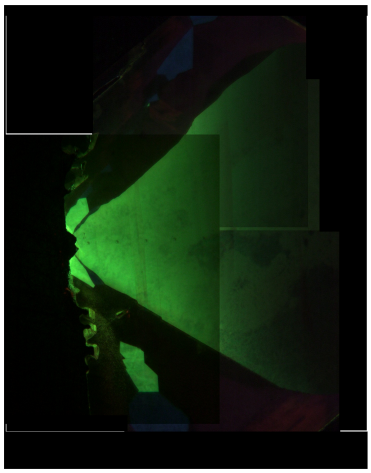

(a) *NL636-01.*

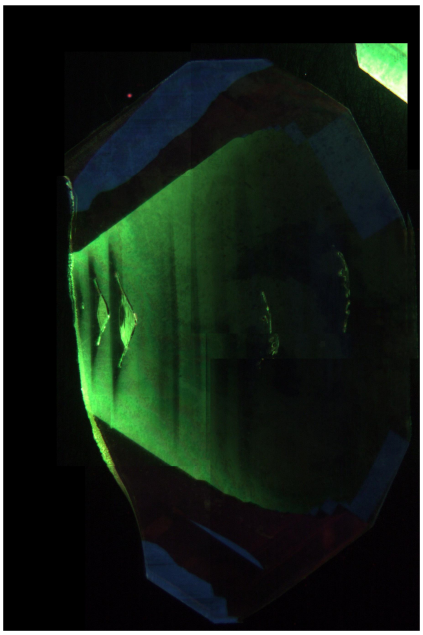

(b) *NL636-02.*

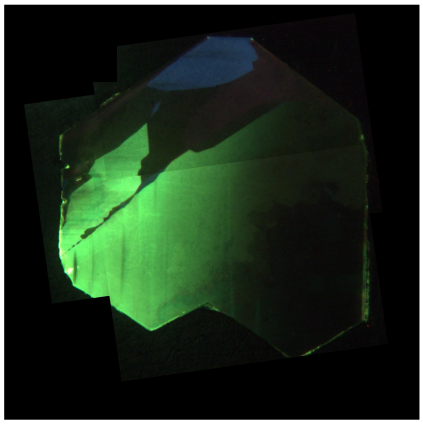

(c) *NL636-03.*

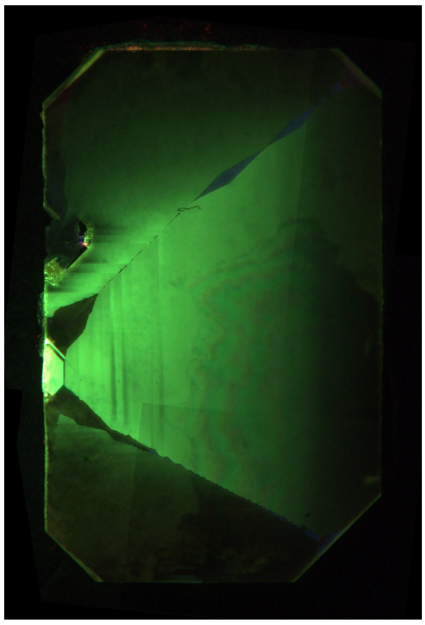

(d) *NL636-04.*

Figure 6.4: *True colour cathodoluminescence images of each diamond slice showing the different growth regions. These samples have the same layout as in figure 6.3, where the sectors are identified.*

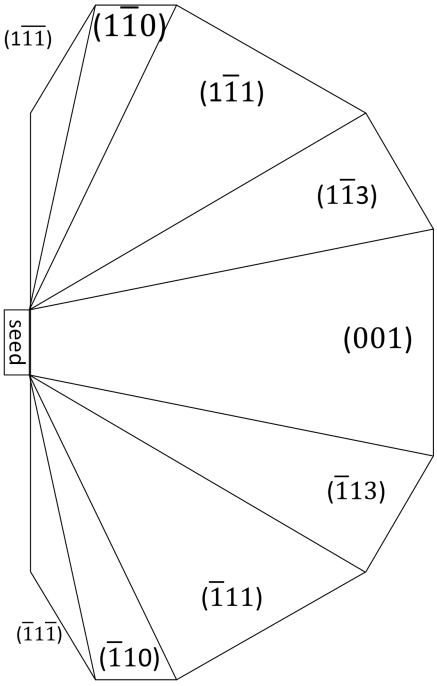

Figure 6.5: *Theoretical HPHT diamond growth morphology in a slice. Image reproduced from [157].*

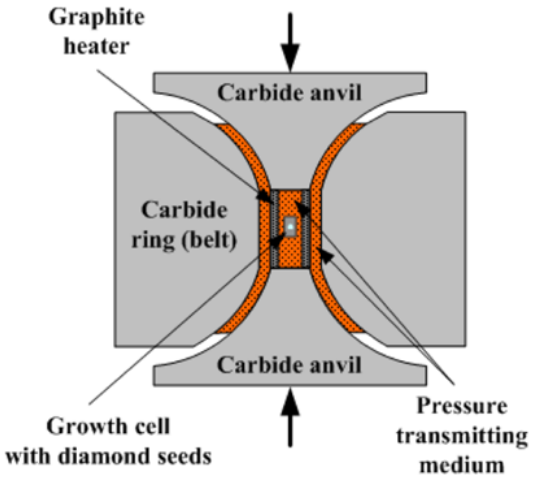

Figure 6.6: *Schematic of belt press used in HPHT fabrication of diamond [159].*

in MgO, are kept at a lower temperature than the source and solvent, usually between twenty and fifty degrees lower. Carbon is transported though the molten solvent to the seed diamond, by convection currents and concentration gradients [30]. When the carbon in the solvent becomes supersaturated carbon begins to precipitate out at the diamond seed as this is the lower temperature region, growing the diamond. The flux of carbon, towards the seed, is determined by the temperature gradient. The gradient along with the temperature determines the growing speed of the diamond, the morphology and impurity uptake [160]. The impurities which are trapped in the diamond are characteristic of the impurities in the melt when that part of the diamond formed. Impurity adsorption and desorption onto the growing diamond surface also affect the growth speed [158].

During growth carbon precipitating out of the melt will form the growing diamond. As carbon precipitates out of the solvent the carbon source will dissolve into the solvent. The isotopic enrichment of the melt around the diamond will determine the enrichment of the diamond.

The carbon source can be amorphous carbon or graphite and the nature of the source affects the dissolving speed of the carbon. Graphite is made of atomicly thick layers of carbon atoms which increases the dissolving speed as the metal atoms of the solvent can easily enter between the layers. Amorphous carbon dissolves more slowly as it does not have a regular crystal structure. The choice of source will have an effect on the speed carbon reaches the growing diamond. In this work the ^{13}C enriched source was amorphous carbon and the natural abundance source was graphite. The differing ^{13}C concentrations in each of the carbon sources for each sample was made up by mixing varying amounts of the ^{12}C and ^{13}C sources. Using two different types of sources meant that their impurity concentration, specifically nitrogen, may not be the same. This may lead to different impurity concentrations in the growth media and hence the resulting diamond.

Nitrogen Incorporation

Diamond has a rigid, high density lattice which makes larger atoms less likely to fit; the most common impurity in HPHT diamond is nitrogen [149]. As nitrogen is present in the atmosphere, it is incorporated from many sources including the solvent, the carbon source and the capsule

HPHT synthesised diamonds are generally type I which have nitrogen as the most

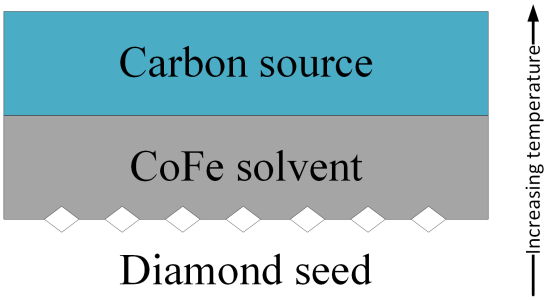

Figure 6.7: *HPHT growing capsule showing the carbon source and the solvent (which also contained carbon). The source and the solvent were both enriched, in differing amounts, to increase the ^{13}C content above that of natural abundance.*

common impurity. This can be in the form of substitutional atoms (type Ib) or as nitrogen pairs (type IaA) or higher order aggregates (type IaB). Both type Ib and IaB (if the aggregates form N_4V) forms of nitrogen create a yellow or brown colour in the diamond (which is the case for the diamonds discussed in this chapter, see figure 6.3). Type IaA diamonds are generally colourless as nitrogen pairs do not absorb in the visible spectrum. Nitrogen aggregates are more likely if the diamond is heated at a higher temperature or for longer. Nitrogen atoms become mobile in the diamond lattice at 1700°C and at this temperature will form pairs and higher order aggregates [161]. As the samples studied here were grown below 1500°C, it is likely the majority of nitrogen is single substitutional [135].

The concentration of nitrogen is typically between 100 and 300 ppm in HPHT diamonds and the incorporation depends on the growth sector and the growth speed [23]. A slower growth speed and a lower temperature will increase the nitrogen incorporation [23]. Nitrogen is highest in the {1 1 1} sector, the {1 0 0} sector has half as much and the {1 1 0} and {1 1 3} sectors have an order of magnitude lower concentration [23]. This is demonstrated graphically by a Kanda diagram in figure 6.8.

Extended Defects

As well as point defects, extended defects are also present in HPHT grown diamonds. These include dislocations, stacking faults and microtwins. Dislocations are more likely in {1 1 1} sectors and near inclusions, which are sources of strain. The balance between stacking faults and dislocations is determined by the growth rate. A high growth rate favours dislocations and a low one favours stacking faults [23].

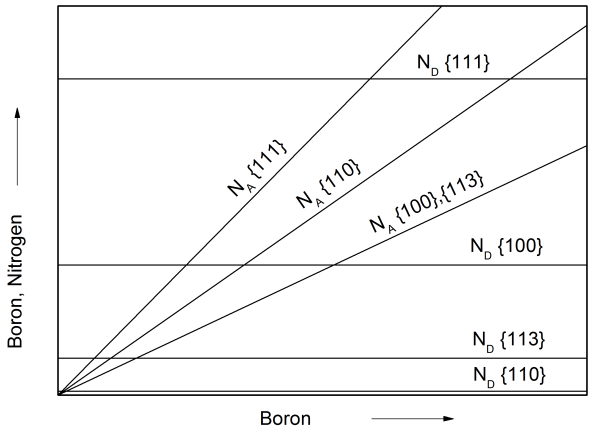

Figure 6.8: *An updated Kanda diagram showing the relative concentration of nitrogen (N_D) in different regions and the relative concentration of boron (N_A) in different regions. Data from reference [162].*

Morphology

The morphology of HPHT diamonds depends on the growth temperature [23, 160]. A lower temperature, and hence a lower growth rate, will results in a cubic diamond and a higher temperature, and hence faster growth rate, will result in an octahedral diamond. As the growth rate decreases the minor faces {1 1 0}, {1 1 3}, {1 1 5} and {1 1 7}, amongst others, increase in growth relative to the major faces [30]. The more prominent faces present are those that have grown most slowly. So slower growth results in a cubic diamond, as the minor faces have grown more quickly and hence only the major faces remain. At a higher growth rate the major faces will grow faster resulting in an octahedral diamond. The morphology is also affected by the nitrogen concentration and nitrogen getters used to reduce nitrogen concentration. Use of nitrogen getters increases the minor faces but these were not used for the samples discussed here. The absorption and desorption of impurities on to the surface also effects the shape [23].

Details of Growth for NL636 Samples

The NL636 set of samples was grown using the temperature gradient method with different concentrations of ^{13}C in the source and solvent. The concentrations used are shown in table 6.1.

Sample name	^{13}C in solvent (%)	^{13}C in source (%)
NL636-01	1.00±0.10	1.00±0.10
NL636-02	1.05±0.10	4.00±0.20
NL636-03	5.59±0.28	5.77±0.29
NL636-04	5.59±0.28	11.57±0.58

Table 6.1: *^{13}C concentrations in solvent and source prior to diamond growth as measured by SIMS by the supplier.*

These isotopic concentrations were made by mixing graphitic ^{12}C and amorphous ^{13}C in different quantities for the source and adding another, separate, mixture to the solvent. The errors are related to the measuring and mixing process.

It is expected that the different samples will have different distributions of ^{13}C uptake as the solvent and source are differently doped. For example in NL636-01 and 03 the solvent and the source have similar doping, hence it is likely that the doping will also be uniform across the diamond. In samples NL636-02 and 04 the source and solvent have very different doping and hence the environment around the diamond changes as they mix, resulting in different ^{13}C concentrations across the samples.

The diamonds all have different morphologies, see figure 6.1, this indicates they were grown at different temperatures. With sample NL636-01 the hottest, hence the large minor faces {1 1 3} and {1 1 0}, and sample NL636-04 the coldest, hence the large {0 0 1}. The solvent used was CoFe, and this may be the content of the inclusions, starred, in sample NL636-01. The diamonds were grown from a carbon source approximately twenty five percent of which was used up in the growth process. A significant fraction of the source was used, which means the composition of the diamond environment changed during growth. The growth took 78 hours.

Sample NL636-04 has been cut differently to the others, this occurred because of it's different shape (cubic) compared to the other samples (cubo-octahedral). A {1 1 0} slice was taken instead of a {1 1 1} slice. Hence different sectors can be seen in the slice (see figure 6.3d).

The difference between NL636-04 and the other samples can be seen by looking at figure 6.3d. The single substitutional nitrogen, as determined by looking at the yellow colour of the diamond which is lowest in what was thought to be the {1 1 1}

type sectors. This is not what is expected, nitrogen take up is usually highest in these sectors, as discussed previously; this can also be seen in the other samples. This indicated that it was not a {1 1 1} but a {1 0 1} instead, as labelled in the image. This difference arose due to the growth temperature difference between the samples, which resulted in a different crystal shape. The difference in growth temperature may also have an effect on the uptake of ^{13}C and nitrogen in the different samples.

The differences between sample NL636-04 and the other samples can be clearly seen in the CL images (see figure 6.4). All samples are green in the (001) sector but samples NL636-01, 02 and 03 are are blue and black in the other sectors, while sample NL636-04 is green in the other sectors. Despite this difference in cutting the results are still comparable, as the sectors have been correctly identified.

6.3 Experimental Techniques

6.3.1 Raman Spectroscopy

Raman spectroscopy was selected as it gives information about the ratio of ^{13}C to ^{12}C in diamond. As discussed in the introduction the phonon mean-free path is effected by scattering points such as isotopes, impurities, dislocations and grain boundaries. Raman scattering involves interaction between laser light and phonons; the Raman line changes can hence give information about the quantities of scattering points in a sample. Previous work has showed that increasing the ^{13}C enrichment decreased the Raman line position; it changes from 1332.9 cm^{-1} for isotopically pure ^{12}C diamond to 1281.2 cm^{-1} for pure isotopically pure ^{13}C diamond [163]. The relationship is roughly linear but exhibits a bowing effect, due to scattering caused by isotropic disorder, an effect also seen in some other alloys [164]. This effect was predicted by Hass et al. using coherent-potential approximation (CPA) [165].

The full width half maximum (FWHM) of the Raman line is affected by disorder in the lattice. A mixture of two different carbon isotopes creates disorder so causes Raman line broadening [165, 164]. This effect has been studied previously by Hass et al. and seen to have an an-harmonic relationship [165].

The spectrometer used was a Renishaw inVia Reflex Raman Microscope with a

442 nm HeCd laser with approximately 10 mW power at the sample. The grating used was a 3600 l/mm with a 50x objective with an NA=0.75 and a slit width of 20 μm. This set up was chosen as it gives high resolution Raman spectra. The spacial resolution is 200 μm^2 and the spectral resolution is 0.8 cm^{-1}. All Raman measurements were taken at room temperature.

The Raman peaks which were measured were fit to a Voigt function using a program written in Matlab. This allowed the peak position and full width half maximum to be extracted reliably.

For more details about the Raman technique see section 4.3.3.

6.3.2 Reference Calibration

In the Raman investigation, it was imperative to know the exact position of the Raman line. When calibrating a Raman spectrometer, the calibration is usually done to the Raman line in silicon [166]. The Raman line of natural abundance silicon is at 520.5 cm^{-1} whereas the Raman line in natural abundance diamond is at 1332.5 cm^{-1}. Due to imperfections in the system, including the non-linearity of the spectrometer, the calibration at these two frequencies may be different. To avoid this potential issue a natural diamond with a natural abundance of ^{13}C was compared to the literature value and the spectrometer was calibrated to this diamond.

Effect of Nitrogen on Raman Line Position

To establish if the effect of nitrogen on the Raman line position will be significant the relative concentrations of nitrogen and ^{13}C can be considered. The nitrogen concentration of a diamond will have an effect on the Raman line position for the same reason ^{13}C has an effect; they both interrupt the periodicity of the lattice and reduce the mean-free path of phonons. Consider a 300 ppm nitrogen containing diamond with a natural abundance of ^{13}C atoms. The number of ^{13}C atoms present are 34 times that of the number of nitrogen atoms. Nitrogen is next to carbon on the periodic table so their atomic masses are very similar. Nitrogen has the same number of neutrons as ^{13}C and one extra proton. When studying diamond samples of differing nitrogen concentrations within the range of HPHT diamonds, the effect on the Raman line position is smaller than the resolution of

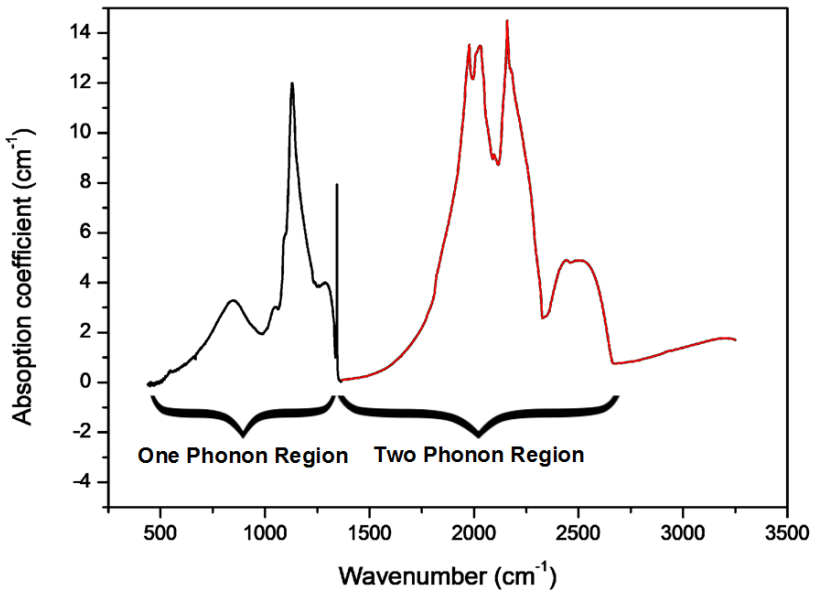

Figure 6.9: *Example infrared absorption spectrum of a reference sample with a concentration of 220 ppm of single substitutional nitrogen.*

the spectrometer. Thus the nitrogen has been assumed to have no effect on the measured Raman line position.

6.3.3 Infrared Absorption

FTIR absorption measurements were done at De Beers in Maidenhead using a ThermoFisher Nicolet iN 10 MX Infrared Imaging Microscope. The spectral resolution was 1 cm^{-1}. The aperture, pixel size and step size for line scans was 150 μm.

IR absorption measures the absorption of light in the IR range of a sample. Absorption at different energies gives information about the species that are present in the diamond. These include different types of nitrogen; in the form of A-centres (two nitrogen atoms and a vacancy) and single substitutional.

Absorption of these diamonds was normalised to path length and compared to a reference spectrum with known concentration in order to quantify the concentration of the different forms of nitrogen.

In figure 6.9 an example of an IR spectrum of a type IIa diamond can be seen.

The two phonon region is between 1332 and 2665 cm^{-1}. Absorption in this region is created by the intrinsic diamond lattice, uninterrupted by impurities [127]. Due to diamond's inversion symmetry single phonons do not interact with radiation so there is no absorption in the one phonon region by pure diamond. At least two phonons are required for absorption. One phonon reduces the symmetry of the lattice by introducing a net charge and a second vibrates the charge, causing a dipole with which radiation can interact. This can also occur with more than two phonons [127].

The one phonon region is below 1332 cm^{-1}. Absorption in this region is created by impurities which disrupt the diamond lattice and create dipoles [127]. For the example shown in figure 6.9 the one phonon region absorption is created by single substitutional nitrogen. This spectra is representative of what was seen for the four diamonds in this study; the main impurity was single substitutional nitrogen.

6.3.4 SIMS

For more details of the specifics of the SIMS system used please refer to Chapter 4.

SIMS is a destructive technique which uses a beam of ions to etch a sample's surface. The removed atoms are then accelerated through a mass spectrometer which determines which species were present in the sample. Different ions are chosen depending on the species being investigated. When measuring an isotope, such as ^{13}C, a ratio is usually taken to another isotope, in this case ^{12}C. These were compared to the ratios in a diamond with a natural abundance of ^{13}C. Delta ^{13}C was then calculated using equation 6.1. Delta ^{13}C has units of $^{0}/_{00}$.

$$\delta^{13}C = \left(\frac{\left(\frac{^{13}C}{^{12}C}\right)_{sample}}{\left(\frac{^{13}C}{^{12}C}\right)_{standard}} - 1 \right) \times 1000 \ {}^{0}/_{00} \tag{6.1}$$

The SIMS measurements were performed at between ten and twelve evenly spaced points on each sample, from close to the seed to the final growth surface. In figure 6.10 the holder used in SIMS can be seen containing the four samples and the reference diamond. The samples were pressed into indium and gold coated, to ensure good electrical conduction of the sample surface in order to ensure charging of the surface did not occur and the whole surface was grounded.

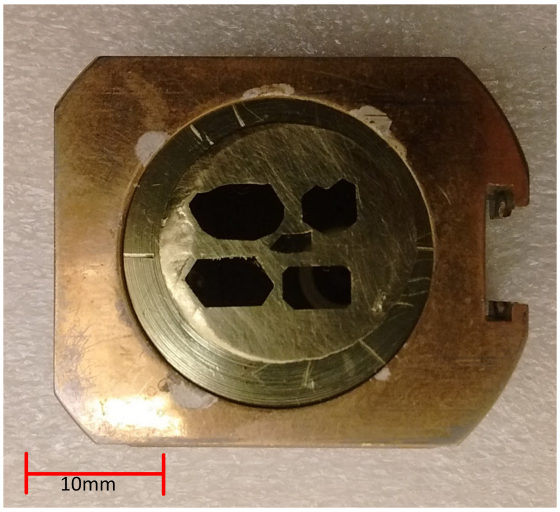

Figure 6.10: *SIMS sample holder with polished samples pressed in indium. Indium is usually used for diamond due to its low carbon and hydrogen contamination. It is a soft metal which allows the samples to be retrieved without damage at the end of the SIMS process. Three full slices and one broken one can be seen. The small diamond in the centre is the natural reference diamond.*

6.4 Results and Analysis

6.4.1 Raman Spectroscopy

The first method employed to investigate the ^{13}C concentration was Raman spectroscopy. Figure 6.11a shows the average Raman line position of each sample, plotted against the nominal ^{13}C abundance, obtained from an average of the source and solvent concentration shown in table 6.1.

As discussed in the experimental details section, Raman line shows a strong dependence on the ^{13}C concentration. Previous work by Hass et al. [165] has investigated this relationship. In figures 6.11a and 6.11b the position and the FWHM of the samples are compared to the data taken by Hass et al. For the sample set NL636 as the samples showed variation across their surface an average value was taken. The position of the Raman line is in agreement with the nominal concentration of the samples. The FWHM is smaller than the FWHM of the Hass samples.

A selection of samples made by General Electric (GE) were also investigated (labelled on figure 6.11b and 6.11a). These also showed good agreement with the data from Hass et al. and because the samples used by Hass et al. were also GE samples agreement of the data is expected. This result demonstrated that the

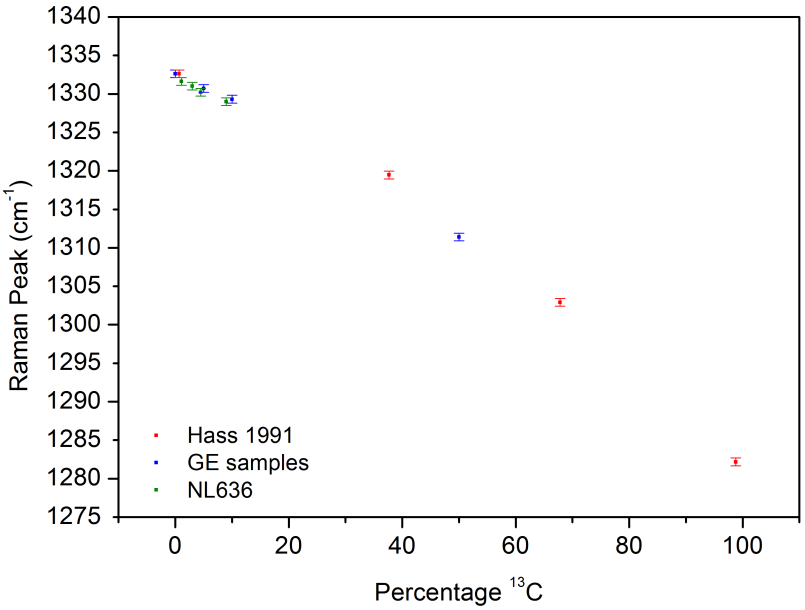

(a) *The average Raman line position versus nominal concentration of the ^{13}C enriched samples compared to some General Electric diamonds of known ^{13}C concentration and to data published by Hass et al. [165].*

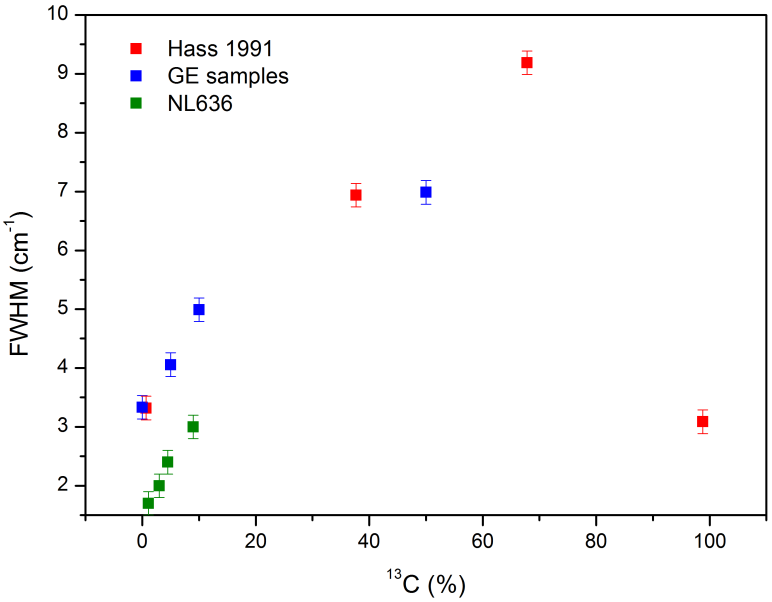

(b) *The average full width half maximum of the ^{13}C enriched samples compared to some General Electric (GE) diamonds of known ^{13}C concentration and to data published by Hass et al. [165].*

Figure 6.11: *Raman line characteristics compared between the NL636, General Electric (GE) and Hass et al. sets of samples.*

experimental method was working as expected.

The Raman line was different between samples and was also different within samples. These data is presented in table 6.2. Figure 6.12 shows the difference in Raman line position for sample NL636-04 when comparing the seed and the growth surface. This figure also shows the fitting of the line. A Voigt fit was used for each line, from which the FWHM and the line centre could be calculated. Figure 6.13 shows the change in Raman line position from the seed to the growth surface for all the samples. This change was taken relative to a GE natural abundance sample. It should be noted that sample NL636-02 Raman line position change has a steeper gradient than sample NL636-03. All samples exhibited a decrease in the Raman frequency away from the seed except the diamond with a natural abundance of ^{13}C (sample NL636-01). This trend showed that the ^{13}C concentration increased from the seed to the growth surface, which may be related to the uptake of ^{13}C during the HPHT growth process.

Sample name	Raman line at seed	Raman line at growth	Error
NL636-01	1332.4 cm^{-1}	1332.4 cm^{-1}	$\pm$0.1 cm^{-1}
NL636-02	1332.2 cm^{-1}	1331.6 cm^{-1}	$\pm$0.1 cm^{-1}
NL636-03	1331.1 cm^{-1}	1330.8 cm^{-1}	$\pm$0.1 cm^{-1}
NL636-04	1330.6 cm^{-1}	1329.2 cm^{-1}	$\pm$0.1 cm^{-1}

Table 6.2: *Raman line positions at the seed surface and the final growth surface.*

The isotopic enrichment has the effect of increasing the FWHM and decreasing the Raman line frequency. For sample NL636-03 a flat region can be seen before the Raman line begins to decrease (see figure 6.13). The CL image indicated that the plateau is not caused by measuring the seed (see figure 6.4).

The ^{13}C concentrations which relate to these Raman line positions can be calculated by comparing them to samples of known concentration. In this case GE samples were used. As shown in figure 6.14, the equation of the line of best fit to the data points was used to calculate the corresponding ^{13}C concentration for the Raman frequency at the seed and growth surface of each sample. These concentrations are shown in table 6.3. It can be seen that despite the averages being close to the nominal concentrations there are large variations within each sample except NL636-01. This approximation to a linear fit is not entirely accurate. There is an an-harmonic effect which is most evident at a 50:50 ratio. This effect is smaller

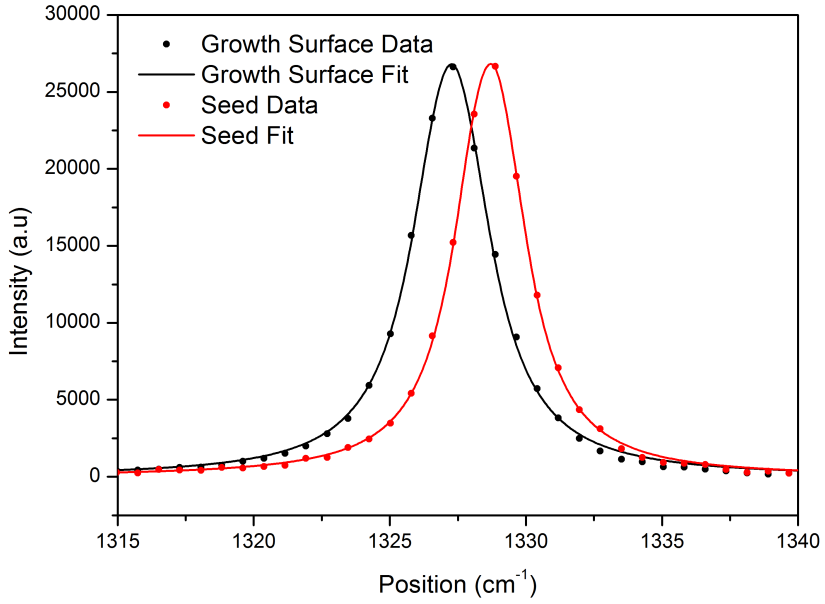

Figure 6.12: *Raman line at the seed and at the growth surface for sample NL636-04. This shows the data points and the Voigt fit which was used to calculate the FWHM and the peak position.*

when a diamond is nearly all ^{12}C or nearly all ^{13}C so has not been taken into account in this fitting as the diamonds being studied are predominantly ^{12}C.

Sample name	^{13}C seed (%)	^{13}C growth (%)	Error (%)
NL636-01	1.1	1.1	±0.5
NL636-02	2.2	3.7	±0.5
NL636-03	4.8	5.5	±0.5
NL636-04	5.9	9.2	±0.5

Table 6.3: *^{13}C concentrations at the seed surface and the growth surface measured by Raman.*

Consider figure 6.16, this shows the Raman frequency across different sectors of the two highest concentration diamonds. It can be seen that the decrease in Raman frequency is not unique to the {0 0 1} sector, it also happens in all other regions.

Comparisons of the FWHM can be seen compared to other samples in figure 6.11b and within each sample in figure 6.15. The FWHM of the Raman line is especially sensitive to impurities and the disorder of the sample. The addition of the ^{13}C isotope increases the disorder and hence broadens the Raman line. Defects

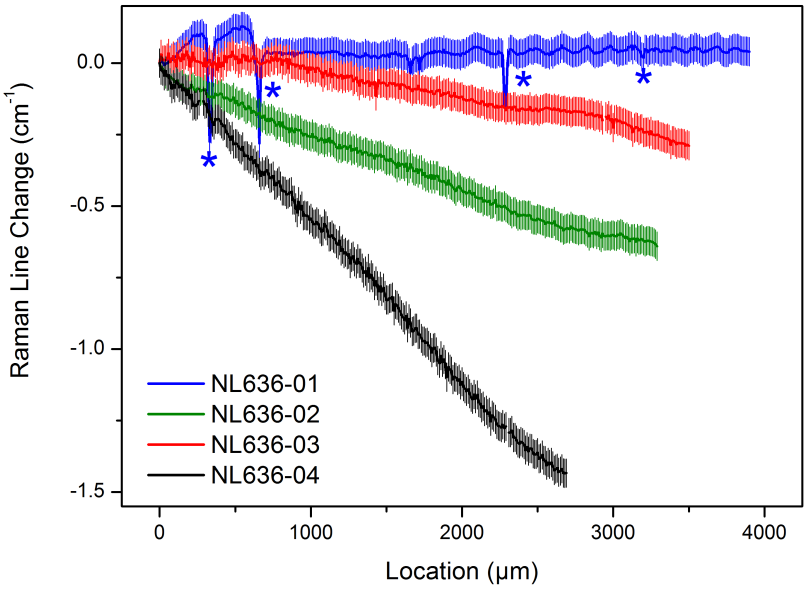

Figure 6.13: *Raman line change from the seed in each diamond as a function of distance from seed in the (001) plane. In sample NL636-01 sharp changes can be seen in the Raman line position at four different starred points. These are due to inclusions, which can be seen, also starred, in figure 6.3. Each point has a line to indicate the error in the measurement. The average ^{13}C concentrations are as given: NL636-01 (1.1%), NL636-02 (2.5%), NL636-03 (5.6%), NL636-04 (9.0%).*

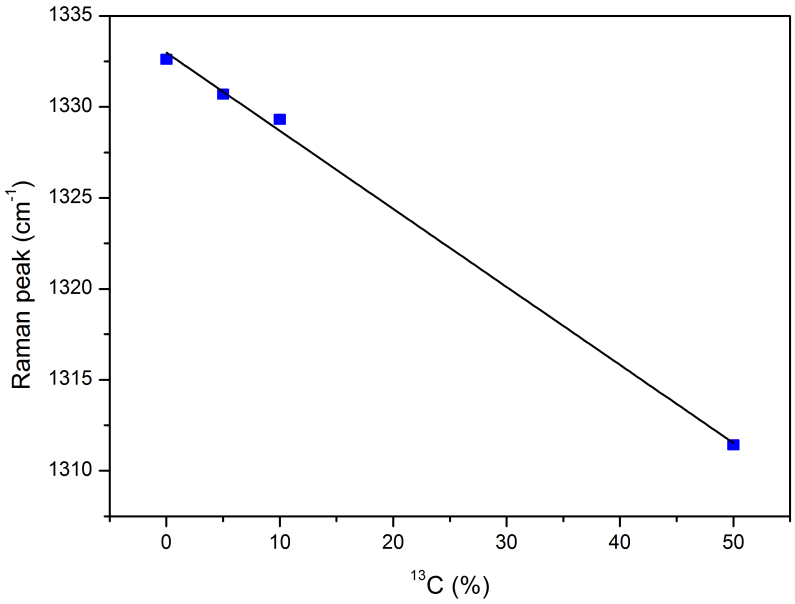

Figure 6.14: *GE samples' Raman line plotted against ^{13}C percentage with a line of best fit. Error bars are not shown as the they are smaller than the data points.*

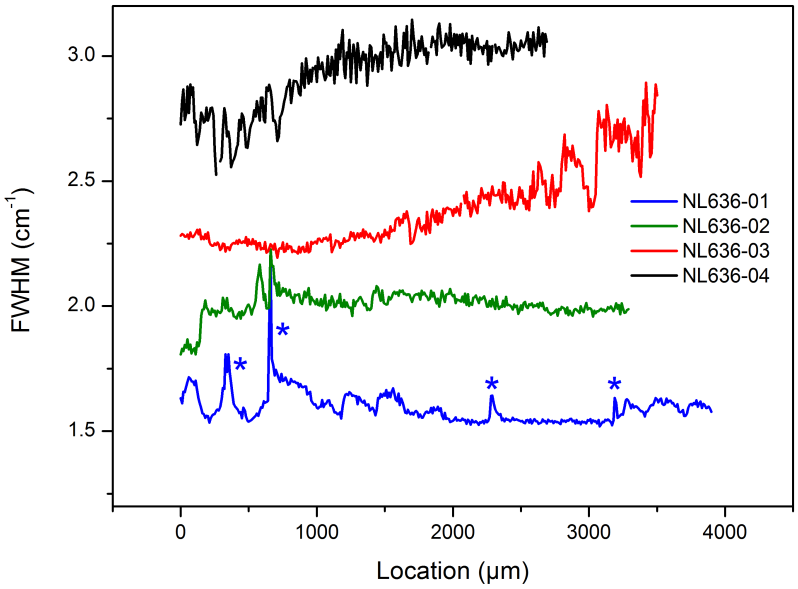

Figure 6.15: *FWHM across each sample, starting from the seed. The blue stars indicate the position of the inclusions, which can be seen in the optical image. The samples show an increase in the FWHM from the seed to the final growth surface, except the natural abundance one, which is consistent with the increase in ^{13}C in each sample. These measurements were taken with a 442 nm laser with a 3600 l/mm grating and a slit width of 20 μm. This resulted in a resolution of less than 1 cm^{-1}, hence these results are not instrument limited. The average ^{13}C concentrations are as given: NL636-01 (1.1%), NL636-02 (2.5%), NL636-03 (5.6%), NL636-04 (9.0%).*

and other impurities also have an effect. From the Raman line width it appears the NL636 samples contain less disorder than the Hass and GE samples. The difference between the NL636 suite and the GE samples is not an experimental artefact as these data were taken using an identical experimental set-up. Raman line broadening may have occurred in the Hass samples due to disorder present. This disorder may be created by impurities or dislocations or another mechanism.

6.4.2 Infra-red Absorption

In order to measure the exact changes in nitrogen concentration IR mapping was used. By studying the IR absorption of the samples it is clear that the main defect is single substitutional nitrogen, and there is no evidence from the FTIR of larger aggregates. This means the samples are classified as type Ib.

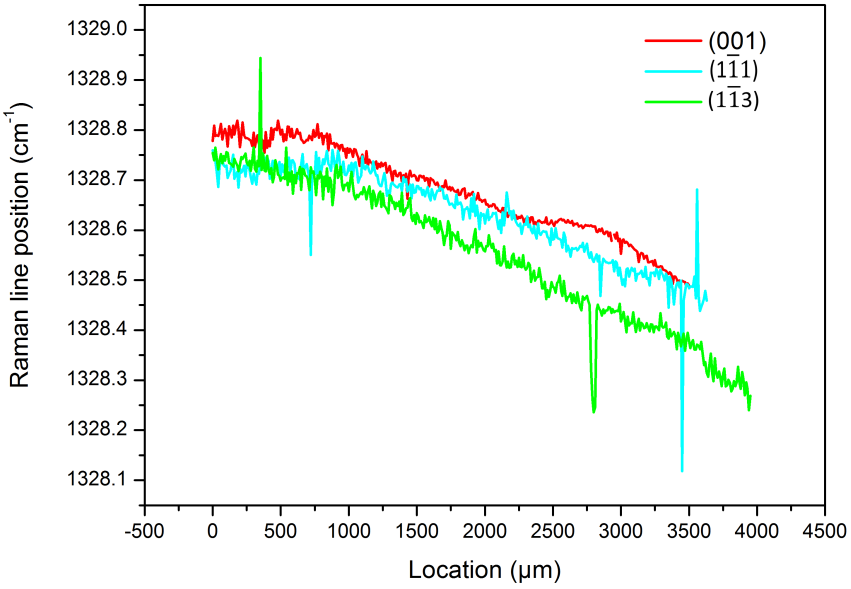

(a) *Raman line position in other sectors of NL636-03.*

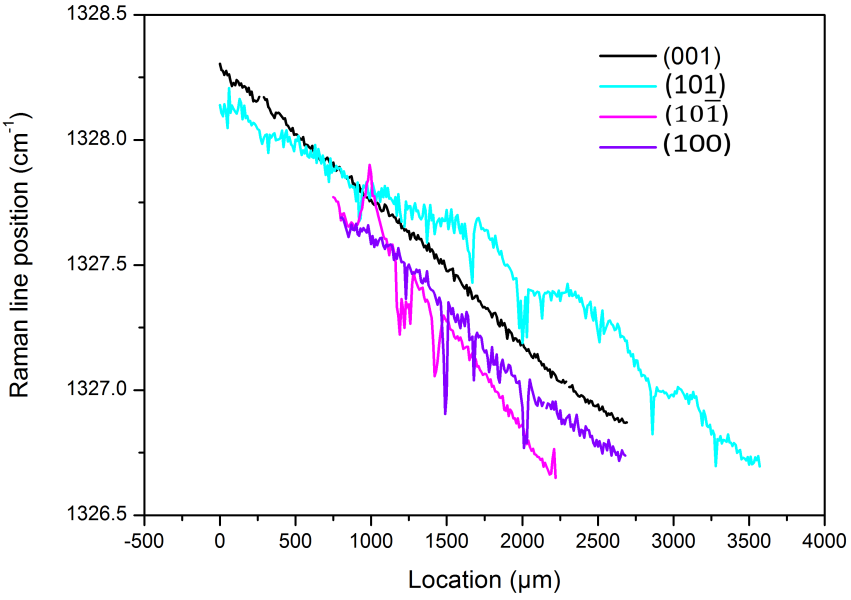

(b) *Raman line position in other sectors of NL636-04. The data for* $(1\,\bar{1}\,\bar{1})$ *and* $(1\,\bar{1}\,0)$ *start at a lower position because these line scans were taken slightly farther away from the seed to avoid the inclusion shown starred in figure 6.3d.*

Figure 6.16: *Raman line position in different sectors.*

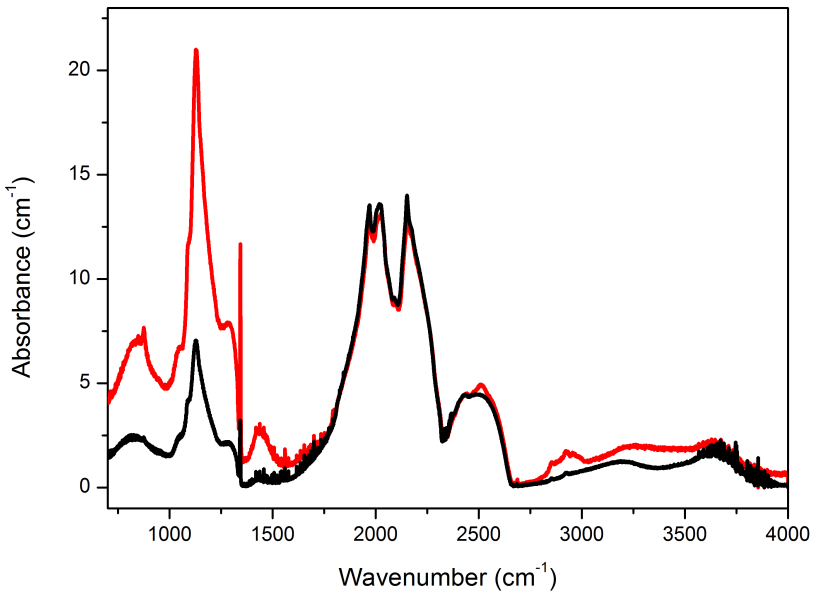

Figure 6.17: *Example of IR spectrum near the seed and near the growth surface of sample NL636-04 in the (001) sector. The first peak is due to single substitutional nitrogen. Fitting the curve from near the seed gives a nitrogen concentration of nitrogen to be 300 ppm ±10 ppm and at the growth surface this has reduced to 150 ppm ±10 ppm. The differences between the two spectra in the two phonon region are due to grease.*

The concentration of single substitutional nitrogen was very high (in the hundreds of ppm for all samples) and did change significantly between the seed and the growth surface. An example, for sample NL636-04, is shown in figure 6.17. In this sample the single substitutional nitrogen concentration halved from 300 ppm to 150 ppm between the seed and the growth surface. The plots of the different sample concentrations is shown in figure 6.18. This shows all isotopically enhanced samples have a high concentration of nitrogen near the seed, which reduces towards the growth surface.

This change may be due to the increasing volume of the diamond during growth. An increasing volume increases the surface area which is available to absorb the nitrogen. In order to calculated whether the total absorption of nitrogen was staying constant, just being absorbed over a larger surface area, the area and the concentration were multiplied for each point at which nitrogen was measured. The surface area of the growing diamond was modelled by making the assumption that the growing diamond was a cuboid which grew with the same ratio of dimensions as the final diamond. A plot of these results is shown in figure 6.19.

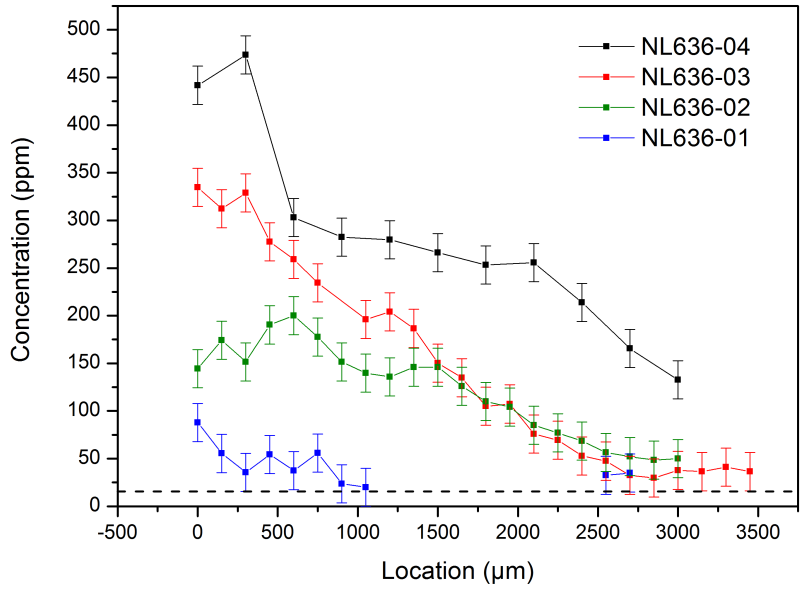

Figure 6.18: *Single substitutional nitrogen concentrations measured by IR absorption in the (001) sector of each sample. This figure shows a trend of decreasing nitrogen concentration across each sample, moving away from the seed, and a higher nitrogen concentration in the diamonds with higher ^{13}C concentration. The black dashed line indicates the detection limit. The average ^{13}C concentrations are as given: NL636-01 (1.1%), NL636-02 (2.5%), NL636-03 (5.6%), NL636-04 (9.0%).*

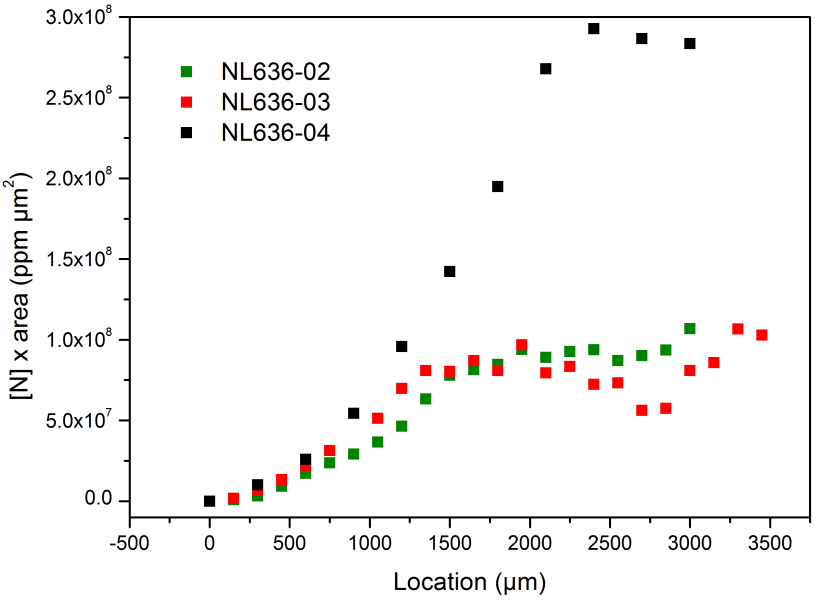

Figure 6.19: *Nitrogen concentration multiplied by surface area versus distance from seed. The average ^{13}C concentrations are as given: NL636-01 (1.1%), NL636-02 (2.5%), NL636-03 (5.6%), NL636-04 (9.0%).*

6.4.3 SIMS

For each sample between 10 and 12 evenly spaced measurements were taken. The most accurate measure of ^{13}C content is to compare the SIMS value to the SIMS value of a reference. This is called δ^{13}C and is calculated using equation 6.1. These data is shown in figure 6.20. It can be seen that the ^{13}C isotope concentration is changing. It is indeed higher at the growth surface than at the seed. This means that the Raman line changes correlated with the change of ^{13}C.

In table 6.4 the ^{13}C concentrations can be seen. These were calculated by comparing to the reference diamond.

Sample name	^{13}C seed (%)	^{13}C growth (%)	Error (%)
NL636-01	1.1	1.1	±0.5
NL636-02	1.8	3.5	±0.5
NL636-03	4.4	5.7	±0.5
NL636-04	5.6	10.4	±0.5

Table 6.4: *^{13}C concentrations at the seed surface and the growth surface as measured by SIMS.*

These numbers show good agreement, within error, to those calculated with the Raman line position. This can be seen graphically in figure 6.21. The Raman data in figure 6.13 can be interpolated to the same points at which the SIMS data was taken. This interpolated data can then be plotted against the SIMS data to calculate the relationship between the Raman line position and the SIMS concentration directly. This is plotted in figure 6.22. These data can be fitted to a linear equation to give the relationship shown in equation 6.2.

$$^{13}\text{C}\ \ (\%) = 2.61 \times (1332.9 - \text{Raman line position}) \pm 0.5 \tag{6.2}$$

The relationship has been assumed to be linear, which as discussed in section 6.3.1 is not the case, but is an adequate approximation over a short range of concentrations and the data taken here is not of a large enough range to model the full relationship. Additionally the intercept when ^{13}C (%) = 0 of the equation is in good agreement with the work by Banholzer et al. who report the Raman line position for isotopically pure ^{12}C to be 1332.9 cm^{-1} [163].

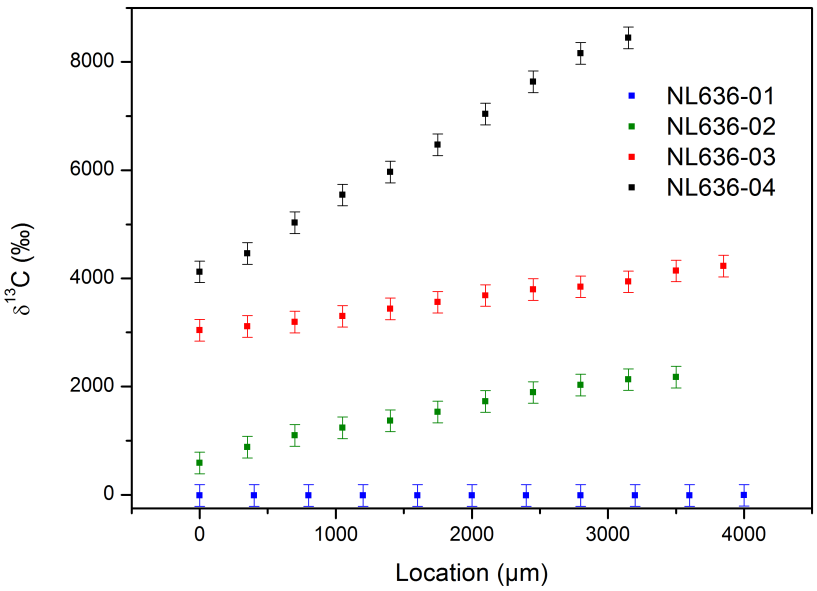

Figure 6.20: *$\delta^{13}C$ as a function of position away from the seed, as measured by SIMS in the (001) sector. The average ^{13}C concentrations are as given: NL636-01 (1.1%), NL636-02 (2.5%), NL636-03 (5.6%), NL636-04 (9.0%).*

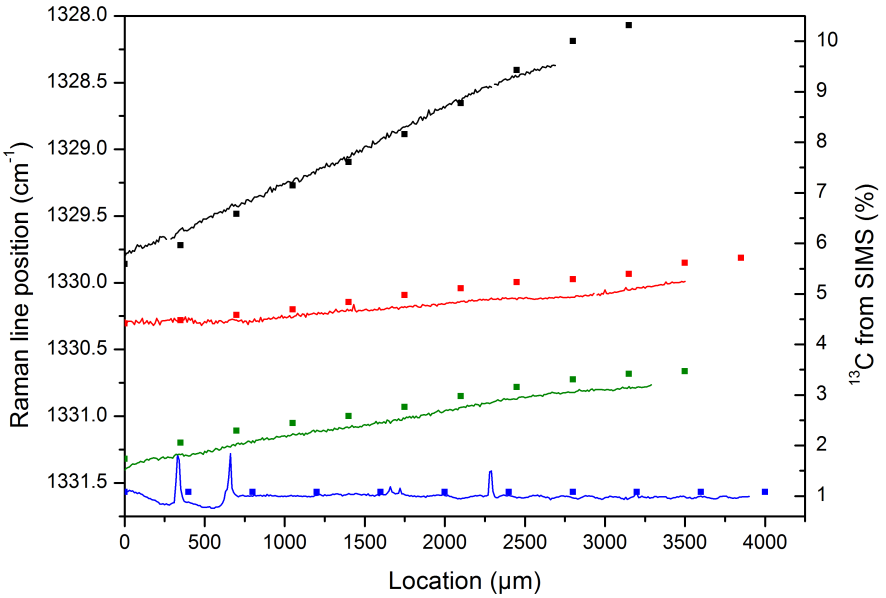

Figure 6.21: *Correlation between Raman line position change and the ^{13}C isotope concentration measured by SIMS. Blue squares and line are the Raman results and SIMS results respectively for sample NL636-01. Green in sample NL636-02, red is sample NL636-03 and black is sample NL636-04. Note: Raman line position is decreasing moving up the y-axis. The average ^{13}C concentrations are as given: NL636-01 (1.1%), NL636-02 (2.5%), NL636-03 (5.6%), NL636-04 (9.0%).*

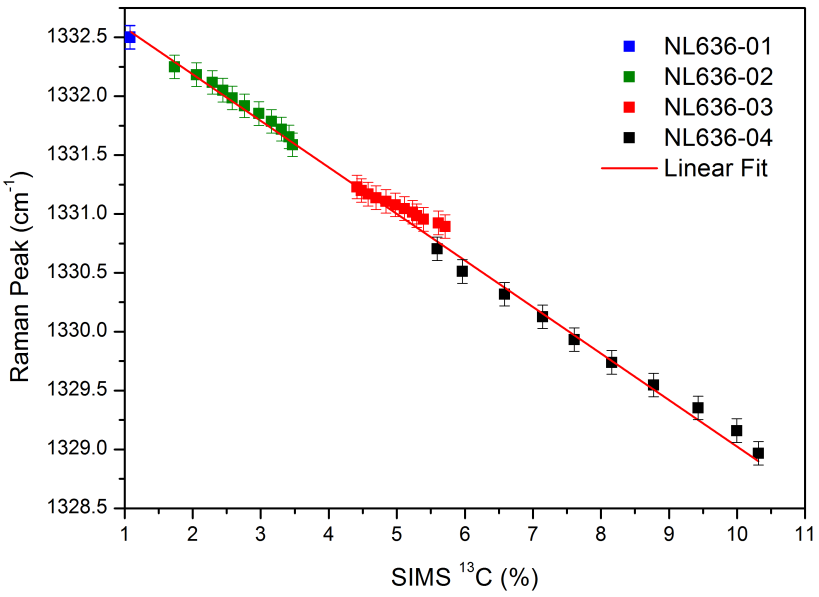

Figure 6.22: *^{13}C percentage measured by SIMS plotted versus interpolated Raman data also showing line of best fit used to calculate equation 6.2.*

The nitrogen concentration was also measured, see figure 6.23. The results confirm the trend of the results obtained by FTIR, the total nitrogen concentration is reducing away from the seed. However the SIMS results suggest a much larger total concentration of nitrogen, with measured concentrations reaching 1200 ppm.

6.5 Discussion

6.5.1 ^{13}C Concentration Changes

The Raman line position changes in each of the four diamonds, except sample NL636-01. These differences have arisen due to the different ^{13}C concentrations in the carbon source and metal solvent. They may also have occurred due to the different sources used for the ^{12}C and the ^{13}C and the resulting difference in dissolving rates.

The data presented in figure 6.13 shows each diamond has a different gradient of ^{13}C concentration as predicted by the Raman line. The natural abundance sample (NL636-01) shows no change in Raman line across the sample, and agrees with

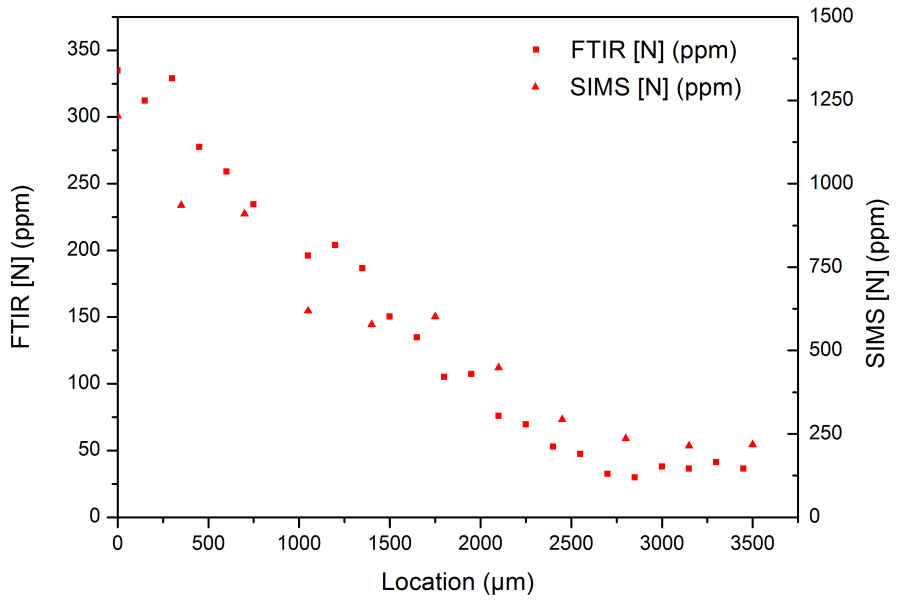

Figure 6.23: *Nitrogen concentration changes with distance from seed in sample NL636-03. Measured by SIMS and FTIR in the (001) sector.*

the position seen in natural samples. Sample NL636-03 shows a change in ^{13}C across the sample. This gradient may be less steep than for samples NL636-02 and NL636-04 because the source and the solvent contain almost the same ^{13}C content (within 0.2%). The concentrations of ^{13}C enrichment in the metal solvent and seed are detailed in table 6.1. However, the change across the sample of the measured ^{13}C concentration is 1.3%. This indicates the different forms of the ^{12}C and ^{13}C, graphitic and amorphous respectively, are having an effect due to the different dissolving rates. The ^{13}C enriched source will dissolve more slowly because it is amorphous rather than graphitic. This sample also shows a flat region before the gradient begins, this may have arisen from the slower incorporation into the melt of ^{13}C due to its amorphous, rather than graphitic, form. The steepest gradients are in samples NL636-02 and 04. These gradients may be due to the large difference in the ^{13}C concentration in the source and the solvent. For both, the carbon source has a significantly higher concentration of ^{13}C than the solvent. This indicates that the melt around the diamond is changing during the growth, as the concentration of ^{13}C enrichment at a particular point in a diamond is directly related to the concentration in the melt when that layer is formed [167].

The results obtained from the SIMS measurement of ^{13}C showed good agreement with those obtained from Raman. This ensured that measuring the Raman line

position was an accurate way of calculating the ^{13}C concentration. Additionally this allowed an equation to be calculated which links the Raman line position to the ^{13}C enrichment directly. The assumption has been made the Raman line changes linearly with ^{13}C enrichment; the equation is accurate over the 0% to 10% range.

6.5.2 Nitrogen Concentration Changes

The nitrogen concentration, as measured by FTIR, decreases across each sample, as shown in figure 6.18. The sample with the largest concentration of nitrogen is also the one with the largest concentration of ^{13}C; the amorphous ^{13}C may have a higher nitrogen contamination. However, across each sample the nitrogen concentration decreases whereas the ^{13}C concentration increases.

Figure 6.19 shows the nitrogen concentration multiplied by the surface area at each point during growth. This figure shows an increase in nitrogen uptake followed by a plateau. This may be the point at which an equilibrium is reached between the melt and the growing diamond.

These results quantified the decrease in nitrogen which was suspected from the colour of the samples. However, even given these high changes in nitrogen concentration, they are not large enough to cause a change in the Raman line position.

The SIMS results did not agree quantitatively with the concentration of nitrogen across the diamond studied although the results did indicate a fall in concentration. This discrepancy is likely to have arisen from the lack of a reference for measuring the nitrogen count rate. Normally, when SIMS is performed to measure the nitrogen concentration of a diamond, the count rate is compared to that of ^{12}C. However this was not possible with these samples as the ^{12}C concentration was also changing. As a result the nitrogen was measured by count rate alone and thus has been over estimated, by approximately 3.5 times.

Additionally other minor problems have previously been identified when measuring nitrogen using SIMS including leaks, contamination and surface impurities [168]. This is usually avoided by comparing the SIMS count rate to that of a diamond with a known nitrogen concentration [169], however this was not done on this occasion.

6.6 Conclusions

Four HPHT samples were studied which had different levels of ^{13}C enrichment. For each sample the source and solvent had been enriched to differing degrees. In the samples, the concentration of the ^{13}C isotope and nitrogen changed with position from the seed. The nitrogen concentration reduced away from the seed in all sectors. The ^{13}C concentration increased with distance from the seed in all sectors. The same behaviour was seen in the different sectors and samples despite different nitrogen concentrations. The samples with higher ^{13}C concentrations also had higher nitrogen concentrations which may have originated from ^{13}C source contamination. However, within each sample increasing ^{13}C was related to decreasing nitrogen.

These diamonds show a distinctive increase of ^{13}C moving away from the seed. Within error the Raman results and the SIMS results agree. There is not an increase in sample NL636-01, sample NL636-02 increases from 1.5% to 3.5%, sample NL636-03 increases from 4.4% to 5.7% and sample NL636-04 increases from 5.7% to 10.4%. This is indicative of changes in the melt during the HPHT process. An increase in ^{13}C was caused by the amorphous ^{13}C source slowly dissolving. The steeper gradients of the samples with different ^{13}C enrichment in the source and solvent also indicated that the carbon source mixes slowly with the solvent during growth.

The main findings of this chapter are:

- It has been demonstrated that a non-uniform ^{13}C enrichment is created when the source of ^{12}C and ^{13}C are in different forms, in this work graphitic and amorphous.
- It has been demonstrated that, due to slow mixing of the carbon source with the solvent, a gradient of ^{13}C enrichment will be created if the source and solvent are differently ^{13}C enriched.
- An equation has been calculated which links the Raman line position to the ^{13}C enrichment, in the 0% to 10% region, shown below.

$$^{13}C\ (\%) = 2.61 \times (1332.9 - \text{Raman line position}) \pm 0.5 \tag{6.3}$$

Further work is required for isotopic enhancement of HPHT synthesised diamonds

before they are of device quality. Large scale manufacturing of devices requires isotopic uniformity, and the samples investigated here do not display this. Improvements could be made by ensuring the ^{12}C and ^{13}C source are of the same form, either graphitic or amorphous. Additionally, the same isotopic enrichment is required for the solvent and the carbon source.

Chapter 7

Heteroepitaxial Samples

7.1 Introduction and Objectives

An interesting new way to make single crystal diamond is heteroepitaxial chemical vapour deposition (CVD) on a lattice matched silicon substrate. The first CVD growth was onto non-diamond substrates but this created polycrystalline diamond [170]. Heteroepitaxial growth is a technique commonly used in industry for gallium nitride grown on a silicon carbide seed [23]. The huge advantage of the heteroepitaxial method for diamonds is that the substrate used can be larger and significantly less expensive than for traditional homoepitaxial CVD. The main issue with the method is lattice mismatch which may result in highly defective single crystal or polycrystalline diamond.

Many applications of diamond make use of its unique properties including: high thermal conductivity, high carrier mobility and high breakdown field. These properties are all diminished by the grain boundaries present in polycrystalline diamond, hence there is a large incentive to make commercially affordable single crystal diamond. A method by which large single crystal diamond could be grown on lattice matched silicon substrates could prove very advantageous in the future and may create many new commercial possibilities.

In this chapter new single crystal heteroepitaxial samples were studied with the aim of identifying the differences between this material and homoepitaxial CVD diamonds. Additionally, the material was investigated to understand the possibility of making devices for commercial applications. Due to the different strain

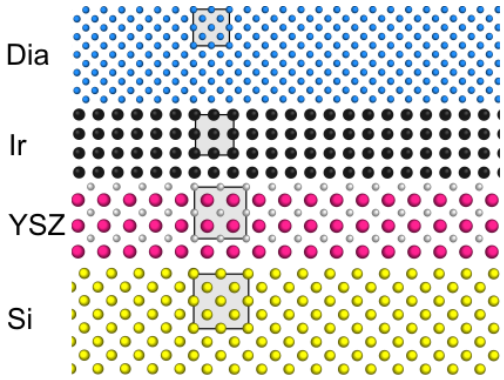

Figure 7.1: *Substrate used for heteroepitaxy growth showing lattice constant matching. Starting with silicon, then yttria-stabilised zirconia, then iridium and finally diamond. The mismatch at each layer is 5.39%, 25.4% and 7.19% starting from the bottom. Image from [171].*

environment arising from the lattice mismatch, point defects and extended defects may be present in differing quantities to homoepitaxial CVD. Two different samples were studied; one 'intrinsic' and one 'nitrogen doped'. These were investigated with a variety of different techniques, including electron paramagnetic resonance and fluorescence imaging.

7.2 The Material

The diamonds discussed in this chapter were made by heteroepitaxial CVD by Augsburg Diamond Technology (Audiatec). Audiatec has developed a substrate which allows single crystal diamond to be grown using this technique [171, 172]. The lattice mismatch is reduced by layering different substances onto a silicon wafer [171]. The first layer on the silicon wafer is yttria-stabilised zirconia (YSZ) and is formed using pulsed laser deposition and is only ∼20 nm thick. The next layer is iridium and is formed using electron beam deposition and is ∼150 nm thick. The diamond layer is formed by microwave plasma CVD onto a {0 0 1} surface. The CVD substrate used is shown in figure 7.1. The choice of material on which to grow diamond is limited by the harsh growing conditions of the CVD reactor. Iridium alone may be a better substrate but is very expensive to produce so silicon wafers are used which are coated with iridium [173]. Silicon wafers can be up to 450 mm in diameter [174]. Silicon has a similar thermal expansion coefficient to diamond so there is less thermal stress after the cool down after growth [175].

The lattice mismatch between iridium and diamond is large, ∼7.19%, and this

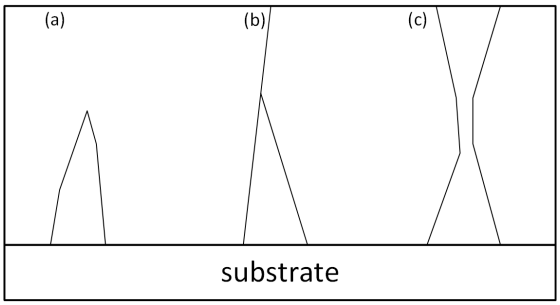

Figure 7.2: *Dislocation interactions. (a) annihilation, (b) addition and (c) scattering. Image recreated from [179].*

creates very defective diamond. The nucleation on the substrate is performed using Bias Enhanced Nucleation (BEN); a technique in which the substrate is put under a negative potential. This creates a localised region of higher field strength above the surface, attracting positive ions, and causes nucleation [176]. The nucleation growth takes approximately twenty minutes and the experimental conditions used are as follows: -250 V, 700°C, 3000 Pa. Once nucleation has occurred the bias is removed. During nucleation domains form of highly defective diamond which grow laterally not vertically. The nucleation of diamond is non-classical and not entirely understood [171] as, if the nucleation conditions are maintained for more than around twenty minutes, the diamond nuclei are etched.

The composition for CVD growth is a mixture of carbon, hydrogen and oxygen. The addition of nitrogen (the order of ppm) gives an order of magnitude higher growth rate [177].

Once the nucleation sites begin to grow a mosaic of single crystal domains form. As the diamond grows further the grain boundaries become dislocation bands. These dislocations have been studied by Schreck et al. using etch pit formation [178]. These dislocations are edge or screw dislocations or a mixture of both [179]. The distortion in the core of the dislocation creates a pit when the surface is etched. The dislocation density is seen to reduce as the distance from the nucleation surface increases. This is due to the interaction between the dislocations. Near the nucleation surface the dislocations are on average ∼10 nm apart. Interactions take the form of annihilation, addition or scattering; if the two dislocations have anti-parallel Burger's vectors they will annihilate otherwise they will add or scatter [178]. These three scenarios are seen in figure 7.2. After ∼1 mm of growth the density of dislocations decreases significantly, and thus the remaining dislocations are less likely to interact.

Device quality is affected by a high dislocation density: including degradation of the electronic properties such as the breakdown field and carrier mobility. However, the internal stresses within the material which the dislocations create may have some potential uses such as strengthening devices using internal compressive stress [179].

7.2.1 The Samples

Two samples were investigated. One was an intrinsic diamond and one was nitrogen doped; both grown on the heteroepitaxial silicon substrate described above. The dimensions of the intrinsic sample are ~ 1.5 mm $\times$ 1.5 mm $\times$ 3.5 mm and the dimensions of the nitrogen doped sample are ~ 1.5 mm $\times$ 3.5 mm $\times$ 3.5 mm. The growth direction was $\langle 001 \rangle$.

7.3 Experimental Methods

A Leica DMI4000 inverted microscope, fitted with cross polarisers, was used to study strain. The polariser and analyser were 90° out of phase which allowed the birefringence of the samples to be imaged. The dislocation bundles within the material create areas of strain and hence an anisotropic matrix. This rotates the light as it passes though the sample, with regions of higher strain rotating the light more. Regions with a high dislocation volume will rotate a significant amount of light and thus appear brighter. A high quality homoepitaxial CVD sample contains few dislocations, which arise from polishing damage of the HPHT or natural diamond from which the sample was grown. The birefringence image of a homoepitaxial CVD sample would be dark with some regions of light due to strain associated with the dislocations [180]. A high quality HPHT diamond would appear black, as it has a very low dislocation density.

Fluorescence imaging was employed to investigate fluorescence by dislocations. This was performed with a DiamondView^{TM} microscope which uses UV light and measures fluorescence and phosphorescence.

Photoluminescence (PL) experiments were performed as detailed in section 4.3.3. Both samples were studied at 90 K with excitation lasers at wavelengths of 532 nm and 633 nm. For these experiments a polarising analyser was used. This

polarised the diamond luminescence. The analyser was aligned either parallel or perpendicular to the growth direction, as determined by studying the dislocations. The phase of the analyser was checked using carbon tetrachloride, a liquid which has a Raman band at 459 cm^{-1} arising from a symmetric vibrational mode. The intensity of the band is related to the relative polarisation of the laser light and the detection. If the laser light and the analyser are 90° out of phase no intensity will be seen from this band [181].

FTIR experiments were performed at room temperature as detailed in section 4.3.1. The experiments were done with and without polarising the input light to see if there was preferential orientation of any defects.

Continuous wave electron paramagnetic studies were conducted as detailed in section 4.2 at room temperature. This was used to quantify the concentration of the defects; N_s^0, NVH^-, NV^- and SiV^0.

7.3.1 Strain Broadening

In the PL experiments the zero-phonon line (ZPL) of different defects including the negative silicon vacancy and neutral nitrogen vacancy were studied.

Theoretically, in a perfect diamond, the linewidth should be excited-state-lifetime-limited and Lorentzian in shape: this has been observed in measurements of single centres [182, 183]. However, when measuring ensembles, actual linewidths are $\sim 10^3$ times larger [184]. The linewidths are broadened by crystal inhomogeneity arising from random electric fields and strain with strain the primary broadening mechanism [185]. The strain broadening occurs due to shifts in the optical transition frequency caused by strain local to each defect in the ensemble [186]. The main mechanisms from which this strain arises are point defects and dislocations local to the species of which the ZPL is being measured. Complex statistical calculations are required to work out the mechanism causing the broadening of a particular ZPL and require assumptions to be made about the material [187, 188]. However, the lineshape can also be studied qualitatively. A low strain sample is likely to have a Lorentzian lineshape. As the dislocation density increases the lineshape becomes Gaussian, with a linewidth proportional to the square root of the dislocation density. Conversely, a sample which has a high point defect concentration will have a Lorentzian shape. A sample with a high point defect concentration and a high dislocation density will be made of approximately equal parts Gaus-

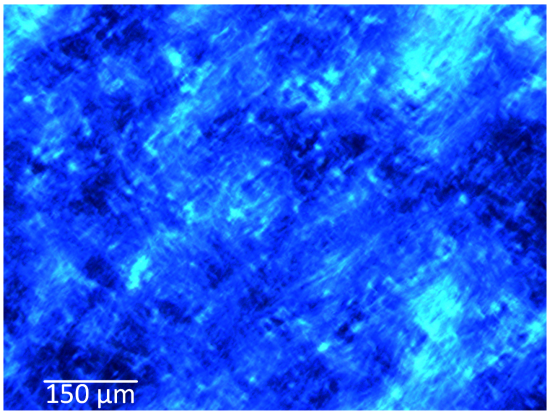

(a) *Nucleation surface of nitrogen doped heteroepitaxial CVD sample.*

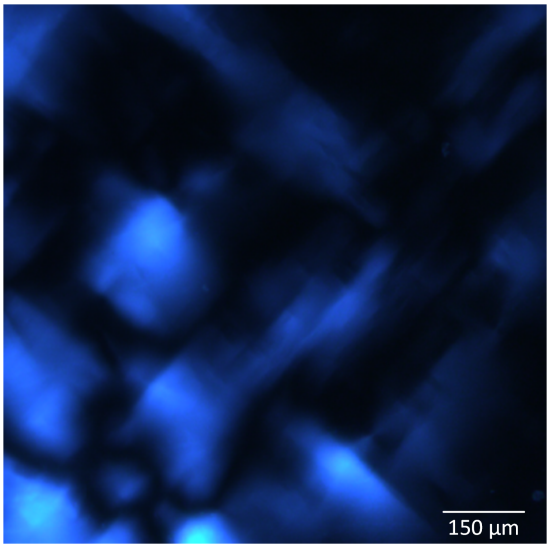

(b) *Birefringence image of a CVD homoepitaxial sample, sample 14.*

Figure 7.3: *Microscope fitted with cross polarisers to image the birefringence of heteroepitaxial and homoepitaxial CVD diamond. The cross polarisers were aligned parallel to the diamond edges with the light going through the sample along the growth direction.*

sian and Lorentzian [189]. This is typically described using a Voigt lineshape, formed of the convolution of a Gaussian and Lorentzian distribution, and is the usual lineshape observed in real measurements of ensembles [190]. However, when studying these lineshapes some assumptions are made which may not be true. These include the uniformity of the material; it is assumed that the point defects and dislocations have a spatially uncorrelated distribution [185]. This may result in an overestimation of strain, as the strain local to the defect is being analysed not the strain throughout the material as the local dislocation and point detect concentration may be different.

7.4 Birefringence Imaging

Birefringence imaging was used to qualitatively study strain as strain changes the local refractive index. This was performed with a microscope fitted with cross polarisers.

In figure 7.3a an image of the nitrogen doped sample can be seen. This sample displays a high amount of strain. This image can be compared to the birefringence of a homoepitaxial CVD sample, as shown in figure 7.3b. The heteroepitaxial

sample is brighter, suggesting a higher degree of strain, and the strain structure is finer which indicates a higher density of dislocation bundles.

7.5 Fluorescence Imaging with UV Excitation

Fluorescence imaging was performed using DiamondView^{TM}. Both samples were imaged. Figure 7.4a shows the top of the nitrogen doped sample. The blue luminescence is assumed to arise from dislocation and dislocation bundles. In figure 7.4b the luminescence from the dislocation bundles can be seen from the side. In CVD samples this allows the nucleation side to be identified as this will be the side with an increased dislocation density. The bottom surface is the one nearest to the nucleation site as a higher dislocation density can be seen in this area. The slight background orange colour arises from NV^0. In figure 7.5 the intrinsic diamond can be seen from the top and side. This sample also shows a high concentration of luminescence from dislocation bundles.

The luminescence from dislocation bundles which can be seen in these images indicate a distinction from high quality homoepitaxial CVD; in homoepitaxial CVD luminescence from dislocation bundles are much less strong. They arise from polishing imperfections on the substrate diamond from which they are grown, and can be heterogeneously distributed. An example of a homoepitaxial CVD diamond is sample 5, discussed in Chapter 8. This diamond can be seen in figure 8.1a. Luminescence, which would indicate the presence of dislocation bundles, is not visible in this image. This indicates a lower dislocation density.

7.6 Photoluminescence

Photoluminescence (PL) experiments were performed at 90 K with excitation lasers 532 nm and 633 nm. This was done to investigate the differences, in terms of defect concentration, of the two samples and to measure the extent of the strain broadening. The PL experiments were done on the top surface of the diamonds.

In figure 7.6 the differences between the two samples can be seen in a Raman normalised spectra. As figure 7.6a shows, the concentration of both the neutral and negative nitrogen vacancy are higher in the nitrogen doped sample, in fact it was not possible to see these signals in the intrinsic sample under these exper-

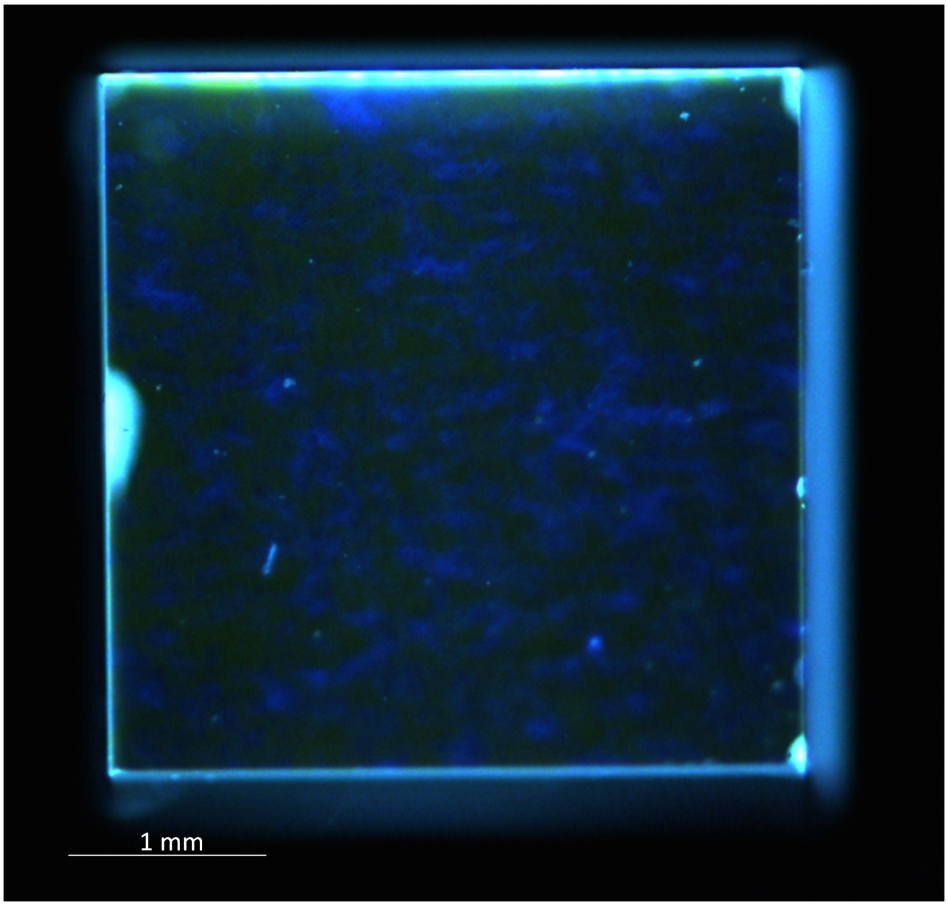

(a) *This image shows the nucleation surface, which was determined by the higher dislocation density. The dislocations can be identified by the blue luminescence. The orange background colour indicates emission from neutral nitrogen vacancy.*

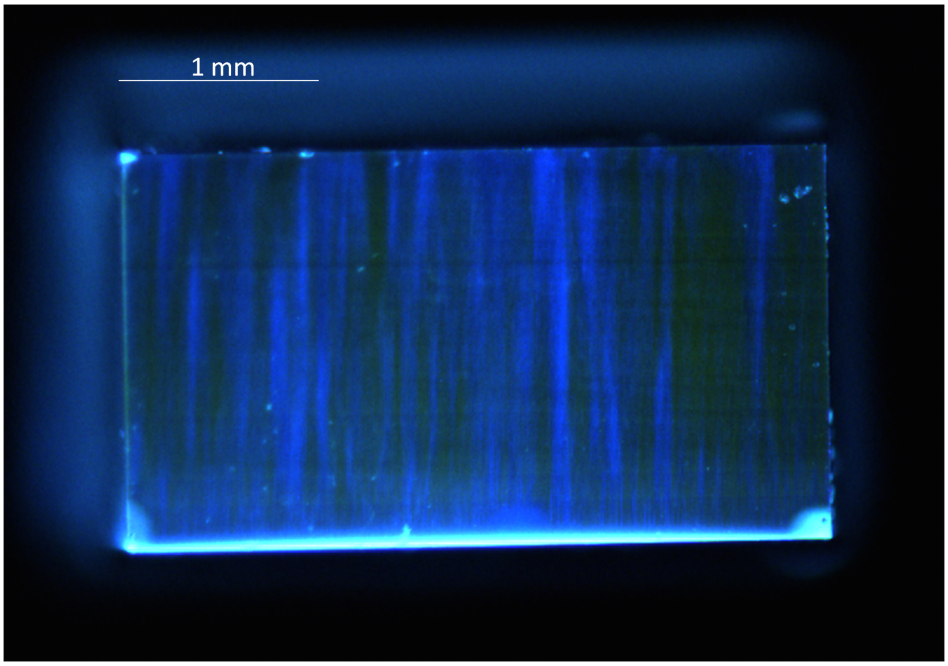

(b) *Side surface. Blue areas show luminescence from dislocations and dislocation bundles. The bottom of the diamond is the nucleation area and shows a higher concentration of dislocations which annihilate as the diamond grows upwards.*

Figure 7.4: *DiamondView^{TM} image of nitrogen doped heteroepitaxial diamond.*

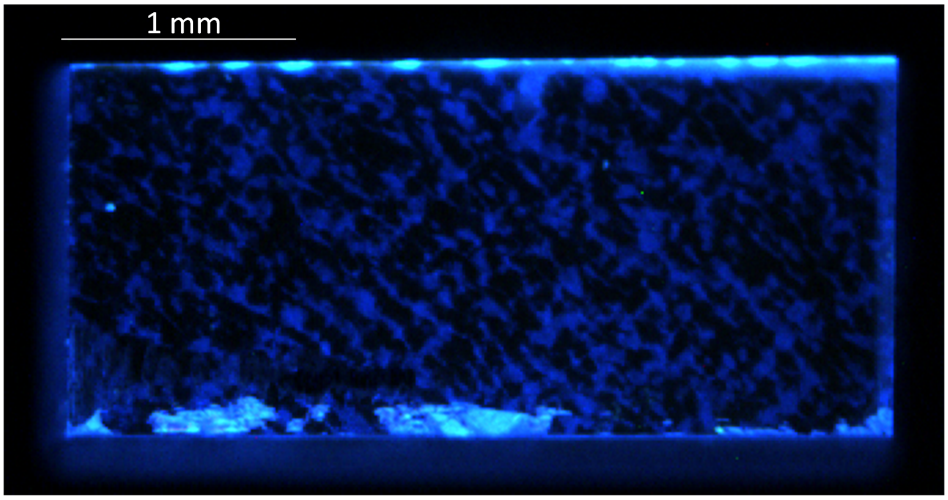

(a) *This image shows the nucleation surface, which was determined by the higher dislocation density. The dislocation bundles can be identified by the areas of blue luminescence.*

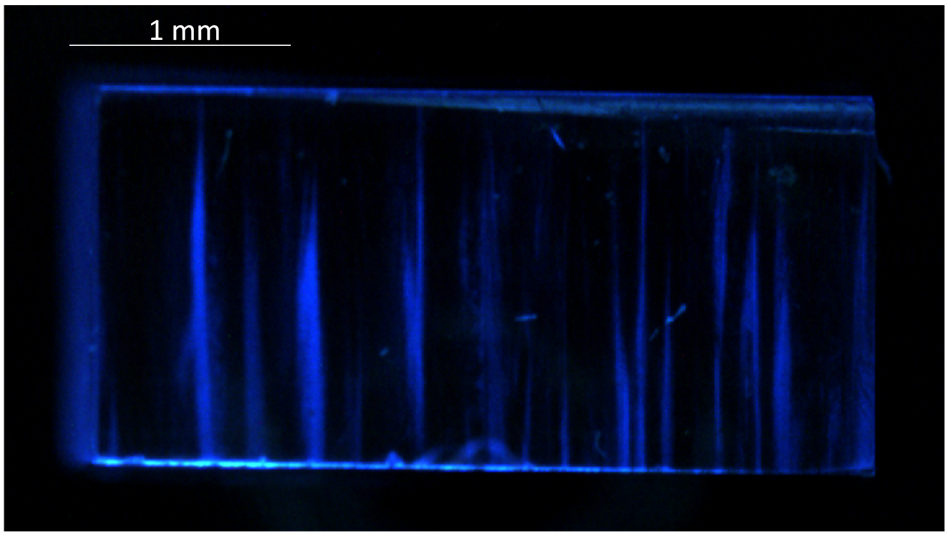

(b) *Side surface. Blue areas indicate dislocation bundles. The bottom of the diamond is the nucleation area and shows a higher concentration of luminescence from dislocations which annihilate as the diamond grows upwards.*

Figure 7.5: *DiamondView^{TM} image of intrinsic heteroepitaxial diamond.*

imental conditions. The relative intensities of the neutral and negative nitrogen vacancies are shown in table 7.1. The nitrogen doped sample also shows a higher concentration of negative silicon vacancy centres as seen in figure 7.6b.

Sample	NV^0 (a.u.)	NV^- (a.u.)	Ratio NV^0/NV^-
Nitrogen Doped	158±16	180±18	0.88
Intrinsic	<0.2	<0.2	-

Table 7.1: *The integrated intensity of the NV^0 peak and the NV^- peak in sample 10 (homoepitaxial), the nitrogen doped sample (heteroepitaxial) and the intrinsic (heteroepitaxial) as measured by PL at 90 K.*

In figure 7.7a a comparison of the PL spectra of the ZPL of the neutral nitrogen vacancy signal can be seen. This shows the comparison between a homoepitaxial CVD sample, a HPHT sample and the nitrogen doped heteroepitaxial sample. As can be seen from this figure the heteroepitaxial sample shows significant strain broadening of the ZPL. This is also the case for both heteroepitaxial samples' negative silicon vacancy signal, as can be seen in figure 7.7b. With the nitrogen doped sample showing the largest degree of strain broadening. The Gaussian and Lorentzian nature of each of these lines can be seen in tables 7.2 and 7.3.

Previous work on the neutral nitrogen vacancy has allowed calculation of the stress parameters of the centre; indicating a line shift of 7.6 meV/GPa [69]. The FWHM presented in table 7.2 can be used to obtain Voigt half width half maximum (HWHM). If it is assumed that the homogeneous linewidth contributed by each centre is significantly smaller than the ensemble linewidth, the contribution of each centre to the overall ZPL may be treated as a delta function. The stress required to cause the shifts of each delta function can then be calculated. The Voigt HWHM and resultant stress is shown in table 7.4.

Sample	Gaussian (meV)	Lorentzian (meV)
Homoepitaxial CVD	1.3±0.1	0.9±0.1
HPHT	1.1±0.1	1.5±0.2
Nitrogen Doped (Heteroepitaxial)	4.1±0.4	4.1±0.4

Table 7.2: *The Gaussian and Lorentzian FWHM linewidths of the 575 nm peak in a HPHT (sample 10), a homoepitaxial CVD (sample 13) and the nitrogen doped sample at 90 K.*

PL experiments were also done using polarised light at ten locations in each sample. The ten locations were in a line on the side of the diamond, going from

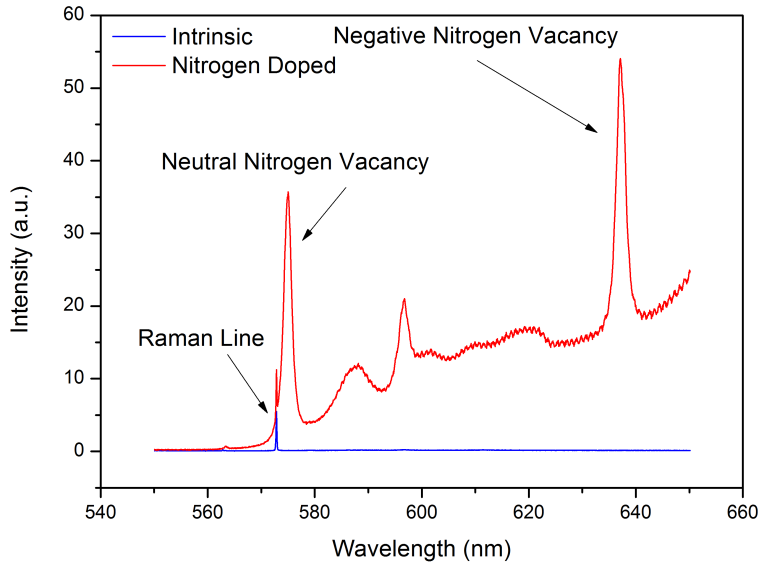

(a) *Photoluminescence spectra of the intrinsic and nitrogen doped sample taken with 532 nm excitation. Both spectra were taken at 90 K normalised to the Raman line.*

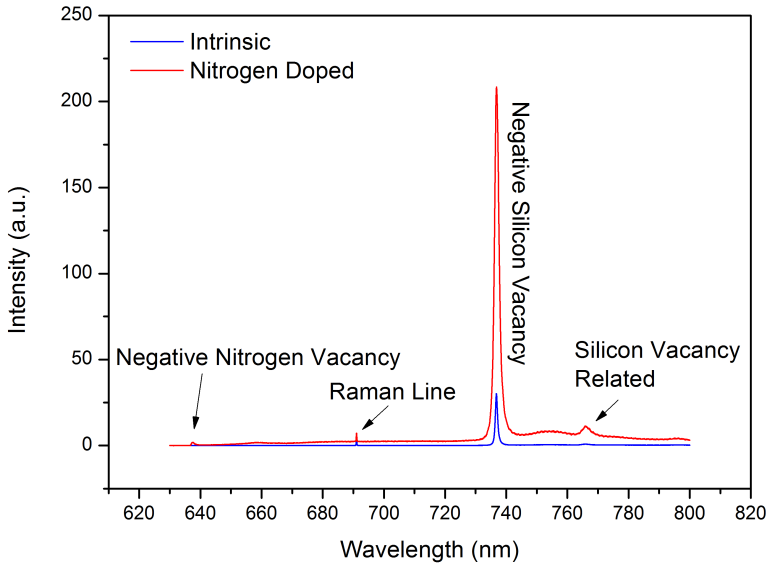

(b) *Photoluminescence spectra of the intrinsic and nitrogen doped sample taken with 633 nm excitation. Both spectra were taken at 90 K normalised to the Raman line.*

Figure 7.6: *Photoluminescence spectra of the two samples compared.*

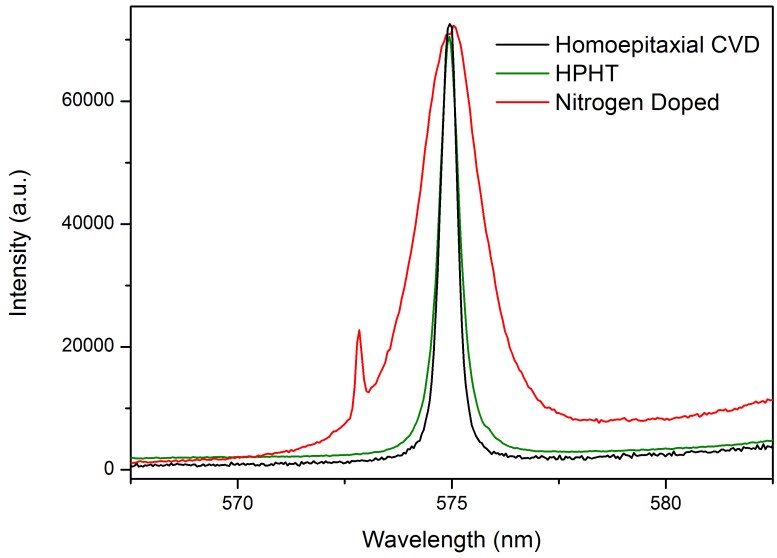

(a) *A comparison of the photoluminescence of the neutral nitrogen vacancy ZPL, at 575 nm, in a homoepitaxial CVD sample (sample 10) and the nitrogen doped, heteroepitaxial sample. All spectra were taken at 90 K and scaled for comparison of lineshape.*

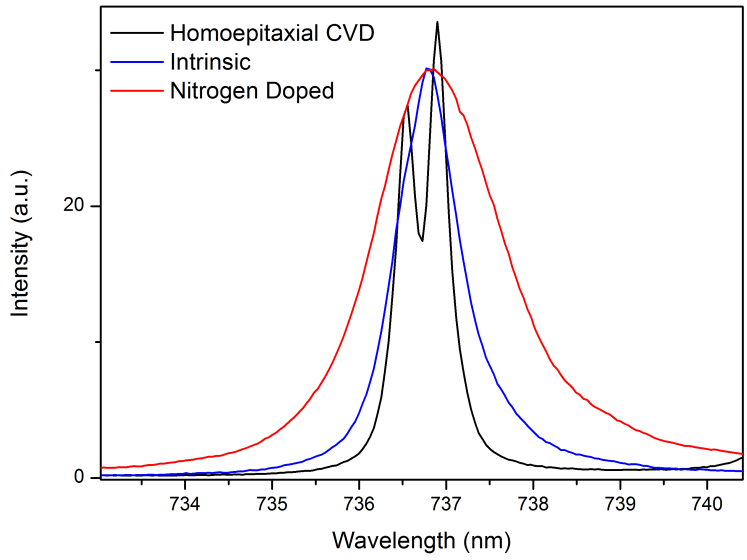

(b) *A comparison of the photoluminescence of the negative silicon vacancy ZPL, at 737 nm, in a homoepitaxial CVD sample (sample 13), a HPHT sample (sample 7) and the nitrogen doped and intrinsic heteroepitaxial sample. All spectra were taken at 90 K and scaled for comparison of lineshape.*

Figure 7.7: *Photoluminescence line broadening in heteroepitaxial sample.*

Sample	Gaussian (meV)	Lorentzian (meV)
Homoepitaxial CVD	0	0.64±0.06
Intrinsic (Heteroepitaxial)	0.78±0.08	1.4±0.1
Nitrogen Doped (Heteroepitaxial)	2.5±0.3	2.3±0.2

Table 7.3: *The Gaussian and Lorentzian FWHM linewidths of the 737 nm peak in the nitrogen doped sample, intrinsic sample and a homoepitaxial CVD (sample 7) at 90 K. Note that the homoepitaxial CVD line was made up of two peaks with the same character.*

Sample	Voigt (meV)	Stress (GPa)
Homoepitaxial CVD	0.89±0.09	0.12±0.01
HPHT	1.1±0.1	0.14±0.01
Nitrogen Doped (Heteroepitaxial)	3.4±0.3	0.45±0.05

Table 7.4: *The Voigt HWHM linewidths of the 575 nm peak in a HPHT (sample 10), a homoepitaxial CVD (sample 13) and the nitrogen doped sample at 90 K and the stress which this indicates.*

nucleation (the side nearest the substrate) to the growth surface. In figure 7.8 a centre can be seen at 467.6 nm. This figure is representative of those seen at all ten locations on the nitrogen doped diamond. This peak has previously been ascribed to a ZPL of a vacancy related defect [33]. The 469.2 nm defect, seen in the figure, has also previously been seen in CVD diamonds [33]. These two peaks behave inversely to one another. When the analyser (the polariser before detection of signal) is parallel to the dislocations the peak at 467.6 nm has a larger signal whereas if the analyser is perpendicular the 469.2 nm has a larger signal. The polarisation of the incoming light does not affect the relative heights.

7.7 Fourier Transformed Infrared Absorption

An FTIR comparison of the two different samples can be seen in figure 7.9. All the spectra presented in this section were taken at room temperature.

The samples differ in the one phonon region (see figure 7.10a) where, in the nitrogen doped sample, a signal related to positively charged single substitutional nitrogen can be seen. The concentration of N_s^+ is 700±70 ppb, when measured under ambient conditions (not after UV illumination or heating in the dark which

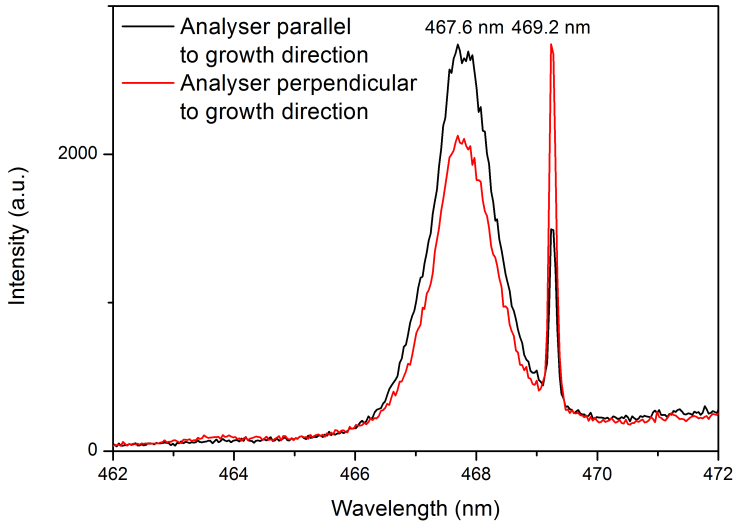

Figure 7.8: *467.6 nm and 469.2 nm peaks. The different lines relate to the orientation of the polariser and analyser with respect to the dislocation orientation. Photoluminescence of nitrogen doped sample with polarisers. Temperature 90 K and laser used was 532 nm.*

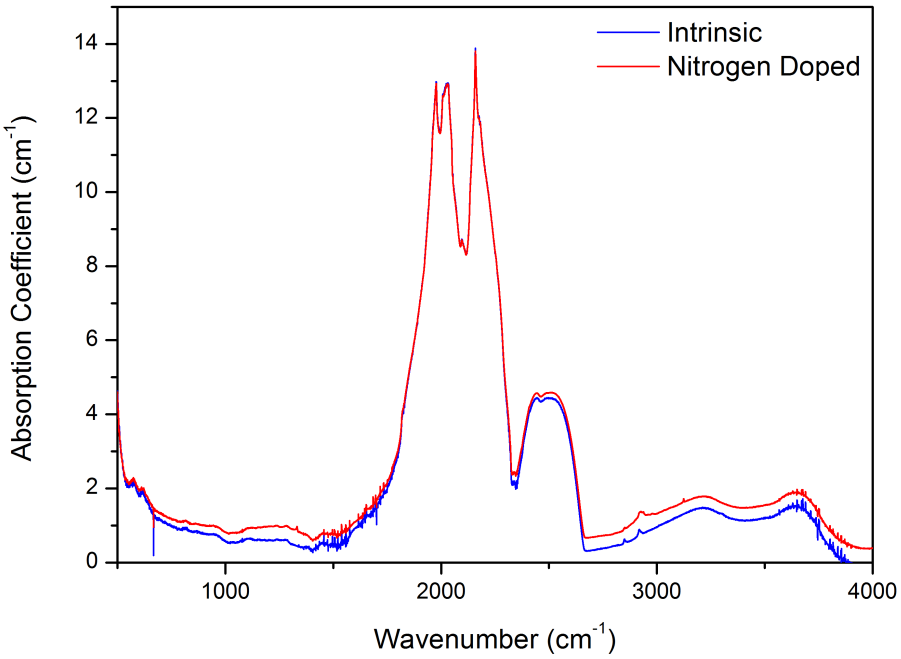

Figure 7.9: *An FTIR spectrum showing the one and two phonon region of the two heteroepitaxial samples compared.*

would cause charge transfer). This signal was not seen in the intrinsic sample. The neutrally charged single substitutional nitrogen did not have a measurable signal in either sample, though must be present beneath the noise as it was seen in EPR. Possibly UV illumination would have enhanced the neutral charge state enough for it to become visible. The noise in the one phonon region may arise from hydrogen incorporation or dislocations, disrupting the periodicity of the lattice. A peak can be seen at 3123 cm^{-1} in figure 7.10b. This peak is related to NVH^0 [191]. The peak height can be used to calculate the concentration of NVH^0 using the method outlined in reference [191]; this gives a concentration of 140±14 ppb. This peak can be seen in the nitrogen doped sample but not the intrinsic, as would be expected for homoepitaxial CVD diamond.

Experiments were done with polarisers to polarise the incoming light either parallel or perpendicular to the dislocation direction. This was to determine whether any of the defects were preferentially orientated. One spectrum which shows preferential orientation is shown in figure 7.11. The three lines shown in this spectrum are at 6425 cm $^{-1}$, 6860 cm $^{-1}$ and 7354 cm $^{-1}$.

Previously the 6425 cm $^{-1}$ and 7354 cm $^{-1}$ peaks have been investigated and appear to be linked as they exhibit the same annealing behaviour [192]. They both anneal out at 1300°C [193, 194, 195]. They have been seen in CVD diamonds but have not been seen in HPHT or natural. The defect has been identified as containing one hydrogen atom by isotropic studies which used samples containing deuterium, an isotope of hydrogen [196, 197]. The 7354 cm $^{-1}$ peak has been identified as an electronic transition and due to the shift in position when the predominate carbon isotope in the diamond has been changed from ^{12}C to ^{13}C it can be assigned to a ZPL [196, 197]. The 6425 cm $^{-1}$ peak has been identified as an excited transition from a low lying excited state as it is not seen at low temperatures [192]. The defect symmetry has been discovered by stressed experiments to be D_{3d} with the electron transitioning from an excited E state to a ground E state [192]. Previous work has tentatively identified the defect as di-vacancy hydrogen [192].

The ZPL of this defect (at 7354 cm $^{-1}$) is seen to preferentially orientate in the nitrogen doped sample as it has only 45% intensity when the light is polarised parallel to the growth direction.

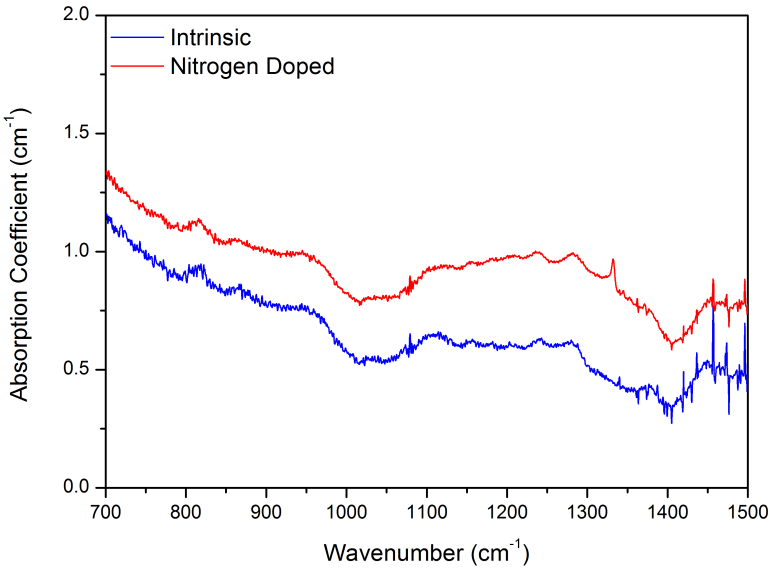

(a) An FTIR spectrum of the differences between the two samples in the one phonon region.

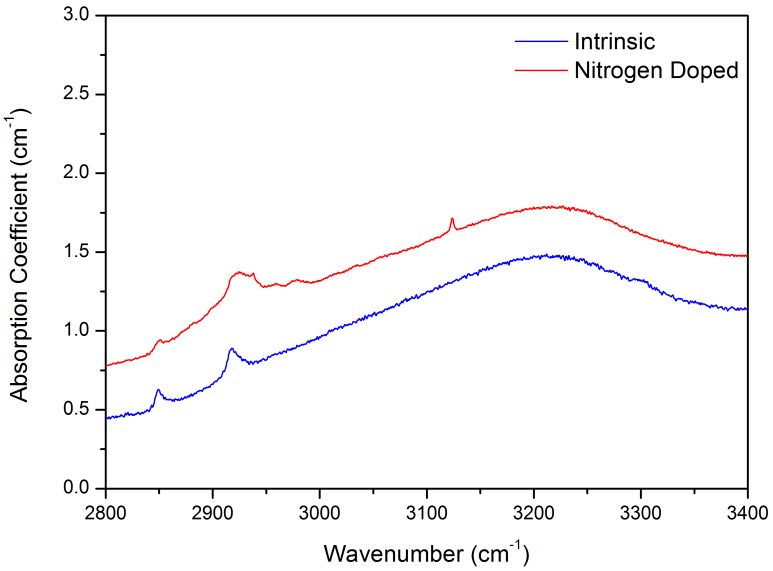

(b) An FTIR spectrum of the differences between the two samples in the two phonon region.

Figure 7.10: *FTIR spectra of the heteroepitaxial samples under ambient conditions.*

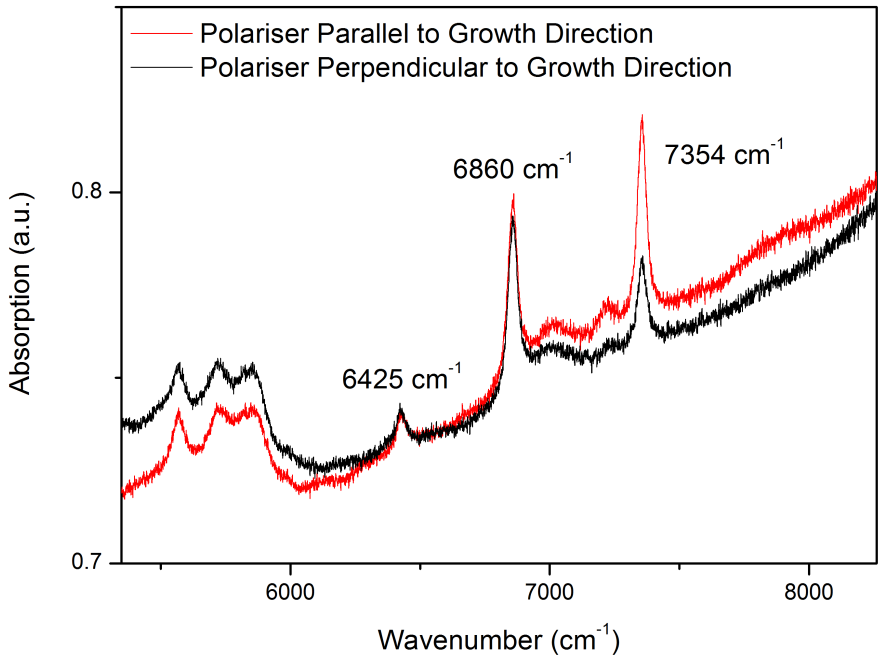

Figure 7.11: *An FTIR spectrum of the nitrogen doped sample. The two different lines indicated the absorption of light which was parallel and perpendicular to the dislocations.*

7.8 Electron Paramagnetic Resonance

Defect concentrations were measured by EPR. The spectrum of the nitrogen doped sample is seen in figure 7.12. This figure shows the signal of N_s^0. The concentrations calculated are shown in table 7.5. These concentrations were calculated after UV illumination performed with the DiamondView^{TM} or after a heat treatment at 550°C for 20 minutes. N_s^0 and NVH^- were detected but NV^- was not. The NV^- signal must be present below the noise however as it was detected in the PL experiment. The spectrum of the intrinsic sample is shown in figure 7.13. This

	UV illumination	Heat treatment	Expected relative concentrations
N_s^0	1700±170 ppb	300±30 ppb	300 [N_s^{Total}]
NVH^-	100±10 ppb	400±40 ppb	30 [NVH^{Total}]
NV^-	<40 ppb	<20 ppb	1 [NV^{Total}]

Table 7.5: *Defect concentrations in the nitrogen doped sample. NV^- could not be measured so these number indicate an upper limit on their concentration. Concentration measurements performed by Dr Breeze. The expected ratio comes from reference [198].*

figure shows a signal from SiV^0. The SiV^0 EPR signal in this spectrum fitted badly to simulations. This may have arisen from the strain causing changes to zero-field splitting. The concentrations calculated are shown in table 7.6. The concentration of N_s^0 was calculated using rapid passage EPR.

	UV illumination (ppb)	Heat treatment (ppb)
N_s^0	2.5±0.3	<0.01
SiV^0	2.0±2	0.7±0.1
NV^-	<40	<20

Table 7.6: *Defect concentrations in the intrinsic sample. NV^- could not be measured so these number indicate an upper limit on their concentration. Concentration measurements performed by Dr Breeze.*

In the intrinsic sample an additional broad signal was seen at approximately $g = 2.0028$. This may be created by hydrogen at dangling bonds [199]. As hydrogen is required for CVD growth and is often the most abundant element, inclusion of it is likely once the diamond is formed. Polycrystalline CVD samples often have this feature as it is thought to be created in regions of non-diamond material within diamonds or at edges and grain boundaries [200].

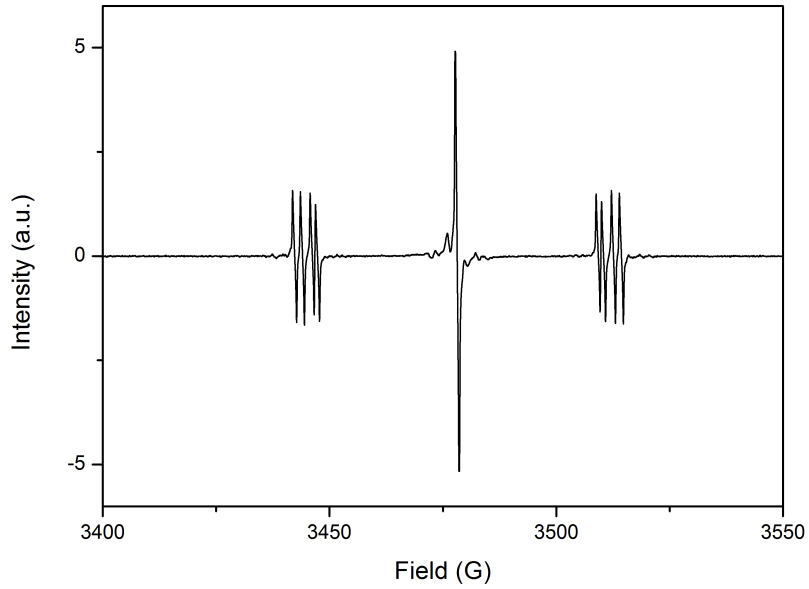

Figure 7.12: *EPR spectrum of nitrogen doped heteroepitaxial sample showing signal from single substitutional nitrogen in ambient conditions. The theory of this signal is discussed in section 3.2.5.*

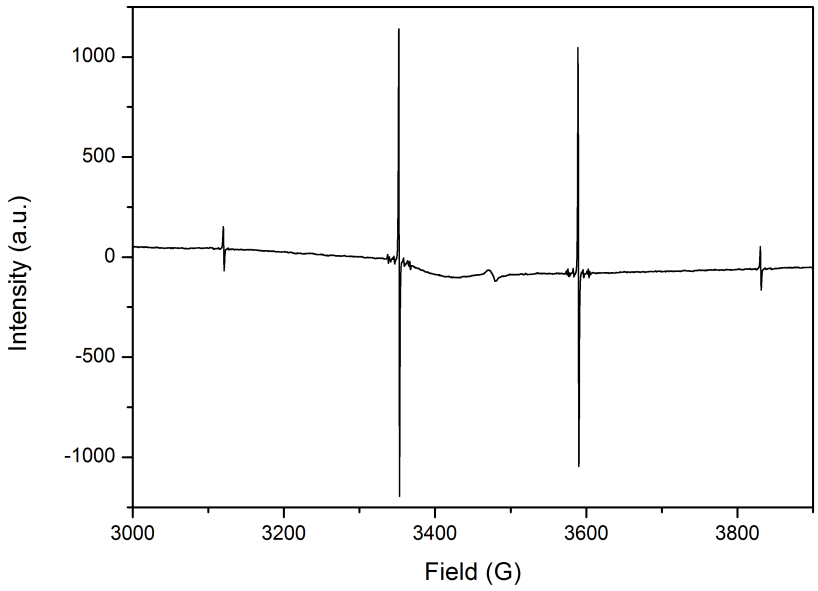

Figure 7.13: *EPR spectrum of intrinsic heteroepitaxial sample showing signal from the neutral silicon vacancy in ambient conditions. The field direction is parallel to* $\langle 111 \rangle$.

7.9 Discussion

7.9.1 Preferential Orientation

Preferential orientation may occur during growth due to the directional strain created by the dislocations. This possibility was investigated using PL and FTIR.

In PL the peaks at 467.6 nm and 469.2 nm were seen to behave differently when the analyser was either parallel or perpendicular to the growth direction. The peak at 467.6 nm is vacancy related and was seen to be stronger when the analyser was aligned parallel to the growth direction. This indicates that these defects may be preferentially orientated, however more work is required to identify their origin.

In FTIR a hydrogen related defect at 7354 cm^{-1} was seen. Hydrogen is required for CVD growth and is often incorporated into imperfect or polycrystalline CVD samples. The defect at 7354 cm^{-1} was seen to preferentially absorb in the direction parallel to the growth direction (see figure 7.11). If the dipole moment of this defect is parallel to the symmetry axis this indicates the defects are preferentially aligned parallel to the growth direction. However the symmetry axis is not known and so further work is required to investigate this defect.

7.9.2 Strain

The nitrogen doped heteroepitaxial sample showed a large degree of birefringence indicative of strain arising from dislocation bundles.

The DiamondView™ allowed the luminescence from the dislocation bundles to be seen. The dislocations are caused by strain due to the large lattice mismatch between the diamond and iridium layer. As discussed previously, they tend to reduce in density away from the substrate as they annihilate or join together and after 1 mm of growth the strain is much reduced [179]. From the DiamondView™ images the luminescence from the dislocation bundles could be seen to be reducing as distance from the nucleation surface increases.

In heteroepitaxial CVD single crystal samples made by Schreck et al. previously there was more strain than in the samples studied here [171]. Earlier samples contained enough strain that the Raman line was split. In the PL data of the

nitrogen doped heteroepitaxial sample shown in figure 7.6 the Raman line was not split and the FWHM was ∼0.2 nm. One possibility is that previous samples may have contained higher strain due to being cut from a closer proximity to the nucleation surface where the strain is highest. However, it is more likely this improvement is due to improvements in synthesis including the growth conditions and the substrate lattice matching.

The PL graphs of the heteroepitaxial CVD samples show large amounts of strain broadening even at low temperature (77 K). Sources of strain broadening include grain boundaries, dislocations and regions of non-diamond carbon as well as point defects like nitrogen and silicon [201]. In these samples the high dislocation density and, for the nitrogen doped sample, the high concentration of point defects are likely to be the most important factors.

The strain broadening was qualitatively understood by comparing the lineshapes of the ZPLs of the neutral nitrogen vacancy centre and the negative silicon vacancy centre to two samples, one made by HPHT synthesis and one by homoepitaxial CVD.

In table 7.2 the Gaussian and Lorentzian components of the neutral nitrogen vacancy ZPL peak were presented for a homoepitaxial CVD sample (sample 13), a HPHT sample and the nitrogen doped heteroepitaxial CVD sample. All samples had a Voigt lineshape, this is, they all had both Gaussian and Lorentzian components to their lineshape character. The homoepitaxial sample had a higher dislocation density than the HPHT sample whilst the HPHT sample had a higher point defect concentration. This was reflected in the lineshape components. The homoepitaxial sample had a lineshape which was more Gaussian in character and the HPHT sample lineshape was more Lorentzian in character. For the nitrogen doped heteroepitaxial CVD sample the character was equal parts Gaussian and Lorentzian. It was also broader. This suggests that the lineshape broadening is related to both a high dislocation density and a high nitrogen defect density. The internal stress within the sample was calculated to be 0.45 GPa, 0.3 GPa greater than the internal stress within the homoepitaxial CVD and HPHT sample to which it was compared.

In table 7.3 the Gaussian and Lorentzian components of the negative silicon vacancy peak were presented for a homoepitaxial CVD sample, the intrinsic heteroepitaxial CVD sample and the nitrogen doped heteroepitaxial CVD sample. Note, the homoepitaxial CVD sample (sample 7) is not the same as was used to

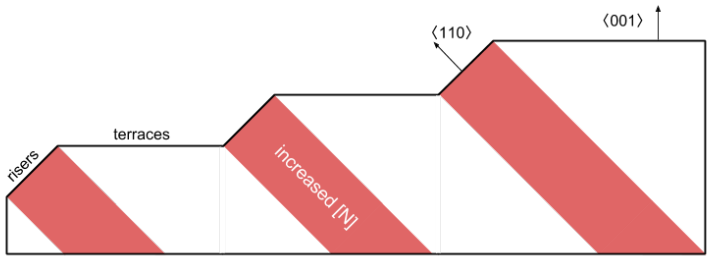

Figure 7.14: *Image showing risers and terraces during CVD growth, with increased nitrogen incorporating into the risers. Figure adapted from reference [202].*

compare the neutral nitrogen vacancy sample. The nitrogen defect concentration of the homoepitaxial sample and the intrinsic sample are of comparable magnitude, 20 ppb and 2.5 ppb respectively. This means differences in lineshape are likely due to the larger dislocation density of the heteroepitaxial intrinsic sample. The larger Gaussian component indicates a larger dislocation density. The nitrogen doped heteroepitaxial CVD sample shows a Voigt character with equal Gaussian and Lorentzian contributions. Again it is more broadened than the intrinsic sample, arising from the higher single substitutional nitrogen concentration and dislocation density. The higher dislocation density may have arisen from non-diamond carbon inclusions resulting from the faster growth.

Whilst EPR can be used to measure the average neutral single substitutional nitrogen concentration the local concentration may be more or less, depending upon the local environment. When a CVD diamond is growing in a ⟨001⟩ direction, as is the case here, the growing surface consists of risers and terraces. The risers are ⟨110⟩ in direction and the terraces are ⟨001⟩. As nitrogen incorporates preferentially in ⟨110⟩ diamond, the riser surfaces will have a larger concentration of nitrogen. This is shown in figure 7.14.

The concentration may be greater in the regions grown from the risers and less elsewhere. Additionally, the dislocation density has previously been investigated in risers and terraces and has been found to be higher in risers [203]. Hence the strain comparisons above may not apply to the whole sample but just the regions where the defects are being measured. These regions will have more strain because of the higher local nitrogen and dislocation concentration. Negative silicon vacancy centres preferentially form (compared to the neutral centre) in locations where the nitrogen concentration is high, as the nitrogen donates an electron to preserve the charge state. Hence the negative silicon vacancy centres under study may exist

in a location which has a higher nitrogen defect concentration and hence give an overestimate of the degree of strain arising from point defects.

These samples show a significant degree of strain compared to the quality of currently available homoepitaxial CVD diamond. It is possible to significantly reduce strain broadening in CVD samples by annealing at 2200°C [204], which is indicative of a reduction of strain. This may be related to dislocation migration. The nitrogen doped sample showed more strain than the intrinsic sample; whilst nitrogen doping speeds up growth it also increases the strain in the sample. The addition of nitrogen to homoepitaxial CVD diamond is known to cause 'bunching' where nitrogen defects interrupt the step growth of the diamond and cause microscopic roughening [205]. This effect may reduce the ability of dislocations to interact and annihilate. Additionally, a faster growth rate will result in more defective growth, possible inclusion of non-diamond carbon regions and the nitrogen itself will cause strain. The intrinsic sample was grown more slowly than the nitrogen doped one. This slower growth rate allows the dislocations more time to interact as the diamond grows increasing the likelihood of annihilating. There is a clear trade-off between faster crystal growth and better crystal quality. Both types of diamond may have commercial applications but the quality has still not reached that of homoepitaxial CVD.

7.9.3 Defects

The defect concentrations were studied qualitatively by PL and quantitatively by EPR. N_s^0 was measured by EPR in both samples, with more seen in the nitrogen doped sample. Additionally N_s^+ was seen in the nitrogen doped sample in FTIR.

NV^- and NV^0 were seen in the nitrogen doped sample; in figure 7.6a the PL of these can be seen. The magnitudes are similar, as quantified by the ratio of NV^0 to NV^-; 0.88. A comparable concentration of NV^- compared to NV^0 would be expected from the large concentration of single substitutional nitrogen donors. NV^- was not seen in EPR. The absence of the NV^- signal in EPR may arise from the strain. A high strain within a diamond can create a variation in the zero-field splitting (ZFS) which will cause a broadening of the EPR lines which will make them harder to detect. Future work could involve studying the half field line of the NV^- defect as this should be less affected by strain. When there is a large concentration of N_s^0 present it may donate electrons, as shown in equation 7.1.

$$NV^0 + N_s^0 \rightarrow NV^- + N_s^+ \tag{7.1}$$

In the intrinsic sample no nitrogen vacancy defects of either charge state were seen in the PL or EPR experiments. Future work could involve investigating this further using electron spin polarisation to increase the EPR signal.

In the nitrogen doped sample SiV^- is seen in PL but SiV^0 was not seen in EPR. This may again be due to N_s^0 donating electrons, as shown in equation 7.2. The N_s^0 seems to preferentially donate electrons to silicon vacancy centres rather than nitrogen vacancy centres [145]. This indicates the silicon vacancy is a deeper acceptor level in the band gap.

$$SiV^0 + N_s^0 \rightarrow SiV^- + N_s^+ \tag{7.2}$$

In the intrinsic sample the concentration SiV^0 was high and as mentioned above little N_s^0 was seen. This may be the reason why the signal from SiV^- was small in comparison to SiV^0, there is a low concentration of electron donors.

Silicon is often included in CVD diamonds as the harsh environment of the plasma etches the silica in the reactor walls and the silicon then mixes with the reactants. The silicon vacancy defect concentration in both samples may be the same, as it had the same source; the silica reactor walls. However, it is in a different charge state as the nitrogen doped sample had a larger concentration of electron donors.

Additionally in the nitrogen doped sample NVH^- was seen in EPR. The peak from NVH^0 was also seen in this sample in FTIR. The concentrations were 100 ppb NVH^- and 140 ppb NVH^0. These were not seen in the intrinsic sample.

In the nitrogen doped heteroepitaxial sample the relative concentrations of $[N_s^{Total}]$, $[NVH^{Total}]$ and $[NV^{Total}]$ were as expected for nitrogen doped homoepitaxial CVD.

7.9.4 Single Crystal Diamond

In the DiamondView^{TM} images dislocation bundles can be seen (see figure 7.4 and figure 7.5). In previous heteroepitaxial diamond samples closed networks of grain boundaries have been seen. Low angle grain boundaries consist of an array

of dislocations. The method of lattice matching has improved these diamonds enough to reduce the dislocation density to make single, defective crystals rather than polycrystalline material.

The single crystal nature of the material is also evident from the two EPR spectra presented (see figure 7.12 and 7.13). For a polycrystalline sample the spectrum would show multiple overlapping signals originating from the different crystals at different orientations, however this was not seen for these diamonds.

7.10 Conclusion

In this chapter two samples were investigated which had been made by heteroepitaxial CVD on a lattice matched silicon substrate using Bias Enhanced Nucleation. Investigation of these samples showed that they were single crystals but contained a high degree of strain arising from the lattice mismatch.

Photoluminescence was used to investigate the point and extended defects within each sample. It was demonstrated that the nitrogen doped sample had a large concentration of nitrogen vacancies in both charge states and also negative silicon vacancy. While EPR demonstrated the optical doped sample had a significant concentration of neutral silicon vacancy.

PL was also used to qualitatively understand the strain broadening and it was seen that the nitrogen doped sample had the highest degree of strain broadening and the intrinsic sample was also broadened compared to a homoepitaxial CVD sample. The relative contributions to broadening from dislocations and point defects were investigated. Both heteroepitaxial samples showed a large degree of strain broadening from dislocations and the nitrogen doped sample also showed a large degree of strain broadening from point defects. The internal stress was calculated for the nitrogen doped sample to be 0.45 GPa. Spectra were taken using a polarising analyser and a vacancy related defect at 467.6 nm was seen to possibly be preferentially orientated in the direction of the dislocations.

FTIR was used to study the samples and the positively charged single substitutional nitrogen content was quantified; it was 700 ppb in the nitrogen doped sample and was below the detection limit in the intrinsic sample. A peak from NVH^0 was also identified in the nitrogen doped sample. A peak related to hydrogen was seen to be absorbing a larger amount of light when the light was polarised

parallel to the growth direction and thus may be preferentially orientated.

EPR was used to quantify the defects present. The concentration of neutral single substitutional nitrogen in the nitrogen doped heteroepitaxial sample was 1700 ppb, a typical concentration for a nitrogen doped homoepitaxial CVD. The ratio of N_s^0 to NVH^- to NV^- was as expected for nitrogen doped homoepitaxial CVD diamond. The concentration of the neutral single substitutional nitrogen in the intrinsic sample was 2.5 ppb which is typical for a low nitrogen homoepitaxial CVD sample and is approximately three orders of magnitude smaller than the nitrogen doped sample. The degree of nitrogen contamination in the intrinsic sample is much less than has been seen in previous heteroepitaxial samples and indicates an improvement in growth methods resulting in an improvement in sample quality. Both samples are within the normal range of CVD diamond for nitrogen defects and in the intrinsic diamond the nitrogen concentration similar to that in electronic grade CVD. However, the intrinsic sample has too large a concentration of silicon vacancy centres to be of electronic grade.

It is clear from this investigation that the material quality is not as high as homoepitaxial CVD due to the high degree of strain arising from the dislocation bundles. The concentration of the bundles is increased by the addition of nitrogen used to speed up growth, as seen in the nitrogen doped sample. Single crystal diamond, however, has successfully been fabricated, a key requirement for device applications. Earlier samples made on heteroepitaxial substrates were polycrystalline and showed significantly more strain and this has been reduced by lattice matching and improved growth chemistry [173]. The elimination of the grain boundaries increases the commercial utility of these diamonds but the high strain still impedes the electronic properties. Some applications, which require less high quality diamond, may be able to utilise the lower quality, larger samples, including films. The quality of these samples has not reached that of homoepitaxial CVD but improvements could be made, including a slower growth speed or post processing, which enhances their quality for use in similar applications. Though more work has to be done to match the quality of homoepitaxial CVD, this method has much potential as it could be used to grow larger scale diamonds on silicon substrates which could be cost effective in the future.

Chapter 8

Irradiation and Annealing of Silicon Doped Diamond

8.1 Introduction and Objectives

Silicon vacancy centres in diamond have the potential to be very useful, due to their electronic and optical properties. Many papers have been published about the negatively charged nitrogen vacancy centre in diamond (almost 1000 since 2010). However, the unique properties of the silicon vacancy centre may result in it being an important alternative for some applications.

The negatively charged silicon vacancy centre has been widely investigated. Properties of the centre include high emission in the zero-phonon line (ZPL) compared to the phonon side band; 70% to 80% of emission is in the ZPL. High spectral stability in a region of low background fluorescence [7]. The centre is the brightest diamond-based single photon source [84]. Emission of indistinguishable photons has been demonstrated [206, 74]. The spin state has been read-out via optically detected magnetic resonance (ODMR) [82, 207].

The neutrally charged silicon vacancy also has properties which could prove useful including; a steeper relationship between zero-field splitting (ZFS) and temperature [80] and the centre emits in a region where downconversion can be used to convert to current communication networks [208]. This demonstrates the incentive for reliably producing silicon vacancy centres.

Silicon vacancy centres have been produced using ion implantation [206] and dop-

ing during Chemical Vapour Deposition (CVD) growth [209, 210] and have also been created by High Pressure High Temperature synthesis (HPHT) [204, 211]. Silicon vacancy centres are very rare in natural diamonds but have been found in a handful [42].

Ion implantation is an effective method which can provide better control of the positioning of the silicon defects [212, 213]. However it also creates damage within the lattice [214, 215]. Some damage can be annealed out by HPHT annealing but there is a limit as with high implantation doses an amorphous carbon layer is formed which, when annealed, turns to graphite [216].

In this chapter a protocol for creating silicon vacancy defects using irradiation and annealing is tested. The protocol used is one which has previously been developed for creating high concentrations of nitrogen vacancy centres [217, 71]. This protocol is tested in two different diamonds. Sample 5 was grown on a {0 0 1}-orientated HPHT substrate and sample 6 was grown on a {1 1 0}-orientated HPHT substrate. Sample 5 was co-doped with boron and silicon and sample 6 began with a relatively high concentration of SiV^0.

The samples are CVD diamonds. A high concentration of silicon was present in these diamonds due to silane doping of the reactants during CVD growth, however the form in which the silicon was incorporated was not known. The method for creating silicon vacancy centres involved electron irradiation to increase the concentration of vacancies. The samples were then annealed to supply energy to allow migration of the vacancies so the substitutional silicon atoms formed silicon vacancy defects.

8.1.1 Irradiation and Annealing of Diamond

The main damage products of electron irradiation of diamond are vacancies and interstitials. It has been shown that these are more likely to be produced in regions of high strain which occur near impurities, such as nitrogen atoms and dislocations [72]. These impurities may trap the vacancies or interstitials. The vacancies created can be negative or neutrally charged. The interstitials created usually include R2 (henceforth called $I_{\langle 001\rangle}$), R1 and higher order interstitial complexes. $I_{\langle 001\rangle}$ consists of one interstitial carbon atom along the $\langle 001\rangle$ direction. R1 consists of two interstitial carbon atoms along the $\langle 001\rangle$ direction. There is more discussion of this in section 2.4.1.

$I_{\langle 001 \rangle}$ becomes mobile at 300°C, this allows it to migrate and recombine with vacancies or impurities. An anneal at 400°C will usually cause a 20 to 30% reduction in vacancy concentration due to vacancy-interstitial recombination [218]. Interstitial complexes can also form, as shown in equation 8.1, where X represents an atom such as nitrogen.

$$I + X \rightarrow complex \tag{8.1}$$

Vacancies become mobile above 600°C and at this temperature can migrate to defects and dislocations, termed traps. If the vacancies were those created near areas of strain related to defects they often become trapped at these centres as it is more energetically favourable to form vacancy defect centres than migrate away. Annealing of vacancies often exhibits two components; a fast component and a slow one. The fast component relates to the vacancies which recombine with interstitials and those which create vacancy related defect centres. The slower component relates to vacancies recombining with impurities, dislocations and surfaces which are farther away [218]. Vacancies can migrate to defects to create complexes as shown in equation 8.2. Di-vacancies can also form at this stage, as shown in equation 8.3.

$$V + X \rightarrow complex \tag{8.2}$$

$$V + V \rightarrow V_2 \tag{8.3}$$

The standard irradiation and annealing procedure to increase the concentration of nitrogen vacancy centres consists of irradiation followed by three anneals at different temperatures; 400°C, 800°C and 1200°C [219, 220, 71]. The first anneal supplies enough energy for the migration of interstitials to vacancies, dislocations and edges. The second anneal supplies enough energy for the migration of the vacancies. These too can migrate to dislocations and edges. It is also energetically favourable to form nitrogen vacancy centres as it reduces the local strain around the nitrogen atom [72, 53] and single substitutional nitrogen is an effective trap for vacancies [73]. This is shown in equation 8.4.

$$N_s + V \rightarrow NV \tag{8.4}$$

The third anneal causes dissociation of di-vacancies, which may then create nitrogen vacancy centres [58]. An anneal at 1200°C supplies enough energy to dissociate di-vacancies but not nitrogen vacancies

The protocol is based on the assumption that there is a higher concentration of single substitutional nitrogen atoms than nitrogen vacancy centres; the ratio is between 300 and 1000 to 1 for a CVD diamond grown on a {0 0 1}-orientated substrate, though these numbers differ for different substrates [221]. For most as-grown diamond the inequality $N \gg NV,\ NV : H$ holds true. Thus if vacancies are created and annealed there are nitrogen atoms at which these vacancies can be trapped.

In diamonds which contain single substitutional silicon atoms these can be an effective trap for vacancies, as shown in equation 8.5, as a vacancy reduces local strain around the silicon atom.

$$Si_s + V \rightarrow SiV \tag{8.5}$$

The concentration of silicon vacancy centres has been found to reach a maximum after an 800°C anneal and decrease with anneals of higher temperatures though can be increased again after anneals of 1300°C [218]. In the intermediate temperatures another defect has been seen by Kiflawi et al. [222] which is thought to be silicon related. This defect is seen in conjunction with negative silicon vacancy in samples with low nitrogen concentration. The defect may be made up of three peaks at 725 nm, 733 nm and 738 nm, though it is not yet certain if these are related. The 733 nm may be related to silicon di-vacancy [222]. When the intention is to increase the silicon vacancy concentration an anneal of four hours at 800°C has been found to be the most effective, after this time the silicon vacancy concentration plateaus [218]. This is the procedure which has successfully been employed previously to create silicon vacancy centres, however, it relies on a high concentration of single substitutional silicon atoms and the inequality $Si \gg SiV,\ SiV : H$ is required to hold.

The Effect of Boron on Irradiation and Annealing

The presence of boron within a diamond has an effect on the concentration of $I_{\langle 001 \rangle}$ and vacancies after irradiation. When comparing the irradiation of a sample with

a significant concentration of boron and one without, a higher irradiation dose is required before vacancies are detected [223, 224]. There exist various theories as to the reason. One reason may be charge transfer effects. The reduced measurable vacancy concentration could arise if the vacancies are present in their positive state (V^+), a state which has not yet been detected experimentally. The lower than expected concentration of $I_{\langle 001 \rangle}$ may be due to a interstitial-boron complex [225]. In heterogeneously doped samples reduction in vacancies and interstitials by boron may be occurring in some regions and not others.

8.2 Treatment Techniques

8.2.1 The Samples

CVD diamonds often have unintentionally silicon contamination due to etching from the reactor walls and windows (more details can be found about this process in section 2.2.4). Silicon can also be added intentionally by the addition of silane gas (SiH_4) to the reaction gas mixture [40]. The silicon atoms add onto the surface of the diamond as it forms, with the final concentration determined by the reaction gas mixture and substrate orientation [40].

Two CVD diamonds were treated, sample 5 and sample 6 both of which were grown using CVD by E6 Global Innovations. Sample 5 is a CVD diamond grown on a {0 0 1}-orientated HPHT diamond substrate. The sample had a silicon doped layer sandwiched between two boron doped layers. The DiamondView^{TM} image is shown in figure 8.1a. The photoluminescence and infra-red absorption results presented in this chapter were all taken through the top of the sample. Sample 6 is a CVD diamond grown on a {1 1 0}-orientated diamond. Sample 5 had a natural abundance of the ^{29}Si isotope, which is 4.7%, whereas in sample 6 it was enhanced to 90%. Silicon vacancy incorporation in CVD samples is higher when the substrate is {1 1 0}-orientation as compared to {0 0 1}-orientation [70].

The concentrations of boron and silicon in the layers as-grown in sample 5 were measured by SIMS. The concentrations measured are shown in table 8.1. Additionally, it is likely that the first material grown is intrinsic (has neither silicon nor boron doping) so the concentration in layer 1 may vary across the layer.

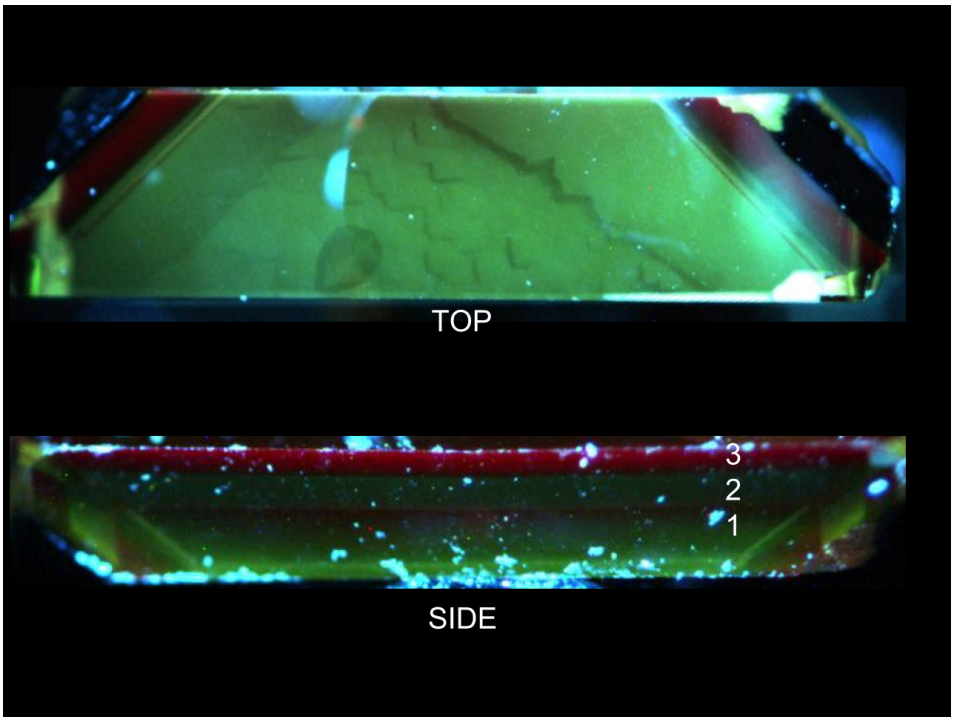

(a) *DiamondView^{TM} image of sample 5. Showing the top growth surface and the side surface with layers visible. Green indicates silicon doped layer and red indicates boron doped layer. Bright spots are dust or scratches on the surface of the diamond. Sample size is* 0.69 mm × 1.02 mm × 4.14 mm. *Image taken after temp1 anneal.*

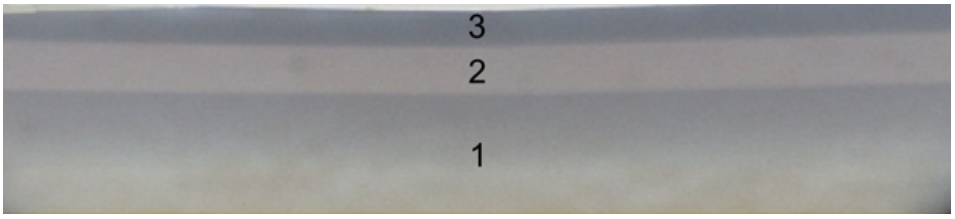

(b) *Optical image of sister sample to sample 5, showing layers of* {1 1 0} *cross section. This sample has not been irradiated.*

Figure 8.1: *Layers of sample 5. Layer 1 is approximately 390 µm and is predominantly boron doped. Layer 2 is approximately 180 µm and is predominantly silicon doped. Layer 3 is approximately 115 µm and is boron and silicon doped.*

Region	Boron (ppb)	Silicon (ppb)	Thickness (μm)
Layer 1	1000	300	390
Layer 2	100	300	180
Layer 3	1000	1000	115

Table 8.1: *Details of doped layers of sample 5. Measurements made by SIMS.*

8.2.2 Electron Irradiation

Electron irradiation was performed, as detailed in section 4.6. Electron irradiation is a technique which introduces disorder into the lattice with high energy electrons. These electrons have enough kinetic energy to knock atoms off their lattice site and create vacancies, interstitials and higher order interstitial complexes. For this work a 2 MeV electron accelerator was used which had a current of 12 mA and the irradiation took 3 hours for sample 5 and 6 hours for sample 6. The samples sat on a water cooled table. The electron gun head was 10 cm by 60 cm. The resulting defect concentration was estimated from the experimental data.

8.2.3 Annealing

The details of the annealing procedure and the furnace used are in section 4.7. During the anneal nitrogen flowed over the surface of the diamond to reduce oxidation of the surface. The standard procedure involves three anneals; one at 400°C for four hours, the second at 800°C for two hours and a third at 1200°C for two hours [71]. In section 8.1.1 this procedure is discussed in more detail. For this work only the two lower temperature anneals were performed as it was assumed that the concentration of di-vacancy centres was small as the majority of vacancies would have migrated to nitrogen or silicon atoms during the second (800°C) anneal. Sample 5 was annealed at temp1 and temp2, as detailed in table 8.2. Sample 6 was annealed at temp1, temp2 and temp3. All anneals lasted four hours.

Anneal Number	Target Temperature
temp1	400°C
temp2	800°C
temp3	800°C

Table 8.2: *Target annealing temperatures.*

8.3 Treatment Results

8.3.1 Photoluminescence Results

Photoluminescence (PL) was performed at 77 K to study the changes in the defects present. Measurements were taken of sample 5 before and after irradiation, after the temp1 anneal and after the temp2 anneal. The PL was done on the top surface of the diamond, as shown in figure 8.1a. Measurements were taken of sample 6 after irradiation, after the temp1 anneal, after the temp2 anneal and after the temp3 anneal. Whilst these results may be used qualitatively, the laser used during PL may be causing charge transfer, so the comparative intensities may not be a true reflection of the comparative concentration.

In figure 8.2a a line scan from the bottom to the top of sample 5 can be seen. This scan was taken before irradiation. This scan shows the concentrations of the neutral and negative silicon vacancy centre and the neutral nitrogen vacancy centre are highest in layer 2 which was silicon doped.

The PL results of the top of the sample after irradiation for sample 5 are shown in figure 8.4. This shows the 737 nm peak from SiV^-, the 741 nm peak from GR1 associated with the neutral vacancy and the peak at approximately 745 nm also associated with the neutral vacancy. The 745 nm peak moves to a lower wavelength position when measured below room temperature. After the temp2 anneal a decrease of 10±1% is seen in the integrated intensity of the neutral vacancy peak and an increase of 35±4% was seen in the SiV^- peak. In figure 8.4b the peak at 946 nm, which relates to the SiV^0 can also be seen.

Line scans of the side of the diamond were also taken after irradiation and annealing and these can be seen in figure 8.2b and figure 8.3. Figure 8.3 indicates the neutral vacancy concentration is highest in the low boron regions. This also shows

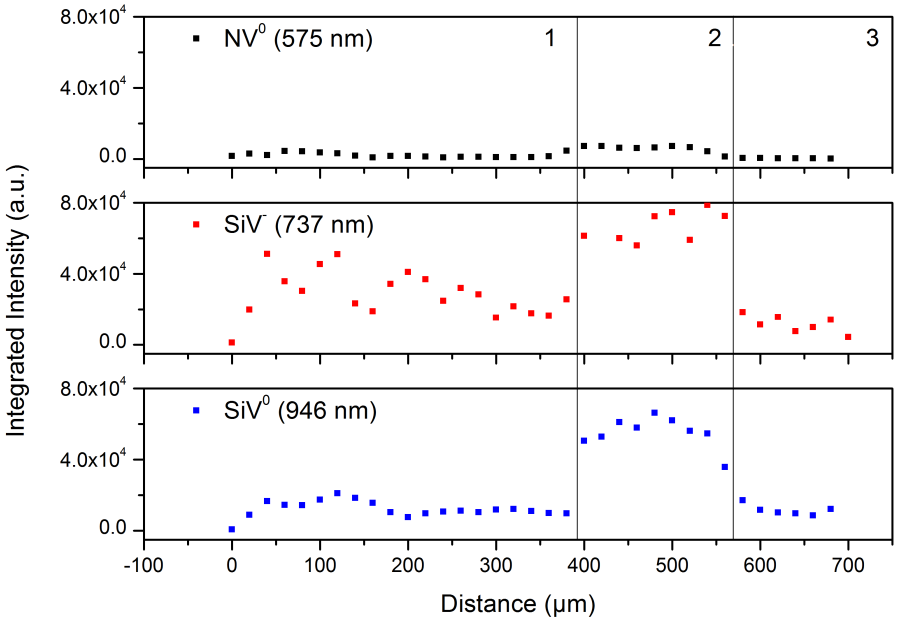

(a) *Photoluminescence line scan of sample 5 before irradiation and annealing. The laser used for each data set was different. The scan over 575 nm was taken with a 514 nm laser, the scan over 737 nm was taken with a 633 nm laser and the scan over 946 nm was taken with a 785 nm laser. Data taken by Dr D'Haenens-Johansson.*

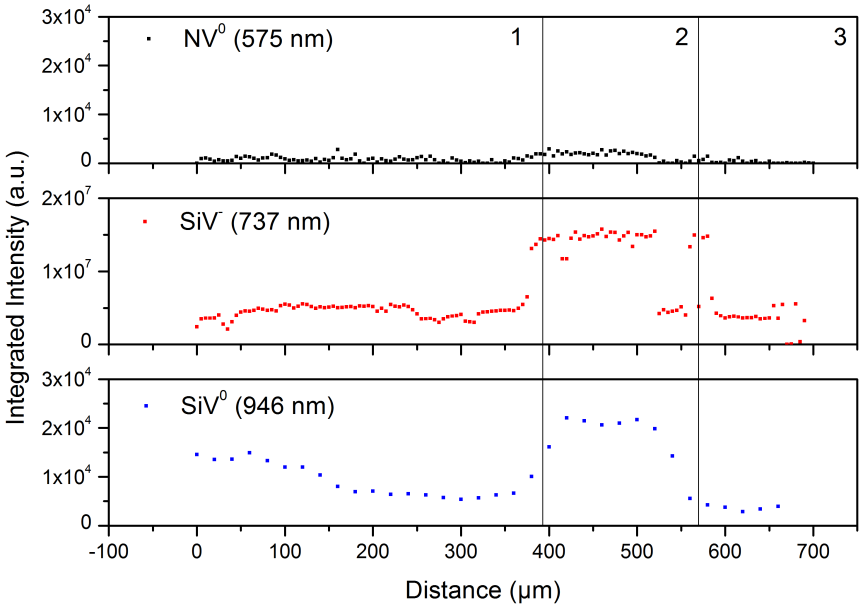

(b) *Photoluminescence line scan of sample 5 after irradiation and annealing. Note scale of second plot (SiV^-) is different to the others. The laser used was 532 nm. Data taken by Dr Breeze.*

Figure 8.2: *Photoluminescence line scans of before and after irradiation and annealing of sample 5, taken at 77 K. Distances are measured from the bottom to the top of the sample, as shown in figure 8.1, showing the three regions. Layer 1 is approximately 390 μm and is boron doped. Layer 2 is approximately 180 μm and is silicon doped. Layer 3 is approximately 115 μm and is boron doped.*

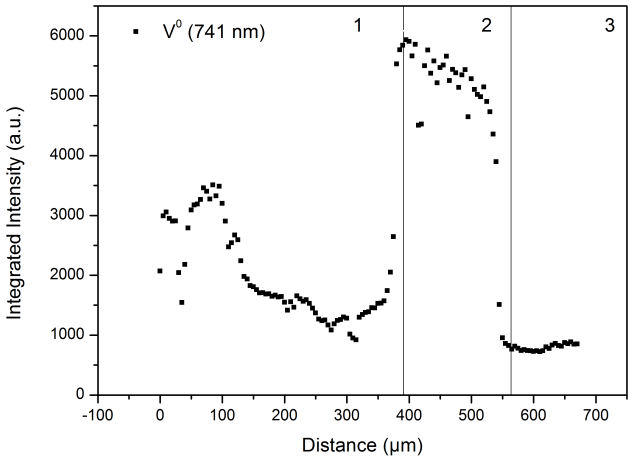

Figure 8.3: *Line scan of neutral vacancy peak after irradiation and all anneals, at 77 K. Data taken by Dr Breeze.*

that there are vacancy centres remaining after the annealing and that another anneal may further increase the silicon vacancy centre concentration.

The PL results for sample 6 are shown in figure 8.5. Figure 8.5a shows three peaks, an unknown 735.7 nm peak, the 741 nm peak from GR1 associated with the neutral vacancy and the 745 nm peak also associated with the neutral vacancy. As can be seen from figure 8.5a the neutral vacancy concentration decreases after each anneal. At 400°C interstitials are mobile so this decrease is caused by vacancy-interstitial recombination. The integrated ZPL intensity shows a decrease of 44±5% after the temp1 anneal. This decrease in the vacancy concentration after the first anneal is consistent with interstitial migration causing interstitial-vacancy recombination. After the third anneal of sample 6 the vacancy concentration is very low.

A peak from a silicon related defect appears after the temp2 anneal at 738.2 nm, along with two other peaks. These three peaks have previously been seen in irradiated and annealed silicon doped CVD diamonds by Kiflawi et al. as discussed previously [222], however that work only studied the centre in absorption not emission. The peak at 738.2 nm increases by 4.0±0.4%, in conjunction with decreasing vacancy concentration, after the temp3 anneal. Kiflawi et al. saw an increase in this peak in conjunction with a decrease in luminescence from the SiV^- peak, however SiV^- recovered after heating to 1300°C. Two other peaks also appear after the temp2 anneal one at 725.0 nm and one at 733.2 nm, again both have been seen by Kiflawi et al and appear to anneal in and out in conjunction. In this spectrum a very small peak can be made out on the side of the 738.2 nm, this

is the 737 nm peak (from SiV^-), however it is swamped by the 738.2 nm peak.

8.3.2 Infra-red Absorption

Infra-red (IR) absorption was used to investigate the changes in the form of boron. The normalised IR absorption for sample 5 can be seen in figure 8.6. The IR was measured though the diamond from the top, shown in figure 8.1a, in the centre. The IR absorption is thus a total absorption for the three layers of the sample. Figure 8.6 shows characteristic absorption from single substitutional neutral boron in the three phonon region (the region above 2664 cm^{-1}). The peak in the one phonon region (below 1332 cm^{-1}) is also associated with boron. After the temp1 anneal the neutral (uncompensated) boron absorption decreases.

The concentration of uncompensated boron present can be calculated by considering the height of the 2802 cm^{-1} absorption peak using the method outlined in reference [226]. This gives the as-irradiated concentration to be 250±25 ppb, the concentration after the temp1 anneal to be 230±23 ppb and the concentration after the temp2 anneal to be 230±23 ppb.

Additionally, this sample was only boron doped in some regions (approximately 50% of the thickness of the diamond) with other regions showing a residual boron concentration, see table 8.1. The boron concentration measured will be an average of the high concentration regions and low concentration regions. If it is assumed that the boron is only present in the boron doped regions this gives these regions a concentration of 500 ppb before annealing. The boron concentrations are shown in table 8.3.

	As-grown	**As-irradiated**	**temp1 Anneal**	**temp2 Anneal**
B^0	1000 ppb	500±50 ppb	460±46 ppb	460±46 ppb

Table 8.3: *Changes in the boron concentration in the boron doped region in sample 5.*

The change in boron gives an indirect measurement of the vacancy concentration after irradiation, if it is assumed that the decrease in uncompensated boron is a result of the increased vacancy concentration as given by equation 8.6. Before irradiation the concentration of boron was 1000 ppb in the boron doped regions, as measured by SIMS. This indicates the vacancy concentration is 500 ppb, after

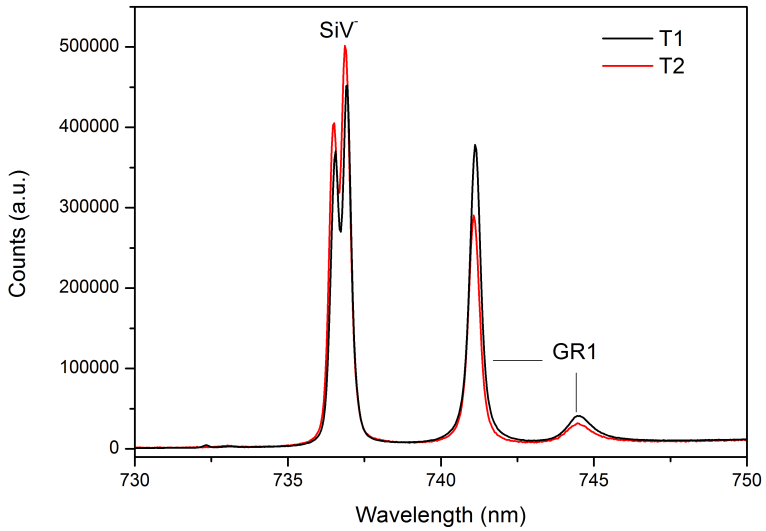

(a) *Photoluminescence spectra after the temp1 and temp2 anneals of sample 5, taken at 77K. Spectra are normalised to the laser Raman line and the laser used was 633 nm.*

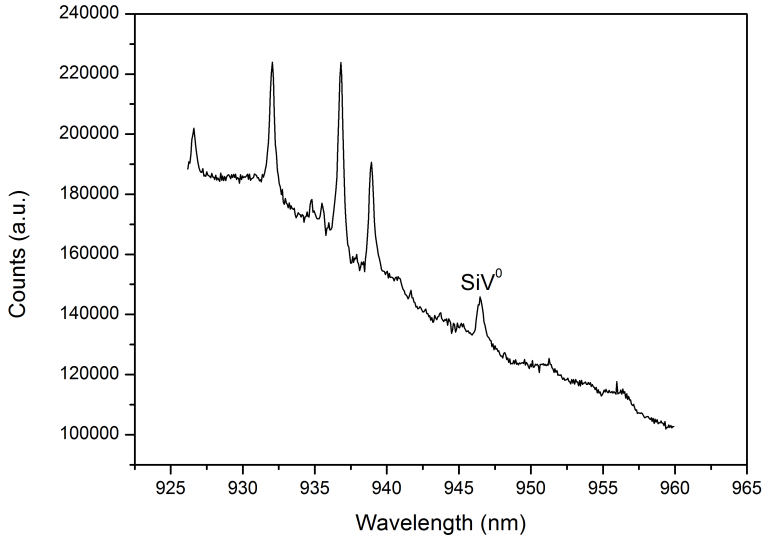

(b) *Photoluminescence spectra after both anneals of sample 5, taken at room temperature. Additional peaks to the left of SiV^0 are boron related. Laser used was 785nm.*

Figure 8.4: *Photoluminescence spectra of before and after annealing of sample 5. PL of top of sample.*

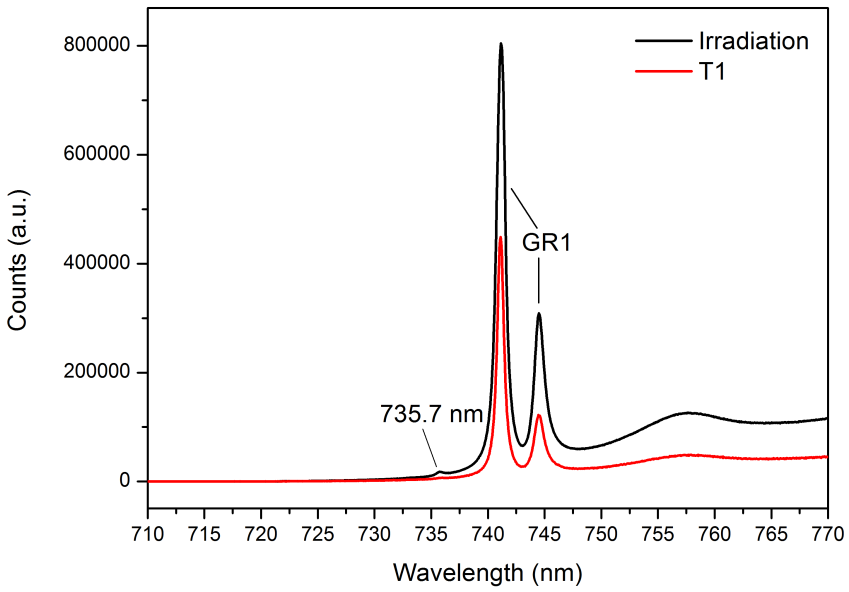

(a) *A photoluminescence spectrum showing the sample after electron annealing and after the temp1 anneal. A decrease in GR1 can be seen, both of which are vacancy related. GR1 after annealing is decreased to 44% of its original value.*

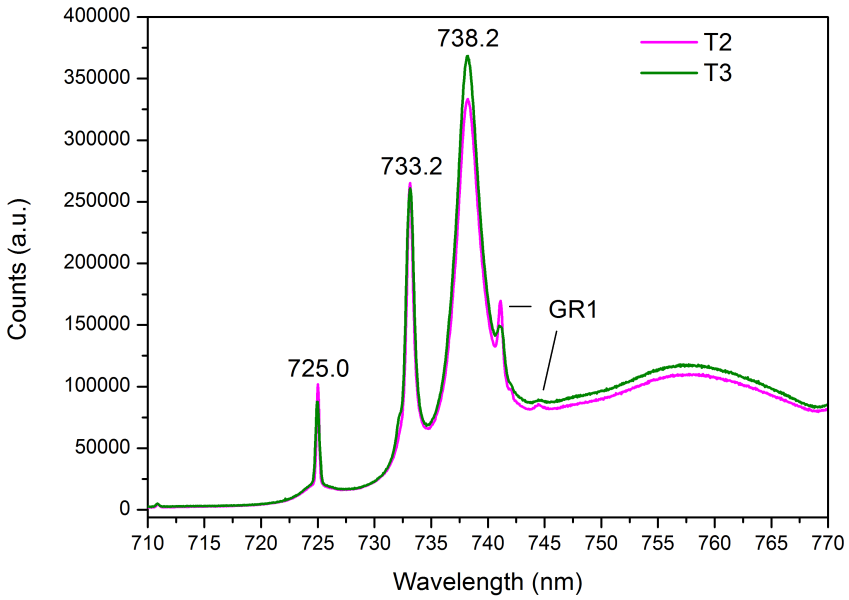

(b) *A photoluminescence graph of after the anneal at temp2 and temp3. The 738.2 peak shows a 4% increase after the second anneal.*

Figure 8.5: *Photoluminescence spectra of before and after annealing the sample, taken at 77K. This is sample 6 which is 90% ^{29}Si enriched. Spectra are normalised to the laser Raman line and the laser used was 633 nm.*

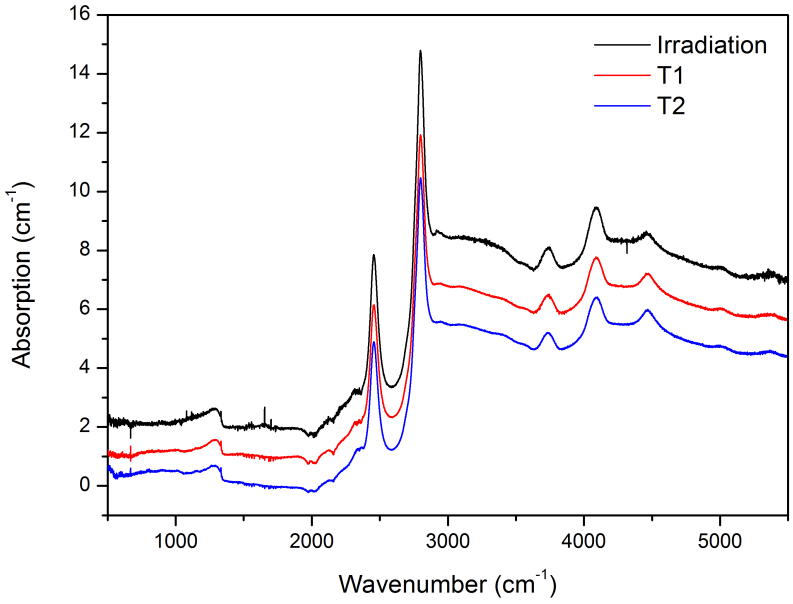

Figure 8.6: *Normalised IR spectrum of sample 5 after irradiation and after the two anneals with the IIa spectrum removed. Spectra offset for clarity.*

irradiation.

$$V^0 + B^0 \rightarrow V^+ + B^- \tag{8.6}$$

After the temp1 anneal the boron concentration decreased by 20 ppb, but this number is within the error of the measurement.

8.3.3 Ultraviolet and Visible Absorption

A UV/visible spectrum of sample 5 after the irradiation and annealing is shown in figure 8.7. This spectrum shows both charge states of the silicon vacancy as well as a significant signal from the neutral vacancy.

8.3.4 Electron Paramagnetic Resonance

Electron paramagnetic resonance (EPR) was used to calculate the changes in the negative vacancy and neutral silicon vacancy defect concentrations. In figure 8.8 the EPR spectrum of sample 5 is seen before and after the second annealing

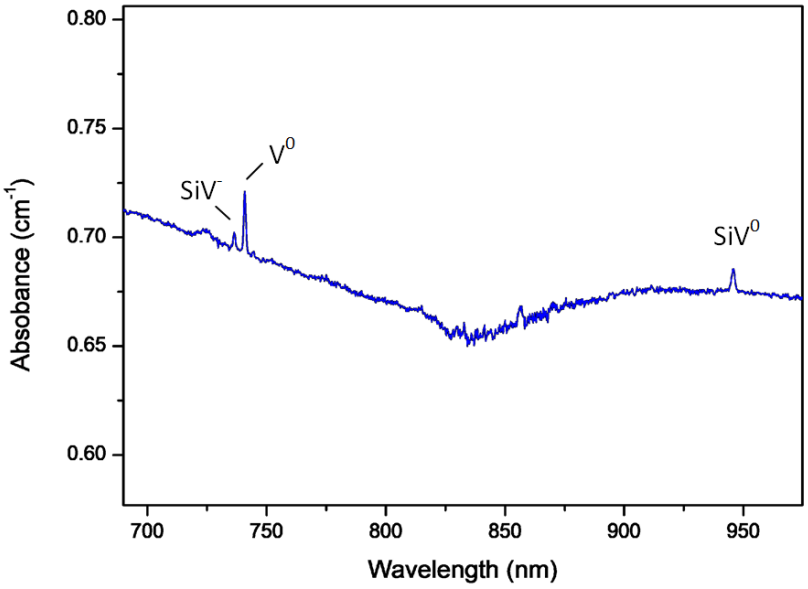

Figure 8.7: *UV/vis spectrum of sample 5 at 77K. Peak at 737 nm is SiV^-, peak at 741 nm is V^0 and peak at 946 nm is SiV^0. Region of noise at 850 nm is due to detector change over. These data was taken after both annealing treatments. Data taken by Dr Breeze.*

treatment. The central sharp feature is SiV^0, the broader feature is V^- and the smaller features seen, symmetrically at 300 G apart and 600 G apart arise from R1.

$I_{\langle 001 \rangle}$ was not seen in sample 5, however the peaks are very broad so can be hard to detect at low concentrations.

In the first spectrum 8.8a R1, SiV^0 and V^- features can be been seen. In the second spectrum 8.8b the R1 signals have reduced to below the detection limit, V^- has reduced and the SiV^0 signal has increased. This spectrum can be seen in more detail in figure 8.9. The concentration changes of each are shown in table 8.4. The EPR signal assigned to the negative vacancy could also have contributions from a neutral boron signal.

Species	After temp1 Anneal (ppb)	After temp2 Anneal (ppb)
SiV^0	2.3±0.4	4.0±0.8
V^-	1.8±0.4	1.7±0.4

Table 8.4: *Concentration of SiV^0 and V^- in sample 5 before and after second anneal as calculated by EPR. The sample was in the lab state when measured.*

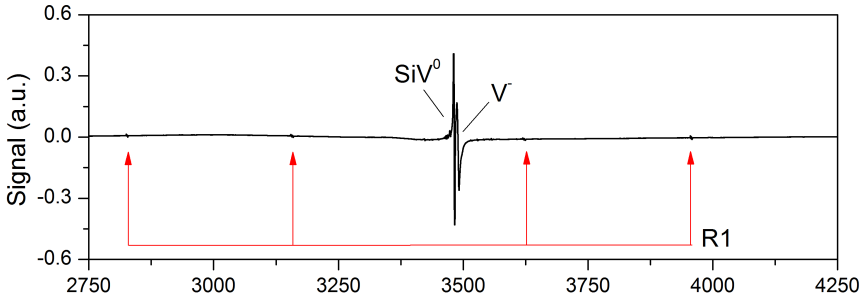

(a) *EPR spectrum of sample 5 after temp1 anneal.*

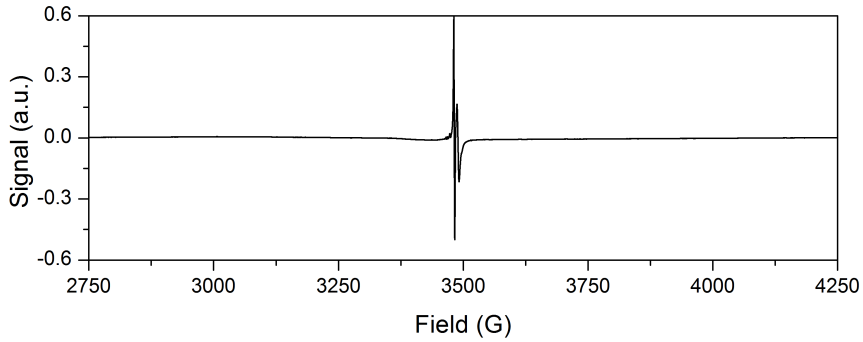

(b) *EPR spectrum of sample 5 after temp2 anneal.*

Figure 8.8: *EPR spectrum changes before and after second annealing of sample 5. Orientation is $B\|\langle 001\rangle$ as determined by the R1 lines. The graphs have been normalised to each other, so changes between the two spectra are indicative of changes in the material. The data was taken at room temperature.*

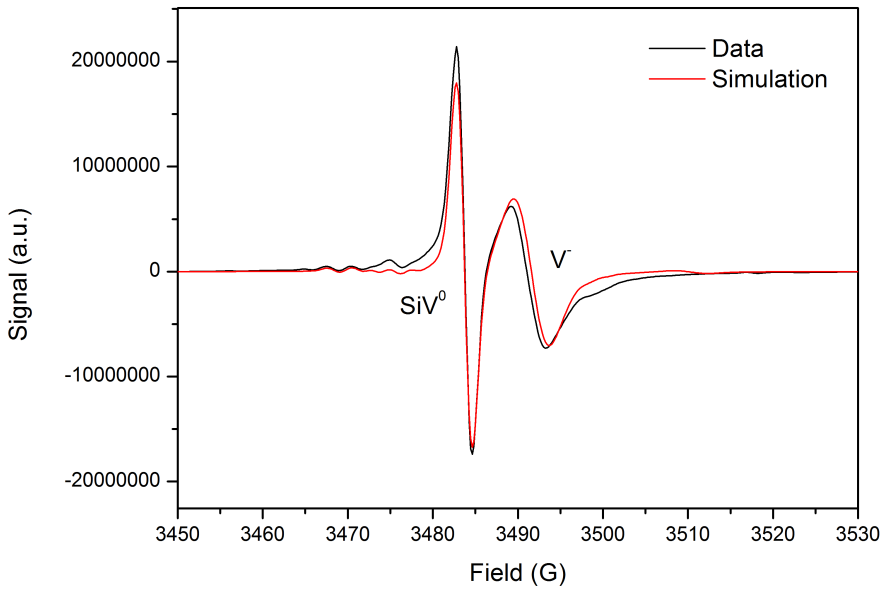

Figure 8.9: *EPR of sample 5 showing simulation of negative vacancy and neutral silicon vacancy.*

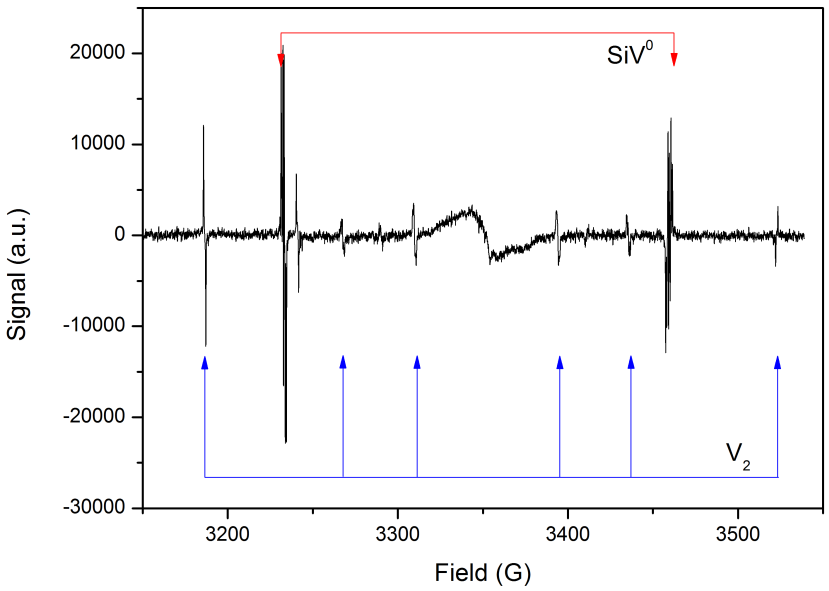

Figure 8.10: *EPR spectrum of V_2 and SiV^0 of sample 5 after annealing. Orientation is B‖ ⟨111⟩ as determined by the SiV^0 lines and microwave power is 60 dB. The outermost high field and low field lines of SiV^0 are not seen as they not within the range of the scan. Temperature is 10 K and illumination is 80 mW at 450 nm.*

In figure 8.10 an EPR spectrum taken at 10 K of sample 5 after both anneals is shown. In this spectrum the V_2 can be seen. The intensities of the lines are not true intensities as the sample is illuminated and V_2 is electron spin polarised.

The EPR spectrum for sample 6 is shown in figure 8.11, orientated in the B‖ ⟨111⟩ direction. Before irradiation and annealing large signals from SiV^0 can be seen. The ^{29}Si hyperfine satellites can be seen either side of the ^{28}Si lines. They are higher than the ^{28}Si lines because the ^{29}Si has been enhanced to 90%.

The figures 8.12a and 8.12b show the EPR spectra after irradiation and annealing respectively. The spectra are orientated in the B‖ ⟨001⟩ direction instead of the B‖ ⟨111⟩ direction. Before annealing signals from both R1 and $I_{\langle 001\rangle}$ are seen. After annealing a decrease in R1 is seen, just as for sample 5. After irradiation there are multiple EPR lines near the central line which are related to irradiation damage. These decrease after annealing but are still present. A neutral silicon vacancy signal was not detected.

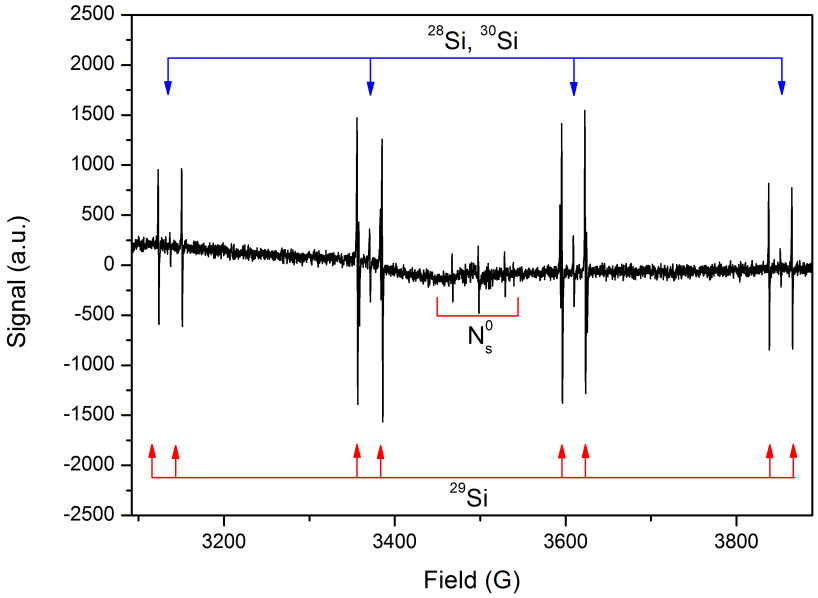

Figure 8.11: *EPR spectrum of sample 6 as grown. Scan taken at room temperature at 40 dB. Orientation is B‖ ⟨111⟩.*

8.4 Discussion and Conclusions

This chapter presented the irradiation and annealing treatment of two samples with the intention of increasing the silicon vacancy concentration. Both samples were doped with silicon during growth and sample 6 also started with a significant concentration of SiV^0, as measured by EPR. The literature discussed indicates that irradiating and annealing silicon doped CVD diamond may increase the concentration of both charge states of the silicon vacancy, as single substitutional silicon atoms present in the material act as traps. To investigate this hypothesis the two CVD diamonds, one of which contained layers co-doped with nitrogen and boron impurities and the other co-doped with nitrogen, were irradiated with 2 MeV electrons and annealed.

8.4.1 Discussion of Sample 5

The IR results show a neutral boron concentration of 500 ppb after irradiation in the boron doped regions, smaller than the initial SIMS measurements, which measured 1000 ppb in the boron doped regions. As the neutral boron decrease

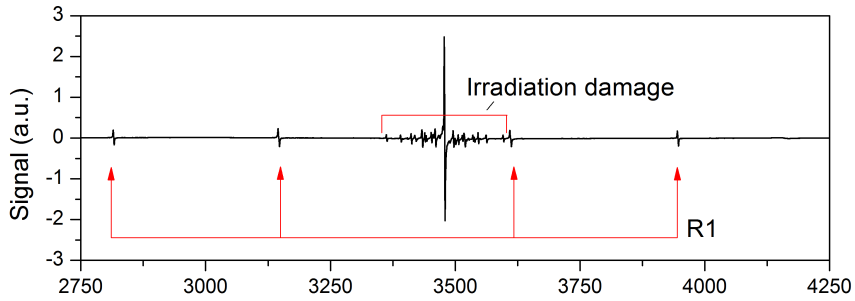

(a) *EPR spectrum of sample 6 after irradiation.*

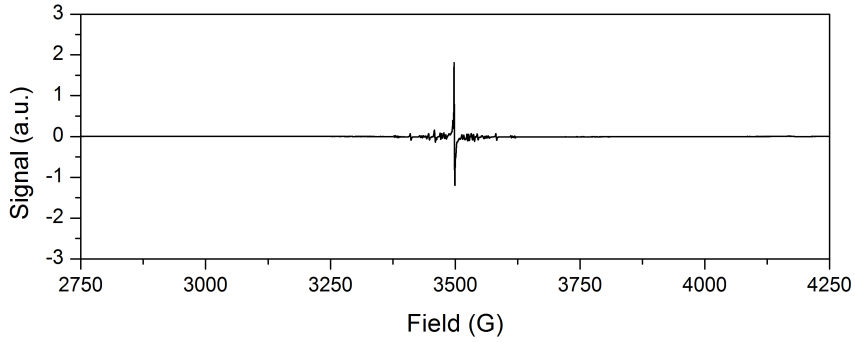

(b) *EPR spectrum of sample 6 after all anneals.*

Figure 8.12: *EPR spectrum changes before and after annealing of sample 6. Orientation is $B\|\langle 001\rangle$ for (a) and unknown for (b) as there were no known signals present to align to. Spectra taken at room temperature. The graphs have been normalised to each other, so changes between the two spectra are indicative of changes in the material.*

is likely due to accepting electrons from vacancies. This allowed an approximate vacancy concentration to be estimated as 500 ppb.

The PL results from sample 5 indicate that after the temp2 (target temperature 800°C) anneal the neutral vacancy peak decreases slightly and the SiV^- peak increases. The presence of vacancies after an anneal at temp2, was confirmed by EPR, PL and absorption experiments. This indicates that the target temperature of 800°C was not reached as vacancies anneal out at temperatures lower than this. PL line scans performed after the annealing showed a higher concentration of neutral nitrogen vacancy and neutral and negative silicon vacancy in the silicon doped region. Additionally, neutral vacancy was also measured after annealing and was highest in the silicon doped region. This indicates boron doping is suppressing the formation of these centres.

Boron will promote the neutral charge state over the negative of the silicon vacancy. This effect has been confirmed by other experiments [143]. The low boron region which was doped with silicon is likely to be the region of highest neutral and negative silicon vacancy concentration and this has been demonstrated by the PL line scans. In the boron doped region a high concentration of neutral silicon vacancy is more likely. The UV/visible absorption data indicates there are similar absorptions of the neutral and negative silicon vacancy which indicates there are likely to be more negative silicon vacancy centres in the non boron doped region. Additionally it is clear from the line scans that both charge states measured of the silicon vacancy are suppressed in the boron doped region. Layer 3 is boron doped and silicon doped to the same degree as layer 2 (where there is a large concentration of silicon vacancies), however the resulting silicon vacancy concentration, of both charge states, is lower. This indicates the boron doping is directly reducing the final silicon vacancy concentration in the negative and neutral charge states. The positive charge state of silicon vacancy has not yet been identified, but it is possible that this charge state is being promoted as boron acts as an acceptor.

The EPR results allowed for quantitative measurements of the SiV^0 concentration and the V^- concentration. After annealing, the concentration of SiV^0 in sample 5 increased from 2.3±0.2 ppb to 4.0±0.4 ppb. As the boron doping suppresses the silicon vacancy centres, the centres are concentrated in the silicon doped region and that local concentrations may be higher. The measured negative vacancy concentration decreased from 1.8±0.2 ppb to 1.7±0.2 ppb, although this change is within error. The vacancy concentration was not measured after irradiation but after the temp1 anneal. An anneal at 400°C (the target of temp1) will cause

vacancy-interstitial recombination and so the vacancy concentration may be less than was initially present. Additionally vacancies are present in the neutral state as can be seen in the PL spectrum. The neutral vacancy concentration was estimated by considering the change in neutral boron in the boron doped regions, giving a concentration of 500 ppb. Even considering both charge states, there are fewer vacancies measured than expected from the dose. The boron may additionally have enhanced the positive vacancy state, which has not yet been identified.

The di-vacancy was seen at low temperatures in EPR. This indicates a possible lack of substitutional silicon or nitrogen atoms with which the vacancies can combine. Possibly the di-vacancies are concentrated in the boron doped layer with less silicon, layer 1. When annealing diamonds to increase their nitrogen vacancy concentration a final anneal at 1200°C is performed to cause dissociation of di-vacancies. For this work that was not done as it was assumed that the silicon concentration was high enough to trap all the vacancies present. This anneal may have been beneficial.

In sample 5 the concentration of silicon vacancy centres was successfully increased. However, boron doping suppressed both the creation of vacancy centres during irradiation and the creation of silicon vacancies during annealing. Additionally, some vacancies remained at the end of the annealing treatment so further annealing, including to 1200°C to disassociate di-vacancies, may have further increased the silicon vacancy concentration. This sample was subsequently used for the experiments in Chapter 5. For the experiments presented in that chapter it was vital to have a significant neutral silicon vacancy concentration to increase signal and reduce experiment time when investigating relaxation times and electron polarisation behaviour.

8.4.2 Discussion of Sample 6

Sample 6 started with a high concentration of neutral silicon vacancy centres, as measured by EPR to be >50 ppb. Sample 6 is also likely to have a higher total silicon content than sample 5, as it was grown on a $\{1\,1\,0\}$-orientated substrate to which incorporation of silicon is more efficient [70]. Additionally, it had a larger concentration of vacancies and interstitials as it was irradiated for longer.

After the irradiation and annealing treatment neither the negative nor the neutral state of the silicon vacancy is present in a measurable concentration. A very

small peak from the negative silicon vacancy is seen in the PL signal, but this is swamped by the larger signal from the peak at 738.2 nm. The decrease in silicon vacancy centres which were grown in could be related to interactions with interstitials. The neutral silicon vacancy EPR signal was below the detection limit after irradiation, which suggests that the silicon vacancies disappeared during the irradiation process. Interstitials are mobile at room temperature so a silicon-vacancy-interstitial complex could have been made. In EPR radiation damage was present after the irradiation treatment which could not be identified. This could possibly be related to a silicon-vacancy-interstitial complex.

Another possibility is that the grown in silicon vacancies are trapping vacancies to become silicon di-vacancies. In the PL spectra the peak seen at 733 nm has previously been linked with the silicon di-vacancy, and this peak is significant in this sample. The creation of silicon di-vacancies could be induced because the local strain around the silicon vacancies already present creates an increased likelihood of vacancy production upon irradiation. These new vacancies are local to the silicon vacancies so silicon di-vacancies are the result.

This result suggests the as-grown diamond contained a higher concentration of silicon vacancy centres than single substitutional silicon atoms, as given by the inequality $SiV \gg Si_s$ and this has resulted in a significant decrease in silicon vacancy centres after irradiation and annealing. This sample demonstrates that the postulate that irradiation and annealing of a silicon doped diamond will result in a high concentration of silicon vacancy centres does not hold true in situations where there are large numbers of traps which are not substitutional silicon atoms.

8.4.3 Conclusions

These results show that the effectiveness of irradiation and annealing procedures for increasing the concentration of silicon vacancy centres is highly sample dependent. The success of the procedure relies on the concentration of silicon substitutional atoms being greater than that of silicon vacancies, and this could be dependent upon the orientation of the substrate from which the sample was grown. If there is an excess of single substitutional silicon atoms the silicon vacancy concentration can be increased. However, for samples which have a high silicon vacancy concentration in the as-grown state this is not the case and the silicon vacancy concentration will decrease while another peak assigned to silicon di-vacancies is created. The details of silicon vacancy defect production, especially in boron

doped diamond, are not yet well understood.

Chapter 9

Summary

In this thesis a variety of spectroscopic techniques have been employed to investigate defect centres in chemical vapour deposition (CVD) and high pressure high temperature (HPHT) diamond. These techniques have consisted of both continuous wave and pulsed electron paramagnetic resonance (EPR), optical absorption, optical polarisation microscopy, photoluminescence (PL) and cathodoluminescence (CL) and secondary ion mass spectroscopy (SIMS).

One of the primary defects investigated was the neutral silicon vacancy (SiV^0), a promising centre for use in quantum technologies. The electron spin polarisation and relaxation behaviour of the defect was studied using EPR in order to further elucidate the electronic structure and spin properties of the centre.

In the second experimental chapter a suite of HPHT diamonds were investigated which had been grown from a source and a solvent which had varying concentrations of the ^{13}C isotope and thus created diamonds with different concentrations of the ^{13}C isotope. These samples were investigated by PL, CL and SIMS and this allowed the HPHT process to be understood in greater detail.

Two diamonds made by heteroepitaxial CVD were investigated. The work presented here indicates the samples are single crystal diamond but are highly strained. The defects and strain were investigated using EPR and PL respectively.

The final chapter of experimental results reports an investigation into some of the complexities of irradiation and annealing silicon doped diamond. Two CVD diamond samples with different doping and growth orientation underwent the same treatment and showed markedly different behaviour. This was investigated using

EPR, optical absorption and PL.

The following sections summarise the results of the experimental chapters in more detail.

9.1 The Neutral Silicon Vacancy Centre

In the first experimental chapter, Chapter 5, the SiV^0 centre is discussed. Whilst much current work on diamond involves investigation of the negatively charged nitrogen vacancy centre (NV^-), the SiV^0 centre is also worth investigation as it has similarities to the nitrogen vacancy centre as well as some distinct advantages. These advantages include higher emission in the zero-phonon line (ZPL) when compared to the phonon side band and a steeper relationship between the zero-field splitting (ZFS) and temperature. In this chapter this defect was studied to understand further the energy levels.

9.1.1 Electron Spin Polarisation of the Neutral Silicon Vacancy Centre

The SiV^0 centre was known to electron spin polarise under illumination. In the first part of this chapter the electron spin polarisation was measured under different illumination wavelengths and at different temperatures. At temperatures below 30 K resonant excitation at the ZPL showed a significantly higher electron spin polarisation than with adjacent wavelengths. However, there was sample to sample variation which indicates the spin polarisation mechanisms are sample dependent. The increase in electron spin polarisation with ZPL excitation conclusively confirmed the link between the ZPL seen at 946 nm and the EPR signal of SiV^0. This also indicated that there exists at least one electron spin polarisation mechanism which is internal to SiV^0 and does not require other defects. Spin polarisation at energies below the ZPL, and at much higher energies indicated that the spin polarisation mechanism is not identical to that observed for the much studied negatively charged nitrogen vacancy defect in diamond and indeed more than one mechanism may be generating or destroying optical spin polarisation. These mechanisms may be occurring concurrently. Two different possible electronic structures were proposed which explain the observed spin polarisation. Further work is required to understand this phenomenon fully, nevertheless these

results suggest that SiV^0 is a promising candidate for a long-range quantum communication technology.

9.1.2 Relaxation Rates of the Neutral Silicon Vacancy

The spin-spin (T_2) and spin-lattice (T_1) relaxation times of the SiV^0 centre were measured at temperatures ranging from 11 to 300 K using pulsed EPR. This utilised optical spin polarisation initialisation, to avoid the rate changing effect of optical illumination, with the use of an acousto-optic modulator (AOM). T_1 was seen to change by six orders of magnitude. The pattern seen was modelled phenomenologically which allowed the dominant effects at different temperatures to be investigated. This indicated the key phenomena are a Raman process and an Orbach process.

9.2 HPHT Growth of ^{13}C Enhanced Diamond

Changing the carbon isotope concentration in diamonds is of interest for technological applications such as stress sensors and heat spreaders. However many of these applications require a reliable and uniform distribution of isotopic enhancement.

In Chapter 6 four diamonds were investigated which had been created by HPHT synthesis. In each of the diamonds different concentrations of the stable isotope ^{13}C were present in the carbon source and the metal solvent. The isotope distribution in the diamonds was investigated using Raman and SIMS and the nitrogen concentrations were investigated using optical absorption.

It was discovered that the ^{13}C isotope concentration was not uniform across each sample. This suggested that the ^{13}C concentration in the melt was changing during growth. This is thought to have occurred because of the difference in doping between the carbon source and the metal solvent. The diamond grew as carbon precipitated out of the metal solvent. As the metal solvent became depleted in carbon the carbon source dissolved into the solvent. The carbon from the carbon source then precipitated out of the solvent forming the diamond. In two of the samples the concentration of ^{13}C was higher in the carbon source than the solvent, and hence as the carbon source dissolved into the solvent the melt

around the growing diamond became increasingly enriched in ^{13}C. Additionally the sources of carbon, which were natural abundance ^{12}C and ^{13}C enriched, were of different forms. ^{12}C was graphitic and ^{13}C was amorphous. Graphitic carbon dissolves more quickly in metal. It consists of crystalline layers, between which the metal atoms can penetrate as the layer spacing is larger than the carbon-carbon bond length. Amorphous carbon dissolves more slowly as it has a non-crystalline structure.

As these samples had a variety of different ^{13}C concentrations at different locations, they provided a useful set of data to correlate the ^{13}C concentration as measured by SIMS and the Raman line position. This allowed a formula to be calculated which linked directly the measured Raman line position to the ^{13}C concentration, as demonstrated by equation 9.1.

$$^{13}\mathrm{C}\ (\%) = 2.61 \times (1332.9 - \mathrm{Raman\ \ line\ \ position}) \pm 0.5 \tag{9.1}$$

These variations of ^{13}C concentration indicates more work is required before HPHT can be used for large scale manufacturing of isotopically enriched diamonds. The improvements which need to be made include uniformity of doping and use of the same form of carbon for ^{12}C and ^{13}C.

9.3 Heteroepitaxial CVD Diamonds

The ability to grow single crystal diamond on silicon wafers greatly increases the number potential applications of diamond as larger crystals can be grown at a lower cost. Whilst it has previously been possible to grow polycrystalline material this way, single crystals have superior electronic and optical properties and hence increased possible applications. The elimination of grain boundaries increases the utility of this material.

In Chapter 7 two diamond samples were investigated which had been made by CVD on a silicon substrate using bias enhanced nucleation. The $\{0\,0\,1\}$-orientated substrate used was coated with yttria-stabilised zirconia and iridium to minimise the lattice mismatch between the silicon and the diamond and thus allowed single crystal material to be grown. The samples were highly birefringent when observed through cross-polarisers suggesting significant concentrations of dislocations and dislocation bundles. However, the samples created contained a high degree of

strain associated with dislocations, arising from the lattice mismatch, and point defects. Two samples were investigated; one which was intrinsic and one which had been nitrogen doped to increase the growth rate.

The samples were studied using a DiamondView^{TM} microscope which showed a large degree of luminescence from dislocation bundles. PL spectroscopy was used to identify the defects present and these spectra also indicated a large degree of strain broadening. The degree of strain was significantly higher for the sample which had been nitrogen doped. This may have arisen due to the nitrogen impurity atoms interrupting the step growth or the higher dislocation density resulting from the faster growth speed. Polarised fourier transform infrared spectroscopy (FTIR) was used to investigate preferential orientation of defects.

EPR was used to quantify the defects present. The nitrogen doped heteroepitaxial CVD sample contained the substitutional nitrogen defect, the nitrogen vacancy hydrogen defect and the nitrogen vacancy defect, and the relative concentrations were consistent with those observed in nitrogen doped homoepitaxial CVD diamond. In the nitrogen doped sample the total nitrogen impurity concentration exceeded 2000 ppb, whereas in the intrinsic heteroepitaxial CVD sample it was less than a few ppb, similar to that in what is often termed 'electronic grade' CVD diamond. However, both samples contain a significant concentration of silicon vacancy defects which means the purity of the intrinsic sample was not great enough to be of commercially useful electronic grade.

This investigation has determined that the material quality of heteroepitaxial CVD has not yet reached that of homoepitaxial CVD due to the high degree of strain arising from the dislocation bundles present due to the lattice mismatch and the point defect concentration. The dislocation bundles are of higher concentration in the sample which was nitrogen doped. The method has successfully created single crystal diamond on silicon, a key requirement for device applications. However, a high degree of strain is still present. This material could still prove useful for applications with less demanding requirements. Future improvements could include a slower growth speed as this could decrease the dislocation density and hence the strain and further decreases in impurity concentrations as this would also decrease the strain. Additionally, post processing the material by annealing could further decrease the dislocation density.

9.4 Irradiation and Annealing of Silicon Doped Diamond

In the final experimental chapter (Chapter 8) two silicon containing samples were discussed. One nitrogen doped and one co-doped with silicon and boron. These samples were irradiated in an attempt to increase the concentration of vacancies and were subsequently annealed. The aim of this investigation was to discover if, like the nitrogen vacancy, the silicon vacancy concentration could be increased by irradiation and annealing, as this had been suggested by previous literature. However, in the case of the nitrogen vacancy there are typically many more single substitutional atoms than nitrogen vacancy centres in an as-grown diamond and as such the vacancies produced by irradiation join with single substitutional nitrogen to create nitrogen vacancies. This is not necessarily the case with silicon vacancy centres. It is possible that the relative starting concentrations of single substitutional silicon atoms and silicon vacancy centres depends on the substrate from which the sample was grown. Of the two samples studied the one grown on a $\{1\,1\,0\}$-orientated substrate had a high concentration of silicon vacancies initially and it appears that the irradiation and annealing treatment caused a reduction in the silicon vacancy concentration and the increase in a peak tentatively assigned to the silicon di-vacancy. In the sample grown on a $\{0\,0\,1\}$-orientated substrate there was a small concentration of silicon vacancies (as determined by PL) but this was successfully increased by the irradiation and annealing treatment. However, the intended final annealing temperature of 800°C was not reached for a sustained period as the vacancy concentration was not reduced to zero (as would be expected). This indicates that with a further anneal at 800°C the silicon vacancy concentration could be increased. Additionally at low temperature (10 K) a signal from the di-vacancy was seen. A 1200°C anneal could be used to disassociate the di-vacancy centres and further increase the silicon vacancy population.

This work suggests that the relative incorporation efficiency of silicon in the form of an isolated substitutional impurity, or a silicon vacancy defect in homoepitaxial CVD diamond may depend on the orientation of the substrate, and that the details of silicon vacancy defect production, especially in boron doped diamond, are not yet well understood.

Bibliography

[1] Pliny the Elder and John F. Healy. *Natural History*. Penguin Books, 1991.

[2] Ian Smillie. *Diamonds*. Polity, 2014.

[3] Samuel Tolansky. *The history and use of diamond*. Methuen, London, 1962.

[4] K. Takahashi, K. Sakamoto, A. Kasugai, T. Imai, J. R. Brandon, and R. S. Sussmann. Chemical vapor deposition diamond window as vacuum and tritium confinement barrier for fusion application. *Review of Scientific Instruments*, 71(11):4139, 2000.

[5] Mark Antonio Prelas, Galina Popovici, and Louis K. Bigelow. *Handbook of industrial diamonds and diamond films*. Marcel Dekker, 1998.

[6] M Nazare and A Neves. *Properties, Growth and Applications of Diamond*. INSPEC, 2001.

[7] Elke Neu, Mario Agio, and Christoph Becher. Photophysics of single silicon vacancy centers in diamond: implications for single photon emission. *Optics express*, 20(18):19956–71, 2012.

[8] J. M. Taylor, P. Cappellaro, L. Childress, L. Jiang, D. Budker, P. R. Hemmer, A. Yacoby, R. Walsworth, and M. D. Lukin. High-sensitivity diamond magnetometer with nanoscale resolution. *Nature Physics*, 4(10):810–816, 2008.

[9] Gopalakrishnan Balasubramanian, I Y Chan, Roman Kolesov, Mohannad Al-Hmoud, Julia Tisler, Chang Shin, Changdong Kim, Aleksander Wojcik, Philip R Hemmer, Anke Krueger, Tobias Hanke, Alfred Leitenstorfer, Rudolf Bratschitsch, Fedor Jelezko, and Jörg Wrachtrup. Nanoscale imaging magnetometry with diamond spins under ambient conditions. *Nature*, 455(7213):648–51, 2008.

[10] J. E. (John Edwin) Field. *The Properties of natural and synthetic diamond*. Academic Press, 1992.

[11] Gordon Davies and INSPEC (Information service). *Properties and growth of diamond*. INSPEC, the Institution of Electrical Engineers, 1994.

[12] Paul W. May. CVD diamond: a new technology for the future? *Endeavour*, 19(3):101–106, 1995.

[13] E. A. Ekimov, V. A. Sidorov, E. D. Bauer, N. N. Mel'nik, N. J. Curro, J. D. Thompson, and S. M. Stishov. Superconductivity in diamond. *Nature*, 428(6982):542–545, 2004.

[14] J. P. Goss, P. R. Briddon, M. J. Rayson, S. J. Sque, and R. Jones. Vacancy-impurity complexes and limitations for implantation doping of diamond. *Physical Review B*, 72(3):035214, 2005.

[15] S. Hadlington. Hot rocks [single crystal diamond for power semiconductor devices]. *IEE Review*, 51(4):30–33, 2005.

[16] Roger J Narayan, Ryan D. Boehm, and Anirudha V. Sumant. Medical applications of diamond particles and surfaces. *Materials Today*, 14(4):154–163, 2011.

[17] Yasar Gurbuz, Onur Esame, Ibrahim Tekin, Weng P. Kang, and Jimmy L. Davidson. Diamond semiconductor technology for RF device applications. *Solid-State Electronics*, 49(7):1055–1070, 2005.

[18] Robert Robertson, J. J. Fox, and A. E. Martin. Two Types of Diamond. *Philosophical Transactions of the Royal Society of London. Series A, Containing Papers of a Mathematical or Physical Character*, 232:463–535, 1934.

[19] RM Chrenko, RE Tuft, and HM Strong. Transformation of the state of nitrogen in diamond. *Nature*, 1977.

[20] G Davies. The A nitrogen aggregate in diamond-its symmetry and possible structure. *Journal of Physics C: Solid State Physics*, 9(19):L537, 1976.

[21] R Berman. *The properties of natural and synthetic diamond*. Academic Press, London, 1992.

[22] A T Collins and A W S Williams. The nature of the acceptor centre in semiconducting diamond. *Journal of Physics C: Solid State Physics*, 4(13):1789–1800, 1971.

[23] Peter Rudolph. *Handbook of Crystal Growth: Bulk Crystal Growth*, volume II. Elsevier, second edi edition, 2015.

[24] Rantala Jukka. Diamonds are a Thermal Designer's Best Friends, 2002.

[25] R. W. (Richard W.) Carlson. *The mantle and core*. Elsevier, 2005.

[26] Reza Abbaschian, Henry Zhu, and Carter Clarke. High pressure-high temperature growth of diamond crystals using split sphere apparatus. In *Diamond and Related Materials*, volume 14, pages 1916–1919, 2005.

[27] Roy S. Lewis, Tang Ming, John F. Wacker, Edward Anders, and Eric Steel. Interstellar diamonds in meteorites. *Nature*, 326(6109):160–162, 1987.

[28] H. Tracy Hall. Ultra-High-Pressure, High-Temperature Apparatus: the "Belt". *Review of Scientific Instruments*, 31(2):125, 1960.

[29] Amanda S. Barnard. *The diamond formula: diamond synthesis: a gemmological perspective*. Butterworth-Heinemann, 2008.

[30] Yu.N. Pal'yanov. High-pressure synthesis of high-quality diamond single crystals. *Diamond and Related Materials*, 7(6):916–918, 1998.

[31] Natalia Dubrovinskaia, Leonid Dubrovinsky, Nobuyoshi Miyajima, Falko Langenhorst, Wilson A Crichton, and Hans F Braun. High-pressure / High-temperature Synthesis and Characterization of Boron-doped Diamond. 61:1561–1565, 2006.

[32] Yafei Zhang, Chuanyi Zang, Hongan Ma, Zhongzhu Liang, Lin Zhou, Shangsheng Li, and Xiaopeng Jia. HPHT synthesis of large single crystal diamond doped with high nitrogen concentration. *Diamond and Related Materials*, 17(2):209–211, 2008.

[33] A.M. Zaitsev. *Optical Properties of Diamond: A Data Handbook*. Springer, 2001.

[34] J. Asmussen, T. A. Grotjohn, T. Schuelke, M. F. Becker, M. K. Yaran, D. J. King, S. Wicklein, and D. K. Reinhard. Multiple substrate microwave plasma-assisted chemical vapor deposition single crystal diamond synthesis. *Applied Physics Letters*, 93(3):031502, 2008.

[35] Yu A. Mankelevich and P. W. May. New insights into the mechanism of CVD diamond growth: Single crystal diamond in MW PECVD reactors. *Diamond and Related Materials*, 17(7-10):1021–1028, 2008.

[36] P W May and Y A Mankelevich. Experiment and modeling of the deposition of ultrananocrystalline diamond films using hot filament chemical vapor deposition and Ar/CH4/H-2 gas mixtures: A generalized mechanism for ultrananocrystalline diamond growth. *Journal of Applied Physics*, 100(2), 2006.

[37] P. W. May, M. N R Ashfold, and Yu A. Mankelevich. Microcrystalline, nanocrystalline, and ultrananocrystalline diamond chemical vapor deposition: Experiment and modeling of the factors controlling growth rate, nucleation, and crystal size. *Journal of Applied Physics*, 101(5), 2007.

[38] J. E. Butler, A. Cheesman, and M. N. R. Ashfold. Recent Progress in the Understanding of CVD Growth of Diamond. *doi.org*, pages 103–124, 2009.

[39] Jocelyn Achard, Alexandre Tallaire, Ricardo Sussmann, François Silva, and Alix Gicquel. The control of growth parameters in the synthesis of high-quality single crystalline diamond by CVD. *Journal of Crystal Growth*, 284(3-4):396–405, 2005.

[40] U. F. S. D'Haenens-Johansson. Near-colourless CVD synthetic gem diamonds with high silicon-vacancy concentrations. In *The 65th Diamond Conference*, 2014.

[41] R. Kalish. Doping of diamond. *Carbon*, 37(5):781–785, 1999.

[42] Christopher M. Breeding and Wuyi Wang. Occurrence of the Si-V defect center in natural colorless gem diamonds. *Diamond and Related Materials*, 17(7-10):1335–1344, 2008.

[43] Vadym N. Mochalin, Olga Shenderova, Dean Ho, and Yury Gogotsi. The properties and applications of nanodiamonds. *Nature Nanotechnology*, 7(1):11–23, 2011.

[44] N Greiner, D Philips, D Johnson, and F Volk. Diamonds in detonation soot. *Nature*, 333:440–442, 1988.

[45] Elke Neu, Martin Fischer, Stefan Gsell, Matthias Schreck, and Christoph Becher. Fluorescence and polarization spectroscopy of single silicon vacancy centers in heteroepitaxial nanodiamonds on iridium. *Physical Review B*, 84, 2011.

[46] Marcus W. Doherty, Neil B. Manson, Paul Delaney, Fedor Jelezko, Jörg Wrachtrup, and Lloyd C.L. Hollenberg. The nitrogen-vacancy colour centre in diamond. *Physics Reports*, 528(1):1–45, 2013.

[47] D C Hunt, D J Twitchen, M E Newton, J M Baker, T R Anthony, W F Banholzer, and S S Vagarali. Identification of the neutral carbon 100-split interstitial in diamond. *Physical Review B*, 61(6):3863–3876, 2000.

[48] Hannah Smith, Gordon Davies, M. Newton, and H. Kanda. Structure of the self-interstitial in diamond. *Physical Review B*, 69(4):045203, 2004.

[49] D. J. Twitchen, M. E. Newton, J. M. Baker, O. D. Tucker, T. R. Anthony, and W. F. Banholzer. Electron-paramagnetic-resonance measurements on the di-001-split interstitial center (R1) in diamond. *Physical Review B*, 54(10):6988–6998, 1996.

[50] K. Iakoubovskii, I. Kiflawi, K. Johnston, A. Collins, G. Davies, and A. Stesmans. Annealing of vacancies and interstitials in diamond. *Physica B: Condensed Matter*, 340-342:67–75, 2003.

[51] J P Goss, B J Coomer, R Jones, T D Shaw, P R Briddon, M Rayson, and S Berg. Self-interstitial aggregation in diamond. *Physical Review B*, 63(195208), 2001.

[52] J P Goss, R Jones, and P R Briddon. Stress tensors and dilatation of interstitial defects in diamond. *Physical Review B*, 65(035203), 2001.

[53] Gordon Davies, Simon C. Lawson, Alan T. Collins, Alison Mainwood, and Sarah J. Sharp. Vacancy-related centers in diamond. *Physical Review B*, 46(20):13157–13170, 1992.

[54] C. A. Coulson and F. P. Larkins. Isolated single vacancy in diamond—I. Electronic structure. *Journal of Physics and Chemistry of Solids*, 32(9):2245–2257, 1971.

[55] J. Isoya, H. Kanda, Y. Uchida, S. C. Lawson, S. Yamasaki, H. Itoh, and Y. Morita. EPR identification of the negatively charged vacancy in diamond. *Physical Review B*, 45(3):1436–1439, 1992.

[56] J. A. Van Wyk, O. D. Tucker, and M. E. Newton. Magnetic-resonance measurements on the 5A2 excited state of the neutral vacancy in diamond. *Physical Review B*, 52(17), 1995.

[57] C. D. Clark and J. Walker. The Neutral Vacancy in Diamond. *Proceedings of the Royal Society of London Series A*, 334(1597):241–257, 1973.

[58] D. J. Twitchen, M. E. Newton, J. M. Baker, T. R. Anthony, and W. F. Banholzer. Electron-paramagnetic-resonance measurements on the divacancy defect center R 4 / W 6 in diamond. *Physical Review B*, 59(20):12900–12910, 1999.

[59] C. A. Coulson and F. P. Larkins. Electronic structure of the neutral isolated divacancy in diamond. *Journal of Physics and Chemistry of Solids*, 30(8):1963–1972, 1969.

[60] R. Jones, P. R. Briddon, and S. Öberg. First-principles theory of nitrogen aggregates in diamond. *Philosophical Magazine Letters*, 66(2):67–74, 1992.

[61] Claire Glover. *A study of defects in single crystal CVD diamond*. PhD thesis, University of Warwick, 2003.

[62] S. Liggins, M. E. Newton, J. P. Goss, P. R. Briddon, and D. Fisher. Identification of the dinitrogen (001) split interstitial H1a in diamond. *Physical Review B - Condensed Matter and Materials Physics*, 81(8), 2010.

[63] S. Liggins. *Identification of point defects in treated single crystal diamond*. PhD thesis, The University of Warwick, 2010.

[64] G. Davies, M H Nazaré, and M. F. Hamer. The H3 (2.463 eV) Vibronic Band in Diamond: Uniaxial Stress Effects and the Breakdown of Mirror Symmetry. *Proceedings of the Royal Society of London. Series A, Mathematical and Physical Sciences*, 351(1665):pp. 245–265, 1976.

[65] R. Jones, J. P. Goss, P. R. Briddon, and S. Öberg. N2 and N4 optical transitions in diamond: A breakdown of the vacancy model. *Physical Review B*, 56(4):R1654–R1656, 1997.

[66] J. Goss, R. Jones, S. Breuer, P. Briddon, and S. Öberg. The Twelve-Line 1.682 eV Luminescence Center in Diamond and the Vacancy-Silicon Complex. *Physical Review Letters*, 77(14):3041–3044, 1996.

[67] Guido Burkard. Diamond Spins Shining Bright. *Physics*, 7:131, 2014.

[68] J Loubser and J Van Wky. Optical spin-polarisation in a triplet state in irradiated and annealed type 1b diamonds. *Diamond Research*, 9(05):11–14, 1977.

[69] G Davies. Dynamic Jahn-Teller distortions at trigonal optical centres in diamond. *Journal of Physics C: Solid State Physics*, 12(13):2551–2566, 1979.

[70] Andrew Edmonds. *Magnetic resonance studies of point defects in single crystal diamond*. Phd thesis, The University of Warwick, 2008.

[71] Y Chu, N P De Leon, B J Shields, B Hausmann, R Evans, E Togan, M J Burek, M Markham, A Stacey, A S Zibrov, A Yacoby, D J Twitchen, M Loncar, H Park, P Maletinsky, and M D Lukin. Coherent Optical Transitions in Implanted Nitrogen Vacancy Centers. *Nano Letters*, 14, 2014.

[72] A R Lang, M Moore, A P W Makepeace, W Wierzchowski, and C M Welbourn. On the Dilatation of Synthetic Type Ib Diamond by Substitutional Nitrogen Impurity. *Philosophical Transactions of the Royal Society of London. Series A: Physical and Engineering Sciences*, 337(1648):497–520, 1991.

[73] Konstantin Iakoubovskii and Guy Adriaenssens. Trapping of vacancies by defects in diamond. *Journal of Physics: Condensed Matter*, 13(26):6015, 2001.

[74] A. Sipahigil, K. D. Jahnke, L. J. Rogers, T. Teraji, J. Isoya, A. S. Zibrov, F. Jelezko, and M. D. Lukin. Indistinguishable photons from separated silicon vacancy centers in diamond. *Physical Review Letters*, 113(11), 2014.

[75] I Aharonovich, S Castelletto, D A Simpson, C-H Su, A D Greentree, and S Prawer. Diamond-based single-photon emitters. *Reports on Progress in Physics*, 74(7):076501, 2011.

[76] T. D. Ladd, F. Jelezko, R. Laflamme, Y. Nakamura, C. Monroe, and J. L. O'Brien. Quantum computers. *Nature*, 464(7285):45–53, 2010.

[77] U. F. S. D'Haenens-Johansson, A. M. Edmonds, B. L. Green, M. E. Newton, G. Davies, P. M. Martineau, R. U. A. Khan, and D. J. Twitchen. Optical properties of the neutral silicon split-vacancy center in diamond. *Physical Review B*, 84(24):245208, 2011.

[78] Lachlan J. Rogers, Kay D. Jahnke, Marcus W. Doherty, Andreas Dietrich, Liam P. McGuinness, Christoph Müller, Tokuyuki Teraji, Hitoshi Sumiya, Junichi Isoya, Neil B. Manson, and Fedor Jelezko. Electronic structure of the negatively charged silicon-vacancy center in diamond. *Physical Review B - Condensed Matter and Materials Physics*, 89(23):235101, 2014.

[79] H. Sternschulte, K. Thonke, J. Gerster, W. Limmer, R. Sauer, J. Spitzer, and P. C. Münzinger. Uniaxial stress and Zeeman splitting of the 1.681 eV optical center in a homoepitaxial CVD diamond film. *Diamond and Related Materials*, 4(10):1189–1192, 1995.

[80] A. Edmonds, M. Newton, P. Martineau, D. Twitchen, and S. Williams. Electron paramagnetic resonance studies of silicon-related defects in diamond. *Physical Review B*, 77(24):245205, 2008.

[81] Ulrika Francine Stephanie D'Haenens-Johansson. *Optical and Magnetic Resonance Studies of Point Defects in CVD Diamond*. PhD thesis, University of Warwick, 2011.

[82] Tina Müller, Christian Hepp, Benjamin Pingault, Elke Neu, Stefan Gsell, Matthias Schreck, Hadwig Sternschulte, Doris Steinmüller-Nethl, Christoph Becher, and Mete Atatüre. Optical signatures of silicon-vacancy spins in diamond. *Nature communications*, 5:3328, 2014.

[83] Elke Neu, Christian Hepp, Michael Hauschild, Stefan Gsell, Martin Fischer, Hadwig Sternschulte, Doris Steinmüller-Nethl, Matthias Schreck, and Christoph Becher. Low-temperature investigations of single silicon vacancy colour centres in diamond. *New Journal of Physics*, 15, 2013.

[84] Elke Neu, David Steinmetz, Janine Riedrich-Möller, Stefan Gsell, Martin Fischer, Matthias Schreck, and Christoph Becher. Single photon emission from silicon-vacancy colour centres in chemical vapour deposition nanodiamonds on iridium. *New Journal of Physics*, 13(2):025012, 2011.

[85] Janik Wolters, Andreas Schell, Gunter Kewes, Nils Nusse, Max Schoengen, Henning Doscher, Thomas Hannappel, Bernd Lochel, Michael Barth, and Oliver Benson. Enhancement of the zero phonon line emission from a single nitrogen vacancy center in a nanodiamond via coupling to a photonic crystal cavity. *Applied Physics Letters*, 97(14):141108, 2010.

[86] Benjamin Pingault, Jonas N. Becker, Carsten H. H. Schulte, Carsten Arend, Christian Hepp, Tillmann Godde, Alexander I. Tartakovskii, Matthew Markham, Christoph Becher, and Mete Atatüre. All-optical formation of coherent dark states of silicon-vacancy spins in diamond. *Physical Review Letters*, 113(26), 2014.

[87] Benjamin Pingault, David-Dominik Jarausch, Christian Hepp, Lina Klintberg, Jonas N Becker, Matthew Markham, Christoph Becher, and Mete Atatüre. Coherent control of the silicon-vacancy spin in diamond. *Nature communications*, 8:15579, 2017.

[88] Adam Gali and Jeronimo R. Maze. Ab initio study of the split silicon-vacancy defect in diamond: Electronic structure and related properties. *Physical Review B*, 88(23):235205, 2013.

[89] J. P. Goss, P. R. Briddon, and M. J. Shaw. Density functional simulations of silicon-containing point defects in diamond. *Physical Review B*, 76(7):075204, 2007.

[90] K. Iakoubovskii and A. Stesmans. Characterization of Defects in as-Grown CVD Diamond Films and HPHT Diamond Powders by Electron Paramagnetic Resonance. *physica status solidi (a)*, 186(2):199–206, 2001.

[91] U. F S D'Haenens-Johansson, A. M. Edmonds, M. E. Newton, J. P. Goss, P. R. Briddon, J. M. Baker, P. M. Martineau, R. U. A. Khan, D. J. Twitchen, and S. D. Williams. EPR of a defect in CVD diamond involving both silicon and hydrogen that shows preferential alignment. *Physical Review B - Condensed Matter and Materials Physics*, 82(15):155205, 2010.

[92] S. Johnson, P. R. Dolan, T. Grange, A. A P Trichet, G. Hornecker, Y. C. Chen, L. Weng, G. M. Hughes, A. A R Watt, A. Auffèves, and J. M. Smith. Tunable cavity coupling of the zero phonon line of a nitrogen-vacancy defect in diamond. *New Journal of Physics*, 17(12), 2015.

[93] Nitin Mohan, Chao Sheng Chen, Hsiao Han Hsieh, Yi Chun Wu, and Huan Cheng Chang. In vivo imaging and toxicity assessments of fluorescent nanodiamonds in caenorhabditis elegans. *Nano Letters*, 10(9):3692–3699, 2010.

[94] P. Neumann, I. Jakobi, F. Dolde, C. Burk, R. Reuter, G. Waldherr, J. Honert, T. Wolf, A. Brunner, J. H. Shim, D. Suter, H. Sumiya, J. Isoya, and J. Wrachtrup. High-precision nanoscale temperature sensing using single defects in diamond. *Nano Letters*, 13(6):2738–2742, 2013.

[95] Matthias Leifgen, Tim Schroder, Friedemann Gadeke, Robert Riemann, Valentin Métillon, Elke Neu, Christian Hepp, Carsten Arend, Christoph Becher, Kristian Lauritsen, and Oliver Benson. Evaluation of nitrogen- and silicon-vacancy defect centres as single photon sources in quantum key distribution. *New Journal of Physics*, 16(2):023021, 2014.

[96] C.-Y. Lu, Y. Zhao, A. N. Vamivakas, C. Matthiesen, S. Fält, A. Badolato, and M. Atatüre. Direct measurement of spin dynamics in InAs/GaAs quantum dots using time-resolved resonance fluorescence. *Physical Review B*, 81(3):035332, 2010.

[97] P. Siyushev, V. Jacques, I. Aharonovich, F. Kaiser, T. Muller, L. Lombez, M. Atature, S. Castelletto, S. Prawer, F. Jelezko, and J. Wrachtrup. Low temperature optical characterization of near infrared single photon emitters in nanodiamonds. *Arxiv*, 2009.

[98] Y. Deshko and A. A. Gorokhovsky. Spectroscopy and micro-luminescence mapping of Xe-implanted defects in diamond. *Low Temperature Physics*, 36(5):465, 2010.

[99] Sang-Yun Lee, Matthias Widmann, Torsten Rendler, Marcus W Doherty, Thomas M Babinec, Sen Yang, Moritz Eyer, Petr Siyushev, Birgit J M Hausmann, Marko Loncar, Zoltán Bodrog, Adam Gali, Neil B Manson, Helmut Fedder, and Jörg Wrachtrup. Readout and control of a single nuclear spin with a metastable electron spin ancilla. *Nature nanotechnology*, 8(7):487–92, 2013.

[100] V A Nadolinny, A P Yelisseyev, J M Baker, M E Newton, D J Twitchen, S C Lawson, O P Yuryeva, and B N Feigelson. A study of 13 C hyperfine

structure in the EPR of nickel-nitrogen-containing centres in diamond and correlation with their optical properties. *Journal of Physics: Condensed Matter*, 11(38):7357–7376, 1999.

[101] A. Sipahigil, R. E. Evans, D. D. Sukachev, M. J. Burek, J. Borregaard, M. K. Bhaskar, C. T. Nguyen, J. L. Pacheco, H. A. Atikian, C. Meuwly, R. M. Camacho, F. Jelezko, E. Bielejec, H. Park, M. Lončar, and M. D. Lukin. An integrated diamond nanophotonics platform for quantum-optical networks. *Science*, 354(6314):847–850, 2016.

[102] A. A. Gorokhovsky, A. V. Turukhin, R. R. Alfano, and W. Phillips. Photoluminescence vibrational structure of Si center in chemical-vapor deposited diamond. *Applied Physics Letters*, page 43, 1995.

[103] Qing Li, Marcelo Davanco, and Kartik Srinivasan. Efficient and low-noise single-photon-level frequency conversion interfaces using silicon nanophotonics. *ArXiv*, 10:1–22, 2015.

[104] Igor I Vlasov, Andrey A Shiryaev, Torsten Rendler, Steffen Steinert, Sang-Yun Lee, Denis Antonov, Márton Vörös, Fedor Jelezko, Anatolii V Fisenko, Lubov F Semjonova, Johannes Biskupek, Ute Kaiser, Oleg I Lebedev, Ilmo Sildos, Philip R Hemmer, Vitaly I Konov, Adam Gali, and Jörg Wrachtrup. Molecular-sized fluorescent nanodiamonds. *Nature nanotechnology*, 9(1):54–8, 2014.

[105] Igor Aharonovich, Dirk Englund, and Milos Toth. Solid-state single-photon emitters. *Nature Publishing Group*, 10(10):631–641, 2016.

[106] Jonas Nils Becker, Johannes Görlitz, Carsten Arend, Matthew Markham, Christoph Becher, G. D. Fuchs, V. V. Dobrovitski, D. M. Toyli, F. J. Heremans, D. D. Awschalom, D. Press, T. D. Ladd, B. Zhang, Y. Yamamoto, L. C. Bassett, K. G. Lagoudakis, W. B. Gao, P. Fallahi, E. Togan, J. Miguel-Sanchez, A. Imamoglu, S. Sun, H. Kim, G. S. Solomon, E. Waks, D. D. Awschalom, L. C. Bassett, A. S. Dzurak, E. L. Hu, J. R. Petta, G. Balasubramanian, E. Neu, A. A. Gorokhovsky, A. V. Turukhin, R. R. Alfano, W. Phillips, A. Sipahigil, C. Hepp, L. J. Rogers, B. Pingault, L. J. Rogers, K. D. Jahnke, J. Riedrich-Möller, R. E. Evans, A. Sipahigil, D. D. Sukachev, A. S. Zibrov, M. D. Lukin, U. Jantzen, L. Kipfstuhl, F. Guldner, J. Riedrich-Möller, Christoph Becher, Carsten Arend, Jonas Nils Becker, H. Sternschulte, D. Steinmüller-Nethl, Christoph Becher, K.-M. C. Fu, K. Bergmann, N. V. Vitanov, B. W. Shore, J. I. Cirac, P. Zoller, H. J. Kimble, H. Mabuchi, M. Hennrich, T. Legero, A. Kuhn, G. Rempe, E. Togan, A. I. Lvovsky, B. C. Sanders, W. Tittel, F. Bussières, and C. G. Yale. Ultrafast all-optical coherent control of single silicon vacancy colour centres in diamond. *Nature Communications*, 7:13512, 2016.

[107] D Le Sage, K Arai, D R Glenn, S J DeVience, L M Pham, L Rahn-Lee, M D Lukin, A Yacoby, A Komeili, and R L Walsworth. Optical magnetic imaging of living cells. *Nature*, 496(7446):486–489, 2014.

[108] V. M. Acosta, E. Bauch, M. P. Ledbetter, A. Waxman, L. S. Bouchard, and D. Budker. Temperature dependence of the nitrogen-vacancy magnetic resonance in diamond. *Physical Review Letters*, 104(7):070801, 2010.

[109] David DiVincenzo. Quantum bits: Better than excellent. *Nature Materials*, 9(6):468–469, 2010.

[110] J R Weber, W F Koehl, J B Varley, A Janotti, B B Buckley, C G Van de Walle, and D D Awschalom. Quantum computing with defects. *Proceedings of the National Academy of Sciences of the United States of America*, 107(19):8513–8, 2010.

[111] Christian Hepp, Tina Müller, Victor Waselowski, Jonas N. Becker, Benjamin Pingault, Hadwig Sternschulte, Doris Steinmüller-Nethl, Adam Gali, Jeronimo R. Maze, Mete Atatüre, and Christoph Becher. Electronic Structure of the Silicon Vacancy Color Center in Diamond. *Physical Review Letters*, 112(3):036405, 2014.

[112] J. R. Bolton J. E. Wertz. J. A. Weil. *Electron paramagnetic resonance: Elementary theory and applications.*, volume 33. Wiley-interscience, New York, 1995.

[113] A. Caragheorgheopol, B. C. Gilbert, M. J. Davies, and D. M. Murphy. *Electron paramagnetic resonance . Volume 20, A review of the recent literature.* RSC Pub, 2007.

[114] P Zeeman. The Effect of Magnetisation on the Nature of Light Emitted by a Substance. *Nature*, 55(1424):347–347, 1897.

[115] A. Abragam and B Bleaney. *Electron Paramagnetic Resonance of Transition Ions.* Oxford University Press Canada, 1970.

[116] Marina Brustolon and Elio Giamello. *Electron Paramagnetic Resonance: A Practitioner's Toolkit.* Wiley, 2008.

[117] W. Heisenberg. Mehrkorperproblem und Resonanz in der Quantenmechanik. *Zeitschrift fur Physik*, 38(6-7):411–426, 1926.

[118] Schweiger Gunnar Jeschke Arthur. *Principles of Pulse Electron Paramagnetic Resonance.* Oxford University Press, 2001.

[119] G. K. (Gordon Kemble) Woodgate. *Elementary atomic structure.* Clarendon, 1983.

[120] R. Sternheimer. On Nuclear Quadrupole Moments. *Phys. Rev.*, 80(1):102–103, 1950.

[121] F. Bloch. Nuclear induction. *Physical Review*, 70(7-8):460–474, 1946.

[122] Ralph T Weber and Aaron H Heiss. *E 580 User's Manual.* 2001.

[123] Sushil K. Misra. *Multifrequency electron paramagnetic resonance: theory and applications*. Wiley-VCH, 2011.

[124] Sandra S. Eaton and Gareth R. Eaton. Relaxation Times of Organic Radicals and Transition Metal Ions. pages 29–154. 2002.

[125] Alexander Savvatimskiy. *Carbon at High Temperatures*, volume 134. 2015.

[126] James R Harbridge, Sandra S. Eaton, and Gareth R Eaton. Electron spin-lattice relaxation processes of radicals in irradiated crystalline organic. *Journal of Physical Chemistry A*, 107(5):598–610, 2003.

[127] Rich P. Mildren. Intrinsic Optical Properties of Diamond. In *Optical Engineering of Diamond*, pages 1–34. Wiley-VCH Verlag GmbH & Co. KGaA, Weinheim, Germany, 2013.

[128] Colin Eaborn. Compendium of chemical Terminology: IUPAC Recommendations, 1988.

[129] Kunie Ishioka, Muneaki Hase, Masahiro Kitajima, and Hrvoje Petek. Coherent optical phonons in diamond. *Applied Physics Letters*, 89(23):231916, 2006.

[130] Mark Fox. *Optical properties of solids*. Oxford University Press, 2010.

[131] Maurice. Pagel, V Barbin, P Blanc, and D Ohnenstetter. *Cathodoluminescence in geoscience*. 2000.

[132] R.W Hinton. *Ion microprobe analysis in geology*. Chapman and Hall, 1995.

[133] John Craven. *Secondary Ion Mass Spectrometry (SIMS)*. http://www.ed.ac.uk/files/atoms/files/sims4.pdf, accessed 23-05-2017.

[134] Mostafa. Fayek. *Secondary ion mass spectrometry in the earth sciences : gleaning the big picture from a small spot*. Mineralogical Association of Canada, 2009.

[135] Matthew Dale. *Colour Centres on Demand in Diamond*. PhD thesis, The University of Warwick, 2015.

[136] Ralph Weber, JinJie Jiang, and David Barr. *EMX User's Manual*. Bruker, manual ver edition, 1998.

[137] Christopher Hartland. *A Study of Point Defects in CVD Diamond Using Electron Paramagnetic Resonance and Optical Spectroscopy*. PhD thesis, The University of Warwick, 2014.

[138] Marina. Brustolon and Elio Giamello. *Electron Paramagnetic Resonance: A Practitioner's Toolkit*. Wiley, 2008.

[139] Isomet. Application Note - Acousto-Optic Modulation. Technical report, 2005.

[140] De Beers. *Diamond View: User Manual*. 7th edition, 2015.

[141] D Hunt. *A Study of Defects in Diamond*. PhD thesis, St. Peter's College, Oxford, 1999.

[142] I Aharonovich, S Castelletto, D A Simpson, C H Su, A D Greentree, and S Prawer. Diamond-based single-photon emitters. *Reports on Progress in Physics*, 74(7):76501, 2011.

[143] Brendon C. Rose, Ding Huang, Zi-Huai Zhang, Alexei M. Tyryshkin, Sorawis Sangtawesin, Srikanth Srinivasan, Lorne Loudin, Matthew L. Markham, Andrew M. Edmonds, Daniel J. Twitchen, Stephen A. Lyon, and Nathalie P. de Leon. Observation of an environmentally insensitive solid state spin defect in diamond. *arXiv*, 2017.

[144] L. Allers and A. T. Collins. Photoconductive spectroscopy of diamond grown by chemical vapor deposition. *Journal of Applied Physics*, 77(8):3879–3884, 1995.

[145] B. L. Green, S. Mottishaw, B. G. Breeze, A. M. Edmonds, U. F. S. D'Haenens-Johansson, M. W. Doherty, S. D. Williams, D. J. Twitchen, and M. E. Newton. Neutral Silicon-Vacancy Center in Diamond: Spin Polarization and Lifetimes. *Physical Review Letters*, 119(9):096402, 2017.

[146] K. Iakoubovskii, A. Stesmans, K. Suzuki, J. Kuwabara, and A. Sawabe. Characterization of defects in monocrystalline CVD diamond films by electron spin resonance. *Diamond and Related Materials*, 12(3-7):511–515, 2003.

[147] A. Jarmola, V. M. Acosta, K. Jensen, S. Chemerisov, and D. Budker. Temperature- and Magnetic-Field-Dependent Longitudinal Spin Relaxation in Nitrogen-Vacancy Ensembles in Diamond. *Physical Review Letters*, 108(19):197601, 2012.

[148] D. A. Redman, S. Brown, R. H. Sands, and S. C. Rand. Spin dynamics and electronic states of N-V centers in diamond by EPR and four-wave-mixing spectroscopy. *Physical Review Letters*, 67(24):3420–3423, 1991.

[149] F. Jelezko and J. Wrachtrup. Single defect centres in diamond: A review. *Physica Status Solidi (A) Applications and Materials Science*, 203(13):3207–3225, 2006.

[150] SobarWiki. Xenon arc-lamp spectrum, www.wikipedia.org accessed 2017-08-19, 2014.

[151] Thomas R. Anthony and William F. Banholzer. Properties of diamond with varying isotopic composition. *Diamond and Related Materials*, 1(5-6):717–726, 1992.

[152] Hugh D. Young and Roger A. Freedman. *Sears and Zemansky's University physics : with modern physics.* 2008.

[153] W H Beyer, R C Weast, and M J Astle. *CRC Handbook of Chemistry and Physics: A Ready-reference Book of Chemical and Physical Data*. 1983.

[154] Ricardo S. Sussmann. *CVD diamond for electronic devices and sensors*. J. Wiley, 2009.

[155] Wei Qiu, Nenad Velisavljevic, Paul A. Baker, Yogesh K. Vohra, and Samuel T. Weir. Isotopically pure C13 layer as a stress sensor in a diamond anvil cell. *Applied Physics Letters*, 84(26):5308–5310, 2004.

[156] R. M. Chrenko. 13C-doped diamond: Raman spectra. *Journal of Applied Physics*, 63(12):5873–5875, 1988.

[157] C M Welbourn, Martin Cooper, and P M Spear. De Beers Natural versus Synthetic Diamond Verification Instruments. *Gems & Gemology*, 32(3):156–169, 1996.

[158] R. H. Wentorf. Diamond growth rates. *The Journal of Physical Chemistry*, 75(12):1833–1837, 1971.

[159] Dmitri Kopeliovich. Synthetic diamonds [SubsTech], www.substech.com accessed 2017-03-10.

[160] H. Sumiya, N. Toda, and S. Satoh. Growth rate of high-quality large diamond crystals. *Journal of Crystal Growth*, 237-239(1-4 II):1281–1285, 2002.

[161] R. M. Chrenko, R. E. Tuft, and H. M. Strong. Transformation of the state of nitrogen in diamond. *Nature*, 270(5633):141–144, 1977.

[162] R. C. Burns, Vesna Cvetkovic, C. N. Dodge, D. J. F. Evans, Marie-Line T. Rooney, P. M. Spear, and C. M. Welbourn. Growth-sector dependence of optical features in large synthetic diamonds. *Journal of Crystal Growth*, 104(2):257–279, 1990.

[163] W. F. Banholzer and T. R. Anthony. Isotope enrichment during diamond growth. *Diamond and Related Materials*, 1(12):1157–1160, 1992.

[164] K C Hass, M A Tamor, T R Anthony, and W F Banholzer. Lattice Dynamics and Raman Spectra of Isotopically-Mixed Diamond. *Phys. Rev. B*, 45(13):7171, 1992.

[165] K. C Hass, M. A Tamor, T. R Anthony, and W. F Banholzer. Effects of isotopic disorder on the phonon spectrum of diamond. *Physical Review B*, 44(21):12046–12049, 1991.

[166] Renishaw. InVia User Guide. Technical report, University of California, Irvine, 2006.

[167] B Harte and J Craven. Carbon Isotope Mapping and Diffusion in Diamond, Report - University of Edinburgh. 2004.

[168] R.A Stern, M Palot, D Howell, T Stachel, D.G. Pearson, P Cartigny, and A. Oh. Methods and reference materials for sims diamond C- and N- isotope analysis. *Canadian Centre for Isotopic Microanalysis, Research Report*, 14-01:University of Alberta, Education and Research Arch, 2014.

[169] Harpreet Dhillon, Daniel James Twitchen, and Rizwan Khan. Single crystal CVD synthetic diamond material, Patent, 2016.

[170] B. V. Spitsyn, L. L. Bouilov, and B. V. Derjaguin. Vapor growth of diamond on diamond and other surfaces. *Journal of Crystal Growth*, 52(PART 1):219–226, 1981.

[171] Matthias Schreck. Synthesis of single crystal diamond wafers by heteroepitaxy: Nucleation, growth, defect engineering & potential applications. Conference Proceedings, Diamond Science and Technology Centre, University of Warwick, 2016.

[172] Matthias Schreck, Jes Asmussen, Shinichi Shikata, Jean-Charles Arnault, and Naoji Fujimori. Large-area high-quality single crystal diamond. *MRS Bulletin*, 39(June):504–510, 2014.

[173] Matthias Schreck, F. Hörmann, H. Roll, J. K. N. Lindner, and B. Stritzker. Diamond nucleation on iridium buffer layers and subsequent textured growth: A route for the realization of single-crystal diamond films. *Applied Physics Letters*, 78(2):192–194, 2001.

[174] F450c. Evolution Of Silicon Wafer, www.f450c.org accessed 2017-09-05, 2017.

[175] Matthias Schreck and B Stritzker. Nucleation and Growth of Heteroepitaxial Diamond Films on Silicon. *Physica Status Solidi (a)*, 154(1):197–217, 1996.

[176] Matthias Schreck, T Bauer, S. Gsell, F. Hörmann, H. Bielefeldt, and B. Stritzker. Domain formation in diamond nucleation on iridium. *Diamond and Related Materials*, 12(3-7):262–267, 2003.

[177] André F. Sartori and Matthias Schreck. Mutual interaction of N, B, and O during heteroepitaxial diamond growth: Triggering the nitrogen induced growth acceleration. *Physica Status Solidi (A) Applications and Materials Science*, 211(10):2290–2295, 2014.

[178] Matthias Schreck, A. Schury, F. Hörmann, H. Roll, and B. Stritzker. Mosaicity reduction during growth of heteroepitaxial diamond films on iridium buffer layers: Experimental results and numerical simulations. *Journal of Applied Physics*, 91(2):676–685, 2002.

[179] Matthias Schreck, Michael Mayr, Oliver Klein, Martin Fischer, Stefan Gsell, André Frota Sartori, and Björn Christoph Gallheber. Multiple role of dislocations in the heteroepitaxial growth of diamond: A brief review. *Physica Status Solidi (A) Applications and Materials Science*, 213(8):2028–2035, 2016.

[180] P M Martineau, M P Gaukroger, K B Guy, S C Lawson, D J Twitchen, I Friel, J O Hansen, G C Summerton, T P G Addison, and R Burns. High crystalline quality single crystal chemical vapour deposition diamond. *Journal of Physics: Condensed Matter*, 21(36):364205, 2009.

[181] Dick Wieboldt, Robert Heintz, and Mark Wall. Fundamentals of Raman Polarization Microscopy. Technical report, 2016.

[182] Carsten Arend, Jonas Nils Becker, Hadwig Sternschulte, Doris Steinmüller-Nethl, and Christoph Becher. Photoluminescence excitation and spectral hole burning spectroscopy of silicon vacancy centers in diamond. *Physical Review B*, 94(4), 2016.

[183] Yu-Chen Chen, Patrick S Salter, Sebastian Knauer, Laiyi Weng, Angelo C Frangeskou, Colin J Stephen, Shazeaa N Ishmael, Philip R Dolan, Sam Johnson, Ben L Green, Gavin W Morley, Mark E Newton, John G Rarity, Martin J Booth, and Jason M Smith. Laser writing of coherent colour centres in diamond. *Nature Photonics*, 11(2):77–80, 2016.

[184] G Davies. No phonon lineshapes and crystal strain fields in diamonds. *Journal of Physics C: Solid State Physics*, 3(12):2474–2486, 1970.

[185] A M Stoneham. Shapes of Inhomogeneously Broadened Resonance Lines in Solids. *Reviews of Modern Physics*, 41(1):82–108, 1969.

[186] G Davies, M H Nazaré, and M F Hamer. The H3 (2.463 eV) Vibronic Band in Diamond: Uniaxial Stress Effects and the Breakdown of Mirror Symmetry. *Proceedings of the Royal Society of London. Series A, Mathematical and Physical Sciences*, 351(1665):pp. 245–265, 1976.

[187] G Davies. Approximate widths of zero phonon lines broadened by point defect strain fields. *Journal of Physics D: Applied Physics*, 4(9):1340–1345, 1971.

[188] A M Stoneham. The theory of the strain broadened line shapes of spin resonance and optical zero phonon lines. *Proceedings of the Physical Society*, 89(4):909–921, 1966.

[189] A E Hughes. Strain broadening of the N1 zero-phonon line in sodium chloride. *Journal of Physics and Chemistry of Solids*, 29:1461–1477, 1968.

[190] P.A. Crowther and P.J. Dean. Phonon interactions, piezo-optical properties and the inter-relationship of the N3 and N9 absorption-emission systems in diamond. *Journal of Physics and Chemistry of Solids*, 28(7):1115–1136, 1967.

[191] Claire Glover, M. E. Newton, P. Martineau, D. J. Twitchen, and J. M. Baker. Hydrogen Incorporation in Diamond: The Nitrogen-Vacancy-Hydrogen Complex. *Physical Review Letters*, 90(18):185507, 2003.

[192] Robin Cruddace. *Magnetic resonance and optical studies of point defects in single crystal CVD diamond*. Phd thesis, The University of Warwick, 2007.

[193] P M Martineau, S C Lawson, A J Taylor, S J Quinn, D J F Evans, and M J Crowder. Identification of Synthetic Diamond Grown Using Chemical Vapor Deposition (CVD). *Gems & Gemology*, 40(1):2, 2004.

[194] W Y Wang, Thomas Moses, R C Linares, J E Shigley, Matthew Hall, and J E Butler. Gem-quality synthetic diamonds grown by a chemical vapor deposition (CVD) method. *Gems & Gemology*, 39(4):268–283, 2003.

[195] S. J. Charles, J. E. Butler, B. N. Feygelson, M. E. Newton, D. L. Carroll, J. W. Steeds, H. Darwish, C.-S. Yan, H. K. Mao, and R. J. Hemley. Characterization of nitrogen doped chemical vapor deposited single crystal diamond before and after high pressure, high temperature annealing. *physica status solidi (a)*, 201(11):2473–2485, 2004.

[196] F. Fuchs, C. Wild, K. Schwarz, W. Müller-Sebert, and P. Koidl. Hydrogen induced vibrational and electronic transitions in chemical vapor deposited diamond, identified by isotopic substitution. *Applied Physics Letters*, 66(2):177–179, 1995.

[197] F. Fuchs, C. Wild, K. Schwarz, and P. Koidl. Hydrogen-related IR absorption in chemical vapour deposited diamond. *Diamond and Related Materials*, 4(5-6):652–656, 1995.

[198] A. M. Edmonds, U. F S D'Haenens-Johansson, R. J. Cruddace, M. E. Newton, K. M C Fu, C. Santori, R. G. Beausoleil, D. J. Twitchen, and M. L. Markham. Production of oriented nitrogen-vacancy color centers in synthetic diamond. *Physical Review B - Condensed Matter and Materials Physics*, 86(3), 2012.

[199] D. Talbot-Ponsonby, M. Newton, J. Baker, G. Scarsbrook, R. Sussmann, A. Whitehead, and Susanne Pfenninger. Multifrequency EPR, 1H ENDOR, and saturation recovery of paramagnetic defects in diamond films grown by chemical vapor deposition. *Physical Review B*, 57(4):2264–2270, 1998.

[200] S. L. Holder, L. G. Rowan, and J. J. Krebs. Electron paramagnetic resonance forbidden transitions from hydrogen in polycrystalline diamond films. *Applied Physics Letters*, 64(9):1091–1093, 1994.

[201] L. Bergman and R. J. Nemanich. Raman and photoluminescence analysis of stress state and impurity distribution in diamond thin films. *Journal of Applied Physics*, 78(11):6709–6719, 1995.

[202] L M Pham, N Bar-Gill, D Le Sage, C Belthangady, A Stacey, M Markham, D J Twitchen, M D Lukin, and R L Walsworth. Enhanced metrology using preferential orientation of nitrogen-vacancy centers in diamond. *Physical Review B - Condensed Matter and Materials Physics*, 86(12), 2012.

[203] Philip Martineau, Mike Gaukroger, Riz Khan, and Dave Evans. Effect of steps on dislocations in CVD diamond grown on {001} substrates. In *Physica Status Solidi (C) Current Topics in Solid State Physics*, volume 6, pages 1953–1957, 2009.

[204] C. D. Clark, H. Kanda, I. Kiflawi, and G. Sittas. Silicon defects in diamond. *Physical Review B*, 51(23):16681–16688, 1995.

[205] A. Chayahara, Y. Mokuno, Y. Horino, Y. Takasu, H. Kato, H. Yoshikawa, and N. Fujimori. The effect of nitrogen addition during high-rate homoepitaxial growth of diamond by microwave plasma CVD. In *Diamond and Related Materials*, volume 13, pages 1954–1958, 2004.

[206] Syuto Tamura, Godai Koike, Akira Komatsubara, Tokuyuki Teraji, Shinobu Onoda, Liam P. McGuinness, Lachlan Rogers, Boris Naydenov, E. Wu, Liu Yan, Fedor Jelezko, Takeshi Ohshima, Junichi Isoya, Takahiro Shinada, and Takashi Tanii. Array of bright silicon-vacancy centers in diamond fabricated by low-energy focused ion beam implantation. *Applied Physics Express*, 7(11):115201, 2014.

[207] Benjamin Pingault, David-Dominik Jarausch, Christian Hepp, Lina Klintberg, Jonas N Becker, Matthew Markham, Christoph Becher, and Mete Atatüre. Coherent control of the silicon-vacancy spin in diamond. *arXiv*, 8:1–17, 2017.

[208] Qing Li, Marcelo Davanco, and Kartik Srinivasan. Efficient and low noise single-photon-level frequency conversion interfaces using Si3N4 microrings. In *2016 Progress in Electromagnetic Research Symposium (PIERS)*, pages 2574–2574. IEEE, 2016.

[209] L.J. Rogers, K.D. Jahnke, T. Teraji, L. Marseglia, C. Müller, B. Naydenov, H. Schauffert, C. Kranz, J. Isoya, L.P. McGuinness, and F. Jelezko. Multiple intrinsically identical single-photon emitters in the solid state. *Nature Communications*, 5:4739, 2014.

[210] Lachlan J. Rogers, Kay D. Jahnke, Mathias H. Metsch, Alp Sipahigil, Jan M. Binder, Tokuyuki Teraji, Hitoshi Sumiya, Junichi Isoya, Mikhail D. Lukin, Philip Hemmer, and Fedor Jelezko. All-optical initialization, readout, and coherent preparation of single silicon-vacancy spins in diamond. *Physical Review Letters*, 113(26), 2014.

[211] Vladimir Nadolinny, Andrey Komarovskikh, Yuri Palyanov, Yuri Borzdov, Igor Kupriyanov, Mariana Rakhmanova, and Olga Yuryeva. Silicon-containing defects in HPHT diamond synthetized in MgSiC system. *Physica Status Solidi (A) Applications and Materials Science*, 212(11):2460–2462, 2015.

[212] Ruffin E. Evans, Alp Sipahigil, Denis D. Sukachev, Alexander S. Zibrov, and Mikhail D. Lukin. Narrow-Linewidth Homogeneous Optical Emitters in Diamond Nanostructures via Silicon Ion Implantation. *Physical Review Applied*, 5(4):044010, 2016.

[213] Chunlang Wang, Christian Kurtsiefer, Harald Weinfurter, and Bernd Burchard. Single photon emission from SiV centres in diamond produced by ion implantation. *Journal of Physics B: Atomic, Molecular and Optical Physics*, 39(1):37–41, 2006.

[214] R. Kalish and S. Prawer. Graphitization of diamond by ion impact: Fundamentals and applications. *Nuclear Instruments and Methods in Physics Research Section B: Beam Interactions with Materials and Atoms*, 106(1-4):492–499, 1995.

[215] G. Braunstein and R. Kalish. Damage and lattice location studies in high-temperature ion-implanted diamond. *Applied Physics Letters*, 38(6):416–418, 1981.

[216] D.P. Hickey, K.S. Jones, and R.G. Elliman. Amorphization and graphitization of single-crystal diamond — A transmission electron microscopy study. *Diamond and Related Materials*, 18(11):1353–1359, 2009.

[217] V. M. Acosta, E. Bauch, M. P. Ledbetter, C. Santori, K. M C Fu, P. E. Barclay, R. G. Beausoleil, H. Linget, J. F. Roch, F. Treussart, S. Chemerisov, W. Gawlik, and D. Budker. Diamonds with a high density of nitrogen-vacancy centers for magnetometry applications. *Physical Review B - Condensed Matter and Materials Physics*, 80(11):115202, 2009.

[218] Alan T. Collins, Lars Allers, Christopher J H Wort, and Geoffrey A. Scarsbrook. The annealing of radiation damage in De Beers colourless CVD diamond. *Diamond and Related Materials*, 3(4-6):932–935, 1994.

[219] I N Kupriyanov, V A Gusev, Yu N Pal'yanov, and Yu M Borzdov. Photochromic effect in irradiated and annealed nearly IIa type synthetic diamond. *Journal of Physics: Condensed Matter*, 12(35):7843–7856, 2000.

[220] Tse Luen Wee, Yan Kai Tzeng, Chau Chung Han, Huan Cheng Chang, Wunshain Fann, Jui Hung Hsu, Kuan Ming Chen, and Eh Chung Yu. Two-photon excited fluorescence of nitrogen-vacancy centers in proton-irradiated type Ib diamond. *Journal of Physical Chemistry A*, 111(38):9379–9386, 2007.

[221] S. Felton, A. Edmonds, M. Newton, P. Martineau, D. Fisher, and D. Twitchen. Electron paramagnetic resonance studies of the neutral nitrogen vacancy in diamond. *Physical Review B*, 77(8):081201, 2008.

[222] I. Kiflawi, G. Sittas, H. Kanda, and D. Fisher. The irradiation and annealing of Si-doped diamond single crystals. *Diamond and Related Materials*, 6(1):146–148, 1997.

[223] H B Dyer and P Ferdinando. The optical absorption of electron-irradiated semiconducting diamond. *British Journal of Applied Physics*, 17(3):419–420, 1966.

[224] S Dannefaer and K Iakoubovskii. Defects in electron irradiated boron-doped diamonds investigated by positron annihilation and optical absorption. *Journal of Physics: Condensed Matter*, 20(23):235225, 2008.

[225] Ben Green. *Optical and magnetic resonance studies of point defects in single crystal diamond*. PhD thesis, The University of Warwick, 2013.

[226] Alan Collins. Determination of the boron concentration in diamond using optical spectroscopy. In *61st Diamond Conference*, Warwick, 2010.